

Development of nanostructured W and WL10 by high-pressure torsion

Zur Erlangung des akademischen Grades
eines **Doktor der Ingenieurwissenschaften**

von der Fakultät für Maschinenbau des
Karlsruher Institut für Technologie (KIT)

genehmigte Dissertation

von

Yiming Wang

aus Nei Mongol, China

Hauptreferent: Priv.-Doz. Dr.-Ing. Jarir Aktaa

Korreferent: Prof. Dr.-Ing. Martin Heilmaier

Tag der mündlichen Prüfung: 31.10.2014

Acknowledgments

This work was conducted in Institute for Applied Materials -Materials and Biomechanics (IAM-WBM) at Karlsruhe Institute of Technology (KIT). I gratefully acknowledge the financial support from China Scholarship Council (CSC), Helmholtz Association (HGF) and the R&D Nuclear Fusion Program of KIT.

Great thanks to my supervisor Priv.-Doz. Dr.-Ing. Jarir Aktaa, Who helped me to decide this research topic, and provided me important guidance during my research. This work will not be possible without his support. I would like to thank Prof. Dr.-Ing. Martin Heilmaier for reviewing my dissertation and providing me valuable suggestions. Grateful thanks to Prof. Dr. rer. nat. Oliver Kraft for his perspective advices and warm encouragement.

I would like to thank Dr.-Ing. Widodo Widjaja Basuki for his inspirable suggestions and fruitful discussions as well as providing me raw materials. Great thanks to Dipl.-Ing. Stefan Knaak for being always warmly accessible when high-pressure torsion experiments conducted. I would like to thank Dipl.-Ing. Daniela Exner for coaching me in electron backscattering diffraction (EBSD). Many thanks to Dr. rer. nat. Ruth Schwaiger for her kind guidance on nanoindentation and data evaluation. Thanks to Dr.-Ing. Mario Walter for the coach in scanning electron microscope (SEM) operation. Thanks to Dr.-Ing. Irène Sacksteder for showing me how to conduct Vickers hardness. I would like to thank Dr.-Ing. Ermile Gaganidze for providing me raw materials and his inspirable suggestions on AK Fusion. I want to thank M.Sc. Michael Mahler for helping me conduct fracture experiment in liquid nitrogen, translating my thesis abstract into German, and many other favors he did to me. I would like to thank Steffen Kohnle and Ralf Dahm for being so vigorous and helpful on teaching me to operate optical microscope, vacuum heat treatment furnace, and solving all kinds of problems. Thanks to Dipl.-Ing. Moritz Wenk for sharing his valuable experiences on EBSD sample preparation.

I would like to thank my colleagues for the warm working atmosphere maintained in my office. Thank Dr.-Ing. Wiebke Sittel for giving me fully and kind support in

research, improving my German language and all the other efforts she made to get me involve in this fabulous German culture. I would also thank Dipl.-Ing. Felipe Guzman for the interesting ideas he shared with me and his generous help. Thank Dr.-Ing. Thomas Weber for sufficient help he provided. Many thanks to Dr.-Ing. Christian Dethloff and Dr.-Ing. Ying Chen for providing me lots of advices on my research.

I would like to thank all my friends, Dr.-Ing. Pei He, Dipl.-Ing. Kuo Zhang, Dipl.-Ing. Dandan Qu for the beautiful time we spent together and their continuous help and encouragements. Thanks to my neighbors Dr. Linxian Li, Dr. Guo Peng and Dr.-Ing. Zhaoping Luo for cooking delicious Chinese food at home. Without them, I would lose 5 Pounds.

Appreciation and thanks should be given to my parents: Ying and Ya Qing, for being always there to understand, care and fully support my life and research.

Last but not least, I would like to state again my appreciation to all the people who have provided contributions to this research, although many of them are not mentioned due to the limited space.

Abstract

In this work, nanostructured pure W and W alloy are fabricated successfully by high-pressure torsion (HPT). The pure W consists of three different product forms with varies original microstructures, and W alloy refers to W-1wt% La₂O₃ (WL10). The process temperature of HPT ranges from 200°C to 700°C. The influences of original microstructure, alloying, process temperature, strain path and strain amount on HPT deformed W and WL10 are investigated. Fracture toughness and thermal stability of HPT deformed W and WL10 are evaluated as well. The evolution of microstructure, misorientation angle distribution, texture and hardness are measured by scanning electron microscopy (SEM), electron backscatter diffraction (EBSD) and nanoindentation.

Obvious microstructure refinements are achieved in pure W and WL10 when subjected to HPT. The grain sizes are decreased from initial coarse microstructure (~10μm) to hundreds of nanometers scale (80nm ~ 400nm) for both materials. Hardness is correspondingly improved from 6GPa to ~15GPa and 19GPa for pure W and WL10 respectively. Grain size is strongly influenced by process temperature and strain path. Lower process temperature results in finer microstructure for both materials. Monotonic torsion path leads to more effective grain refinement than cyclic torsion path. While for pure W, strain amount only has significant influence on microstructure refinement before saturation stage is reached. It is found that La₂O₃ particles in WL10 can benefit the grain size reduction process. No saturation region is observed for WL10 at process temperature of 400°C. Besides, the oxide particles facilitate the thermal stability of nanostructured WL10. Vickers indentation-induced cracking experiments indicate that fracture toughness of W at room temperature is enhanced by HPT. In order to improve the homogeneity along radial direction for HPT deformed W, multi-center HPT is introduced and W sample with uniform hardness distribution is efficiently achieved by this mean.

Zusammenfassung

In dieser Arbeit werden nanostrukturiertes W und W-Legierung erfolgreich durch das HPT Verfahren hergestellt. Das Ausgangsmaterial besteht aus drei Arten von reinem W mit unterschiedlichem Ausgangsgefüge, sowie WL10 (W-1% La_2O_3). Die HPT Prozesstemperatur liegt zwischen 200°C bis 700°C . Die Verfeinerung der Mikrostruktur wird für alle Materialien durch die Beobachtung der Änderung der Morphologie und des Fehlorientierungswinkels innerhalb der Körner oder der Korncluster untersucht. Der Einfluss von Ausgangsgefüge, Legieren, Prozesstemperatur und Verformungsgrad auf durch HPT verformten Proben wurde mittels der Rasterelektronenmikroskopie (SEM), der Rückstreuungselektronenbeugung (EBSD) und Nanoindentation untersucht. Ebenfalls wurde die Bruchzähigkeit und thermische Stabilität des HPT verformten W und WL10 untersucht.

Generell wird durch HPT die Korngröße sehr stark von der groben Ausgangsstruktur ($\sim 10\ \mu\text{m}$) auf die Nanometer-Skala (81nm-400nm) reduziert. Die Nanohärte stieg entsprechend von 6GPa auf 11GPa und 18GPa für reines W und WL10. Die erreichte Korngröße ist stark von der Legierung, der Prozesstemperatur und dem Formänderungsweg abhängig. Die Höhe der Belastung während des Torsions-HPT hat einen wesentlichen Einfluss auf die Fragmentierung der Probe bevor der Sättigungsbereich erreicht ist. Es hat sich gezeigt, dass die Existenz von La_2O_3 in WL10 sich nicht nur vorteilhaft auf die Reduktion der Korngröße, sondern auch auf die Stabilität der Mikrostruktur während der Wärmebehandlung auswirkt. Eine Reduktion der Prozesstemperatur könnte zu einer feineren Mikrostruktur und monotone Torsion zu einer besseren Kornverfeinerung im Gegensatz zur zyklischen Torsion führen. Außerdem wird durch Bruchversuche mit Hilfe der Indentation festgestellt, dass die Bruchzähigkeit von Wolfram bei Raumtemperatur durch HPT qualitativ verbessert wird. Um Probleme mit der Inhomogenität von HPT verformten Proben zu umgehen, wurde die „multi-center“ HPT eingeführt. Sie zeigt eine Verbesserung in Bezug auf die Homogenität.

List of symbols

γ_{SFE}	Stacking fault energy
ϵ_E	Engineering equivalent strain
ϵ_{HPCT}	Equivalent strain of HPCT
ϵ_T	True equivalent strain
ϵ_{zz}	Axial strain component
$\epsilon_{\varphi z}$	Shear strain component
β	Constant
η	Efficiency factor
θ	Torsion angle
θ_{hkl}	Bragg angle
λ	Wavelength of incident electron beam
ν	Poisson's ratio
ν_i	Poisson's ratio of Berkovich indenter
σ_0	Lattice frictional stress
σ_y	Yield stress
$\varphi_1, \Phi, \varphi_2$	Euler angles
b	Magnitude of the Burgers vector
d_{hkl}	Interplanar spacing of crystal plane $\{hkl\}$
d_{min}	Minimum grain size
g	Bunge Euler angles
g	Gravitational acceleration
h	Thickness of specimen
h_{max}	Maximum depth of the indenter penetrated in sample
h_s	Sink-in depth of sample during nanoindentation
k	Hall-Petch slope
k_B	Boltzmann's constant
n_c	Number of HPT cycles

n_r	Order of reflection
r	Distance from torsion axis
v_0	Constant relates to dislocation velocity
A	Projected contact area between the indenter and the sample
CS_c	Crystal-axis coordinate system
CS_s	Sample coordinate system
D	Grain size
$D_{\text{equivalent}}$	Equivalent grain diameter
D_{po}	Diffusion coefficient
E	Young's modulus
E_i	Young's modulus of Berkovich indenter
F_{max}	Maximum force during nanoindentation
G	Shear modulus
H	Hardness
H_{nano}	Hardness obtained from nanoindentation
H_0	Hardness of sample in as-received state
H_s	Hardness of sample in saturation state
N	Torsion revolution
\mathbb{N}	Natural number
P_{max}	Maximum load during nanoindentation
Q	Self-diffusion activation energy
R	Gas constant
S	Area
T	Absolute temperature
V	Volume

List of abbreviations

ARB	Accumulated Roll Bonding
BCC	Body-Centered Cubic
CSM	Continuous Stiffness Mode
CVD	Chemical Vapor Deposition
DBTT	Ductile-to-Brittle Transition Temperature
DDW	Dense Dislocation Walls
DEMO	Demonstration Power Plant
DRV	Dynamic Recovery
D-T	Deuterium and Tritium
EBSD	Electron Backscatter Diffraction
EBSF	Electron Backscatter Pattern
ECAE	Equal Channel Angular Extrusion
EDM	Electrical Discharge Machining
EDX	Energy Dispersive X-ray Analysis
GDR	Geometry Dynamic Recrystallization
HAGB	High Angle Grain Boundary
HB	Brinell Hardness
HK	Knoop Hardness
HPCT	High-Pressure Cyclic Torsion
HPT	High-Pressure Torsion
HR	Rockwell Hardness
HV	Vickers Hardness
IPF	Inverse Pole Figure
ITER	International Thermonuclear Experimental Reactor
LAGB	Low Angle Grain Boundary
LB	Lamellar Boundaries
MB	Micro-Band

ODF	Orientation Distribution Function
OIM	Orientation Image Map
OM	Optical Microscopy
OPS	Oxide Polishing Suspension
PF	Pole Figure
PVD	Physical Vapor Deposition
RD	Radius Direction
SD	Shear Direction
SEM	Scanning Electron Microscopy
SFE	Stacking Fault Energy
SPD	Severe Plastic Deformation
SPN	Shear Plane Normal direction.

Contents

Acknowledgments

Abstract

Zusammenfassung

List of symbols

List of abbreviations

Contents

1	Introduction	1
1.1	Motivation	1
1.2	Background	2
2	State of the research	7
2.1	Principles of high-pressure torsion.....	7
2.2	Grain refinement during severe plastic deformation.....	12
2.3	Development of materials by severe plastic deformation	15
3	Materials and approaches	17
3.1	W and WL10	17
3.2	Approach	18
3.2.1	Structure and plan.....	18
3.2.2	Fabrication methods	21
3.2.3	Optical microscopy	25
3.2.4	Scanning electron microscopy.....	25
3.2.5	Electron backscatter diffraction.....	26
3.2.6	Vickers indentation	34
3.2.7	Nanoindentation	36
3.2.8	Heat treatment	38
4	Results and discussions	39

4.1	Grain fragmentation during high-pressure torsion	39
4.1.1	Grain fragmentation of W	39
4.1.2	Grain fragmentation of WL10.....	44
4.1.3	Discussion	48
4.2	Influence of original microstructure and alloy	50
4.2.1	Torsion torque	50
4.2.2	Microstructure	51
4.2.3	Grain boundary misorientation.....	68
4.2.4	Texture	68
4.2.5	Hardness	70
4.2.6	Discussion	72
4.3	Influence of process temperature	75
4.3.1	Torsion torque	76
4.3.2	Microstructure	76
4.3.3	Grain boundary misorientation.....	87
4.3.4	Texture	88
4.3.5	Hardness	89
4.3.6	Discussion	90
4.4	Influence of strain path.....	92
4.4.1	Torsion torque	92
4.4.2	Microstructure	93
4.4.3	Grain boundary misorientation.....	97
4.4.4	Texture	98
4.4.5	Discussion	98
4.5	Thermal stability	99
4.5.1	Microstructure	99
4.5.2	Grain boundary misorientation.....	110
4.5.3	Texture	111
4.5.4	Discussion	113

4.6	Hall-Petch relationship.....	115
4.7	Fracture toughness.....	116
4.8	Homogeneity improvement.....	117
4.8.1	Increasing torsion revolution.....	118
4.8.2	Multi-center high-pressure torsion.....	118
4.8.3	Discussion.....	122
5	Conclusions and outlook.....	123
5.1	Conclusions.....	123
5.2	Outlook.....	124
	Bibliography.....	125
	Appendix.....	135
A.	Equivalent strain calculation.....	135
B.	Cone-shaped sample method.....	140
	List of publications.....	143
	Curriculum Vitae.....	145

1 Introduction

1.1 Motivation

Tungsten (W) has the highest melting point among all metals, and exhibits outstanding high temperature performances, such as creep resistance. Furthermore, it shows distinguished erosion resistance, thermal conductivity and low activation under neutron irradiation [1, 2]. Therefore, W is chosen to be one of the candidate armor and structure materials for future fusion reactor. Besides, researchers found out that La_2O_3 dispersion in W can facilitate the machinability and increase the recrystallization temperature [3, 4]. Hence WL10 (W-1wt% La_2O_3) becomes a competitive choice for future fusion reactor as well. However, the relative high ductile-to-brittle transition temperature (DBTT) particularly of coarse-grain W and WL10 limits their application [4]. High-pressure torsion (HPT) is a promising severe plastic deformation (SPD) method to fabricate nanostructured materials, which may exhibit high strength and toughness simultaneously. Therefore, in this work, nanostructured W and WL10 are fabricated by HPT and their microstructure, thermal stability, mechanical properties are investigated.

Three questions frequently arisen are pursued:

- i. How to enhance the room temperature toughness of W and WL10?
- ii. How about the thermal stability of nanostructured W and WL10?
- iii. How to improve the homogeneity along radial direction of HPT deformed sample?

The first question is one of the most important issues for W and W alloys. Researchers make great efforts to decrease the DBTT of W, and the details are addressed in section 1.2. In this work, nanostructuring is employed on W and WL10 to improve their room temperature fracture toughness. Due to the limited dimension of the sample fabricated by HPT, indentation-induced cracking experiments are carried out for the fracture toughness evaluation.

For the second question, nanostructured material is considered to be in metastable state. Thermal stability measurements of HPT deformed W and WL10 are essential. The operation temperature window for cooling finger in divertor has been estimated to be in the range of 800 to 900°C [5]. Therefore in this work, heat treatments are performed at 1000°C in vacuum, and the duration is up to 9 hours. Microstructure evolution as well as hardness changes are analyzed.

For the third question, owing to the character of HPT, the as-deformed material exhibits inhomogeneity along radius direction [6-9]. It is reported that by increasing torsion revolution, a

relative homogenous microstructure of pure aluminum can be obtained after 20 turns [10], which is time and energy consuming. Besides, researchers found out if the HPT setup is in perfect alignment, the un-deformed central region of specimen remains even after more than 10 torsion revolutions [9, 11]. In this work, multi-center HPT procedure is invented so as to improve the homogeneity of HPT deformed materials efficiently.

A fundamental question about HPT is concerned: How can one crystal be fragmented into many volume elements with different orientations? To pursue the answer, the subtle changes of microstructure and crystal orientation caused by high-pressure torsion are observed. The role of oxide particles play in WL10 on grain fragmentation is emphasized.

Furthermore, in order to systematically investigate the HPT deformed W and WL10, four influence factors are considered:

- i. Original microstructure. Three kinds of pure W with different original microstructures are taken analysis, which are named W_rod1, W_rod2 and W_plate after their raw material product forms. The following question is discussed later in the thesis: Whether pure W from different product forms result in the same microstructure after HPT? If so, under which condition?
- ii. Alloying. The deformation behavior is highly affected by alloying, and so as the subsequent microstructure and mechanical property after deformation. In this work, W-1wt% La₂O₃ (WL10) is employed to compare with pure W (W_rod2), since they have identical original microstructure and product form of raw material.
- iii. HPT process temperature. Process temperature has huge impact on deformation behavior of materials as well. Considering the DBTT of W is around 400°C [12], the HPT experiments conducted in this wok step across DBTT, which are from 200°C to 700°C. The microstructure and hardness changes with varies process temperatures are examined.
- iv. Strain path. Conventional HPT refers to monotonic torsion path, while in order to study the strain path influence, high-pressure cyclic torsion (HPCT) is introduced. As the name suggests, HPCT refers to reverse torsion strain path during the deformation process.

1.2 Background

Ever since the mass-energy equivalence has been proposed by Einstein described by the famous equation [13]: $E = mc^2$, people start to realize that there is huge amount of energy stored in nuclei. Nuclear fission was discovered in 1938, and compared with traditional chemical reaction like coal burning, nuclear fission can generate 3 million times more specific energy (Coal: 8.14 kWh/kg, U235-Pu239: 22800000 kWh/kg) [14]. Nowadays, power reactors are built worldwide. However, there are drawbacks come with nuclear fission. For example, due to the high half-life

periods of raw materials, the used fuel rods have to be stored for hundreds of thousands of years in salt-mines. Furthermore, nuclear leakage can lead to catastrophe, such as the accidents happened in Chernobyl, Ukraine (1986) and Fukushima, Japan (2011).

Nuclear fusion is considered to be an alternative energy solution. Small amounts of deuterium (D) and tritium (T) are fueled in nuclear fusion reaction to produce helium nucleus (He), neutron and energy [15], as described below:



There are several advantages come with nuclear fusion: firstly, it has even higher capacity to generate energy. By nuclear fusion, about 4 million times more specific energy can be produced compared to the burning of coal (D-T: 33.2kWh/kg) [14]. Besides, the fuel materials D and T are abundantly available and their fusion reaction is inherently safe. In addition, nuclear fusion emits no greenhouse gases and thus is environmental friendly.

To generate extreme high temperature in fusion reaction, a tokamak device is employed as magnetic fields to confine the hot plasma in International Thermonuclear Experimental Reactor (ITER) and Demonstration Power Plant (DEMO). The conceptual illustration of DEMO reactor is shown in Fig. 1.1.

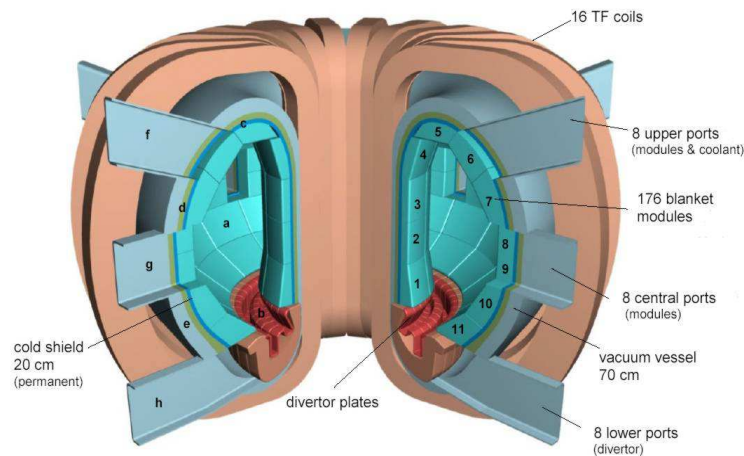


Fig. 1.1: Conceptual view of fusion DEMO reactor [16].

Hot plasma will run within the torus-shaped vacuum vessel, and the inner components of the reactor will expose to extreme high heat fluxes and erosion. As indicated in Fig. 1.1, blanket modulus and divertor plates are involved in plasma-facing components. Low-activation ferritic

and martensitic steels are selected as structure materials for blanket [17]. While for preventing blanket from erosion damage, W / W alloy might be an option as armor material. Furthermore, divertor is positioned on the bottom of the vacuum vessel and responsible for extracting heat, helium ash and other impurities from the plasma. Materials in this region should consist of excellent high temperature strength, high erosion resistance, low activation under neutron irradiation and distinguished thermal conductivity. Therefore W and W alloys are chosen as structure and/or armor materials for divertor as well.

According to the expectation for structure material in fusion reactor, W and W alloys are expected to exhibit DBTT in the range of 200°C to 400°C [4]. However, as mentioned before, the DBTT of coarse-grain W is normally around 400°C [12] or even higher [18]. Besides, WL10 exhibits a DBTT at 950°C [4]. This inherent brittleness of W and WL10 at room temperature constrains their application.

The ductility behavior of single crystal W indicates that grain boundary weakness is the main reason for the embrittlement of polycrystalline W and W alloys [1]. Consequently, methods related to grain boundary strengthening are of interest. This could be achieved by reducing the concentration of impurities on the grain boundaries via refining grain size, or by introducing complicated grain boundary structures through deformation [1]. The factors which can affect DBTT of W and W alloys are listed in Table 1.1, and they are cataloged into mechanical, microstructural and chemical aspects.

Table 1.1: Factors influencing the DBTT of W / W alloys [19]

Mechanical	Microstructural	Chemical
Stress state (tensile/compressive /shear stress)	Grain size/grain area	Distribution of interstitial/substitutional impurities (C, N, O, P, S, Re)
	Cold work	
Strain rate	Texture; grain shape	
	Twins; sub grain boundaries	
	Dislocations	
	Surface roughness (notches, surface cracks)	

There are several courses to increase the ductility of W, which are mainly including solid solution [20, 21], nanostructuring [22, 23] and fabricating composite materials [24-26]. It has long been recognized that Rhenium and Iridium additions can increase the ductility of W at low

temperatures, and also improve their high temperature strength and plasticity. However, W-Re/Ir solid solutions are cautiously employed because of their high expense and irradiation brittleness. The key feature of nanostructured material is that the volume fraction of grain boundary area is comparable to the interior grain area, leading to sorts of distinct properties, such as high strength, increased ductility, enhanced super-plasticity at lower temperatures, etc. [27-29]. Among all the nanostructuring methods, HPT is chosen to be performed in this work, mainly because of its extreme high efficiency on grain refinement. More details about the superiority of HPT beyond other methods are stated in section 2.1.

In chapter 2, state of the research will be introduced. The principles of HPT, in particular how to calculate the equivalent strain on HPT deformed sample will be provided. The grain refinement procedures during severe plastic deformation (SPD) will be overviewed. Recent development of SPD deformed materials will be addressed. Chapter 3 refers to materials and approach. Chapter 4 consists of the results and discussions. Conclusions and outlook can be found in chapter 5.

2 State of the research

2.1 Principles of high-pressure torsion

As stated in last chapter, nanostructuring is a competitive method to improve the fracture toughness of coarse-grain W. In general, nanostructuring methods can be classified into bottom-up and top-down methodologies. Bottom-up method involves with consolidation, such as chemical vapor deposition (CVD) [30, 31], physical vapor deposition (PVD) [32] as well as mechanical alloying [33]. Top-down method refers to crystallization from metallic glass [34, 35] and severe plastic deformation (SPD). SPD mainly consists of high-pressure torsion (HPT), equal channel angular extrusion (ECAE) [36] and accumulated roll bonding (ARB) [37].

HPT is firstly invented by Bridgman at the beginning of last century [38], and the facility are further developed by Valiev [29, 39]. During the process, specimen is positioned in between two anvils, as illustrated in Fig. 2.1 a). After applying a high pressure of several GPa along axial direction, one anvil rotates with a given speed while the other anvil is fixed. Thereby material undergoes both axial and shear strain while maintains its 2-dimensional geometry during HPT. The sample used is usually in disk-shape, as is illustrated in Fig. 2.1 b).

Among all the methods related to nanostructuring, HPT has the advantages beyond others, as listed below:

- i. Most of the bottom-up methods are associated with the so called “two-step” procedure, which refers to powder synthesis at the first step. The volume defects such as porosity and impurity are more likely introduced through powder synthesis. For example, when W is deformed by ball milling, NiW intermetallic is formed due to impurities introduced through fabrication and consequently degrade the materials properties [33]. In contrast to bottom-up methods, top-down means including HPT are usually not consisting of powder synthesis [40], therefore the possibility of impurity dopant incorporation is rare through HPT process, and HPT becomes a more economical way to produce nanostructured materials.
- ii. The inhibition of micro-crack formation is essential during deformation especially for brittle materials like W. Therefore by conducting HPT, even brittle materials can be deformed due to the high compressive load applied on sample, and ends up with condensed materials.
- iii. Among all the SPD methods, HPT is the most efficient way to generate extreme large strain on sample. The strain rate is well controllable and the torsion torque can be measured during the procedure.

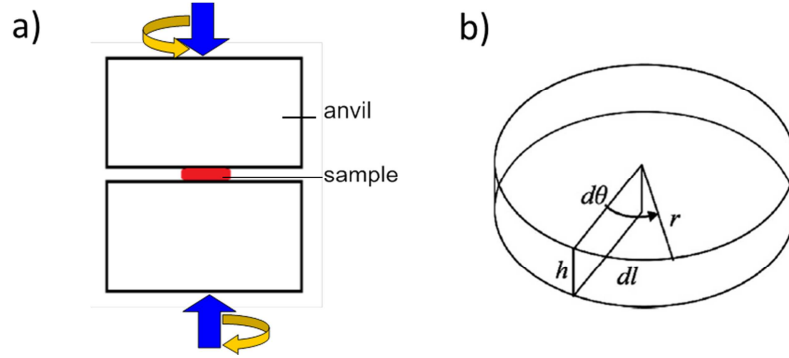


Fig. 2.1: Illustrations of a) high-pressure torsion (this work) and b) disk-shaped sample [41].

High pressure is quite necessary to accomplish large torsion deformation on sample. An example of cast iron is shown in Fig. 2.2 [42]. Without compressive load, sample rupture occurs at small angular displacement. However with compressive load, the twist angle can increase to over 70° before fracture. Another advantage of applying high pressure is that the slippage between sample and anvil can be reduced during deformation, so that the measurement of strain is more accurate. Moreover, as mentioned above, the micro-crack formation in brittle material can be retarded due to the high pressure.

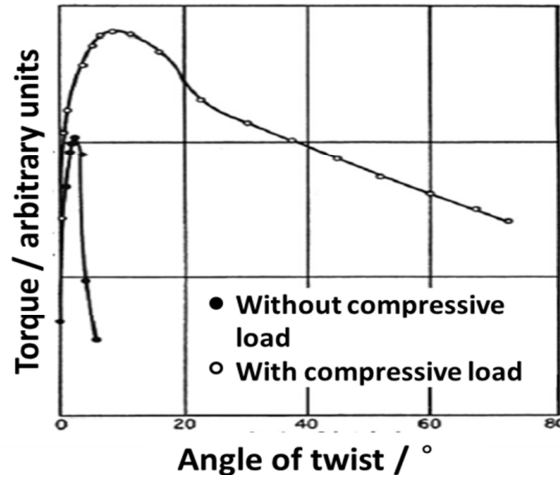


Fig. 2.2: Torque versus angle of twist for cast iron [42].

During HPT, the sample withstands uniaxial and shear strain concurrently, according to von Mises yield criterion, the equivalent strain under such strain state can be written as:

$$\varepsilon_v = \sqrt{\frac{2}{3} \varepsilon : \varepsilon} = \sqrt{\varepsilon_{zz}^2 + \frac{4}{3} \varepsilon_{\varphi z}^2} \quad (2.1)$$

where ε_{zz} is the axial strain component, $\varepsilon_{\varphi z}$ refers to simple shear strain component. If one assumes that the sample height (h) is kept constant during HPT, which is to say, ε_{zz} is equal to zero. The eq. (2.1) can be reduced correspondingly:

$$\varepsilon_E = \frac{2\varepsilon_{\varphi z}}{\sqrt{3}} = \frac{2\pi Nr}{\sqrt{3}h} \quad (2.2)$$

where N is torsion revolution, r represents the distance from torsion axis. The derivation process can be found in Appendix-A. Even though eq. (2.2) is widely employed by researchers [43-46], it is actually only suitable for constrained HPT with monotonic strain path. By constrained HPT, it means that sample is deformed in a fixed space without losing its original dimension including height. While under most conditions, unconstrained HPT is applied. In this case, material is free to flow outwards due to consistent uniaxial pressure. The reduction in sample height will reach certain value until the friction between sample and anvil is sufficient to prevent material from outflow [38]. Fig. 2.3 shows the changes of sample height along with torsion revolution in this work for HPT deformed W. A simple fitting function is employed:

$$h(\theta) = h_{\infty} - (h_{\infty} - h_0) \cdot e^{-b \cdot 2\pi N} \quad (2.3)$$

in which h_0 refers to sample height after compression but before torsion, while h_{∞} is the sample height after infinite torsion revolutions, and b corresponds to material property. The following fitting parameters are obtained: $h_{\infty}=0.2\text{mm}$, $h_0=0.8\text{mm}$ and $b=0.28$.

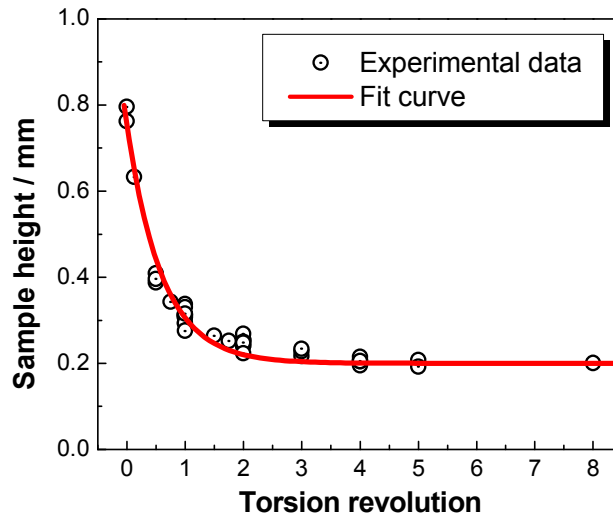


Fig. 2.3: The changes of sample height along with torsion revolution.

Taking sample height reduction during HPT into consideration, the von Mises equivalent true strain can be expressed as:

$$\varepsilon_T = \sqrt{\left(\ln\left(\frac{h_\infty - (h_\infty - h_0)e^{-b*2\pi N}}{h_0}\right)\right)^2 + \frac{4}{3}\left[\frac{r}{2bh_\infty}\left(\ln\left(e^{b*2\pi N} - \left(1 - \frac{h_0}{h_\infty}\right)\right) - \ln\left(\frac{h_0}{h_\infty}\right)\right)\right]^2} \quad (2.4)$$

The detail derivation processes can be found in Appendix-A. Fig. 2.4 provides equivalent strain curves obtained from different algorithms. All of them are related to 3mm from torsion axis on the sample (ie. $r = 3\text{mm}$). The engineering strain is plotted by employing eq. (2.2) with a constant sample height of 1mm. While equivalent true strain is calculated by subjecting eq. (2.4). In addition, another equivalent true strain is calculated by finite element simulation (see details in Appendix-A), as is indicated by the green stars in Fig. 2.4. Furthermore, an equivalent strain calculated by using eq. (2.2) with height value of 0.2mm (h_∞) is plotted to exhibit the upper limit of equivalent strain under this experimental condition. Fig. 2.4 a) refers to different strain values within 1 torsion revolution, while Fig. 2.4 b) exhibits larger scope up to 8 torsion revolutions. It is observed that before around 0.2 torsion revolution, equivalent true strain is close to equivalent engineering strain, which is colored in red and black respectively. However the equivalent true strain increases towards upper limit with torsion revolution, as is seen clearly in Fig. 2.4 b). Besides, the calculated equivalent true strain is verified by the finite element simulation, as is indicated by the overlapping of green stars and red line in Fig. 2.4 a). The relationship between equivalent true strain and equivalent engineering strain is provided in Fig. 2.5. In this thesis, equivalent true strain is employed to interpret the results in chapter 4.

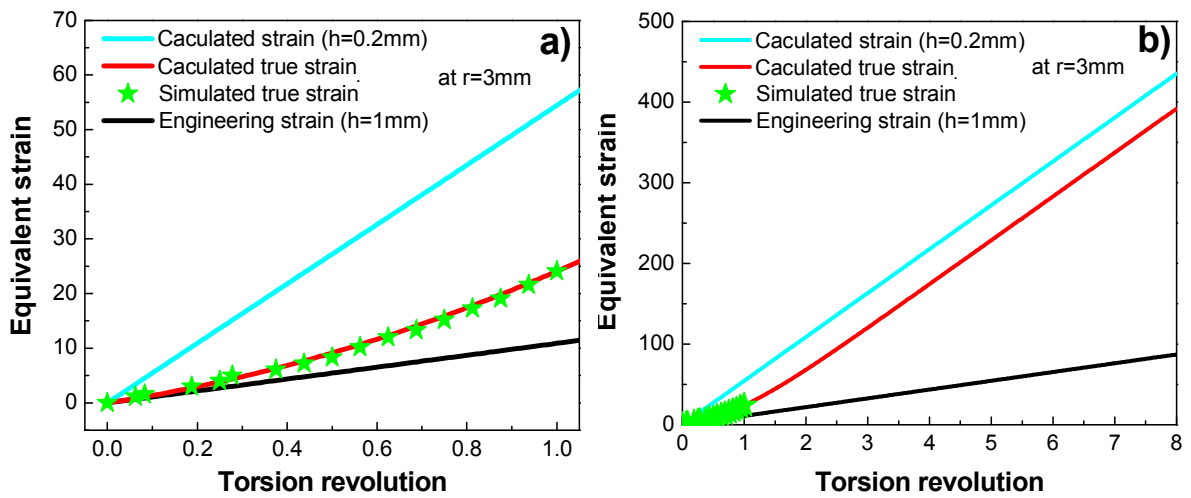


Fig. 2.4: Equivalent strain as function of torsion revolution during high-pressure torsion (HPT) from different algorithms.

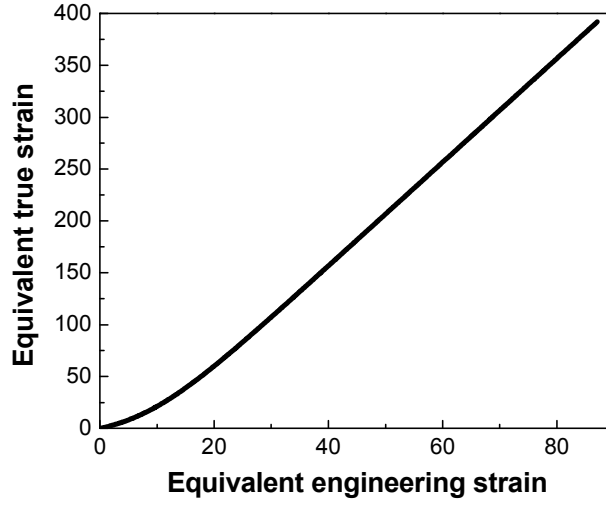


Fig. 2.5: Relationship between equivalent true strain and equivalent engineering strain for high-pressure torsion (HPT) deformed W.

The equivalent strain algorithms in Fig. 2.4 are all referring to monotonic strain path. In order to study the strain path effect, high-pressure cyclic torsion (HPCT) is conducted in this work. HPCT is associated with strain path reversal after each torsion angle of 90° , as shown in Fig. 3.6. In this case, an efficiency factor should be considered when calculating the equivalent strain [46]:

$$\varepsilon_{HPCT} = \eta \sum_{i=1}^{2n_c} |\Delta\varepsilon_i| \quad (2.5)$$

where n_c is the number of torsion cycles and η is the efficiency factor. According to dislocation density theory, there are two extreme cases during cyclic torsion [46]:

- i. All of the dislocations generated by the reversal strain path turn back into their sources and disappear, then the efficiency factor η would be zero after a complete cycle of deformation;
- ii. New sets of dislocations are created through reversal strain path and it is assumed that all dislocations remains in the material after a complete cycle of deformation, in this case, η equals to 1.

If we assume the efficiency factor during monotonic torsion is 1, the efficiency factor for HPCT is in this range: $0 < \eta < 1$, which means that HPCT results in slower microstructure refinement compared to monotonic process. An example of obvious microstructure difference between HPT and HPCT deformed Ni is shown in Fig. 2.6 [47]. The torsion revolutions applied for both

processes are the same. This phenomenon can be found for Al-3%Mg-0.2Sc [48], Armco iron [49], Fe-0.03%C [9] and high purity Al as well [9].

Two mechanisms are proposed to explain the coarsening during HPCT. In dislocation movement aspect, as stated above, dislocations with different signs can be generated from back and forth shear deformation, thus the chance of dislocation annihilation is larger during HPCT than its counterpart [46]. In strain-induced grain boundary movement aspect, as schematically depicted in Fig. 2.6, in which a cube volume element is representing a grain [47], the geometrically required volume change is limited for HPCT.

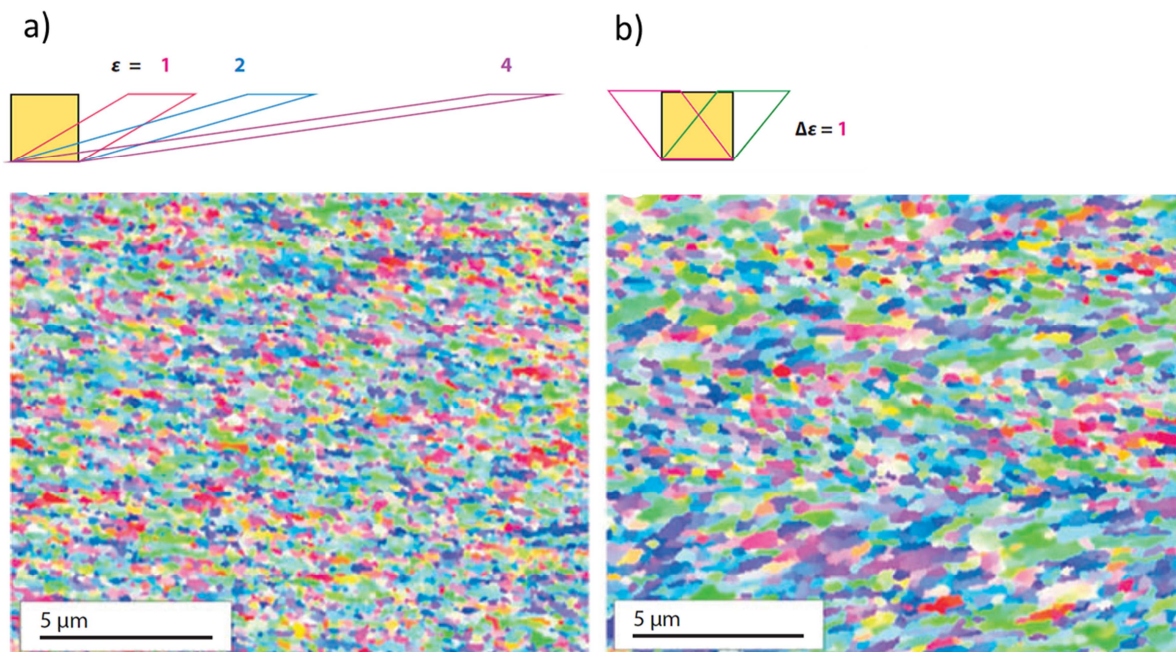


Fig. 2.6: Illustrations of grain geometry changes and orientation image maps from a) high-pressure torsion (HPT) and b) high-pressure cyclic torsion (HPCT) [47].

2.2 Grain refinement during severe plastic deformation

During severe plastic deformation, crystal fragmentation occurs and results in materials with considerable refined microstructure. Besides, the grain refinement process exhibits saturation for most of the reported metals. In this section, grain fragmentation and saturation mechanisms during SPD are reviewed. A quantitative model involves with saturation grain size is introduced.

In general, grain refinement and saturation have both extrinsic and intrinsic reasons [50, 51]. The extrinsic influence factors involve with deformation history of materials [52] and current

deformation procedure. The latter consists of strain amount, stress state, deformation temperature and so on. The intrinsic reason is related to material composition, alloying etc., which can influence the stacking fault energy (SFE) of material. Intensive studies have been reported about how SFE affects refinement process [44, 50, 52-54] and saturation process during SPD [6, 55].

When deformation occurs, in order to maintain the continuity of material, local stress field varies within one grain. As for materials with medium to high SFE such as Ni, Al and W, this variation of stress state facilitates the activation of dislocation slip systems in assorted parts of grain. Dislocation cell blocks are formed within crystal after small strain amount, as shown in Fig. 2.7 a). A dislocation cell block consists of micro-band (MB), dense dislocation walls (DDW) and equiaxed cells. Experimental observation shows that misorientation angle across these areas increases along with strain amount [51], due to the interaction and tangling of dislocations during the deformation [53]. High angle grain boundaries (HAGB) are formed and further induce the fragmentation of original crystals. With increase of strain amount, elongated grains with lamellar boundaries are commonly observed. A typical microstructure after rolling is demonstrated in Fig. 2.7 b). The elongation direction is parallel to material flow. Besides, this lamellar structure is also observed at the beginning of HPT process in this work. However after certain strain amount, the grain aspect ratio is reduced to near to 1, as is shown in Fig. 2.7 c). This transition with strain amount is well documented [47, 55-57], and can be attributed to dynamic recovery (DRV) or geometric dynamic recrystallization (GDR).

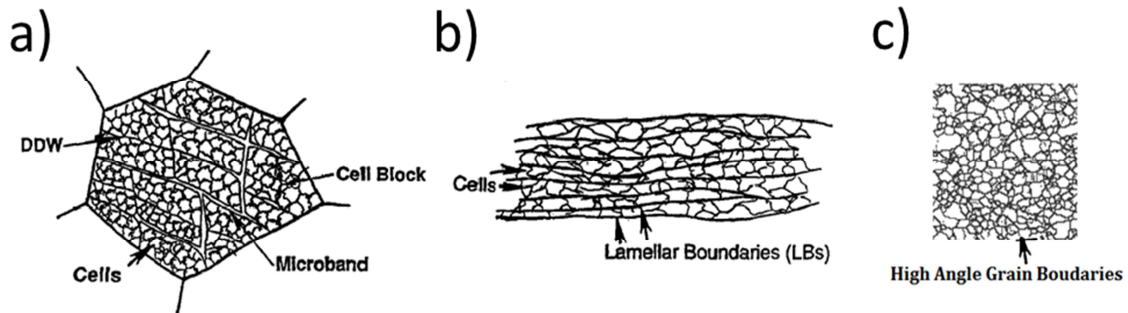


Fig. 2.7: Schematic illustration of deformation microstructures and grain subdivision for medium to high SFE materials. a) Small to medium strain deformation, $\epsilon_{vM}=0.06-0.08$ with long microbands (MB) and dense dislocation walls (DDW) surrounding groups of cells in cell blocks [51]; b) large strain deformation, $\epsilon_{vM}>1$ with lamellar boundaries (LBs) parallel to the deformation direction, sandwiching in narrow slabs of cells or equiaxed subgrains [51]; c) Severe strain deformation, $\epsilon_{vM}>25$ with more equiaxed grains separated by high angle grain boundaries (HAGB) (this work).

For materials with low SFE, twinning is the main deformation mode during SPD. The grain fragmentation procedure is illustrated in Fig. 2.8 [53]. Twin boundaries are formed after small amount of strain (s. Step 1). Afterwards, high density dislocations are accumulated at twin boundaries (s. Step 2). With further strain amount, the original atomically flat coherent stacking faults and twin boundaries are curved (s. Step 3). HAGBs are generated by interaction of twins and secondary stacking faults, as shown in step 4 in Fig. 2.8. When deformation continues, this interaction process goes on and leads to grain refinement with equiaxed grain shape (s. Step 5).

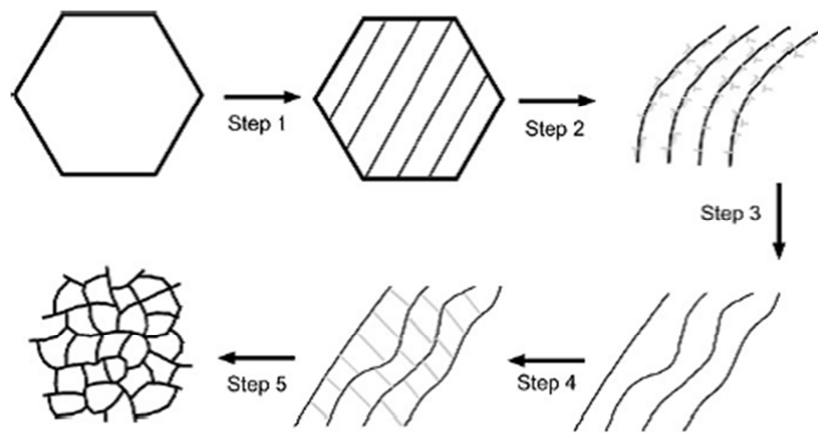


Fig. 2.8: Schematic illustration of the grain refinement mechanism for low SFE materials during severe plastic deformation (SPD) [53].

Several models are proposed by researchers to quantitatively study the grain refinement process during SPD. It is found out that W in W–25%Cu composite demonstrates a multi-fractal behavior during HPT [58]. In addition, Mohamed developed a comprehensive model to predict the minimum grain size in saturation region after ball milling [59], which is given as:

$$\frac{d_{min}}{b} = A \left(e^{-\frac{\beta Q}{4RT}} \right) \left(\frac{D_{po} G b^2}{v_0 k_B T} \right)^{0.25} \left(\frac{\gamma_{SFE}}{G \cdot b} \right)^{0.5} \left(\frac{G}{H} \right)^{1.25} \quad (2.6)$$

where d_{min} is the minimum grain size, b is the magnitude of the Burgers vector, A and β are constants, Q is the self-diffusion activation energy, R is the gas constant, T is the absolute temperature, D_{po} is the diffusion coefficient, G is the shear modulus, v_0 is a constant relates to dislocation velocity, k_B is Boltzmann's constant, γ_{SFE} is the stacking fault energy and H refers to hardness. This model is based on the balance between dislocation generation by imposed strain

and dislocation annihilation/recombination by thermal recovery. It has successfully predicted the minimum grain size for materials with medium to high SFE such as Ni, Al and W [59]. Despite this model is designed for ball milling, the results from HPT deformed Cu and Cu–10% Zn show well consistency [60].

2.3 Development of materials by severe plastic deformation

SPD materials with improved mechanical properties are extensively reported recently, as electively listed in Table 1.2. Such as high yield strength, high hardness, improved fracture toughness even for intrinsic brittle materials and super-plasticity at elevated temperatures.

According to Hall-Petch relationship, smaller grain size leads to higher strength/hardness [61], which is normally given as:

$$\sigma_y = \sigma_0 + kD^{-\frac{1}{2}} \quad (2.7)$$

where σ_y is the (local) yield stress, σ_0 refers to lattice frictional stress and all the other contributions to flow stress without the influence of grain size, k is the Hall-Petch slope, and D is the grain size. A detail interpretation of the fundamental theories can be found in [62]. Hall-Petch relationship has been successfully applied to many systems, including SPD deformed materials, such as HPT deformed Ni [63, 64] and Cu [65]. Moreover, the deviation from regular Hall-Petch relationship is also reported concerns varies materials [66-68] and is named “inverse Hall-Petch relationship”. A review about inverse Hall-Petch relationship for nanostructured materials can be found in [69]. It usually occurs when the grain size is at least smaller than 100nm. However the physical background of this phenomenon is not clearly understood yet.

Besides, the fracture toughness of materials is improved because of reduced grain size, increased misorientation angle between adjacent grains and/or additional edge dislocation induced by severe deformation [70].

Furthermore, it is suggested that the twinning capability and grain refinement together improve the ductility of SPD deformed Cu-Zn alloys [71]. While excessive free volume and nanoscale microstructural heterogeneity are suspected to be the reasons for ductility improvement in HPT deformed metallic glass [72].

In the next chapter, materials and approaches will be stated.

Table 1.2: Development of SPD deformed materials.

Synthesis	Materials	Mechanical properties	Ref.
HPT	Al alloy	Superplasticity at 673K	[73]
HPT	Al-Mg-Sc	High-strain-rate superplasticity at 673K	[8]
HPT	Mg-Al alloy	Superplasticity at 423K	[74]
HPT	Ti-6Al-4V	Superplasticity at above 377K	[75]
HPT	Cu-Zn alloys	Ductility	[71]
HPT	Cu-Ag alloy	High tensile strength of 1420 MPa	[44]
HPT	Cu-Al alloy	Strength–ductility synergy	[76, 77]
HPT	Zr-Cu-Ni-Al metallic glass	Ductility	[72]
ECAP-HPT	Cu–Zn alloys	Optimizing strength and ductility	[78]
HPT	Zn	High strength and reasonable ductility	[45]
ECAP	Al	Superplasticity at 673K	[79]
HPT	Ti-Nb-Ta-Zr	High hardness	[80]
HPT	Ni	High strength and ductility	[81]
ECAP	Cu–Al alloys	Both strength and ductility	[82]
HPT	Cu	Fracture toughness and high strength	[83]
HPT	Cu–Cr	High hardness	[84]
HPT	Cr	Increase of strength and ductility (limited)	[85]
ECAP	Fe	Fracture toughness	[86]
HPT	Fe-Cu alloys	High hardness and enhanced thermal stability	[87]
HPT	2024 Al alloy	High hardness to three folds	[88]
HPT	W, WVM, WL10	Fracture toughness	[70]
HPT	W	High strength, localized shearing is observed under uniaxial dynamic compression	[89]
HPT	Ta	High strength	[90]
HPT-annealing	Ti	Both high strength and ductility	[91]
HPT-annealing	Ni	High strength and ductility	[92]
HPT/HPCT	W and WL10	High strength, better fracture toughness High thermal stability(nano-WL10)	This work

3 Materials and approaches

3.1 W and WL10

Three kinds of pure W are employed in this work, namely W_rod1, W_rod2 and W_plate according to their product forms of raw materials. W_rod1, W_rod2 are from rod materials with diameters of 18mm and 8mm respectively and delivered from PLANSEE, Austria. W_plate is from plate material with 1mm in thickness. Distinct from other three materials with uniform microstructures, W_plate is occupied by inhomogeneous microstructure containing both coarse and fine grains, as is demonstrated in Fig. 4.12. Besides, WL10 is from rod material with 8mm in diameter, which has the same geometry as W_rod2 raw material. The non-metallic impurities of corresponding materials are provided in Table 3.1. The guaranteed purity of W in W_rod1 and W_rod2 are 99.96wt% and 99.97wt% respectively, and the content of W in WL10 ranges from 98.9wt% to 99.1wt%.

Table 3.1: The contents of non-metallic impurities in the investigated materials.

Element	W_rod1		W_rod2		WL10	
	Guaranteed/ $\mu g/g$	Typical/ $\mu g/g$	Guaranteed/ $\mu g/g$	Typical/ $\mu g/g$	Guaranteed/ $\mu g/g$	Typical/ $\mu g/g$
C	30	15	30	6	30	6
H	5	1	5	0	5	0
N	10	<5	5	1	5	1
O	30	<5	20	2	-	-
P	50	20	-	-	-	-
Si	20	<10	20	1	20	1
S	5	<2	-	-	-	-

Before HPT is subjected, disk-shaped specimen is firstly machined from raw materials by Electrical Discharge Machining (EDM). The positions colored in red in Fig. 3.1 indicate where we take the specimen from original rod or plate materials. The geometry of specimen is 8mm in diameter and 1mm in height for all materials.

Secondly, both sides of sample are grinded to 2500# in order to remove the oxidation layers from sample surface, as well as to obtain a relative smooth contact surface between anvil and specimen.

Thirdly, samples are cleaned by acetone in ultrasonic bath for 15min.

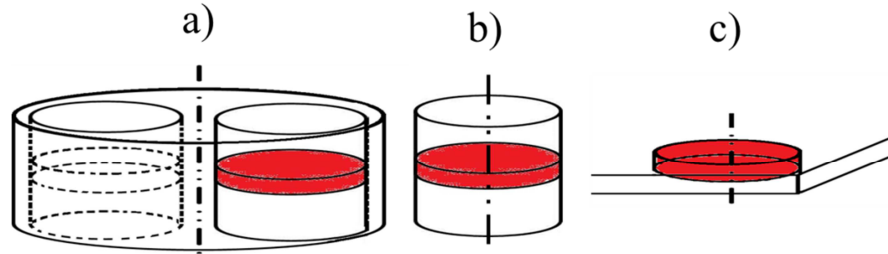


Fig. 3.1: Original position of specimen (colored in red) from raw materials.
a) W_rod1; b) W_rod2 and WL10; c) W_plate.

3.2 Approach

3.2.1 Structure and plan

Figure 3.2 demonstrates the structure tree of experiments and results in this thesis. Since HPT is acknowledged by its powerful capability of grain refinement, the grain fragmentation procedures of W and WL10 during HPT are firstly addressed in section 4.1.

Secondly, from section 4.2 to section 4.4, three factors which influence the HPT deformed W and WL10 are studied as followings: The effects of original microstructure and alloying are discussed in section 4.2. The influence of HPT process temperature is provided in section 4.3 and the strain path effect is discussed in section 4.4.

In section 4.5, thermal stability of HPT deformed W and WL10 is investigated. Heat treatments are taken place at 1000°C up to 9 hours. The evolutions of grain and subgrain sizes, grain boundary character and texture are studied.

In section 4.6, Hall-Petch relationships of as-deformed and deformed-annealed W and WL10 are assessed.

In section 4.7, room temperature fracture toughness of HPT deformed W is qualitatively evaluated by observing Vickers indentation-induced crack.

At last, several improvements on fabrication of radial direction homogeneous materials by HPT are brought out in section 4.8. Nanoindentation is employed to reveal the effectiveness of those methods.

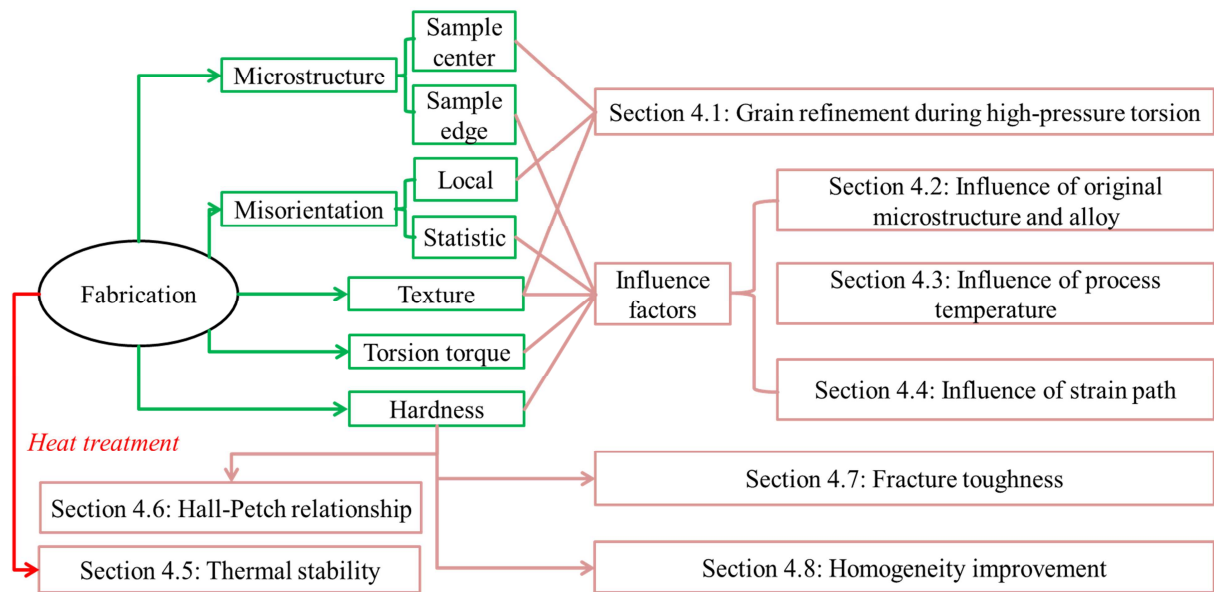


Fig. 3.2: Structure tree of experiments and results in this work.

In Fig. 3.2, the contents encircled in green frames refer to direct experiment results from this work. The interpretations of them and the corresponding experiment measurement methods are provided as following:

- i. Microstructure evolution at sample center and edge region. The edge region involves with position at 3mm from torsion axis. The experiment methods related are: scanning electron microscopy (SEM) and electron backscatter diffraction (EBSD);
- ii. Local misorientation means accumulated relative misorientation angle within a grain or several adjacent grains. Statistic misorientation refers to correlated grain boundary misorientation angle distribution, which displays the misorientation data between neighboring points in an area. The analyzed area contains more than 500 grains normally to acquire sufficient information. The experiment method employed is EBSD;
- iii. Texture evolution is displayed by series of pole figures (PF), which are obtained by EBSD;
- iv. Torsion torque can be observed during HPT process directly from sensors connected in biaxial machine;
- v. Hardness value of as-received and deformed W and WL10 are obtained by nanoindentation. Moreover, Vickers indentation measurements are performed to observe the crack induced by indentation. The impressions of indents are observed by optical microscopy (OM) and SEM.

Table 3.2 summarizes the specimen fabrication plan for all materials under different experimental conditions.

Table 3.2: Investigated HPT samples under given conditions

Material	Torsion revolution	Process temperature and fabrication method			
		300/200°C* ¹	400°C	550°C	700°C
W_plate	0.5r	-	HPT	-	-
	1r	-	HPT	-	-
	2r	-	HPT	-	-
	4r	-	HPT	-	-
	5r	-	HPT	-	-
W_rod1	0.5r	-	HPT	-	-
	1r	-	HPT, multi-center HPT* ²	-	-
	2r	-	HPT, multi-center HPT	-	-
	4r	-	HPT	-	-
W_rod2	0.5r	-	HPT.	-	HPT
	1r	-	HPT	-	HPT
	2r	HPT	HPT, HPCT	HPT	HPT
	4r	-	HPT	-	HPT
	8r	-	HPT	-	HPT
WL10	0.5r	-	HPT	--	HPT
	1r	-	HPT	-	HPT
	2r	HPT, HPCT	HPT, HPCT	HPT	HPT
	4r	-	HPT, HPCT	-	HPT

*¹: This step temperature means that the first torsion revolution is operated at 300°C and the second revolution is performed at 200°. The reason for not subjecting 2 torsion revolutions at 200°C is that the sample will be crushed under such condition. While after pre-torsion at 300°C, the formability of sample is improved and can be performed under 200°C without failure.

*²: Multi-center HPT refers to a technical improvement of HPT process, see details in section 3.2.2.

3.2.2 Fabrication methods

1) Conventional HPT

The HPT facility used in this thesis is illustrated in Fig. 3.3. It is installed in biaxial testing machine, as shown in Fig. 3.4 a).

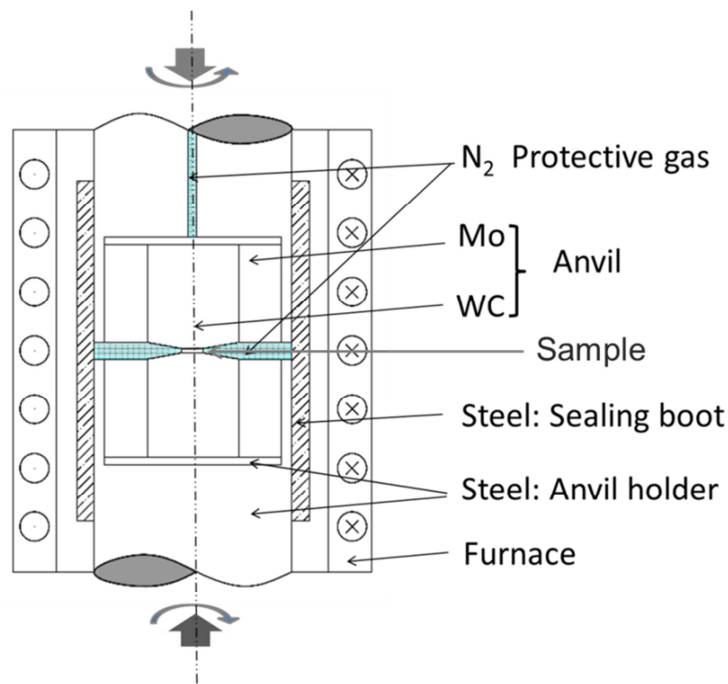


Fig. 3.3: Schematic illustration of high-pressure torsion (HPT) facility in this work.

There are mainly three parts concerned in HPT facility in Fig. 3.3:

- i. HPT setup. The setup consists of anvil and anvil holder, and anvil includes head and ring. The HPT setup can be clearly viewed by its cross section image in Fig. 3.4 b), in which the geometry and material of each part are indicated. From setup center to edge: the head is fabricated by WC-7%Co due to its outstanding compressive yield strength even at high temperature, and it is delivered from Barat Carbide. The diameter of the head stage is 8mm, which is exactly the same with sample diameter. Moreover, in order to prevent WC-7%Co head from rupture, a ring part is adopted to generate compressive stress field by interference fit joining at experimental temperatures. Ring part is made of Mo, which possesses both desirable strength and ductility. The most out part of HPT setup is anvil holder, which is fabricated by steel (RGT). The connection of anvil holder and ring part is through screw fasten.
- ii. Furnace. It is positioned outside the HPT setup to generate necessary heat during HPT. There are two thermocouples in the facility, one is positioned inside furnace, and the other is located in the anvil.

- iii. Protective gas system. Since oxidation of W occurs at 400°C to 500°C [1], and some of the deformation temperatures are beyond that (s. Table 3.2). It is fairly necessary to introduce a protective gas system into the facility. As shown in Fig. 3.3, a N₂ channel (Ø8.5 mm) is drilled throughout the upper anvil holder, and a sealing boot made of steel is positioned tightly near anvil holder.

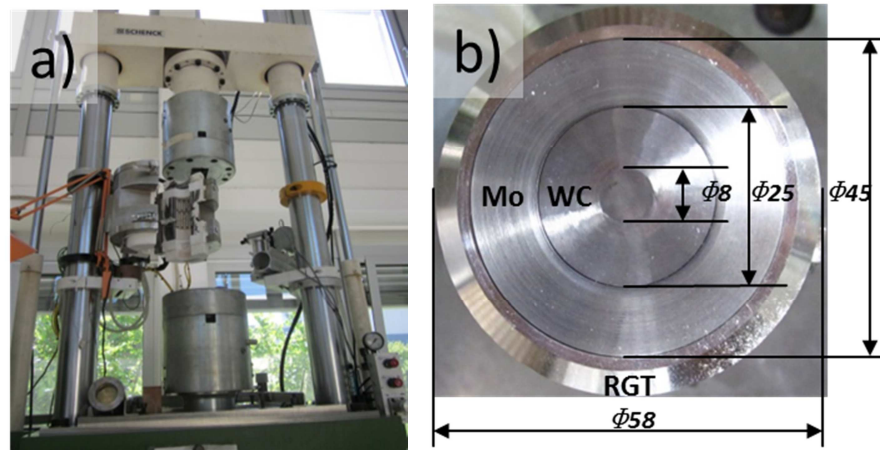


Fig. 3.4: a) The biaxial test machine (SCHENCK); b) Cross section image of setup.

For conventional HPT, the following routine procedures are conducted:

- i. Before testing, straight measurement of upper and lower setups is conducted to make sure the system is in well alignment.
- ii. The HPT setup is heated up to required temperature without sample under protective atmosphere. As mentioned before, the temperatures in furnace and anvil are measured by thermocouples. The typical temperature increase curves along with heat time are shown in Fig. 3.5. It is noticed that for our facility, to reach 400°C in anvil region, the furnace should be kept at 600°C, and at least 1 hour is needed to let the temperature becomes stable in anvil region.
- iii. After the experimental temperature is reached in anvil region, HPT sample is carefully placed on the lower anvil by the assistant of optical light to indicate the edge line of head stage. Before any load is applied, holding time of 15min is needed to ensure the temperature in the sample is consistent with anvil.
- iv. A compressive pre-load of around 100N is subjected on sample to generate steady contact before HPT.
- v. The uniaxial pressure is 5GPa for all the HPT experiments. After each 90° torsion angle, the compressive load withdraws to almost zero, at the meantime anvil moves back to its

starting position. Thereafter a new cycle of pressure and torsion begins, as is plotted in Fig. 3.6 a). By this mean the torsion moment is mono-directional.

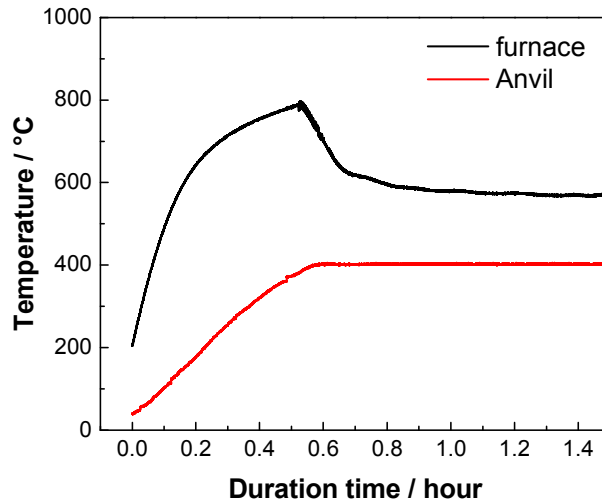


Fig. 3.5: Heating curves with duration for furnace and HPT anvil.

2) High-pressure cyclic torsion

The anvil position changes during HPT and high-pressure cyclic torsion (HPCT) within 1 torsion revolution are compared in Fig. 3.6. During HPT, torsion path is monotonic under pressure, as is shown in Fig. 3.6 a). Whereas the torsion moment direction is reversed after each 90° during HPCT, and the uniaxial pressure is constant of 5GPa, as is displayed in Fig. 3.6 b).

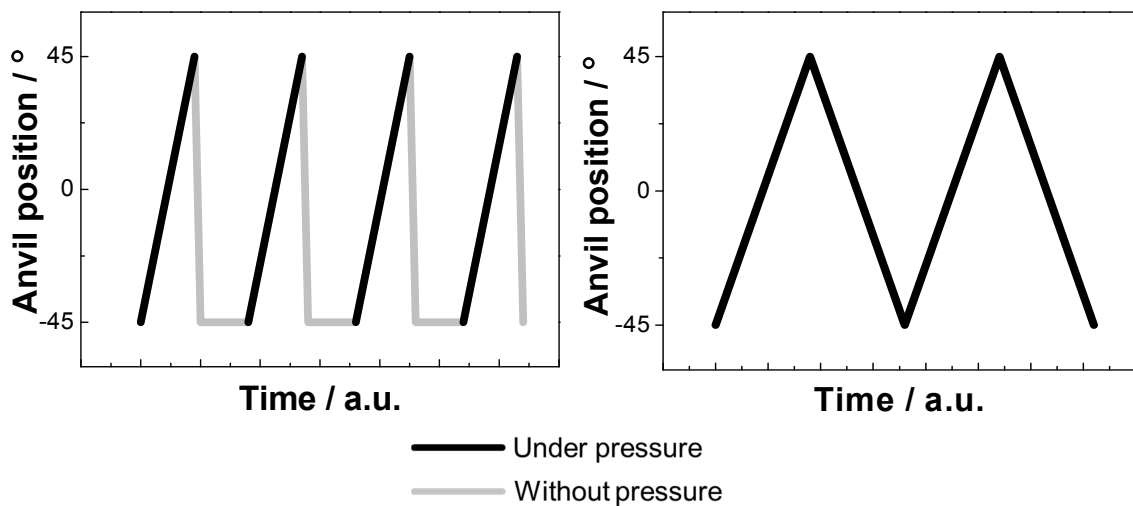


Fig. 3.6: Illustrations of anvil position change within 1 torsion revolution for a) high-pressure torsion (HPT) and b) high-pressure cyclic torsion (HPCT).

3) Multi-center HPT

To improve the homogeneity of HPT deformed materials along radial direction, a multi-center HPT is introduced in this work. Fig. 3.7 demonstrates the procedure of multi-center HPT with 1 and 2 torsion revolutions, in which RD refers to radial direction, SD is shear direction and SPN stands for shear plane normal direction. The hollow circle represents ideal sample. During conventional HPT, the sample center position is still. While during the multi-center HPT, movements of sample position are conducted manually, following certain step order. The deviation of sample center from anvil center is indicated by the dashed circles in Fig. 3.7. The step order is indicated by number. The small red solid circle has no number in it because there are steps overlapped in the same position. Step 1 and 4 are at the same position for multi-center with 1 revolution, while step 1, 4, 7 and 8 are overlapped for multi-center with 2 revolutions. Besides, the red solid circle refers to the original position of specimen and also the center of anvil. By each step, torsion angle of 90° is applied on the sample.

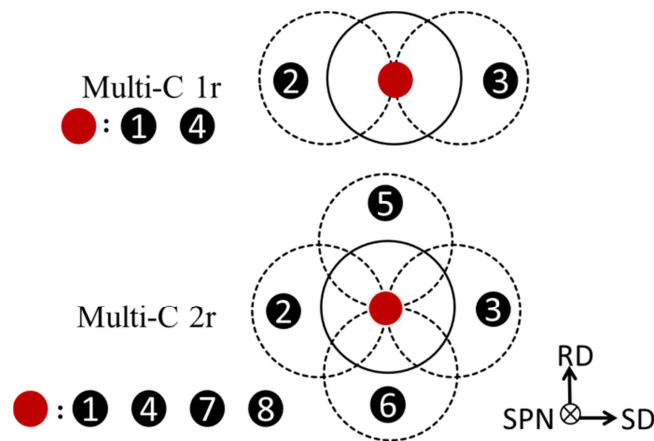


Fig. 3.7: Illustrations of multi-center high-pressure torsion (HPT) method after 1 and 2 torsion revolutions.

In this work, W_{rod1} is conducted on both conventional and multi-center HPT for 1 and 2 torsion revolutions respectively. The process temperature is 400°C . The equivalent strain on deformed whole sample after multi-center HPT is apparently less than conventional HPT after the same torsion revolution. However they are still compared because that what we concern most is the efficiency on sample homogeneity improvement along radial direction.

3.2.3 Optical microscopy

The principle of optical microscopy (OM) refers to using visual light and series of objective lenses to magnify sample to thousands magnification at maximum.

In this work, OM is employed by KEYENCE to reveal the surface condition of sample after grinding, as well as to measure the diagonal dimensions of indent impression after Vickers indentation. KEYENCE contains two lenses: VH-Z20R (with magnification from 20 to 200) and VH-Z100R (with magnification from 100 to 1000). The microscope is connected to a digital camera for image capture and subsequent measurements. The Dual Light Base Unit (OP-84430) and the Adjustable Illumination (OP-72402) are attached in this OM system. The sample preparation consists of grinding and polishing. Details procedures are given in Table 3.3.

Table 3.3: Grind and polish parameters for HPT W/WL10

Method	Grind/Polish materials	Abrasive size	Rotation	Process time
			Speed / min- 1	
Grind	SiC paper and water	220#	500	20s
		320#		30s
		500#		1min
		800#		2min
		1200#		3min
		2500#		5min
Polish	Diamond suspension	6 μ m	200	8min
		3 μ m, 1 μ m, 0.1 μ m	200	15min
		Oxide polishing suspension (OPS)	200	30min

3.2.4 Scanning electron microscopy

In order to observe the interested areas on the sample surface by larger magnification than OM can reach, scanning electron microscopy (SEM) is conducted.

SEM is collecting interaction information from focus electron beam and sample. The signals can be used to generate secondary electron image and backscattered electron image. In this work, a Philips XL30 field emission SEM is employed. Secondary electron images are obtained to analyze the sample surface morphology. Besides, chemical composition of certain area can be

obtained by conducting energy dispersive X-ray analysis (EDX) which is an appendage to SEM equipment. During the SEM observation, the vacuum degree is less than 6×10^{-5} mbar and the electron beam accelerating voltage is 25kV. Working distance between sample upper surface and beam gun is 10mm for image capture while is 7.5mm for composition determination. Sample preparation for SEM is provide in Table 3.3.

3.2.5 Electron backscatter diffraction

Electron backscatter diffraction (EBSD) is a powerful method for microstructure analysis by providing extensive crystallographic information about bulk crystal materials at a grain-specific level. In this work, EBSD is employed as the primary measurement manner for as-received and HPT deformed W and WL10.

The following information can be obtained from EBSD:

- i. Morphological parameters such as grain size and grain shape;
- ii. Crystal orientation mapping with texture characterization;
- iii. Grain boundary analysis.

In this section, principle of EBSD is reviewed at first. Crystal orientation determination and representation are introduced next. Grain boundary characterization is stated thereafter. At last the main technical parameters used in this work are provided.

3.2.5.1 Principle of EBSD

The main components of electron backscatter diffraction (EBSD) system are shown in Fig. 3.8 [93]. It contains two parts: one refers to regular SEM system, in which a 70° -titled sample holder is employed. The other is related to electron backscatter pattern (EBSP) collection and interpretation system.

Crystallography interpretation is based on the understanding of Kikuchi pattern. The first observation of Kikuchi pattern was by Nishikawa and Kikuchi in 1928 [94]. In general, Kikuchi pattern can be generated under both transmission electron microscope (TEM) and SEM. The principle of Kikuchi pattern formation under SEM is demonstrated in Fig. 3.9 a). When the incident electron beam encounters sample surface, the interaction between electrons and crystal lattice occurs. Primary backscattered electrons are then diffused in all directions during this process, among which there must be some electrons reflected by certain sets of crystal plane at particular angle obeying Bragg's law:

$$n_r \lambda = 2d_{hkl} \sin \theta_{hkl} \quad (3.1)$$

where n_r is the order of reflection, λ is the wavelength of incident electron beam, d_{hkl} is the interplaner spacing of crystal plane $\{hkl\}$ and θ_{hkl} is the Bragg angle.

In 3-dimensional space, the backscattered electrons from the same source which obey Bragg's law generate two cones, as shown in Fig. 3.9 b). One is from $\{hkl\}$ and the other is from $\{\bar{h}\bar{k}\bar{l}\}$. The edges of these two reflection cones are captured by phosphor screen and thus a pair of Kikuchi lines is displayed. While in crystal materials, more than one sets of crystal plane can participate in the Bragg reflection, therefore series of intersected line pairs can be produced correspondingly, which is called Kikuchi pattern, as illustrated in Fig. 3.8 (top-right image). One can easily conclude from equation (3.1) that under the stable electron beam with fixed λ , different crystal planes can represent different Bragg angles. Besides, as shown in Fig. 3.9 b), the angular width of Kikuchi pair $\{hkl\}$ is twice of the Bragg angle θ_{hkl} . In addition, the intersection point of Kikuchi band corresponds to zone axe or pole. Therefore, by acknowledging the position and width of certain number of Kikuchi bands in the EBSP, crystal orientation can be determined. For example 3 or 4 families of Kikuchi bands are sufficient to index a cubic crystal [95].

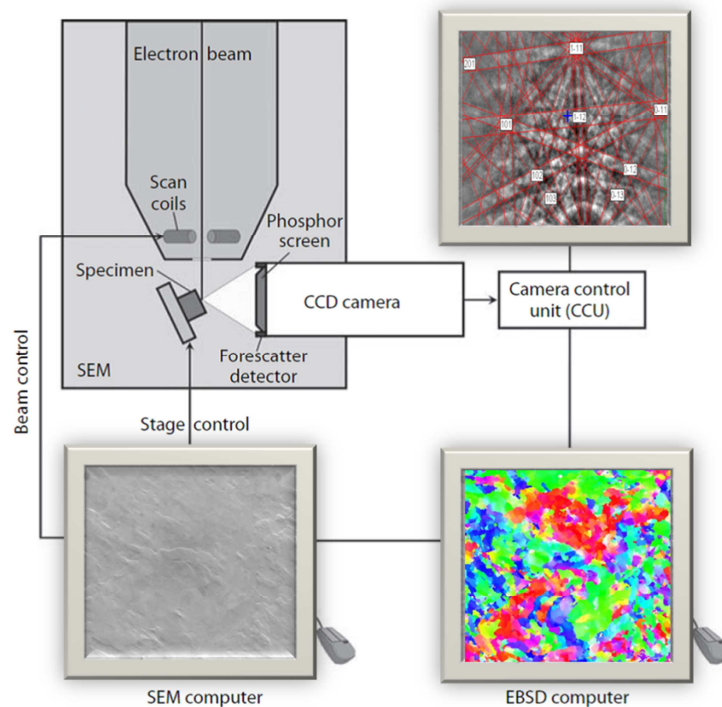


Fig. 3.8: Components of EBSD system [93].

Top-right image: Kikuchi pattern;
Bottom-right image: inverse pole figure (IPF) (this work).

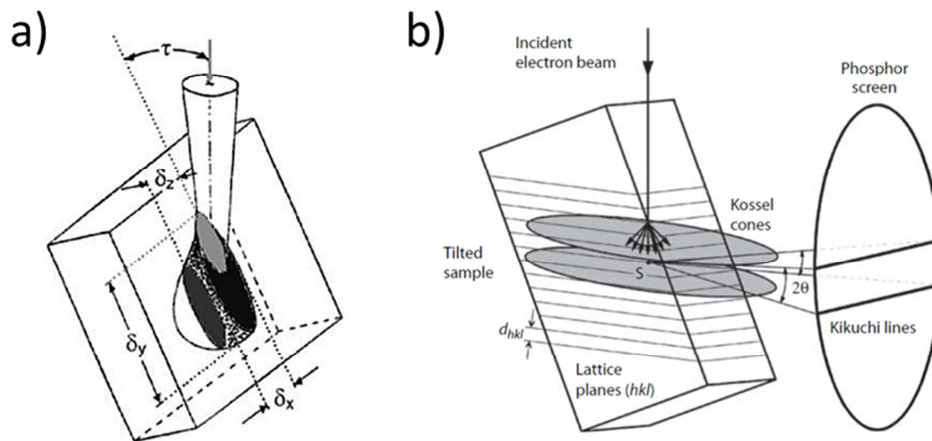


Fig. 3.9: Schematics of the a) interaction volume and spatial resolutions (δ) between incident beam and titled sample for EBSD under SEM;
 b) Diffracting cones with respect to one reflecting plane [95].

3.2.5.2 Crystal orientation and texture

There are several methods to display the crystal orientation from EBSD, including pole figure (PF), inverse pole figure (IPF) and orientation distribution function (ODF).

1) Pole Figure

The PF represents orientation of crystal in specimen coordinate system (SD: shear direction; RD: radial direction; SPN: shear plane normal direction). Since it is difficult to intuitively exhibit crystal orientations in 3-dimensional space, stereographic projection is introduced to transform 3-dimensional information into 2-dimensional plane, as is demonstrated in Fig. 3.10. By stereographic projection, a crystal is placed in the center of an imaginary unit sphere, three axis of the unit sphere referring to SD, RD and SPN respectively as depicted. Since every crystallographic plane can be specified by its normal line, a specific crystal plane can be represented by the intersection point of normal line and positive hemisphere. After that, by drawing a straight line from the pole point of negative hemisphere to the intersection point of crystal plane in positive hemisphere, the projection point of given crystal plane is obtained on the projection plane. Theoretically, any orthogonal right-handed angle crystal coordinate can be chosen as projection plane. However several low index planes such as $\{100\}$, $\{110\}$ and $\{111\}$ are the most common used projection planes. Fig. 3.10 illustrates the generation of $\{100\}$ pole figure in cubic crystal.

Besides stereographic projection, an alternative approach named equal area projection is also used. Compared with the former one, it preserves the area information however sacrifices the precise relative angle information during the projection. In this work, stereographic projection method is employed.

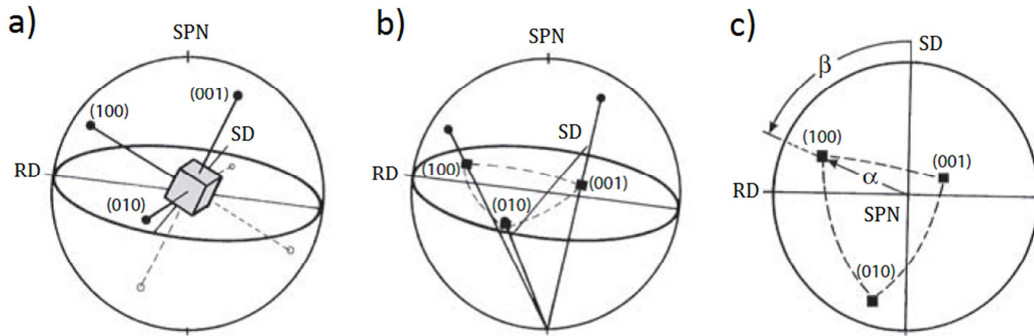


Fig. 3.10: Presentation of the $\{100\}$ poles of a cubic crystal in the stereographic projection.
 a) Crystal in the unit sphere; b) projection of the $\{100\}$ poles onto the equator plane;
 c) $\{100\}$ pole figure and definition of the pole figure angles α and β for the (100) pole [93].

As mentioned before, the crystal orientation in PF has already been limited to specific planes. Therefore sometimes combination of series of PFs is required to fully characterize the texture. Take HPT deformed W for example, as shown in Fig. 3.11, the crystallographic projection planes of $\{111\}$, $\{110\}$ and $\{100\}$ are displayed by stereographic projection.

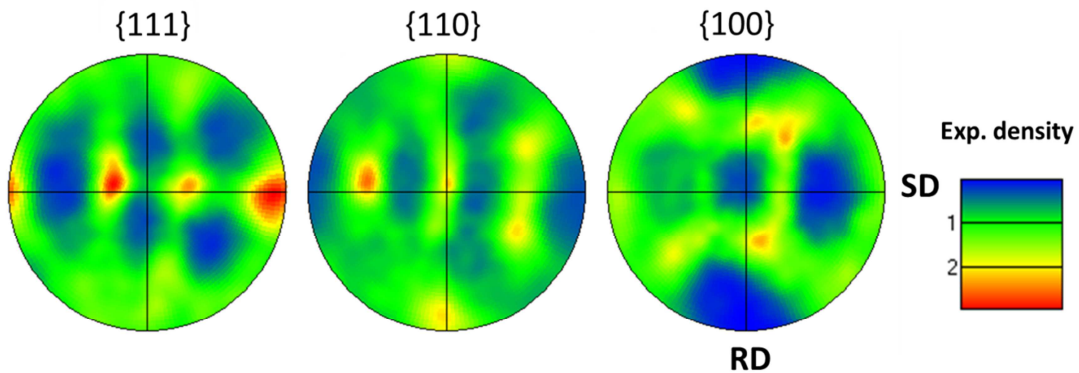


Fig. 3.11: Pole figures with projection crystallographic plane of $\{111\}$, $\{110\}$ and $\{100\}$ respectively, the corresponding density is given on the right column (this work).

Combining the three PFs in Fig. 3.11, $[111] \parallel SD$ texture component, $\{110\} \parallel SPN$ component and a weak $[100] \parallel SD$ can be observed from each PF separately, and the texture exist here can

written as $\{110\} [111]$. The expression of $\{110\} [111]$ suggests that $\{110\}$ crystal plane is parallel to the shear plane of investigated specimen and $[111]$ direction aligns with sample shear direction. In addition, strong texture is indicated by sharp cluster of the poles and high pole density, whereas weak texture referring to a broad distribution of the poles and low pole density in contrary.

2) Inverse Pole Figure

Inverse pole figure represents which crystallographic direction aligns with the specimen direction. A standard stereographic projection along SPN is plotted in Fig. 3.12 a). Due to symmetric it can be divided into twenty four stereographic triangles, and a standard triangle intercepted from stereographic projection is sufficient to deliver the information, as outlined in Fig. 3.12 a) and showed in Fig. 3.12 b).

One of the advantages for IPF is that it can conveniently observe fiber texture. Fiber texture means certain lattice plane is preferentially parallel to specific specimen direction. The IPF of HPT deformed W is provided in Fig. 3.12 c), and a $\{110\} // \text{SPN}$ texture can be observed, which is consistent with the interpretation from PF in Fig. 3.11.

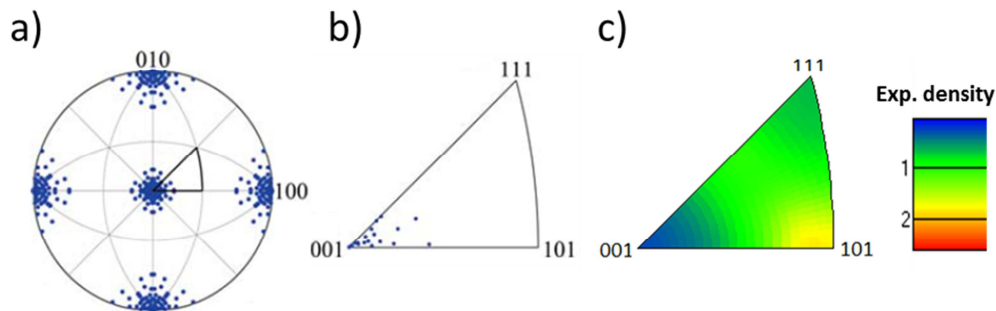


Fig. 3.12: Shear plane normal (SPN) direction inverse pole figures. a) Standard stereographic projection with a cube texture; b) Standard stereographic triangle of the cube texture corresponding to a) [95]; c) Inverse pole figure (this work).

3) Euler space and orientation distribution function

Both PF and IPF provide the crystallographic information by 2-dimensional projection, and are described in miller indices ($\{hkl\} [uvw]$). However the crystallographic orientation in 3-dimensional space can be described by all Euler angles, the sample coordinate system (CS_s) is transformed into crystal coordinate system (CS_c). There are several conventions to accomplish the rotation, and the most commonly used one is proposed by Bunge [96, 97]. Three notations are

employed as Bunge Euler angles, which is $(\varphi_1, \Phi, \varphi_2)$. The rotation of sample coordinate system is performed in Fig. 3.13 a), and corresponding manipulations are:

- i. Rotating CSs about SPN with φ_1 to transform RD to RD' and SD to SD', while [001], SPN and RD' are in the same plane.
- ii. Rotating CSs about SD' with Φ so that [001] coincides with SPN.
- iii. Rotating CSs about SPN'' with φ_2 , so as [100] coincides with SD' and [010] coincides with RD'.

Every point in Euler space has three Euler angle and represents a 3-dimentional crystallography in given sample. Furthermore, for quantitative evaluation, the orientation distribution function (ODF) of projection poles can be obtained by using series of pole figures. ODF reflects the normalized probability density associated with the occurrence of the texture in the sample [93, 98], and the expression is as below:

$$f(\mathbf{g}) = \frac{dV(\mathbf{g})/V}{d\mathbf{g}}, \quad \mathbf{g} = \{ \varphi_1, \Phi, \varphi_2 \} \quad (3.2)$$

where V is referring to total sample volume and $dV(\mathbf{g})/V$ is the volume fraction of crystals that have the same crystallographic orientation \mathbf{g} , and \mathbf{g} is described in Bunge Euler angles. In general, the Euler space size is in the range of $0 \leq \varphi_1, \varphi_2 \leq 2\pi$, and $0 \leq \Phi \leq \pi$. However, the crystal symmetry as well as sample symmetry can reduce the Euler space size. Taking cubic crystal for example, the Euler space can be fully described within $0 \leq \varphi_1, \Phi, \varphi_2 \leq \pi/2$. An example involves with ODF of HPT deformed W is given in Fig. 3.13 b).

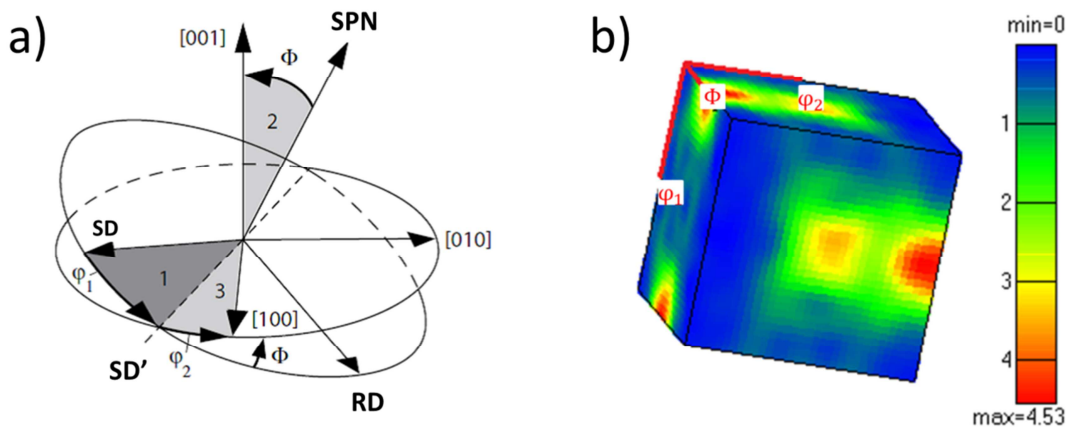


Fig. 3.13: a) Rotation illustration through the Euler angles $\varphi_1, \Phi, \varphi_2$ following the order 1, 2, 3 [93]; b) Orientation distribution function plotted in Euler space (this work).

3.2.5.3 Grain boundary characterization

The powerful crystallography analysis ability of EBSD offers efficient measurements for grain size determination. A detail review about grain and subgrain characterization by EBSD is written by Humphreys [99].

In this work, grain sizes are determined by both high angle grain boundary (HAGB) and low angle grain boundary (LAGB). HAGB is defined by the misorientation angle of adjacent grains $\theta_m \geq 15^\circ$, while LAGB refers to $15^\circ \geq \theta_m \geq 2^\circ$.

Four steps are required to obtain grain size distribution in this work:

- i. Obtain crystallography map displayed in all Euler angles. An example of Euler contrast map of as-received W is illustrated in Fig. 3.14 a), which is colored by combination of three color strips according to three Euler angles ($\varphi_1, \Phi, \varphi_2$) respectively. It is noticed that there are white regions on the map, which represent non-index area, referring to absent or blur of Kikuchi pattern. The reasons for non-index area are listed as followings [95]: 1) Overlap of crystal orientations between adjacent grain/subgrain, and it usually occurs at grain/subgrain boundaries; 2) Lattice distortion and/or micro-fragmentation within grain due to large deformation; 3) Second phase. In this work, the above three reasons are all involved.
- ii. Conduct noise reduction and/or grain reconstruction procedure. The noise reduction procedure is necessary to obtain a reasonable grain size distribution, because otherwise some of the grain boundaries are not completely visible. By this procedure, two adjacent points are considered to be part of the same grain if their misorientation angle is below a critical value [99, 100]. The comparison before and after noise reduction are given in Fig. 3.14 b) and c).
- iii. Apply linear intercept method to the noise-reduced map to obtain the grain distribution. This process is accomplished by a program named ``Line Cut`` which runs in MATLAB [101]. Furthermore, it is observed that HPT deformed materials consist of elongated grains under certain condition, thus the grain size distribution is calculated along the direction parallels to SD and RD respectively, and at least 500 grains are typically required for obtain a statistically significant result. Lognormal distribution fittings are applied thereafter. The expected value corresponding to peak value of lognormal distribution from both directions are named L_{RD} and L_{SD} respectively. The example of grain size distribution of as-received W is illustrated in Fig. 3.15 a). Besides, the error bar is obtained by measuring the width at half height of the lognormal fit.

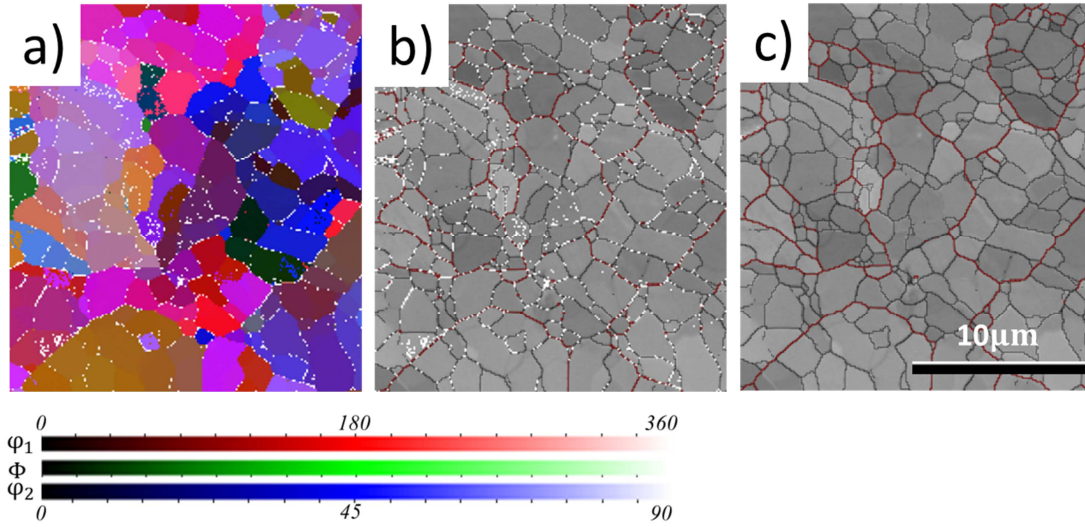


Fig. 3.14: a) Euler contrast map with its color code; b) Grain boundary map (high angle grain boundary in red, low angle grain boundary in black) without noise reduction. and c) after noise reduction of as-received W_rod2.

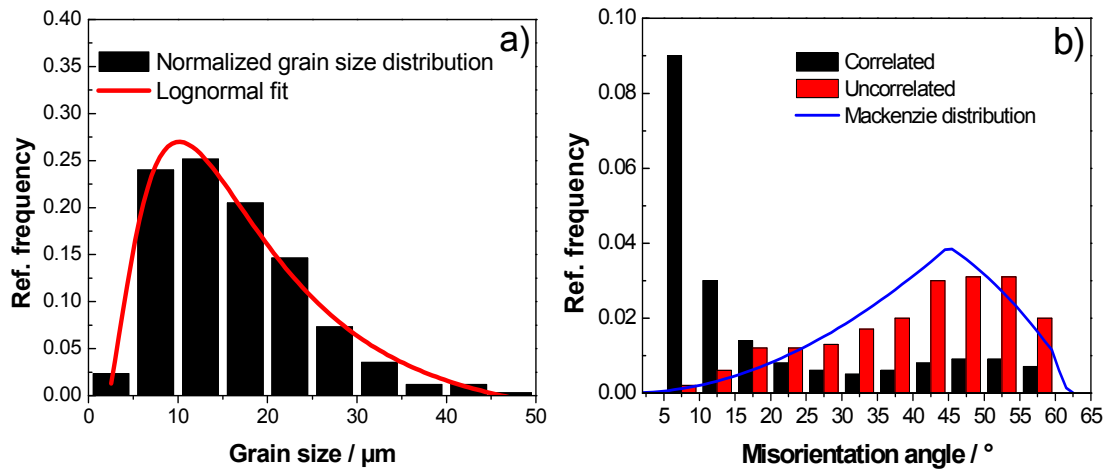


Fig. 3.15: a) Grain size distribution and its corresponding fitting curve; b) Misorientation angle distribution including correlated and uncorrelated misorientation histograms, and Mackenzie distribution line.

iv. For better comparison, equivalent grain size ($D_{equivalent}$) is introduced, and it is calculated by equation 3.3. The corresponding illustration is given in Fig. 3.16.

$$D_{equivalent} = 2 \times \sqrt{\frac{L_{RD} \times L_{SD}}{\pi}} \quad (3.3)$$

Furthermore, misorientation angle distribution can be derived from EBSD measurement. An example is given in Fig. 3.15 b), in which the correlated misorientation histogram reflects the misorientation between neighboring points. While uncorrelated misorientation displays the misorientation between randomly chosen points in the map. For randomly oriented assembly of grains, a Mackenzie distribution is plotted as reference [102].

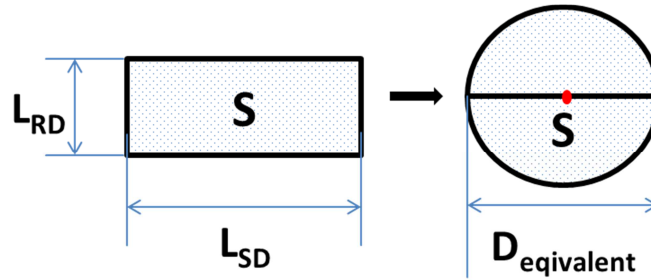


Fig. 3.16: Illustration of peak grain size along radial direction (RD), peak grain size along shear direction (SD) and equivalent grain size ($D_{equivalent}$).

3.2.5.4 Technique parameters and sample fabrication

Experimental settings refer to SEM: electron accelerating voltage is 20kV, beam current is 2.6nA and aperture is 50 μ m. The 70 $^\circ$ -titled copper sample holder is applied. Working distance between sample upper surface and beam gun is around 7mm to 10mm.

Experimental settings refer to EBSD: the control and process software is CHANNEL 5 from HKL Technology. The step size was set to be 5 times smaller than predicted grain diameter of investigated sample, and the minimum step size is 0.03 μ m. Before scanning, background noise is acquired and reduced from data to obtain a better contrast of Kikuchi pattern. Signal capture distance calibration is applied.

Sample preparation is the same as listed in Table 3.3. Conductive silver is employed as Adhesive.

3.2.6 Vickers indentation

Compared to other indentation methods, including Brinell hardness test (HB), Rockwell hardness test (HR) and Knoop hardness test (HK), Vickers hardness (HV) has the widest test material range, and is usually chosen to evaluate hard materials.

During Vickers hardness test, a square-based pyramid indenter made of diamond is pressed into material surface. After removing the indenter, a square expression is left on the sample. The

principle of Vickers indentation is illustrated in Fig. 3.17. The angle between two faces of indenter is $\alpha = 136^\circ$. F stands for the constant test force. The diagonal lengths of indents are d_1 and d_2 , respectively. The determination of Vickers hardness in Kg is given by:

$$HV = \frac{1}{g} \frac{F_{\max}}{A} = \frac{1}{g} \frac{F_{\max}}{4S} = \frac{1}{g} \frac{2F_{\max} \sin \alpha/2}{d^2} = 0.1891 \frac{F_{\max}}{d^2} \quad (3.4)$$

in which A refers to the whole area of indent, S is the area from one of the four cones, F_{\max} is the maximum force in N unit, and g is gravitational acceleration (equal to 9.80665).

The Vickers hardness tests are conducted on Zwick machine, the maximum load is 10N, loading speed is 0.1N/s and holding time at peak load is 12 seconds for each measurement. To avoid the influence from work-hardening induced by other indents, the distance between every two indents should be kept larger than 2.5 times of indentation diagonal dimension. The diagonal lengths of indents are measured afterwards under OM, and thus HV values can be obtained by using equation (3.4).

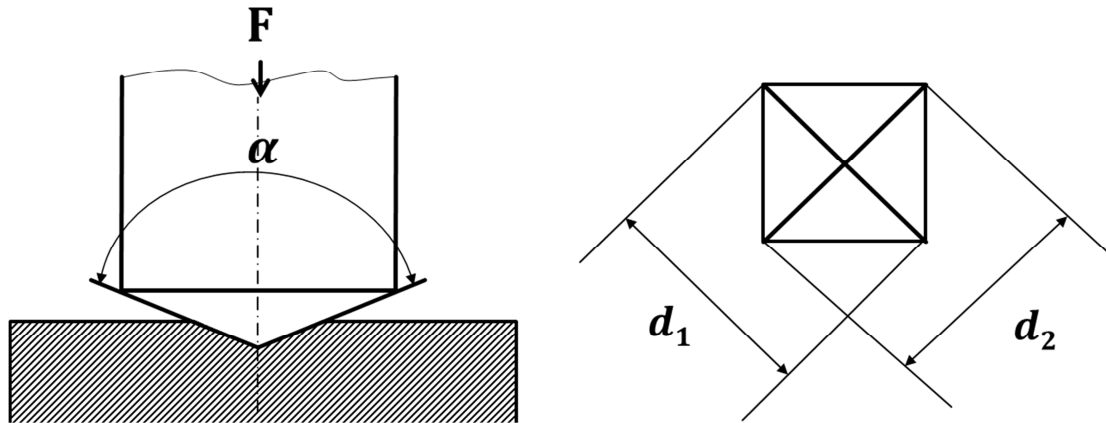


Fig. 3.17: Illustration of Vickers indentation.

Furthermore, Vickers indentation is employed for assessing fracture toughness of HPT deformed W in this work. This method is attractive because of its experimental expediency. When Vickers indentation is applied on brittle materials under certain condition, visible cracks may appear around indents. With assistant of fracture theories and/or finite element simulation, several models are developed for fracture toughness evaluation [103-107]. Fracture toughness can be determined by considering the applied load and indentation induced crack area. Under the same experimental condition, the shorter the cracks are, the better the fracture toughness is.

3.2.7 Nanoindentation

Oliver and Pharr have done fundamental works on measurements with respect to nanoindentation [108, 109]. Based on the understanding of elastic-plastic contact mechanics in materials, hardness and Young's modulus (E) can be determined without observing the image of indent impression. This is important because that indent impression related to nanoindentation is too small to be measured precisely. A typical load-displacement curve under nanoindentation is given in Fig. 3.18 a), in which several important parameters are depicted.

For most metals, loading procedure consists of both elastic and plastic deformation, while unloading refers to only elastic recovery. Therefore the hardness and Young's modulus can be determined from unloading curve. Hardness (H_{nano}) can be calculated from equation (3.5),

$$H_{nano} = \frac{P_{max}}{A(h_c)} \quad (3.5)$$

in which P_{max} refers to the maximum load. A means projected contact area between indenter and sample, and it can be described by area function $A(h_c)$ as shown in equation (3.6),

$$A(h_c) = \sum_{n=0}^8 C_n h_c^{(2^{1-n})} = C_0 h_c^2 + C_1 h_c + C_2 h_c^{1/2} + \dots + C_8 h_c^{1/128} \quad (3.6)$$

in which C_0 to C_8 are constants without physical significance determined by curve fitting procedures over a given range of depths. The value is dependent on tip condition, a perfect Berkovich tip has only one constant, which is $C_0=24.5$. The geometric meaning of h_c is illustrated in Fig. 3.18 b). It refers to the depth along which contact is made between the indenter and the sample at the maximum load, and it can be described by:

$$h_c = h_{max} - h_s = h_{max} - \epsilon \frac{P_{max}}{S} \quad (3.7)$$

where h_{max} is the maximum depth when the indenter penetrates in sample, and h_s refers to the sink-in depth, which can be calculated from elastic models with the assumption that pile-up during indentation is negligible [109]. Furthermore, ϵ is a constant that depends on the geometry of the indenter, for example $\epsilon=0.75$ is widely accepted for Berkovich tip from empirical observation and is then confirmed by a physical justifiable procedure involves with Sneddon's

method [110]. Besides, S stands for stiffness, and it can be derived from unloading curve as well, shown in Fig. 3.18 a) and equation (3.8),

$$S = \frac{dP}{dh} = \beta \frac{2}{\sqrt{\pi}} E_r \sqrt{A} \quad (3.8)$$

in which β is a constant that refers to deviation in S account for any physical processes. E_r is reduced Young's modulus, which considers that elastic displacement takes place in both sample and indenter during nanoindentation, and it can be exhibited by:

$$E_r = \left(\frac{1 - \nu^2}{E} + \frac{1 - \nu_i^2}{E_i} \right)^{-1} \quad (3.9)$$

in which ν and E are the Poisson's ratio and Young's modulus of specimen, while ν_i and E_i are Poisson's ratio and Young's modulus of indenter.

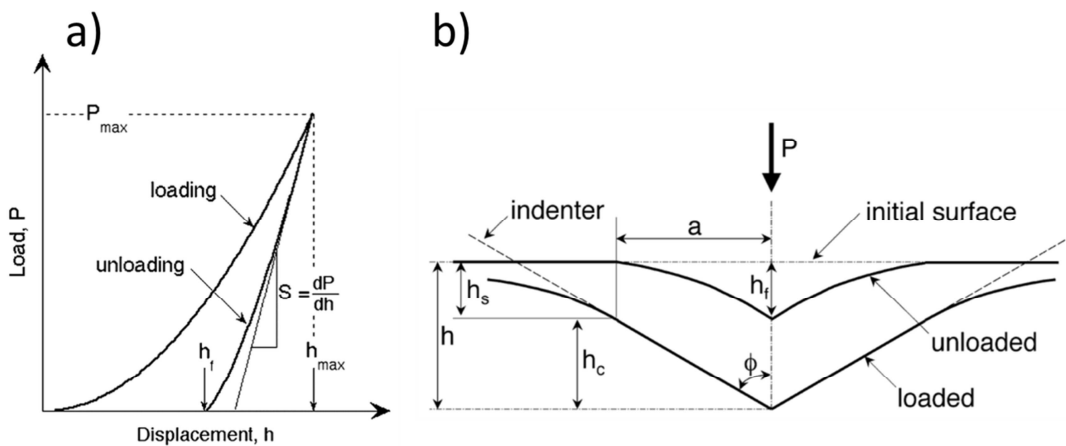


Fig. 3.18: Schematic illustrations of a) indentation load-displacement curve; and b) unloading process [109].

Continuous stiffness mode (CSM) is regarded to be one of the most important improvements in nanoindentation techniques because that it facilitates the measurement and calibration process. By this mean, a small dynamic oscillation signal is superimposed on the force (or displacement). Therefore the stiffness can be measured continuously during the loading process [62]. It has many advantages [109]. First of all, the continuous measurements can be provided as a function of depth. Secondly, it could avoid some of the complex effects of time-dependent plasticity and thermal drift. Thirdly, the initial contact surface can be precisely measured.

In this work, G200 is employed to perform nanoindentation. Berkovich tip is used as indenter, which is a triangle-based pyramid made of diamond. Fused quartz is employed as reference sample to calculate the area function of Berkovich tip. All the indentation measurements are conducted under CSM. A constant nominal strain rate of 0.05s^{-1} is taken place. During the measurement, the homologous temperature is kept to 20°C . The indentation depth is larger than 1100nm , but only the data from 800nm to 1000nm depth range is taken into account for hardness and Young's modulus determination.

3.2.8 Heat treatment

Thermal stability of HPT deformed W and WL10 are investigated by heat treatment. It is conducted in vacuum furnace. The degree of vacuum is smaller than 10^{-6} mbar, the heat treatment temperature is 1000°C , and the duration is 1 hour, 3 hours, 6 hours and 9 hours respectively.

4 Results and discussions

4.1 Grain fragmentation during high-pressure torsion

In this section grain fragmentation procedure during HPT is discussed. W_rod2 and WL10 are performed to be compared since they possess identical grain size in as-received state.

The sample coordinate system is illustrated in Fig. 4.1, where RD refers to radial direction, SPN is shear plane normal direction and SD represents shear direction. The microstructure images from RD-SPN plane are provided for both materials to reveal the changes along axial direction before and after HPT. Besides, so as to capture the subtle changes on microstructure at the beginning of grain fragmentation process, sample center region is mainly observed from observation plane of RD-SD (shear plane). Relative misorientation distributions within a grain or several adjacent grains are analyzed as well. Texture evolution during HPT is evaluated by exhibiting IPFs and PFs.

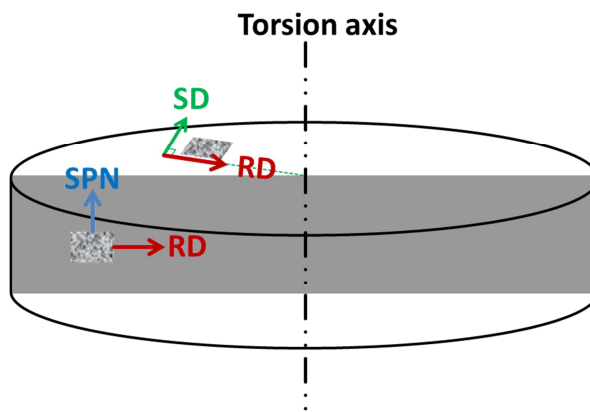


Fig. 4.1: Schematic representation of the sample coordinate system.

4.1.1 Grain fragmentation of W

Fig. 4.2 shows the cross section (RD-SPN) images of W_rod2 before and after HPT, the HPT conducted here refers to 1 torsion revolution at 400°C, as indicated in Fig. 4.2 b). Both as-received and deformed W_rod2 are manually broken in liquid nitrogen before observing under SEM. Grain boundaries are clearly visualized in Fig. 4.2. Please notice that different scale bars are used for as-received and deformed W. It is apparent that W grains are highly pressed along SPN direction after HPT, and the layer height is around 50nm.

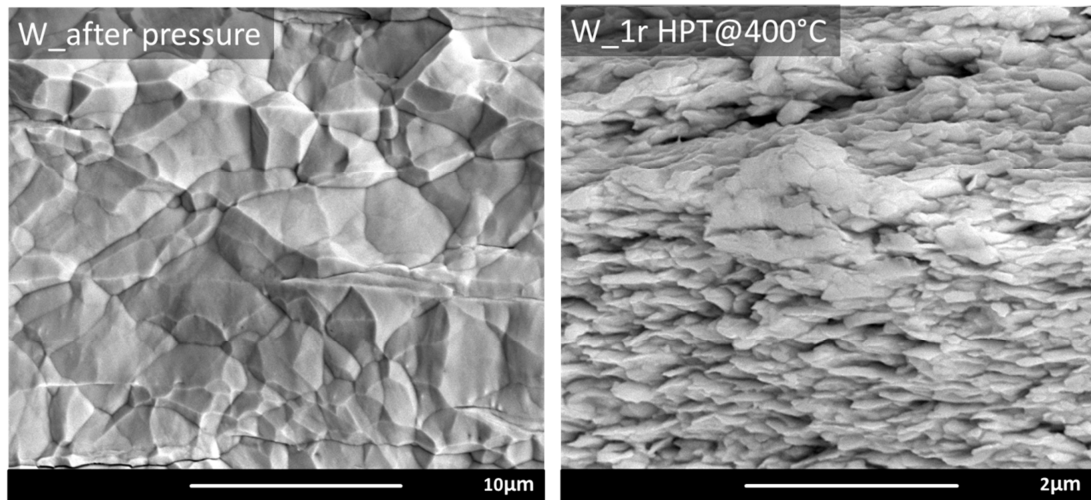


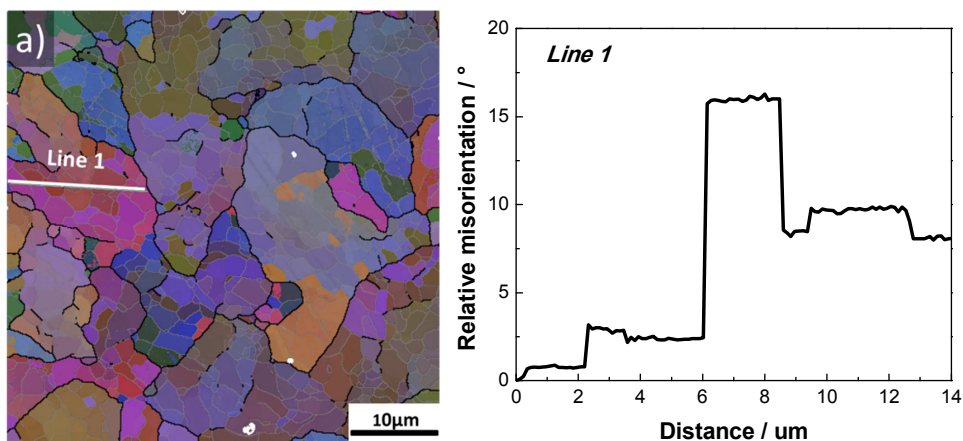
Fig. 4.2: Cross section (RD-SPN) microstructure images of as-received W_rod2 and W_rod2 deformed by high-pressure torsion at 400°C after 1 revolution.

Fig. 4.3 shows Euler contrast maps of HPT deformed W_rod2 regarding to different strain amount. All the images are taken from sample center region and observed from RD-SD direction. Colors in the map are corresponding to all Euler angles to reflect crystal orientation, and the color code is shown in Fig. 3.14. Besides, the bold black line refers to HAGB while grey line represents LAGB. In each image, a bold white line is drawn across a grain or several grains to obtain relative misorientation angle as a function of distance. The reference point is set to be on the most left of the bold white line. The corresponding relative misorientation angle distribution is provided near to the Euler contrast map. From Fig. 4.3, the following aspects can be observed:

- i. Fig. 4.3 a) refers to as-received W_rod2, line 1 is drawn across one random chosen grain, and the corresponding relative misorientation distribution curve is shown beside the image. It can be noticed that a stair shape appears on the misorientation curve, each stair represents a subgrain and within the subgrain, the crystal orientation is quite steady.
- ii. After small strain amount is applied on sample, such as $\epsilon < 0.1$, the distance between HAGBs is basically the same compared with as-received state, as shown in Fig. 4.3 b). However the morphology of subgrain change is dramatically, instead of a stair-shape misorientation curve, a smoothed curve is exhibited along line 2, which implies that subgrains can adjust their orientation after applying small amount of strain in this area.
- iii. In other cases, usually as for original large grains, with increasing imposed strain, different slip systems may activate within them. Micro-bands (MB) are therefore formed, as shown in Fig. 4.3 c). The relative misorientation curve along line 3 demonstrates three distinct micro-bands, which is suggesting that this grain has high tendency to be divided into three separate grains if the deformation continuous.

-
- iv. Figure 4.3 d) illustrates the misorientation distribution across several refined grains which locate among coarse grains. Line 4 is drawn across them. It is noticed that even though there are jumps on the relative misorientation angle curve, which is corresponding mainly to HAGBs, a slope baseline can be found underneath. Suggesting that these refined grains might come from the same original coarse grain and the misorientation gradient still maintains after grain fragmentation.

Figure 4.4 illustrates the statistical grain boundary misorientation angle distribution of W_rod2 during HPT. Different color represents different torsion revolution. The results are obtained from sample center and sample edge region respectively, in which sample edge region refers to 3mm from torsion axis. It is observed from Fig. 4.4 that with increasing torsion revolution, the fraction of LAGB in center region decreases gradually while the percentage of HAGB increases correspondingly. The peak of misorientation distribution curve moves from 7.5° to 47.5° after 4 torsion revolutions, as shown in Fig. 4.4 a). The curve merely changes after 4 revolutions up to 8 revolutions. Same trend is noticed in sample edge region, as shown in Fig. 4.4 b). However, the torsion strain imposed on sample edge region is larger than sample center under same torsion revolution. Therefore the transition of LAGB to HAGB is faster at sample edge region than center, and the steady state of grain boundary misorientation angle distribution is reached after only 2 torsion revolutions at sample edge. The other point is that even after extreme large strain, such as after 8 torsion revolutions, which is 391 of equivalent true strain, the misorientation distribution curves from sample center and edge region are not coincident. The LAGB fraction is still higher in sample center region than sample edge region. This implies that the heterogeneity can't be eliminated even after 8 torsion revolutions.



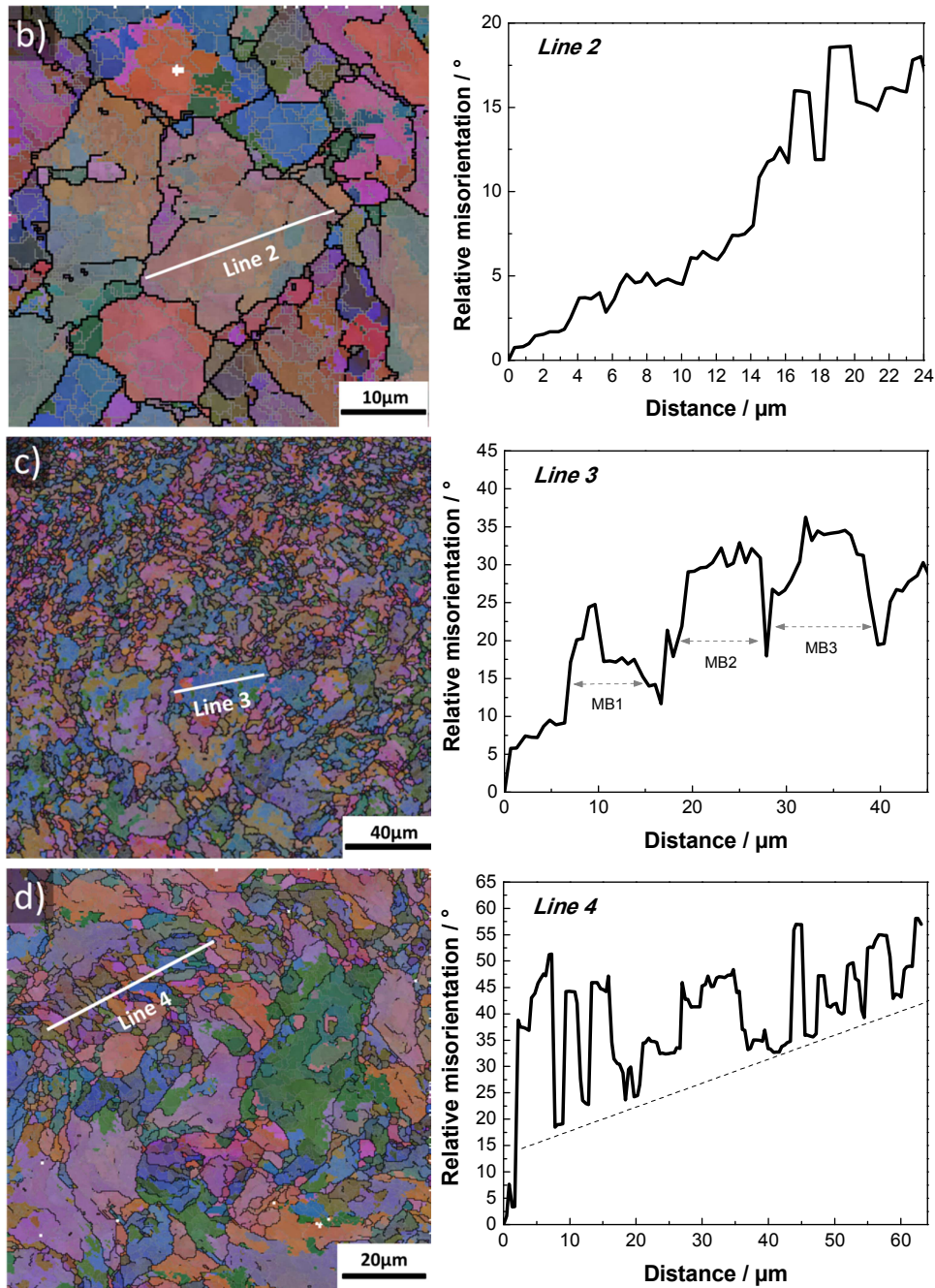


Fig. 4.3: Euler contrast images of W_rod2 deformed by high-pressure torsion after a) $\epsilon=0$; b) $\epsilon \leq 0.1$; c) $\epsilon \leq 0.8$; d) $\epsilon \geq 0.8$.
 (Bold black line refers to high angle grain boundary)
 Corresponding relative misorientation angle distributions are along line1 to line 4.

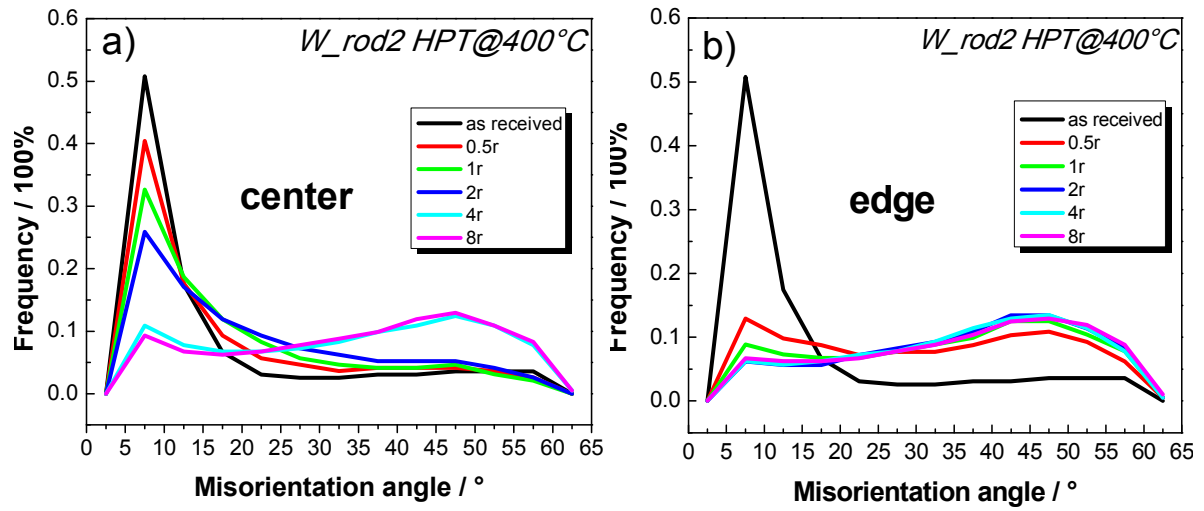


Fig. 4.4: Illustrations of statistical misorientation distribution along with torsion revolution from a) sample center and b) sample edge for W_rod2 deformed by high-pressure torsion at 400°C.

Figure 4.5 provides the IPFs and PFs of as-received W_rod2 and HPT deformed W_rod2 at center region. The IPFs exhibited on the left column are coded by the color triangle, which is shown in between the two IPFs. PFs are shown on the right column with projection crystal planes of $\{111\}$, $\{110\}$ and $\{100\}$ respectively.

So as to obtain better comparison with HPT deformed W by employing the same scale bar, the IPF of as-received W_rod2 possesses a relative small area with limited amount of grains. It is observed from these IPFs in Fig. 4.5 that the green regions become dominate after HPT, which refers to $\{110\} // \text{SPN}$ crystal orientation.

The PF of as-received W_rod2 contains more than 500 grains so as to show a sufficient statistical analysis of texture. From the sharp cluster of PF density in as-received W_rod2, one could tell that the texture is relatively strong compared to as-deformed state. Texture components include $[111] // \text{SD}$, $[100] // \text{SD}$, a weak $\{110\} // \text{SPN}$ as well as $\{100\} // \text{SPN}$ are observed on as-received W_rod2. However after 0.5 torsion revolution, the intensity of texture is diminished by showing faint halos instead of sharp cluster in PFs of HPT deformed W_rod2. Besides, it is obvious that the $\{110\} // \text{SPN}$ is the strongest texture component after high-pressure torsion, which is consistent to the observation from PFs. At the mean time the originally existing $\{100\} // \text{SPN}$ texture disappears and $[111] // \text{SD}$ becomes weak after deformation of W_rod2.

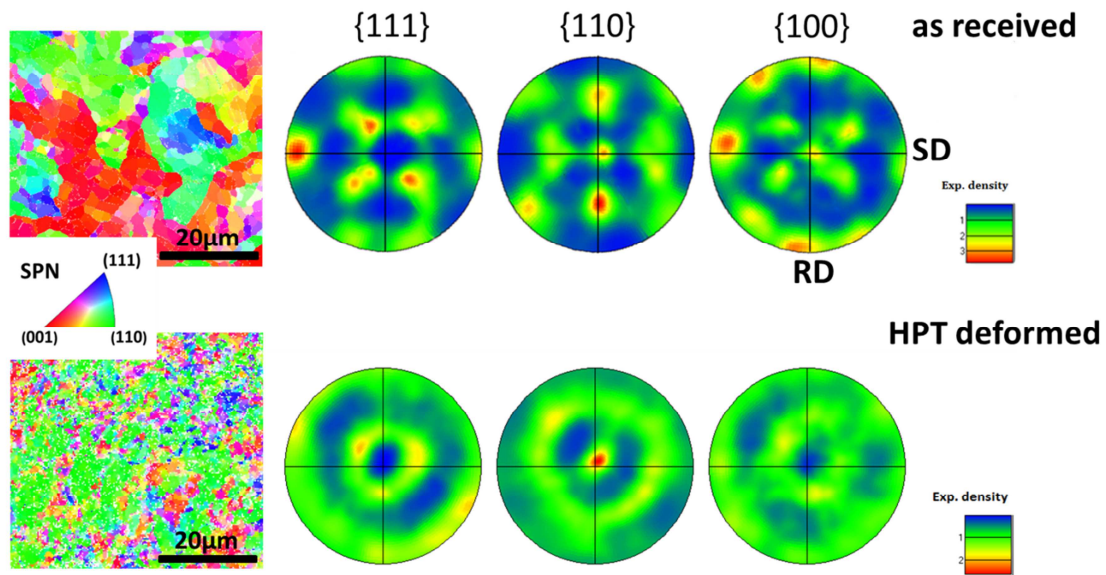


Fig. 4.5: Inverse pole figures and pole figures of W_rod2 in as-received state and deformed by high-pressure torsion at 400°C after 0.5 torsion revolution at sample center region.

4.1.2 Grain fragmentation of WL10

The cross section images of as-received and HPT deformed WL10 are shown in Fig. 4.6. Samples are prepared by the same method as for W_rod2 in Fig. 4.2. From Fig. 4.6 a), the La_2O_3 particles are clearly visible and indicated by red dash rectangular. It is observed that La_2O_3 particles are doped in W matrix, and are in needle-shape from cross section view. The length of oxide particle is in several micrometers range. As is shown in Fig. 4.6 b), after 1 torsion revolution, W grains are harshly deformed and the morphology is quite different from deformed pure W in Fig. 4.2 b). The microstructure for deformed pure W consists of grain layers and the grain boundary can be clearly observed. While the microstructure from HPT deformed WL10 is more like batches of matchsticks and the grains are difficult to distinguish from each other from cross section SEM (second electron) view, as is shown in Fig. 4.6 b).

Fig. 4.7 exhibits series of SEM images from WL10_0.5r HPT@400°C (refers to HPT deformed WL10 after 0.5 torsion revolution at process temperature of 400°C). All the images are observed from shear plane (RD-SD) and are concerning with different radius positions at the same sample, which are 0mm, 0.5mm, 1mm and 3mm from torsion axis respectively. The corresponding equivalent true strain values are indicated on the images as well, from 0.05 to 7.5. It is observed that after compressive load, La_2O_3 particles are pressed to spherical shape, which is shown clearly on the left-top image of Fig. 4.7. Thereafter along with imposed strain, the oxide particles are elongated and the width of which becomes narrower and narrower.

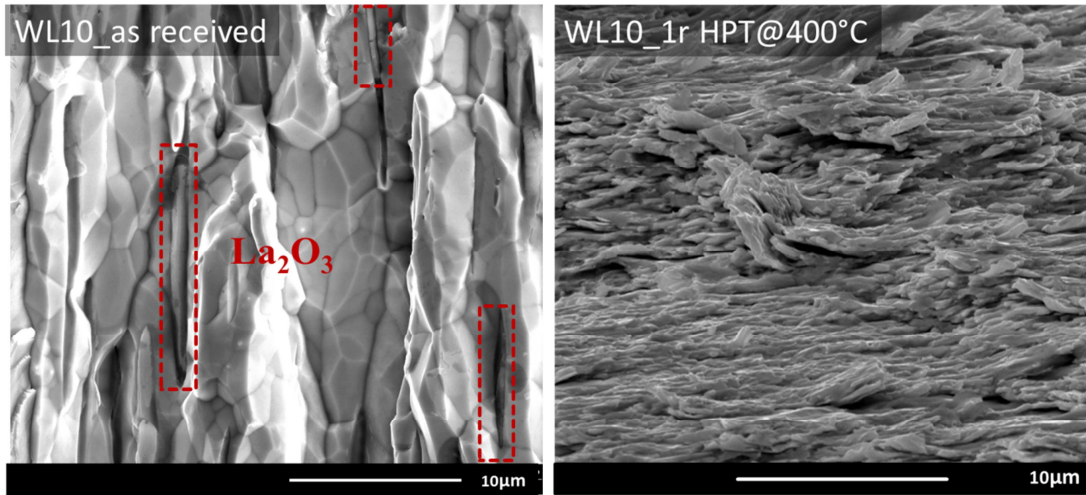


Fig. 4.6: Cross section (SD-SPN) microstructure images of as-received and high-pressure torsion deformed WL10 at 400°C after 1 torsion revolution.

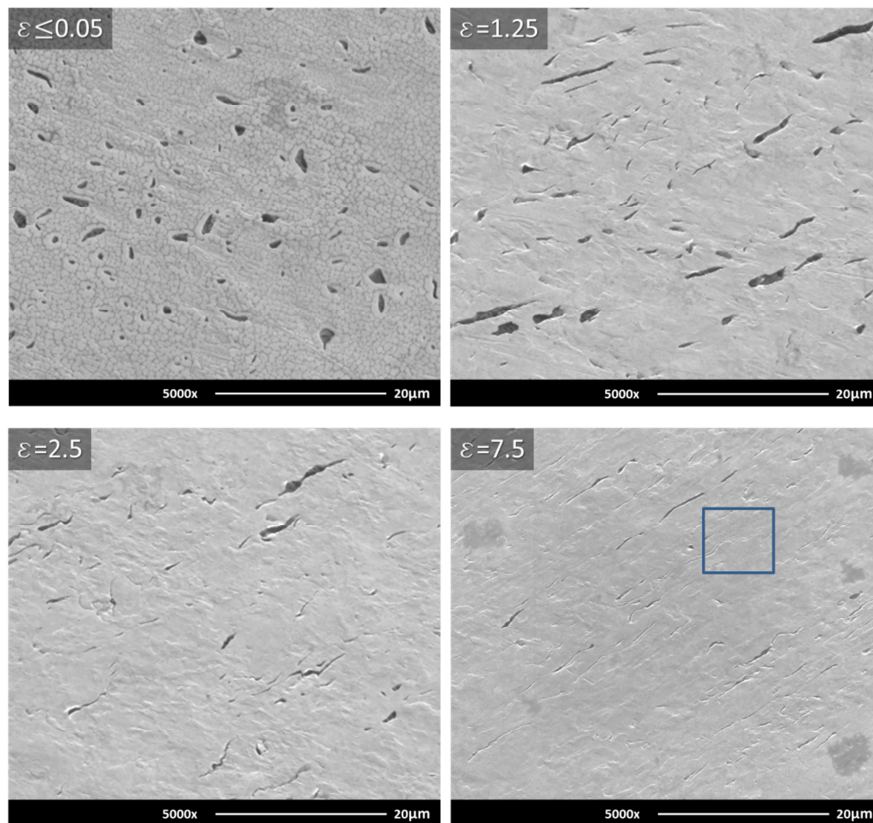


Fig.4.7: SEM (secondary electron) images of high-pressure torsion deformed WL10 at 400°C after 0.5 torsion revolution, at sample radius of 0mm, 0.5mm, 1mm and 3mm respectively. All the images are observed from shear plane direction (RD-SD).

Crystal orientation image maps (OIM) related to WL10 are provided in Fig. 4.8. OIM with different strain amount are displayed. The relative misorientation angle distribution curves along certain lines are exhibited beside each OIM as well. Moreover, SEM image and IPF in Fig. 4.9 are provided as assistant information related to Fig. 4.8 b), since they are all taken from the same position of one sample. It can be noticed from Fig. 4.8 and Fig. 4.9 that:

- i. In as-received WL10, as shown in Fig. 4.8 a), the grain and subgrain can be clearly observed with sharp boundaries. The relative misorientation angle distribution curve displays stair shape, which is identical with as-received W (s. Fig. 4.3 a). The white region refers to oxide particle and distributes both at grain boundary and grain interior.
- ii. Fig. 4.8 b) exhibits the transition from un-deformed center to slightly deformed region from image right to left. Line 6 is drawn across this typical area. A gradual change in relative misorientation angle is observed. From right to left along line 6, the stair-shape curve turns into horizontal baseline with high angles misorientation fluctuations. From Euler contrast map, we notice that these HAGBs are most distributed near the oxide particles in slightly deformed region, as indicated in bold black lines in Fig. 4.8 b).
- iii. To make sure those bold black lines in Fig. 4.8 b) are not impurities introduced from sample preparation, SEM image and IPF are provided in Fig. 4.9. The color code for IPF is given in Fig. 4.5. No impurities are observed on the sample surface in Fig. 4.9 a). More importantly, Fig. 4.9 b) shows the crystal with orientation of $\{111\} // \text{SPN}$ (blue) and $\{110\} // \text{SPN}$ (green) are intersected with each other in the slightly deformed region. It can be assumed that oxide particles can stabilize the original crystal orientation, which is $\{111\} // \text{SPN}$ (blue) in this case, while other region turns into $\{110\} // \text{SPN}$, since the $\{110\} // \text{SPN}$ is discovered to be the most favorite texture component in HPT deformed W.
- iv. Fig. 4.8 c) is taken from the position where the blue frame indicated in Fig. 4.7. As mentioned before, the oxide particle traces are elongated and become quite narrow after certain strain, and W grain changes its shape accordingly. Line 7 is drawn across an elongated W in between two oxide particle traces. Subtle variation in misorientation angle can be observed along line 7. LAGB is formed near grain B, and about to be formed near grain A, as indicated in color changes in IPF and angle jumps in relative misorientation angle distribution. Note that both grain A and B possess a crystal orientation of near to $\{110\} // \text{SPN}$.

Fig. 4.10 shows the IPFs and PFs of as-received and HPT deformed WL10. The changes in texture are quite identical to pure W (s. Fig. 4.5). In contrast to as-received WL10, after HPT deformation, the $\{110\} // \text{SPN}$ is the most favorite crystal orientation.

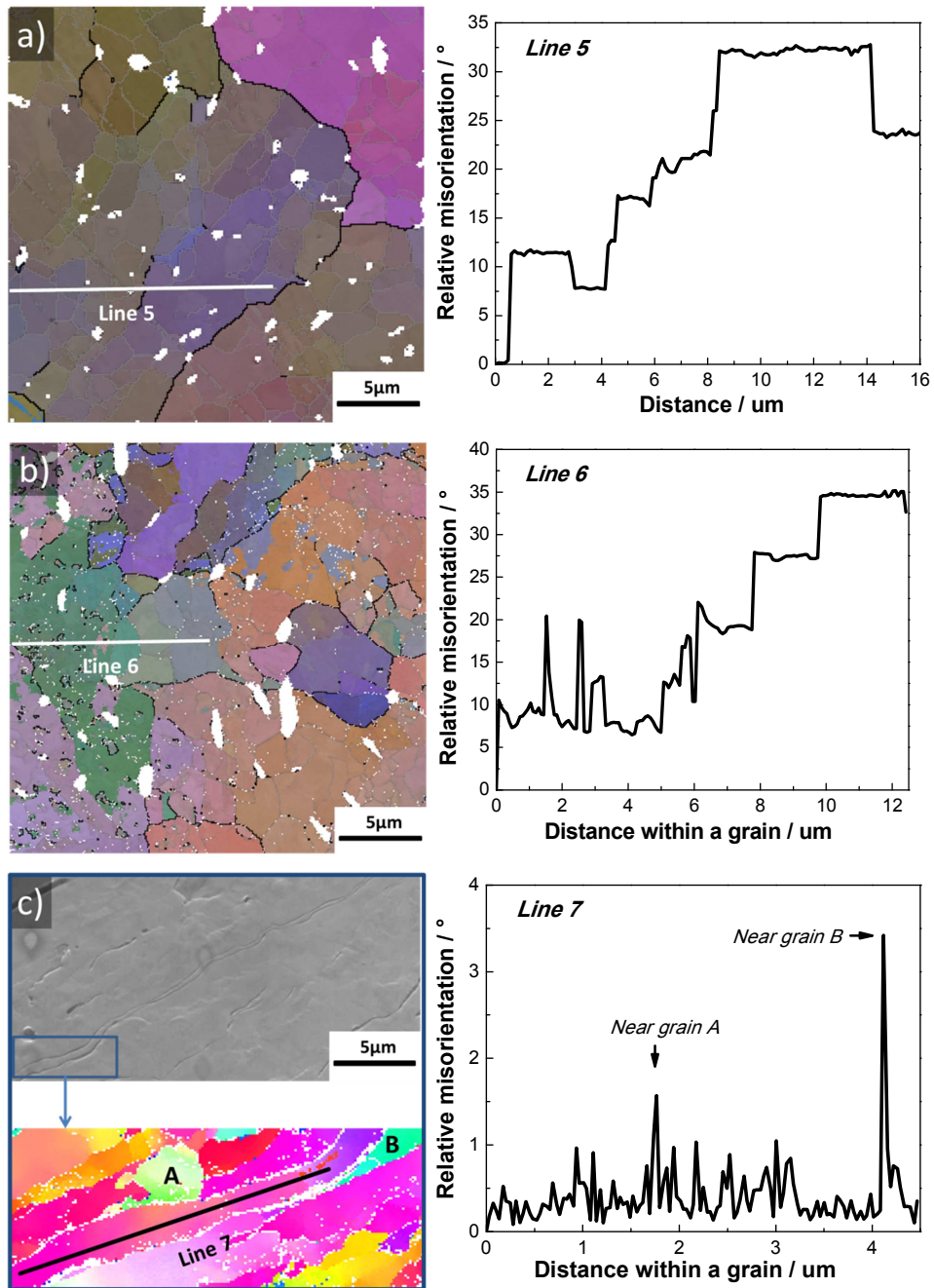


Fig. 4.8: Orientation image maps (OIM) and SEM (secondary electron) image of WL10 in a) as-received state, and deformed by high-pressure torsion with equivalent true strain of b) $\varepsilon \leq 0.1$ and c) $\varepsilon = 7.5$.

(Bold black line refers to high angle grain boundary;

Grey line refers to low angle grain boundary;

White region refers to un-indexed point, including La_2O_3 particles)

Relative misorientation angle distributions are along line 5 to line 7.

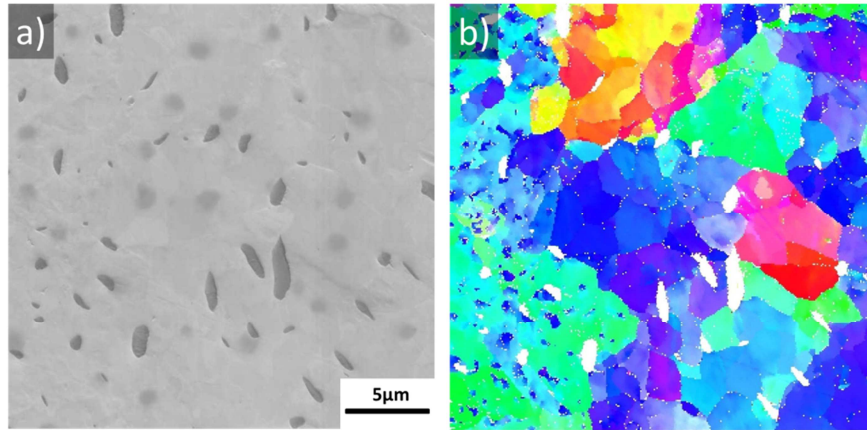


Fig. 4.9: a) SEM (secondary electron) image and b) inverse pole figure of deformed WL10. (Same position with Fig. 4.8 b).

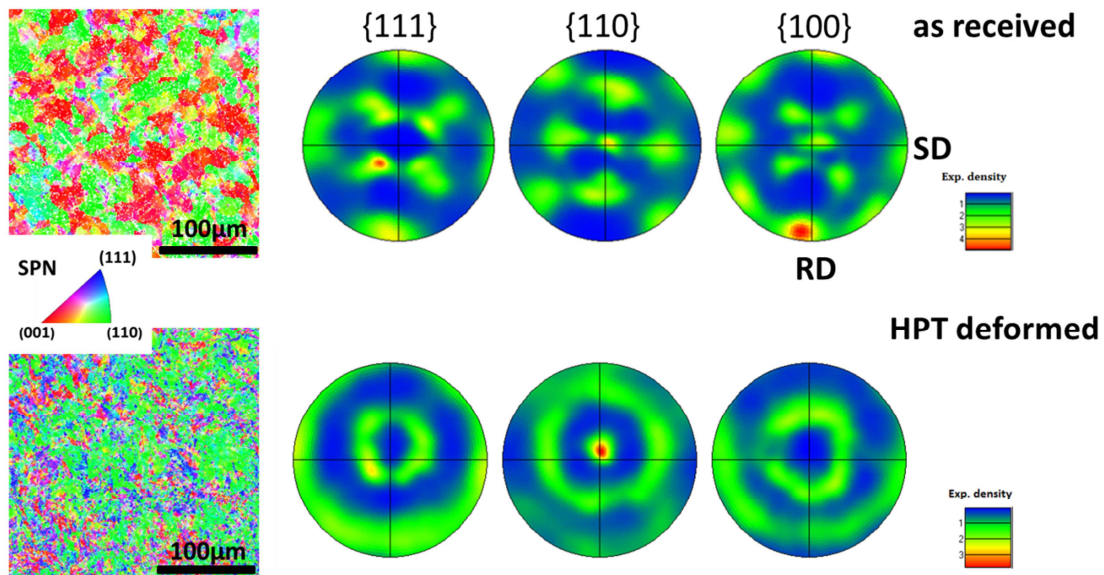


Fig. 4.10: Inverse pole figures and pole figures of WL10 in as-received state and deformed by high-pressure torsion at 400°C after 0.5 torsion revolution at sample center region.

4.1.3 Discussion

As mentioned in the state of the research in Chapter 2, the grain fragmentation process for materials is highly dependent on SFE. For materials with high SFE, such as W and WL10, grain fragmentation is induced by dislocation movement. The grain fragmentation procedures for pure W and WL10 are discussed separately in this section.

For pure W, large amount of dislocations are generated in the material during HPT. According to the work hardening theories [111], dislocation prefers to stay at grain boundaries to obtain the lowest free energy for the whole system. After small strain amount, dislocation sweeps across the subgrain and grain, then accumulates at boundaries. There are two possible consequences after this process: 1) Subgrains adjust their orientations while dislocations pass by; 2) continuous growth in relative misorientation angle within grain. The grain size determined by HAGB can maintain under certain strain amount, as demonstrated in Fig. 4.3 line 2. This is the preparation stage for grain fragmentation.

With further increase in strain amount, the transfer from LAGB to HAGB takes place, which is clearly shown in the statistic results in Fig. 4.4. There are two aspects of explanations for this phenomenon: On one side, to maintain the material continuity, local stress field varies within one particular grain, which induces activation of different slip systems (s. Fig. 4.3 c). The boundary where different slip systems encounter transfers from LAGB to HAGB with increase of strain amount [56]. On the other side, crystal with a stable orientation maintains through deformation while crystal with unstable orientation is easier to be rotated [51]. If the rotation process is not uniform through the grain territory, grain fragmentation can occur. In this work, $\{110\}$ // SPN is proved to be the most favorite crystal orientation after HPT (s. Fig. 4.5). Since $\{110\}$ is the densest crystal plane for BCC (body-centered cubic) material, it is reasonable that $\{110\}$ plane acts as slip plane for pure W during HPT.

For WL10, La_2O_3 particles play an important role in grain fragmentation procedure. In general, the presence of oxide particles facilitates the formation of HAGB during HPT. On one hand, the oxide particles act as obstacles and hinder the movement of dislocations, thus HAGB is formed easily around them. On the other hand, as stated before, the rotation process of unstable crystal is non-uniform during deformation, and this situation is more obvious when La_2O_3 particles exist. The original crystal orientation can be stabilized while other region turns into the favorite orientation $\{110\}$ // SPN (s. Fig. 4.8 and Fig. 4.9). Besides, deformed W shows slope baseline in grain boundary misorientation angle curve within one grain (s. Fig. 4.3), however the deformed WL10 exhibits a horizontal baseline, which means the misorientation gradient in WL10 is less significant than in W, but the grain fragmentation efficiency is almost the same at the beginning of HPT. This implies the existence of oxide particles make misorientation gradient less required for grain fragmentation during HPT. With increase of strain amount, the oxide particles are elongated and so as the W grains (s. Fig. 4.7 and Fig. 4.8 c). The crystal orientation within elongated grain can be influenced by the surrounding grains more sensitively, especially when the neighbor grains are with strong orientation (s. Fig. 4.8 c).

The texture of deformed WL10 (s. Fig. 4.10) is the same to deformed W (s. Fig. 4.5), which suggests that La_2O_3 particles have little influence on texture evolution under small strain amount. This may be attributed to the relatively large particle size of oxide at beginning of deformation.

4.2 Influence of original microstructure and alloy

In this section, results relevant to influence of initial microstructure and alloy on HPT process are presented. HPT procedures are performed at 400°C , uniaxial pressure is 5GPa and torsion rate is 5rpm. Four kinds of materials are compared, which are W_rod1, W_rod2, W_plate and WL10. The first three materials are all pure W but with different original microstructures, while WL10 is studied for alloying effect by comparing with W_rod2.

Torsion torque curves during HPT process are provided at first, followed by microstructure evolution, which is interpreted by Euler contrast map and grain boundary map. Texture changes are revealed by displaying pole figures. In the end mechanical properties are analyzed by nanoindentation.

4.2.1 Torsion torque

A typical torsion torque curve during HPT is given in Fig. 4.11 a). It is simplified by picking peak value in each 90 torsion degree, as indicated by red solid circle. The torsion torque curves displayed in the thesis are all simplified in this way. Fig. 4.11 b) exhibits torsion torque curves of 4 materials during HPT. For better comparison with other measurements, equivalent strain of the position which is 3mm from torsion axis is used as variable for the x-axis instead of torsion revolution.

Three distinct regions can be depicted from Fig. 4.11 b):

- i. Region I relates to the continuous growing of torsion torque with strain. The peak value appears at around 0.75 torsion revolutions ($\varepsilon=16$) for W_rod1, W_rod2 and WL10. While W_plate, as a pre-deformed material, shows an earlier torque peak at $\varepsilon=5$.
- ii. With increasing strain amount, torsion torque decreases and drops to certain value, this procedure is named region II.
- iii. Region III refers to saturation in torsion torque for all three pure W, which starts from equivalent strain of about 50. All of the three pure W have similar deformation behavior in this region. Specifically, W_rod1 and W_rod2 saturate at the torque value of 168 Nm, while a slight lower value of 152 Nm is reached by W_plate. However the difference between pure W and WL10 is obvious. As for WL10, the torque increases again with imposed strain in region III. After 4 revolutions ($\varepsilon=174$), deformed WL10 shows 22% (50 Nm) higher torsion torque value than the peak torque in region I.

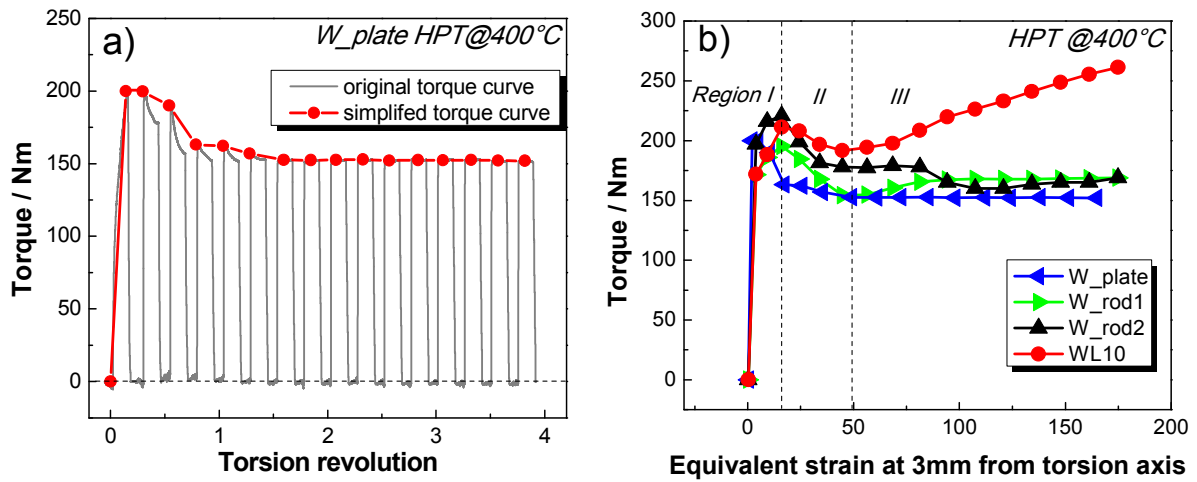


Fig. 4.11: a) Typical torsion torque from pure W_plate during high-pressure torsion at 400°C; b) Torsion torque vs. equivalent strain for four materials during high-pressure torsion at 400°C.

4.2.2 Microstructure

The microstructures of investigated materials in as-received state are displayed in Fig. 4.12. The first column refers to orientation image map (OIM), which is interpreted by all Euler angles (color code is seen in Fig. 3.14) and without any noise reduction procedure. The middle column refers to grain boundary map, in which HAGBs are drawn in bold red line and LAGBs are represented in grey line. The last column regards to grain boundary map in larger magnification to show more details as well as for better comparison in grain size among different materials. Moreover, the corresponding grain size distribution diagrams are exhibited in Fig. 4.13, determined both from HAGB (grain size) and LAGB (subgrain size). All the other microstructure evolutions in the thesis are presented in this order.

From Fig. 4.12 and Fig. 4.13, it is noticed that:

- i. Among four as-received materials, W_rod1, W_rod2 and WL10 exhibit similar microstructure morphology, which contains almost equiaxed grains with sharp boundaries. While W_plate demonstrates distinct microstructure. Irregular grain shape and wide range of grain sizes can be observed in as received W_plate.
- ii. The expected value (peak value from lognormal fit curve) of grain size determined from HAGB is ranked as: $W_{rod1} > W_{rod2} = WL10 > W_{plate}$. The determination of equivalent grain size can be found in section 3.2.5.
- iii. W_plate shows the finest peak subgrain size of $0.5\mu\text{m}$. The other materials have a peak subgrain size in the range of $2\text{-}3\mu\text{m}$.
- iv. The oxide particles can be seen in bottom-right image in Fig. 4.12. Most of them have diameters in micrometer range and distribute mainly on the grain/subgrain boundaries.

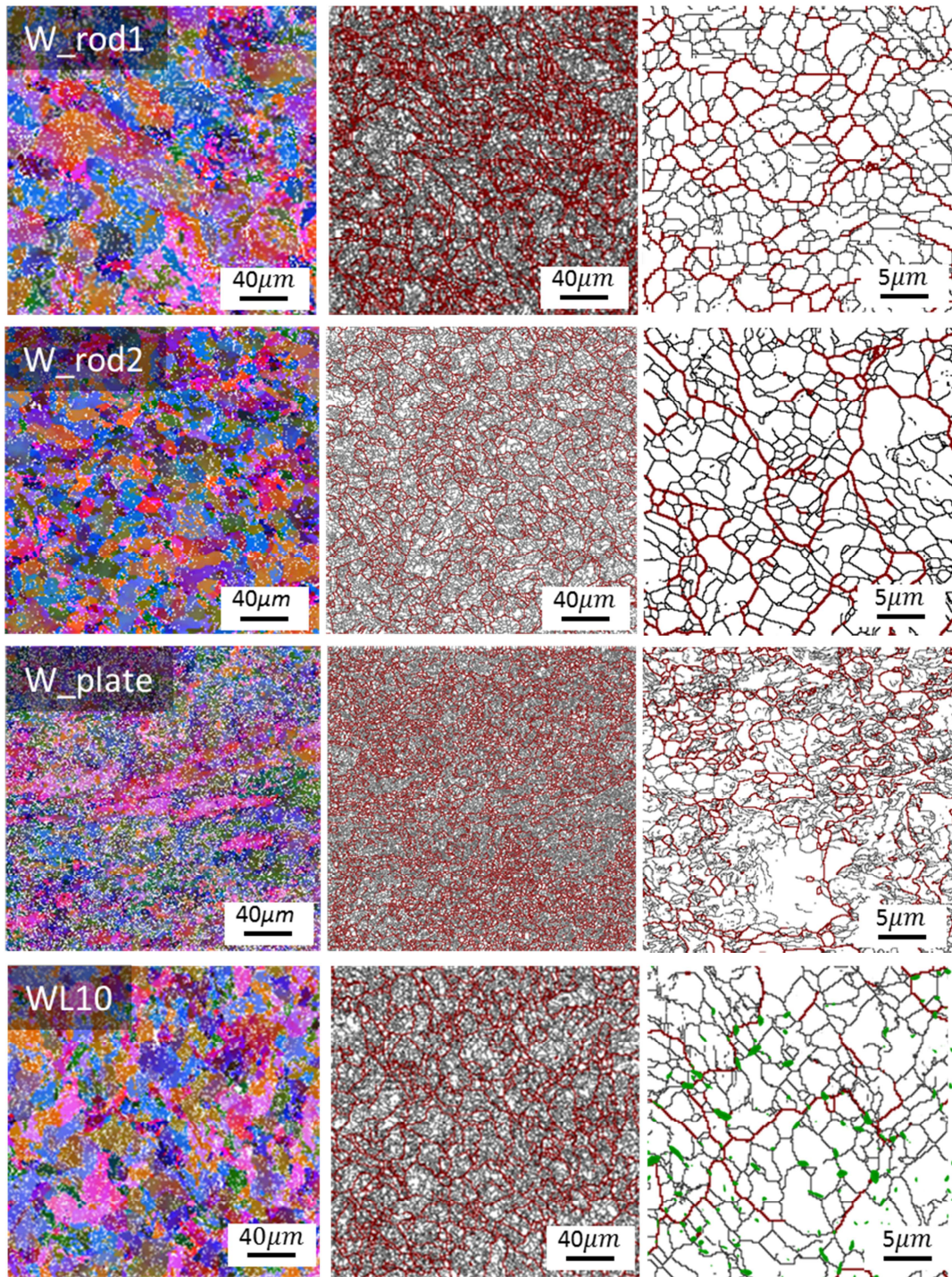


Fig. 4.12: Euler contrast map, grain boundary map and grain boundary image with larger magnification of as-received materials. The La₂O₃ particles in WL10 are colored in green in the magnified grain boundary image.

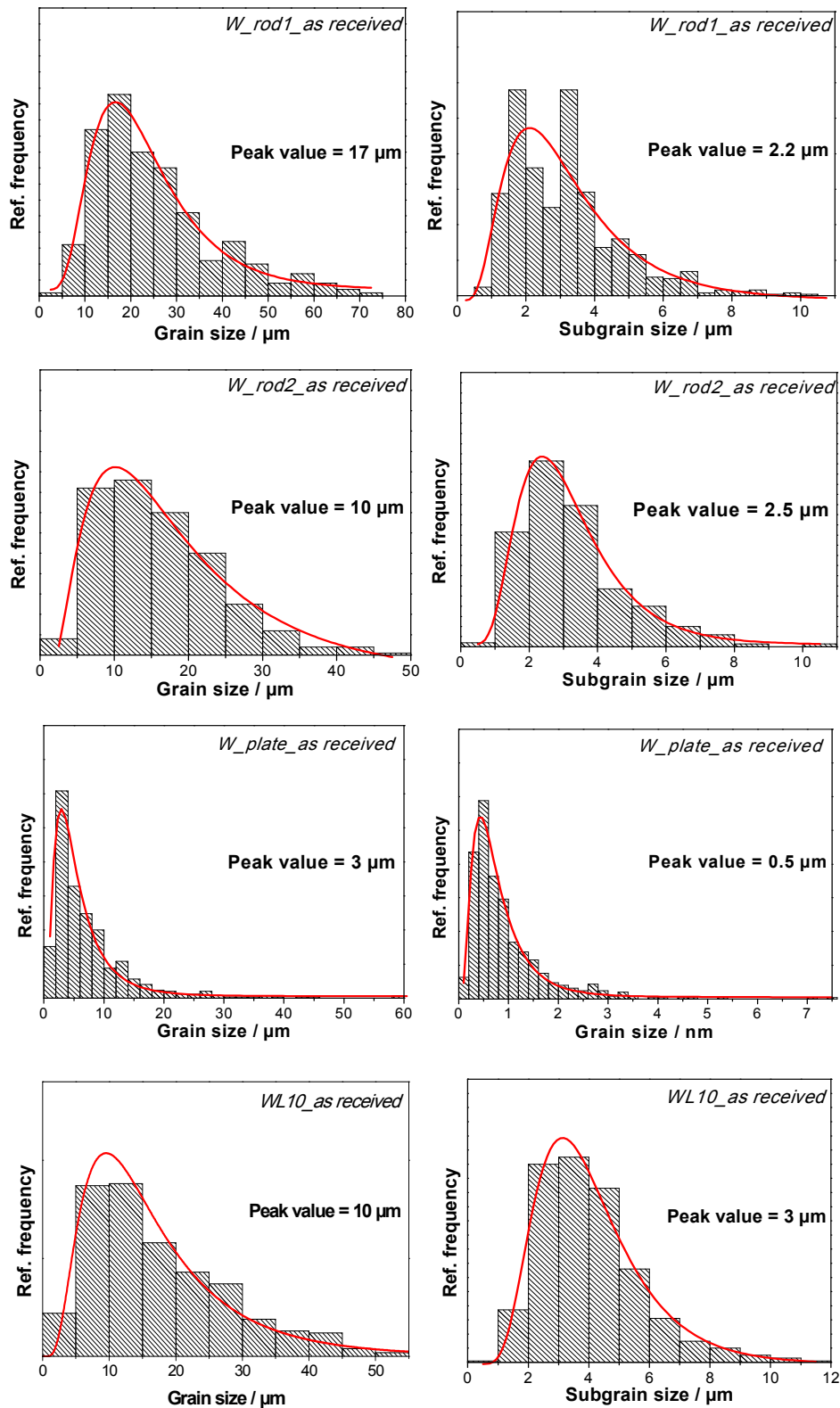
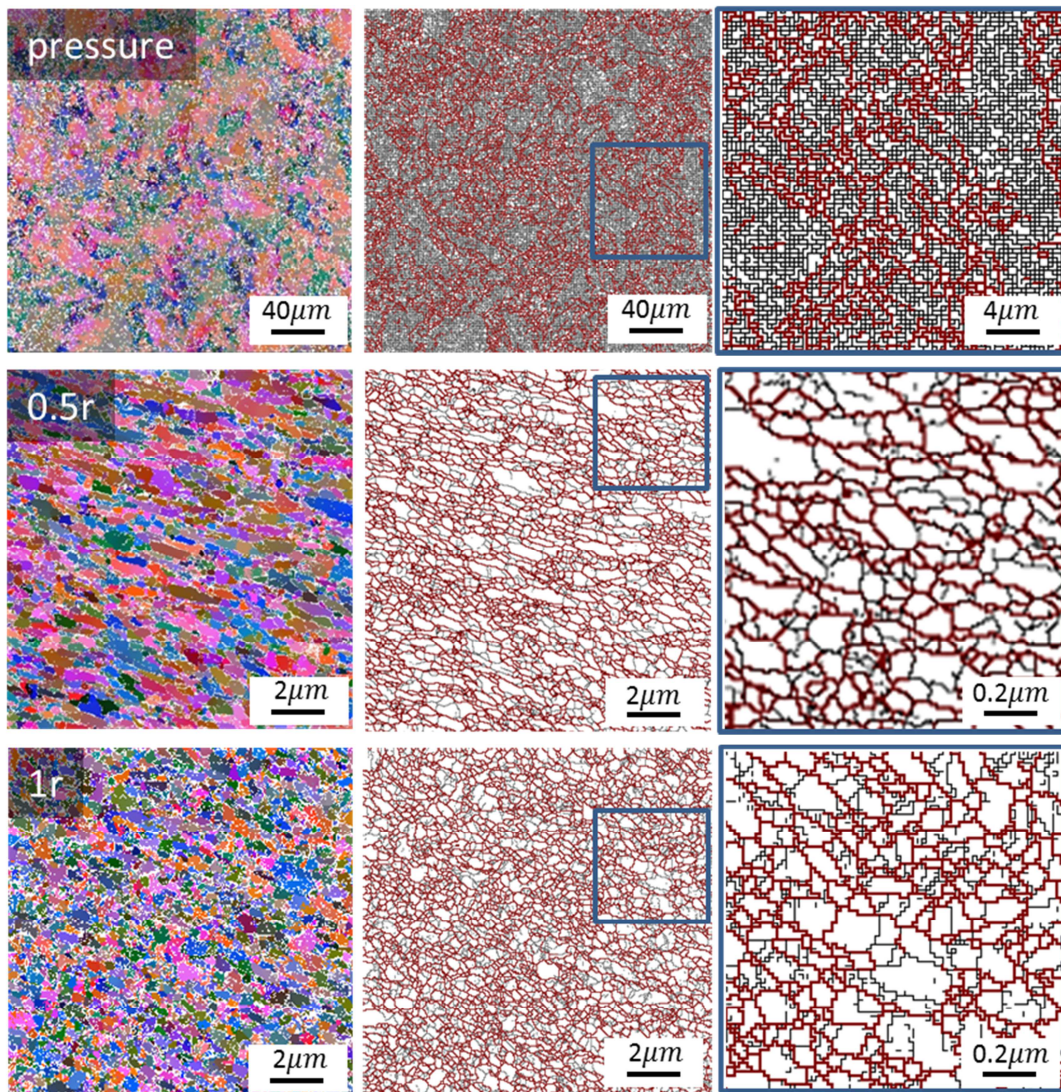


Fig. 4.13: Grain size and subgrain size distribution diagrams of as-received *W_rod1*, *W_rod2*, *W_plate* and *WL10*. Peak value from lognormal distribution fit is given.

The microstructure evolutions of as-deformed materials are exhibited from Fig. 4.14 to Fig. 4.22. The sample edge is observed, referring to position at 3mm from torsion axis. The grain size distribution along SD and RD are calculated respectively. Observations from each material are noticed following the order of W_rod1, W_rod2, W_plate and WL10.

W_rod1 (s. Fig. 4.14 and Fig. 4.15): Compared with as-received state in Fig. 4.12, after compressive load, W_rod1 shows a slight grain size reduction at the sample edge, but the grain size is still in micrometer range. After shear deformation, grains are harshly elongated after only 0.5 torsion revolution with an aspect ratio of 1.8. Further deformation leads to finer grain size and grains become equiaxed concurrently. The microstructure of W_rod1 becomes steady after 2 torsion revolutions.



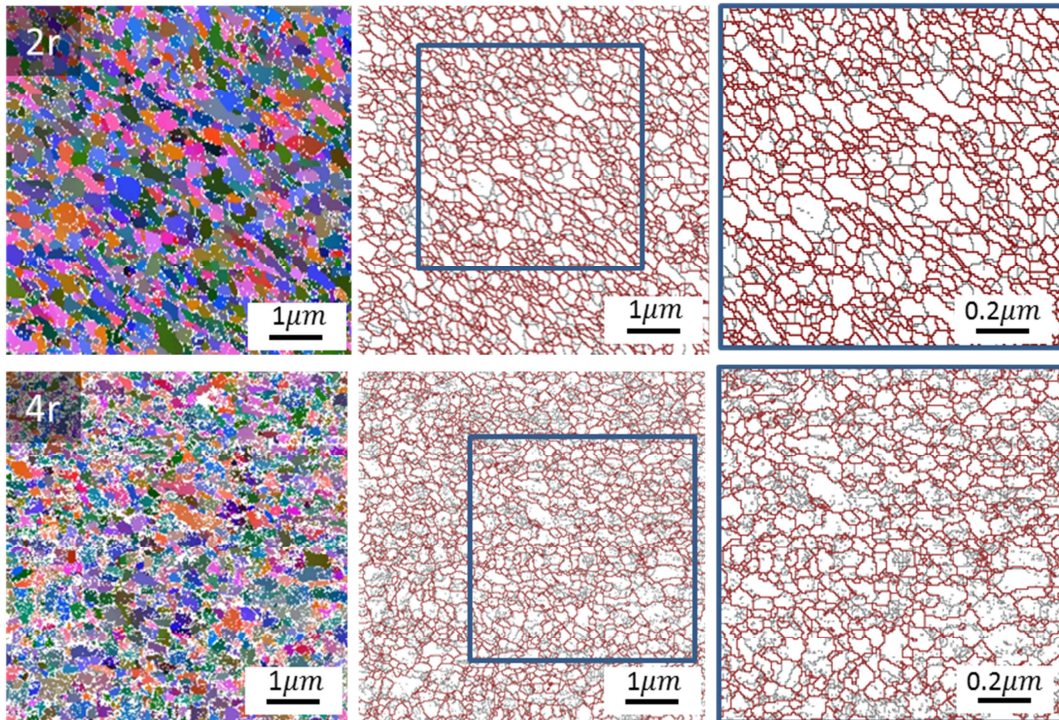
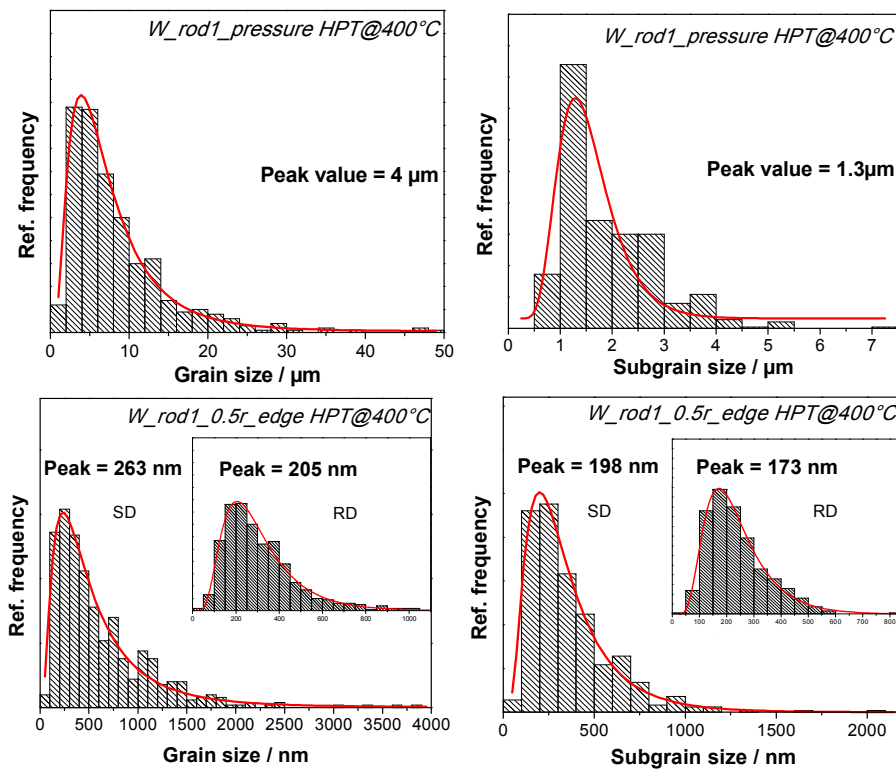


Fig. 4.14: W_{rod1} deformed by high-pressure torsion at 400°C after pressure and different torsion revolutions.

Left column: Euler contrast maps; Middle column: grain boundary maps;
Right column: larger magnification of blue-frame-covered region in middle column.



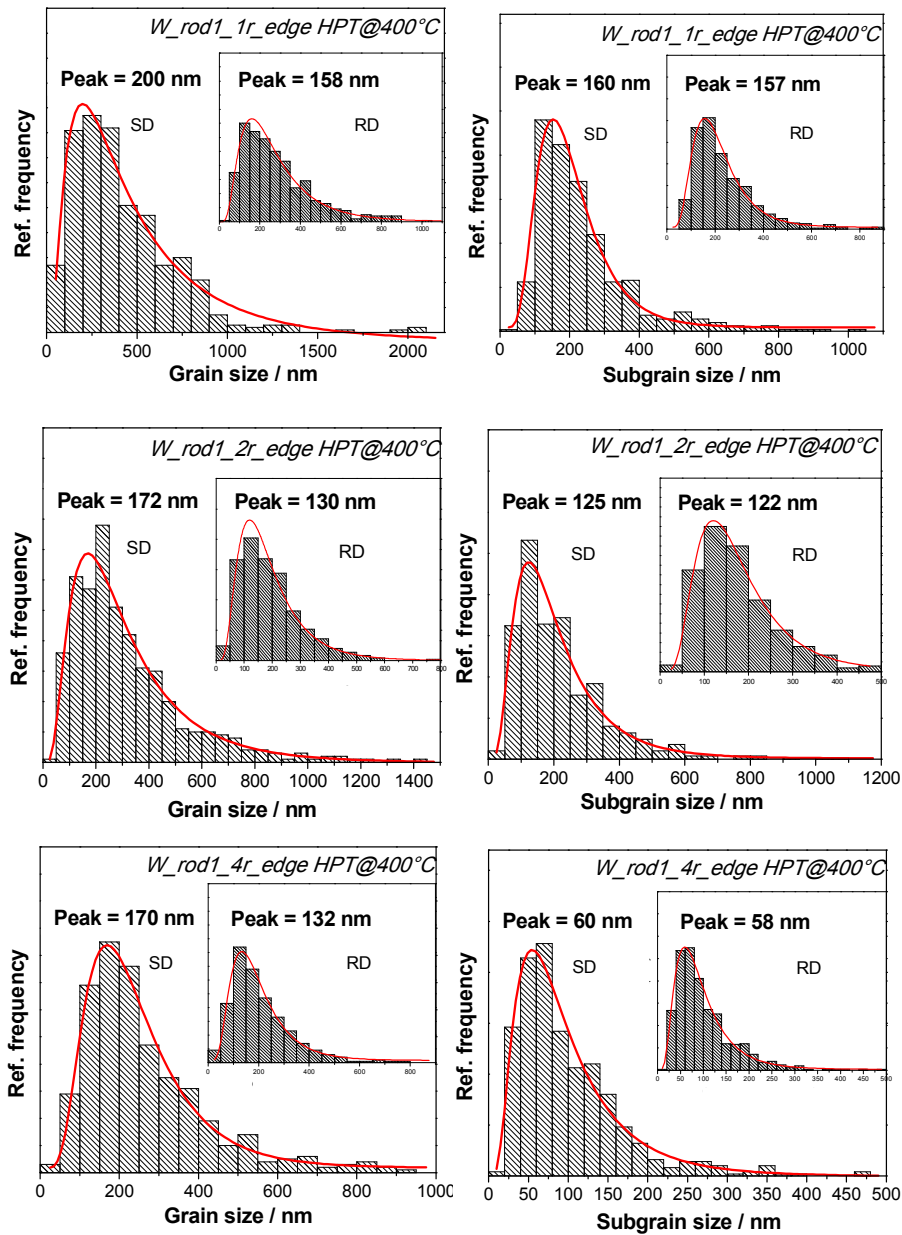
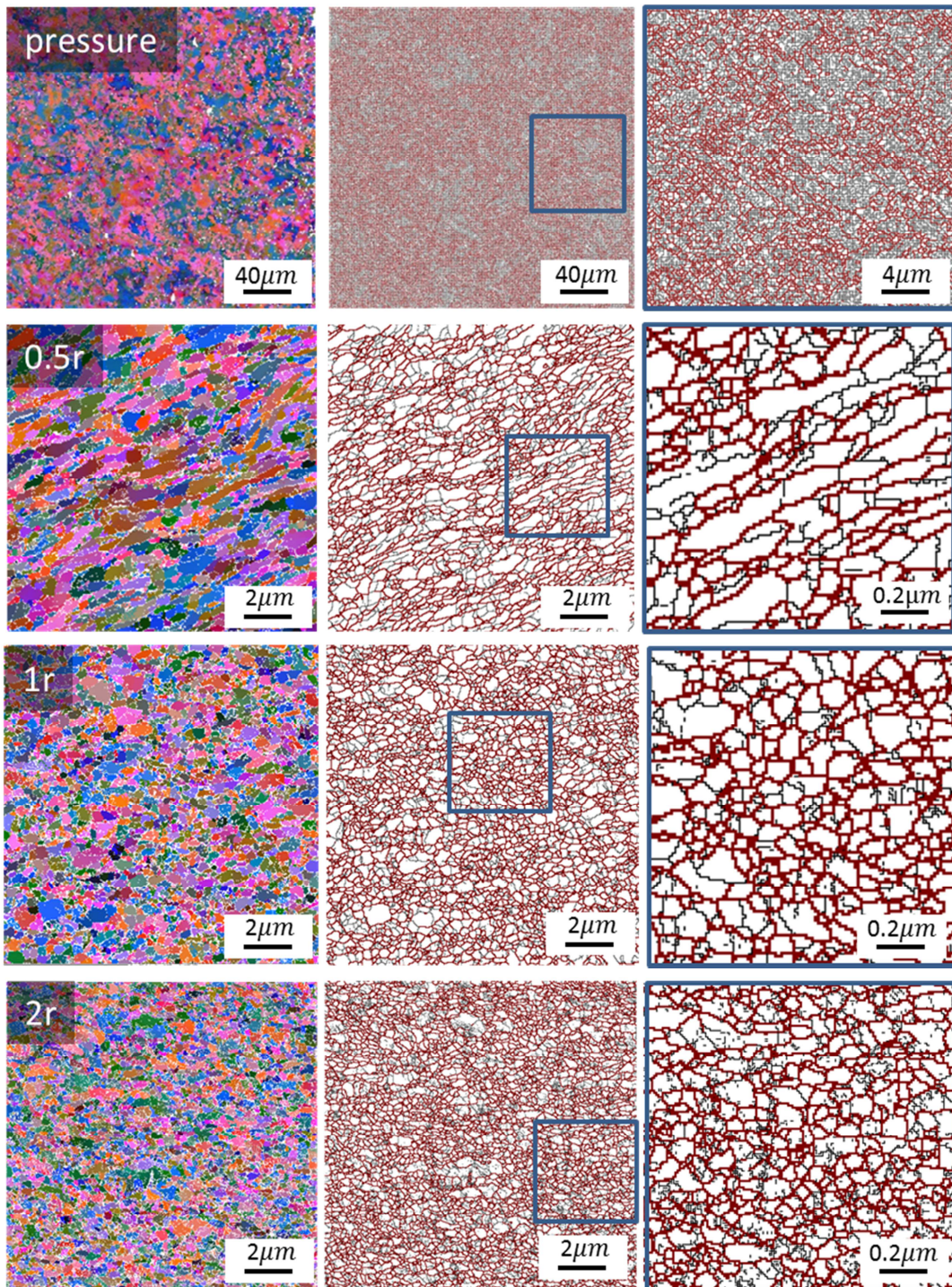


Fig. 4.15: Grain size and subgrain size distribution diagrams of W_rod1 deformed by high-pressure torsion at 400°C after pressure and different torsion revolutions.

W_rod2 (s. Fig. 4.16 to Fig. 4.18): The morphology is similar with W_rod1 after pressure. The aspect ratio of grain is 1.7 after half revolution of torsion, which is also identical with W_rod1. The microstructure is finer and grain aspect ratio decreases to 1.1 after 1 torsion revolution. The grain refinement rate is obviously slow down after 2 revolutions. There are vortices in microstructure after 4 turns and 8 turns, and their SEM images and IPFs are provided in Fig. 4.18. Small elongated grains are arranged aligning a vortex, while coarse grains are formed at the

surrounding area. The crystallography of coarse grain mainly exhibits $\{110\} // \text{SPN}$. The crystallography from inner part of vortex cannot be detected due to the highly distorted lattice. Therefore the grain size distribution diagram for W_rod2 after 8 torsion revolutions in Fig. 4.17 only considers the coarse grains. It is also seen that the diameter of vortex region grows from around $5\mu\text{m}$ after 4 revolutions (s. Fig. 4.18 a) to $10\mu\text{m}$ after 8 turns (s. Fig. 4.18 b).



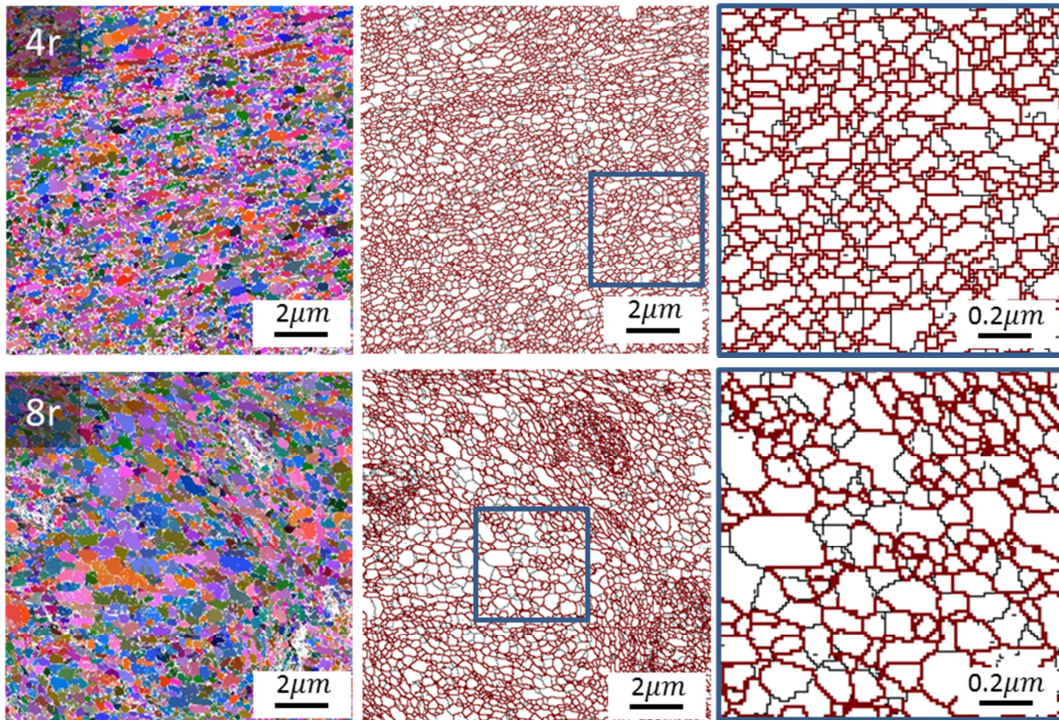
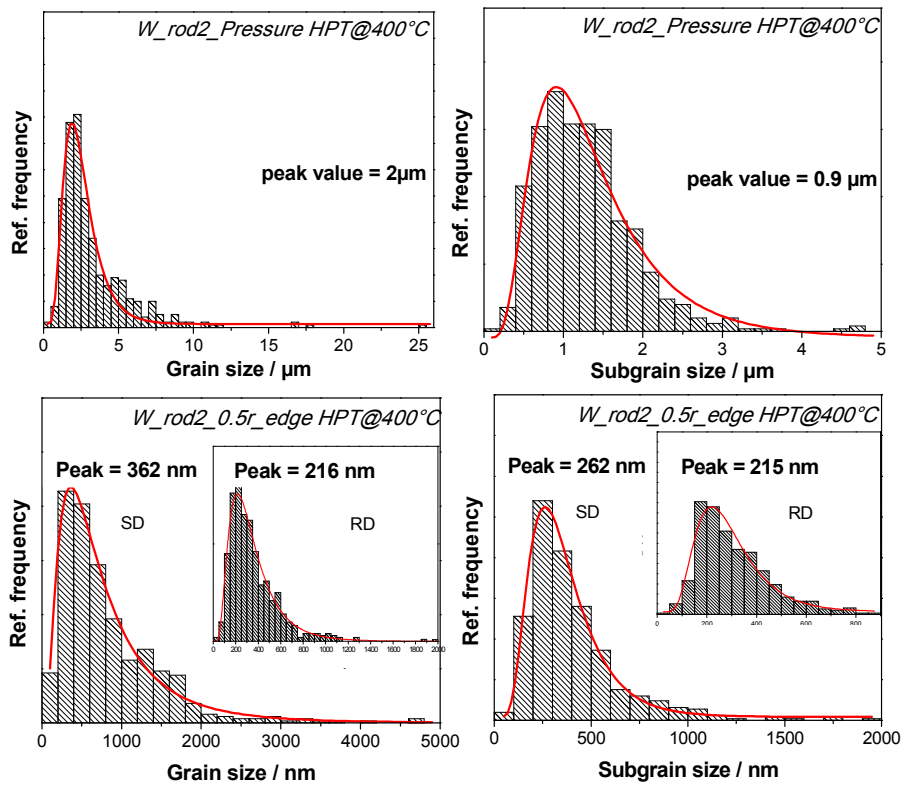


Fig. 4.16: W_{rod2} deformed by high-pressure torsion at 400°C after pressure and different torsion revolutions.

Left column: Euler contrast maps; Middle column: grain boundary maps; Right column: larger magnification of blue-frame-covered region in middle column.



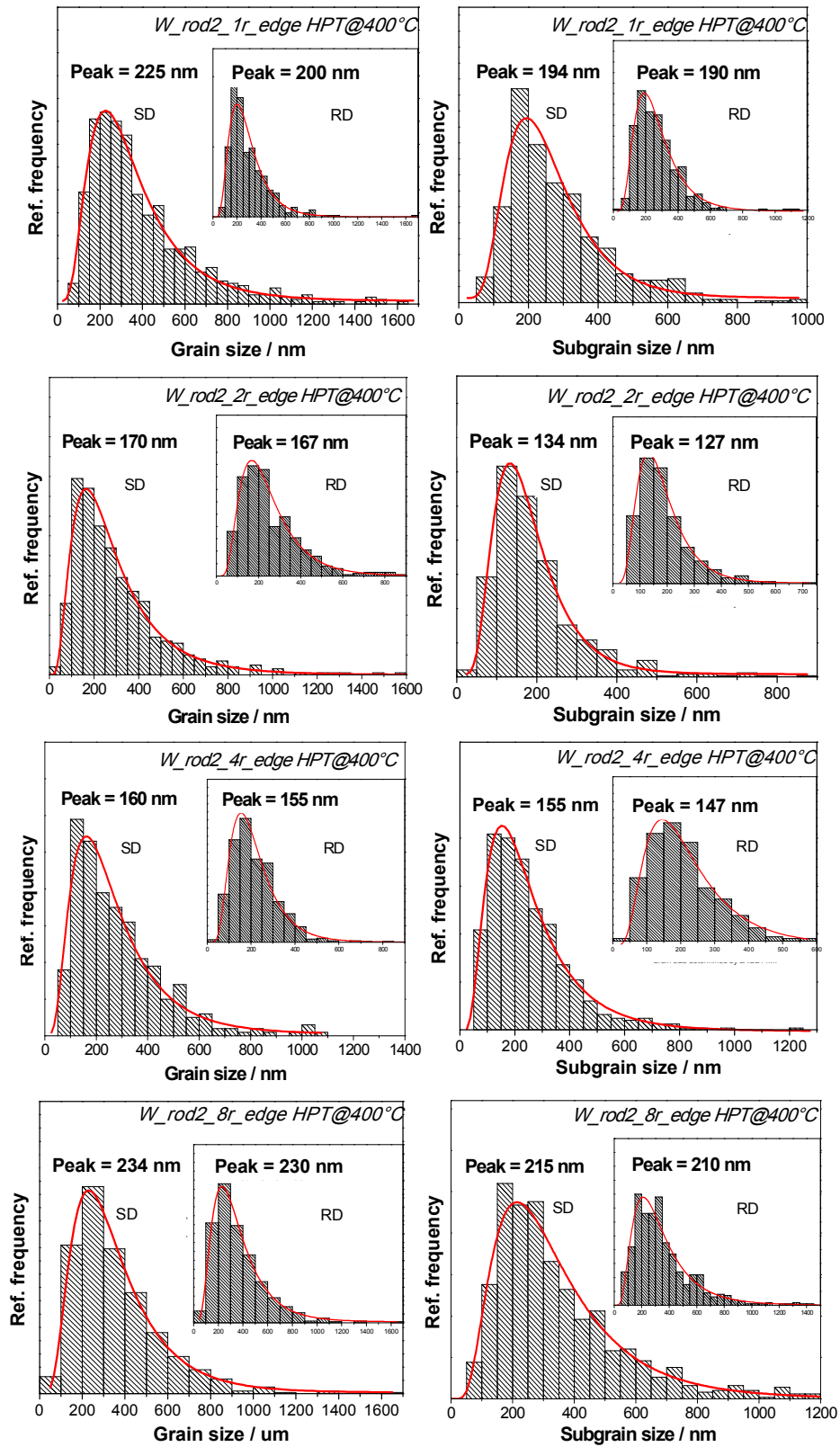


Fig. 4.17: Grain size and subgrain size distribution diagrams of W_rod2 deformed by high-pressure torsion at 400°C after pressure and different torsion revolutions.

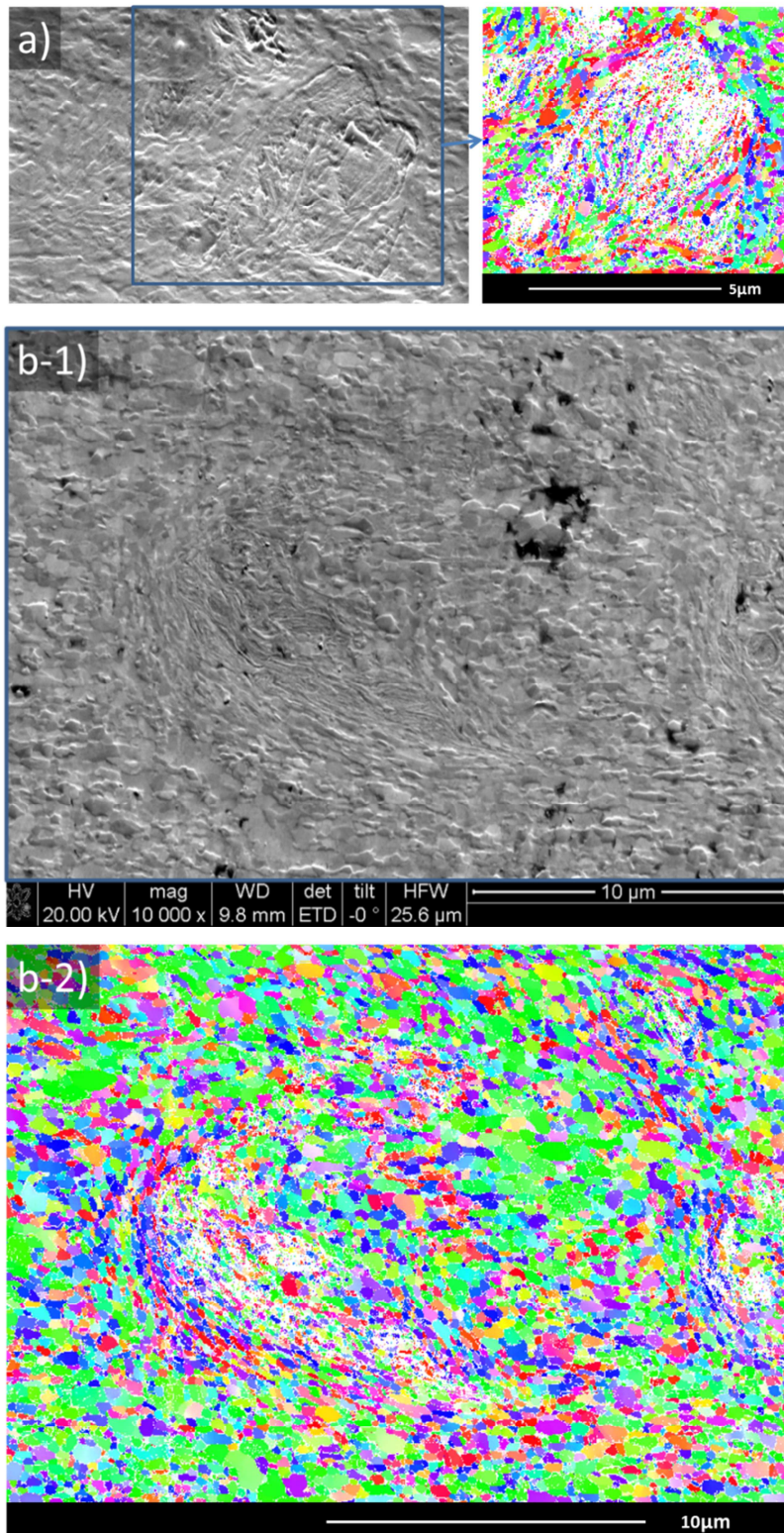
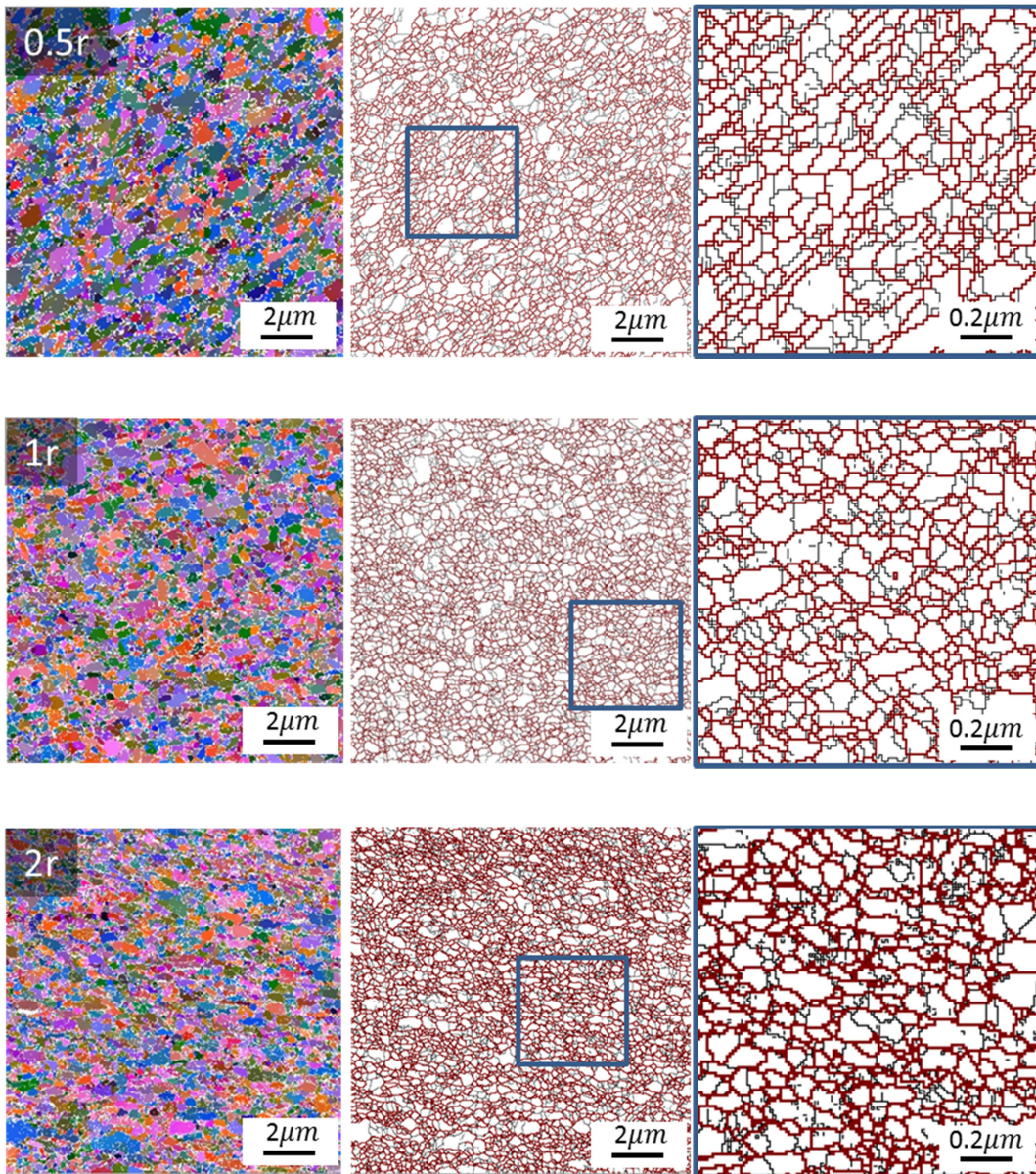


Fig. 4.18: SEM (second electron) images and corresponding inverse pole figures of W_{rod2} deformed by high-pressure torsion at 400°C. a) after 4 torsion revolutions and b) after 8 torsion revolutions.

W_plate (s. Fig. 4.19 and Fig. 4.20): As-received W_plate has the most non-uniform original microstructure among all investigated pure W, and possesses the smallest grain and subgrain size. After half torsion revolution, the grains in W_plate exhibit no significant elongation with the smallest grain aspect ratio of 1.34 comparing to others. After one torsion revolution, the grain size saturates, and it is earlier than other two pure W, which saturate after 2 torsion revolutions.



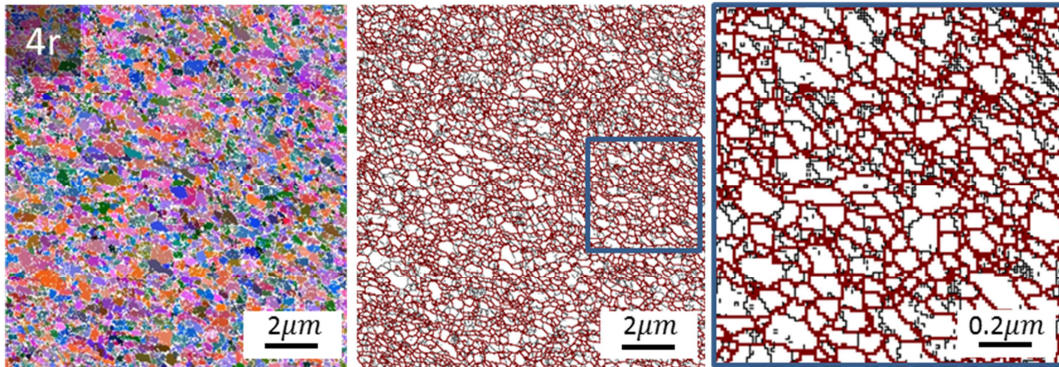
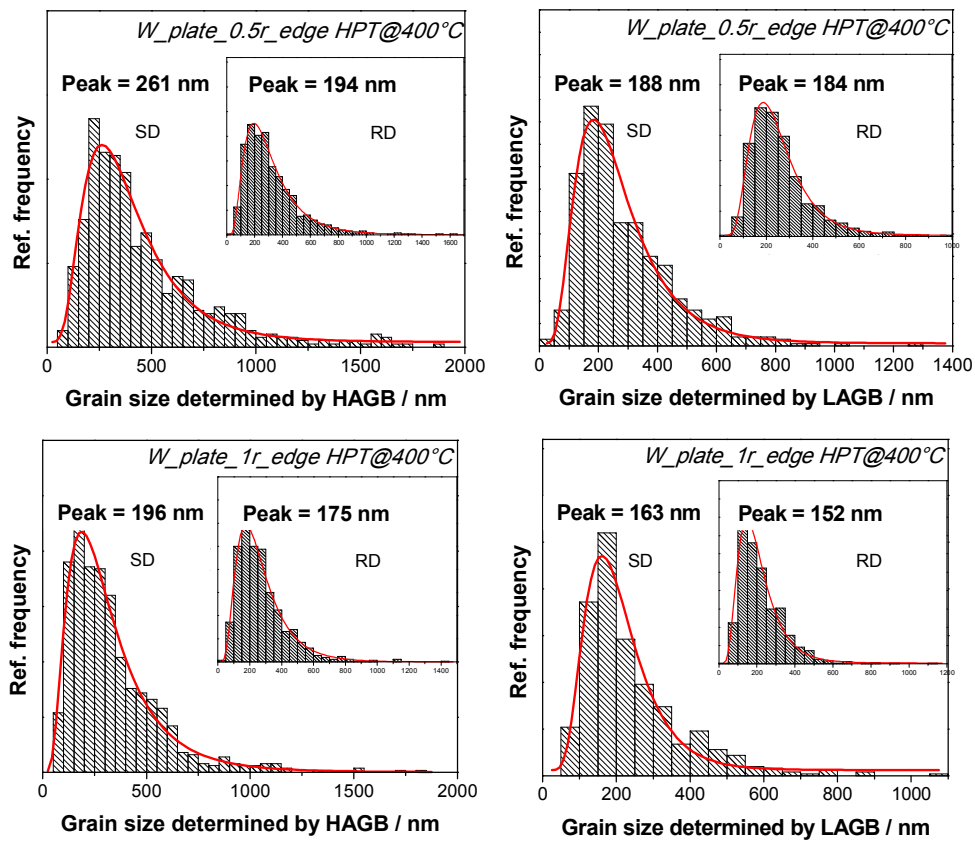


Fig. 4.19: W_{plate} deformed by high-pressure torsion at 400°C after different torsion revolutions.
 Left column: Euler contrast maps; Middle column: grain boundary maps;
 Right column: larger magnification of blue-frame-covered region in middle column.



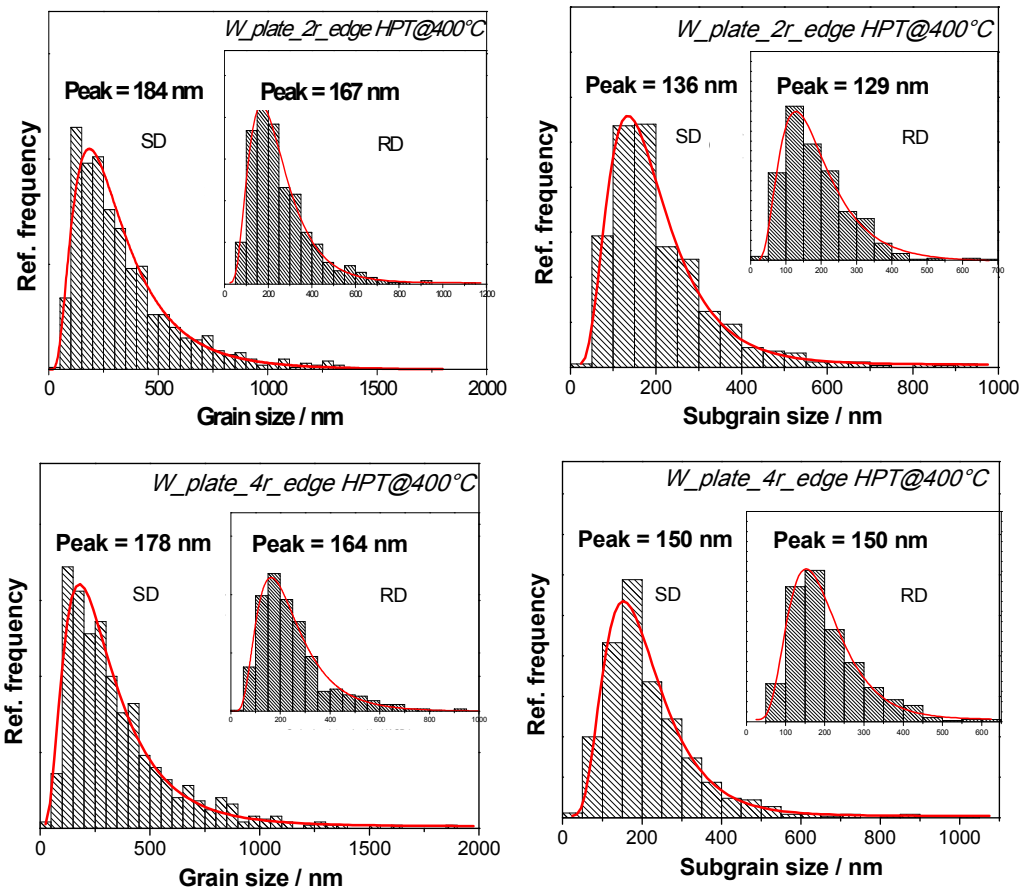


Fig. 4.20: Grain size and subgrain size distribution diagrams of W_{plate} deformed by high-pressure torsion at 400°C after different torsion revolutions.

WL10 (s. Fig. 4.21 and Fig. 4.22): Even though WL10 has comparable grain size with W_{rod2} , it exhibits distinct microstructure evolution. After 0.5 torsion revolution, the La_2O_3 particles can still be observed on the sample, as indicated by white arrows in Fig. 4.21. The grain is elongated with aspect ratio of 1.42 which is similar to W_{rod2} after 0.5 torsion revolution.

After 1 torsion revolution, the grain size of deformed WL10 is around 160nm, which is 30% smaller than the grain size of W_{rod2} . Beyond 2 torsion revolutions, the grain size in WL10 continues to become smaller and no obvious saturation is observed up to 4 torsion revolutions. The grain shape turns to be equiaxed with aspect ratio of 1.1 by then.

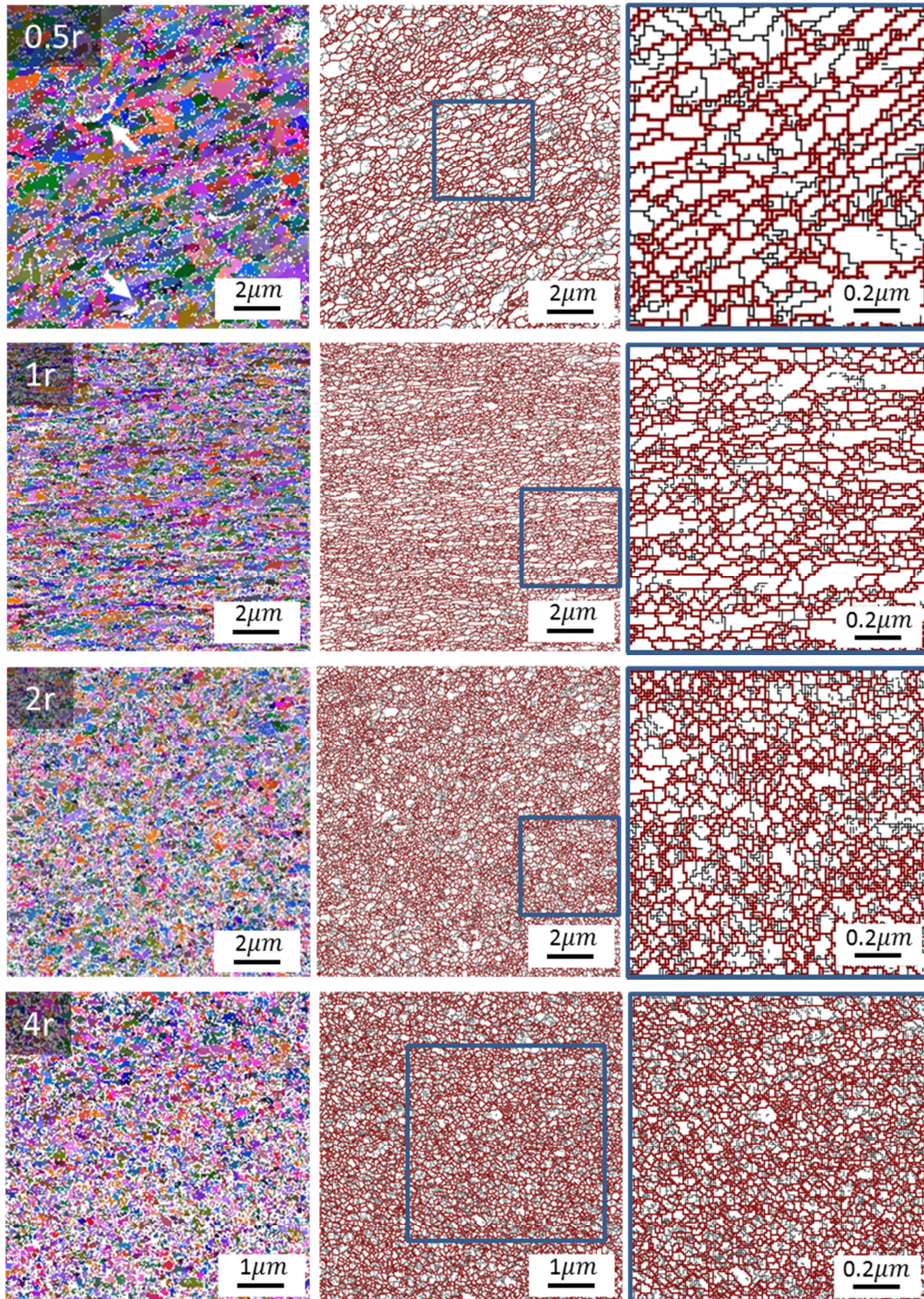


Fig. 4.21: WL10 deformed by high-pressure torsion at 400°C after different torsion revolutions.
Left column: Euler contrast maps; Middle column: grain boundary maps;
Right column: larger magnification of blue-frame-covered region in middle column.

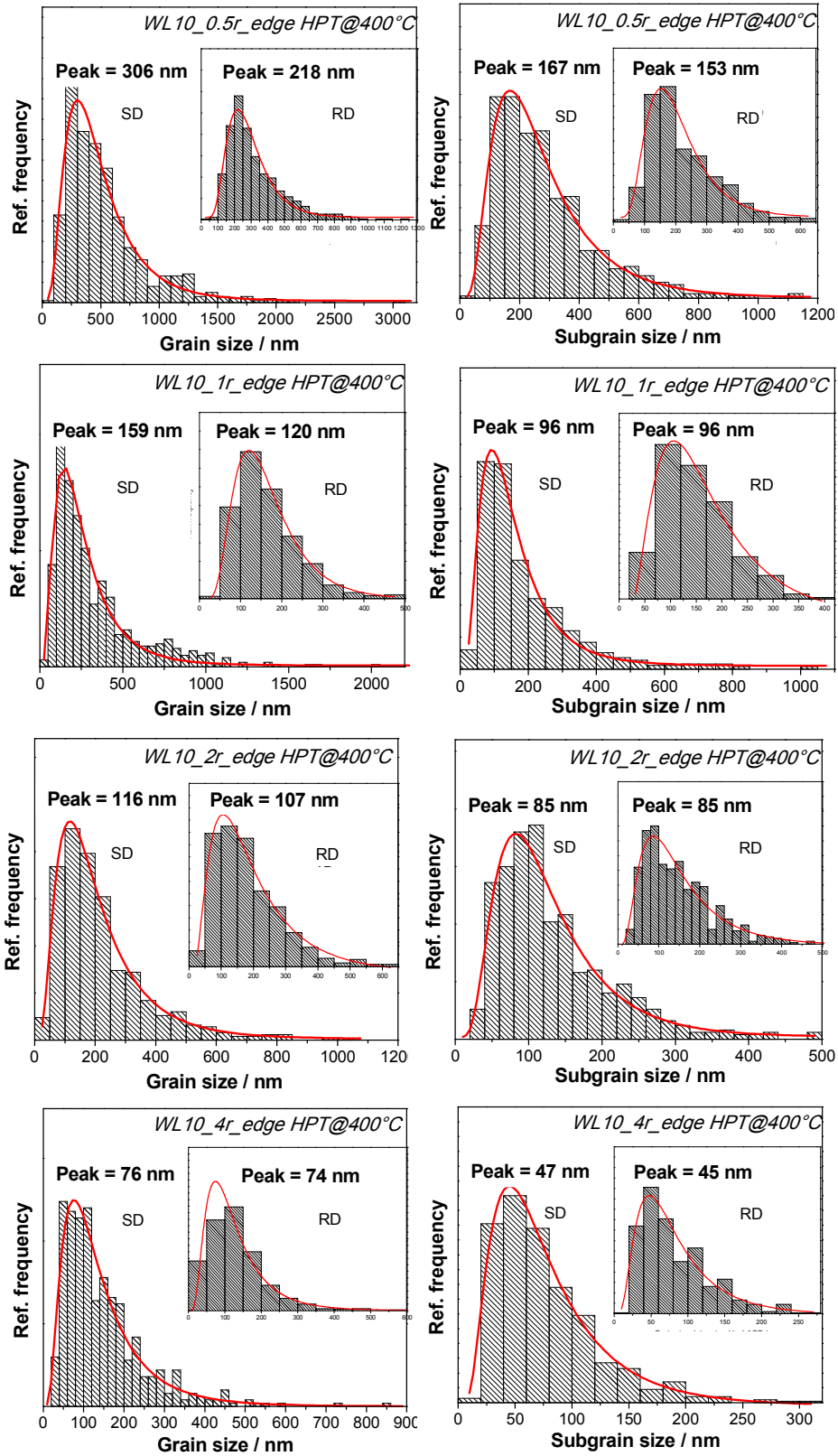


Fig. 4.22: Grain size and subgrain size distribution diagrams of WL10 deformed by high-pressure torsion at 400°C after different torsion revolutions.

The equivalent grain and subgrain sizes from all materials deformed by HPT at 400°C are compared in Fig. 4.23, in which a) and b) are referring to grain sizes while c) and d) are related to subgrain sizes. The measurement of equivalent strain size is provided by eq. (3.3) and Fig. 3.16. The sample position observed is 3mm from torsion axis, and the corresponding equivalent strain is shown as x-variable.

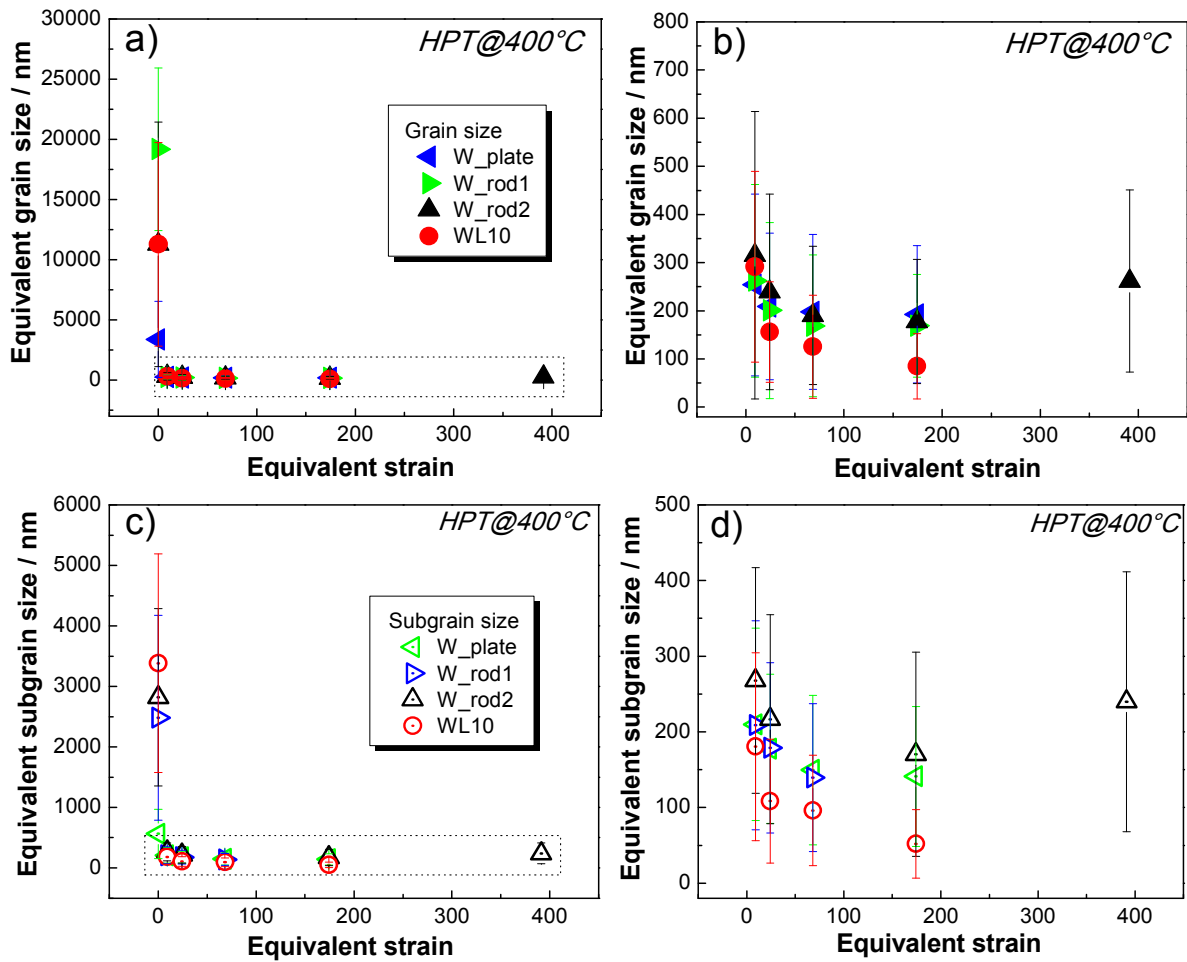


Fig. 4.23: Equivalent grain size along with equivalent strain for W_plate, W_rod1, W_rod2 and WL10 after high-pressure torsion at 400°C, the equivalent grain size is determined from a) high angle grain boundaries with b) a detail view of selected region and c) low angle grain boundaries with d) a detail view of selected region.

From Fig. 4.23 a) and c), it is observed that both grain size and subgrain size are reduced dramatically by HPT for all materials. For example, the equivalent grain size of W_rod2 is refined by 2 orders of magnitude after HPT at 400°C with half torsion revolution. The data in Fig. 4.23 b) and d) exclude as-received state and exhibit the enclosed-region in Fig. 4.23 a) and Fig.

4.23 c). Despite the microstructure differences in as-received materials. All of the three pure W exhibit similar grain size evolution, which includes three stages:

- i. Grain refinement stage. The rapid reduction in equivalent grain size is obvious after only half revolution ($\epsilon=9$), and this procedure continues to 1 and 2 revolutions ($0 < \epsilon < 68$).
- ii. Saturation stage. After 2 torsion revolutions ($\epsilon > 68$), the grain sizes don't change much along with increasing strain. The corresponding equivalent grain size is around 170nm for all three pure W.
- iii. Slightly coarsening stage. A grain size growth phenomenon is observed in W_rod2 after 8 torsion revolutions (true strain of 391), which is from 160nm (after 4 torsion revolutions) to 234nm (after 8 torsion revolutions).

As for WL10, at the beginning of deformation, it has similar equivalent grain size with W_rod2. While the difference between WL10 and pure W starts after 1 revolution and becomes significant with increasing strain. No obvious saturation in grain size can be found up to 4 revolutions for WL10 during HPT at 400°C. In contrary, the equivalent grain size of WL10 after 4 turns is below 100nm, specifically 76nm in grain size and 47nm in subgrain size.

Figure 4.24 shows the percentage of equivalent subgrain size with respect to equivalent grain size along with strain. This ratio generally reflects the subgrain amount within one grain. $\epsilon=0$ refers to as-received state and the ratio is in between 10% to 30% for four materials. While after HPT deformation, the ratio becomes larger until it scatters in the range of 60% to 100% after 4 torsion revolutions. Specifically, after 4 turns, WL10 shows 60% in subgrain/grain ratio while W_rod2 maintains the ratio of near 100%. The increase of subgrain/grain ratio implies that fewer subgrains occupy one grain as deformation continues, and this is a reasonable consequence from LAGB-to-HAGB transition.

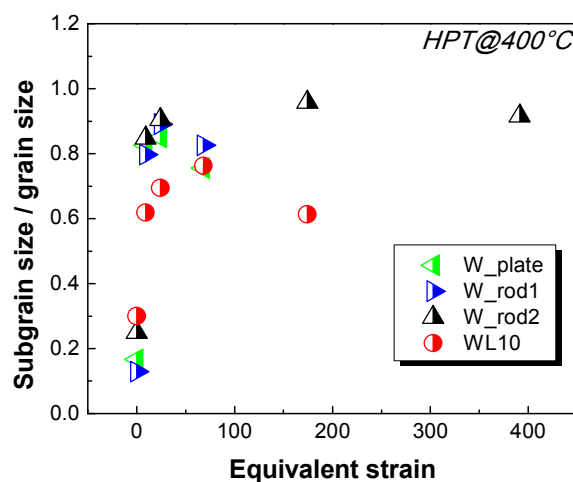


Fig. 4.24: The subgrain/grain ratio after high-pressure torsion at 400°C.

4.2.3 Grain boundary misorientation

The evolution of average grain boundary misorientation angle along with equivalent strain during HPT is plotted in Fig. 4.25. Four materials are all displayed.

It is observed from Fig. 4.25 that all materials exhibit the same trend, which contains a rapid growth stage and a saturation stage. The rapid growth of misorientation angle starts from the beginning of deformation and end up at true strain of around 40. Thereafter saturation appears. Among four materials, W_rod1 and W_rod2 have nearly the same value at saturation stage. While W_plate has a slight lower value after 2 revolutions ($\epsilon \geq 68$) compared with the other two pure W. As for WL10, after small strain amount, such as before half revolution ($\epsilon < 9$), the average misorientation is consistent with deformed W. However after 1 revolution ($\epsilon \geq 20$), HPT deformed WL10 exhibits higher average misorientation, the difference is 2° to 3° .

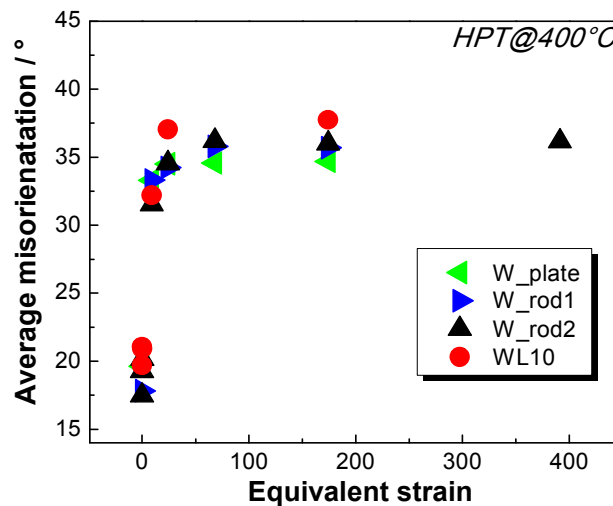


Fig. 4.25: The changes of average misorientation angle along with equivalent strain for different materials after high-pressure torsion at 400°C .

4.2.4 Texture

The pole figures (PF) in Fig. 4.26 reveal the texture changes of four investigated materials after HPT. Projection crystal planes of $\{111\}$, $\{110\}$ and $\{100\}$ are chosen. The color in PF refers to texture intensity, which is influenced by image pixel. Therefore it is only comparable when the observation area and step size are identical.

The PFs from as-received state are illustrated on the left column. Despite the intensity differences, W_rod1, W_rod2 and WL10 have analogous texture, which is $\{110\} // \text{SPN}$. While W_plate

exposes a distinct texture with a relative strong $\{100\} // \text{SPN}$ and a weak $\{111\} // \text{SPN}$ component, as shown in Fig. 4.26 a). The existence of these textures in as-received state is due to the pre-deformation of raw products.

The PFs of HPT deformed materials are shown on the right column in Fig. 4.26. All of the three pure W are deformed after 2 torsion revolutions and in saturation regime. HPT deformed WL10 after 4 torsion revolutions is displayed. It is observed that all of the three pure W exhibit the same texture eventually, which consists of $[111] // \text{SD}$ and $\{110\} // \text{SPN}$ components. This texture implies that after sufficient imposed strain, for all pure W, $[111]$ direction in crystal tends to align shear direction and $\{110\}$ crystal plane tends to align parallel to shear plane. Compared with initial state, the textures after deformation show more diffuse pattern and less intensity. Moreover, different slip system may activate in WL10 compared with pure W during HPT by showing distinct texture after HPT. Instead of $\{110\} // \text{SPN}$, a weak $\{100\} // \text{SPN}$ texture is observed, and $[100] // \text{SD}$ and $[111] // \text{SD}$ components appear.

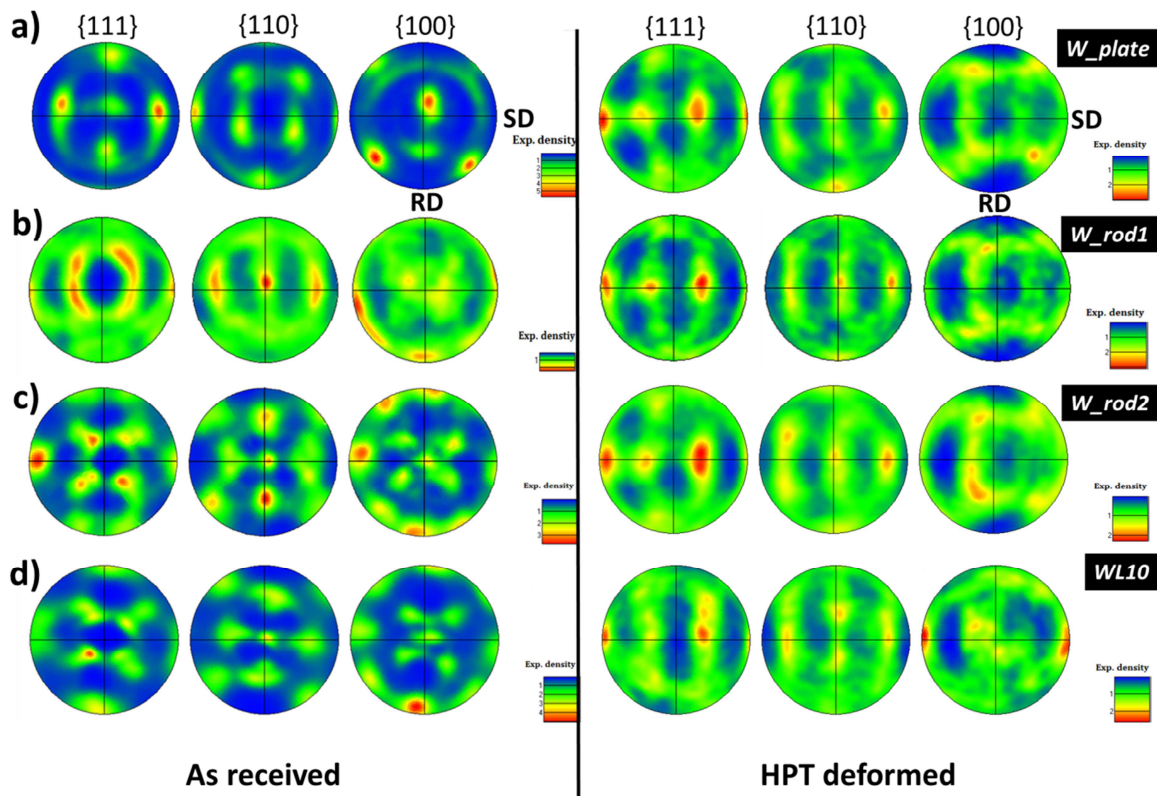


Fig. 4.26: Pole figures of as-received and high-pressure torsion deformed
a) W_plate, b) W_rod1, c) W_rod2 and d) WL10.

4.2.5 Hardness

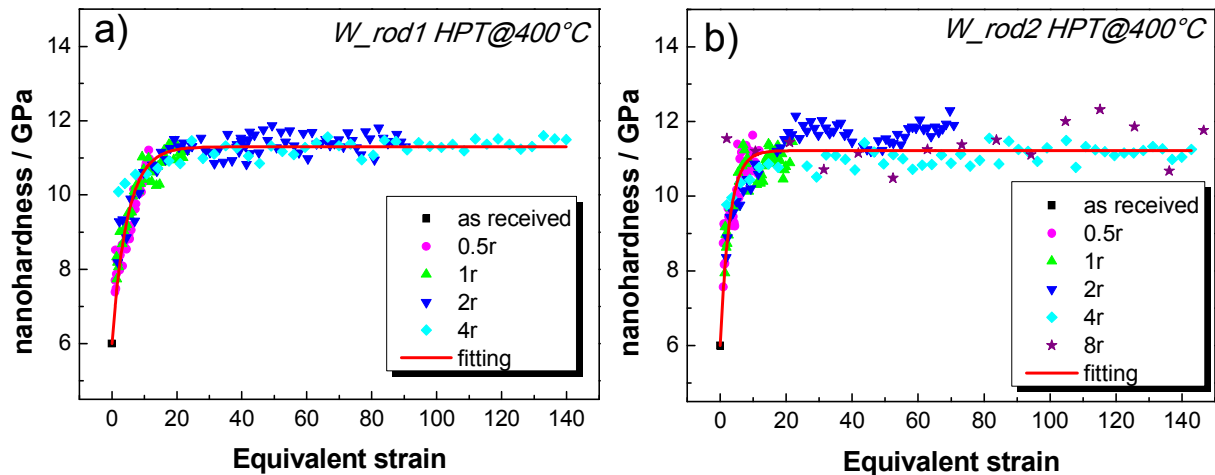
Fig. 4.27 demonstrates the hardness along with equivalent strain for all the four materials. The hardness value is obtained from nanoindentation. As for the initial coarse-grain materials, Vickers indentation is performed to calibrate hardness value obtained from nanoindentation, and 6GPa is accepted for all of the four as-received materials. For each material, a simple fitting equation is employed to evaluate the strain hardening behavior during HPT:

$$H = H_0 + (H_s - H_0)(1 - e^{-c\varepsilon}) \quad (4.1)$$

in which H_0 and H_s refer to the hardness in as-received state and saturation region respectively, while c is a constant corresponding to material property. Four fitting curves are compared in Fig. 4.7 e). The corresponding fitting parameters are displayed in Table 4.1

Three pure W exhibit similar evolution in hardness along with equivalent strain, as shown in Fig. 4.27 a), b) and c). Two stages are observed from Fig. 4.27: 1) a rapid growth of hardness is seen from equivalent strain of 0 to about 20, and the corresponding hardness is from 6GPa to above 11GPa, which is 1.8 times compared to initial state; 2) When the equivalent strain is larger than 20, hardness does not grow any further no matter how much strain imposed. In other words, saturation in hardness exists. The specific onset strain values required for saturation are summarized in discussion section.

Distinct from pure W, WL10 demonstrates a parabolic growth in hardness along with equivalent strain, as is shown in Fig. 4.27 d). The hardness is improved from 6GPa to around 16GPa after equivalent strain of 174, which is 2.6 times compared to as-received state. Furthermore, no obvious saturation in hardness can be seen within the investigated strain range.



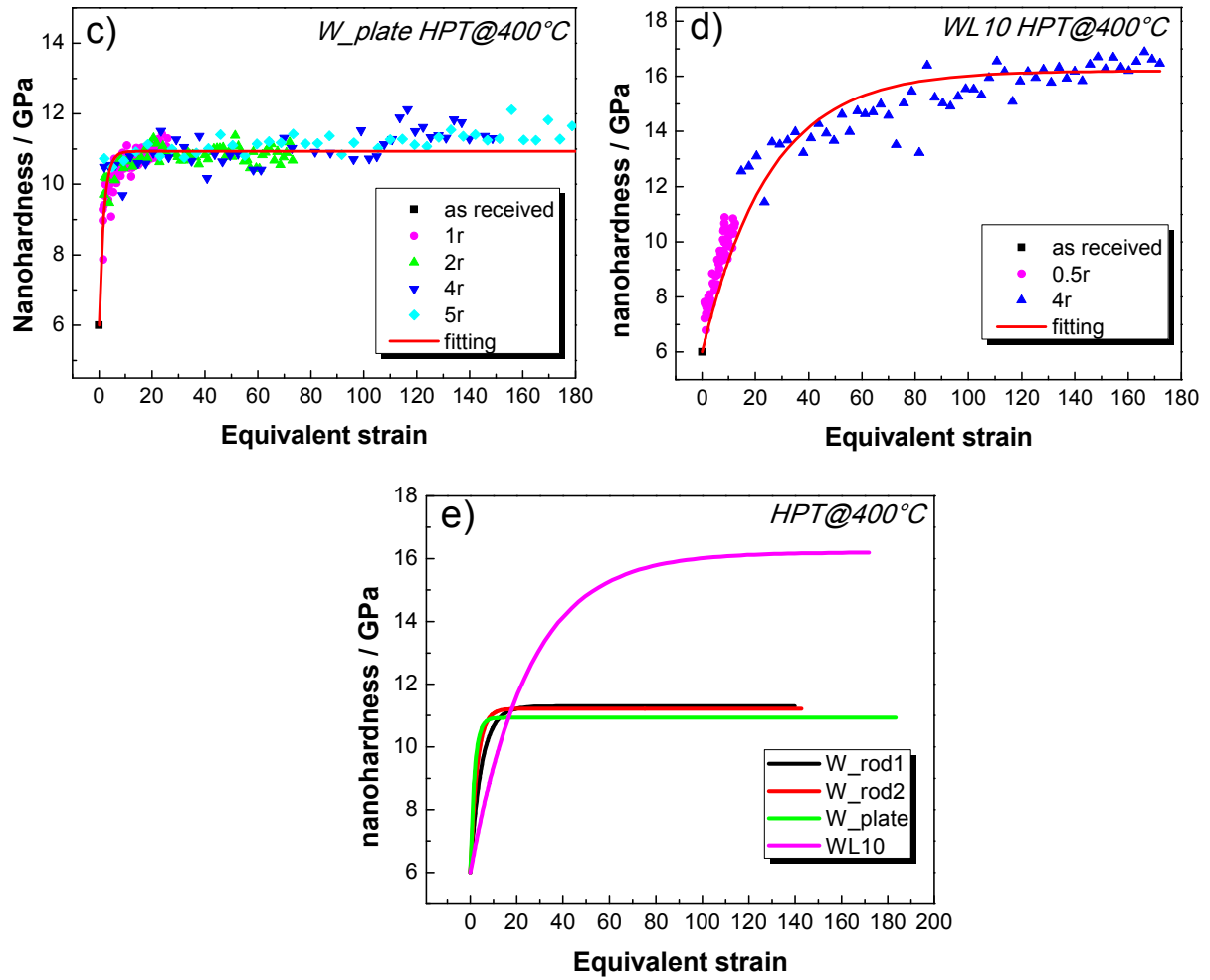


Fig. 4.27: Nanohardness vs. equivalent strain for high-pressure torsion deformed a) W_rod1, b) W_rod2, c) W_plate, d) WL10 and e) all fitting curves.

Table 4.1: fitting equation and fitting parameters

	H_0/GPa	H_s/GPa	c
WL10	6	16.2(\mp 0.22)	0.04
W_rod2	6	11.22(\mp 0.08)	0.35
W_rod1	6	11.30(\mp 0.07)	0.21
W_plate	6	10.93(\mp 0.06)	0.17

4.2.6 Discussion

In this section, three aspects are discussed: influence of original microstructure, alloying effect as well as grain coarsening phenomenon at large strain.

Influence of original microstructure:

Three pure W (W_rod1, W_rod2 and W_plate) are employed in this thesis to investigate the original microstructure effect during HPT. Despite the difference in morphology and grain size at initial state, all of them exhibit similar deformation behavior under given condition. The microstructure refinement procedure consists of a rapid grain fragmentation stage and a following saturation. The hardness value changes correspondingly. The typical values of torsion torque, minimum grain/subgrain size, hardness and average grain boundary misorientation angle are provided in Table 4.2. It is clearly seen that all pure W have identical values for the above mentioned features.

Table 4.2: Critical values from HPT deformed W and WL10.

Material	Torsion torque evolution	Hardness /GPa	Min. structure size /nm		Grain boundary misorientation/ $^{\circ}$
	at $\epsilon=80$		Saturation	grain	
W_rod1	166	11.2	172	125	35.7
W_rod2	168	11.2	170	134	36.2
W_plate	152	11	178	150	34.7
WL10	250	16	76	47	37.7

Researchers state that the microstructure obtained is associated with strain hardening induced refinement and dynamic recovery induced coarsening [112]. Both of them depend on stacking fault energy (SFE) of material, which is an instinct property. Therefore despite the original microstructure differences, all of the pure W activate the same slip system during HPT. As indicated by the texture evolution (s. Fig.4.26), the densest packed crystal direction [111] acts as slip direction and {110} crystal plane acts as slip plane. The microstructure difference inherited from as-received state diminishes gradually, and eventually resulting in identical grain sizes, hardness and texture in saturation region. This result is consistent with the argument from eq. (2.6), which states that the minimum grain size in saturation region is proportional to square root of SFE. If the materials composition are identical (same SFE), the minimum grain sizes obtained should be the same. Moreover, the torsion torque in steady state reflects the flow stress within

materials, while flow stress is proportional to square root of dislocation density. The similar torque value in saturation means dislocation density for all pure W has also the same level by then.

During HPT, torsion torque grows with imposed strain due to dislocation interactions, after the peak value is reached materials undergo softening with further strain. This reduction of torsion torque may attribute to several reasons:

- i. Micro-crack accumulation within material [62]. The possibility is quite high since W is inheriting brittle. However micro-crack is not observed in this work under resolution of EBSD, which is 30nm.
- ii. Texture softening, referring to grains rotate to favorite crystallographic orientation [45]. It has already observed that $\{110\}$ $[111]$ is the dominate slip system in deformed W from the beginning of deformation.
- iii. Thermal softening [62], relating to local heating due to intense torsion straining [113]. Even though the sample temperature is controlled to be constant by a program connected to furnace in this work, sudden local heat accumulation is still hard to detect and avoid.
- iv. Dynamic recrystallization (DRX) [88]. It is reported that grain rotation and coalescence can occur during deformation [114]. Besides, serrations are developed from high angle grain boundaries due to interaction of deformation substructure, and by this process, geometric dynamic recrystallization (GDR) more likely happens.
- v. Strain softening [115] and stress-enhanced grain growth [116].

In this work, the observed shear texture and equiaxed grain shape provide evidences to texture softening and dynamic recrystallization mechanism, and the latter mechanism weigh more because that texture appears from the very beginning of deformation and the intensity is quite low.

Since the torsion torque, grain size, hardness and grain boundary misorientation all exhibit saturation during HPT, the onset strain values of them and torsion torque peak are summarized in Table 4.3, in which saturation onset is defined as 99.95% of steady state value on fitting curve. It should be mentioned that among all the features shown in Table 4.3, torsion torque is consecutive along with equivalent strain, while hardness measurements consist of sufficient discrete data which can be treated as approximate consecutive. However, grain size and grain boundary misorientation angle distribution are associated with several critical values, such as after 0.5, 1, 2, 4 and 8 torsion revolutions. Therefore the saturation onset value obtained from torsion torque or hardness has relatively high credibility. It is found out that distinct from torsion torque, other three features demonstrate monotonic evolution. Besides, the onset of grain size saturation and grain boundary misorientation is more or less close to torsion torque saturation. The hardness

saturation occurs earlier than grain size saturation for all pure W. From section 4.1, we acknowledge that grain refinement is along with LAGB-HAGB transition. It is reasonable if the grain boundary misorientation angle evolution saturates at certain equivalent strain, the grain size saturates simultaneously. According to work hardening theory [88, 117, 118], with increase of imposed strain, large amount of dislocations can be generated and interact with each other, dislocation tangles and cells are formed in materials. With further deformation, cell boundaries become sharp and turn into grain boundaries, therefore small grains are formed. However, hardness can be improved both by grain size refinement as well as by complex dislocation structures introduced, even when cells haven't turned into grains yet. Therefore hardness value saturates earlier than grain refinement. Furthermore, compared to other pure W, W_plate shows earlier work hardening, and so as the hardness, grain size and grain boundary misorientation saturation. This is associated to its deformation history before HPT. The microstructures of as-received W show clearly that W_plate has the most non-uniform morphology due to larger amount of pre-deformation compared to others.

Table 4.3: Critical onset values of equivalent strain for HPT deformed W and WL10.

Material	Torsion torque evolution		Hardness	Grain size	Grain boundary misorientation
	peak	Saturation	Saturation	saturation	Saturation
W_rod1	16	50	33	~ 68	40
W_rod2	16	50	20	~ 68	40
W_plate	5	30	12	~ 24	28
WL10	16	-	-	-	55

Influence of alloying:

From Table 4.2, it is noticed that HPT deformed WL10 has remarkable finer grain size than pure W after 4 torsion revolutions, which is 85nm and the corresponding hardness is the highest of 16GPa. This phenomenon is attributed to La₂O₃ particles addition. In as-received WL10, oxide particles have relative large scale which is in micrometer range. According to Zener pinning effect, when the particle volume fraction is fixed, reducing the particle size can increase the pinning pressure. Therefore the influence of original large oxide particles on grain refinement and material strengthening are not obvious. With increase of strain, the oxide particles are elongated and fragmented into small scale. When the equivalent strain is larger than around 20, it is assumed that the oxide particles are small enough to strengthening the material obviously by exhibiting higher torsion torque than pure W (s. Fig. 4.11 b). The results from grain refinement and hardness evolution are consistent with this assumption. Especially for hardness evolution, a

clear surpass point of WL10 with respect to W can be found at around 18 equivalent strain. With further deformation, a re-increasing in torsion torque for WL10 indicates that the oxide particles become even smaller and thus more effective at material strengthening. The grain refinement in WL10 is more rapid than in pure W after same amount of strain, and no obvious saturation region is seen up to 4 torsion revolutions.

As is mentioned in section 4.1, the grain refinement during HPT is related closely to LAGB-HAGB transition and deformation texture. However, there is little difference when comparing WL10 to pure W in average grain boundary misorientation angle after equivalent strain of 20. The former is only 2°-3° higher than the latter (s. Fig. 4.25), which can be treated suspiciously as measurement error. On the deformation texture side, the difference for the two materials is that {110} // SPN texture disappears in deformed WL10 and the texture intensity is relatively weak. This is implying that oxide addition alters the slip system during HPT and retard the formation of strong texture such as {110} // SPN. However, the transition of LAGB-HAGB is almost equally complete with or without oxide particles

Grain coarsening at extreme large strain:

The grain coarsening is observed at extreme high strain level, such as after 8 torsion revolutions for both pure W and WL10. The coarse grain is about 250nm in diameter which is larger than the grain size obtained from sample edge after 4 torsion revolutions. High intensity texture component of {110} // SPN is related to these coarsened grains. It is noticed that coarsening region is always formed aside with a swirl core microstructure. The grains in swirl are only 50nm in diameter. We assume that the swirl structure is the reason for grain coarsening surrounding them. The existence of swirl may due to material instability under severe plastic strain. The reported vortexes are usually observed in SPD deformed alloys and in hundred micrometer scale [80, 119, 120]. While in this work, the swirl structure is found not only in WL10 but also in pure W, and the scale of whole vortex region is in several micrometers. Swirl structure can generate high stress field during deformation and induce variation of material deformation direction locally, as is indicated by the material flow in Fig. 4.18. In this case, dislocations with opposite signs annihilate and slip plane {110} // SPN becomes domination.

4.3 Influence of process temperature

In last section, all the materials are deformed at 400°C, while in this section the temperature range widens to 200°C ~ 700°C, in which 300/200°C refers to deforming specimen for 1 torsion revolution under 300°C and subsequently the second revolutions under 200°C. This step-deformation aims to prevent sample from low-temperature deformation induced smash. Since W_rod2 and WL10 have identical morphology and grain size, they are chosen to be compared.

Torsion torque, grain and subgrain size evolution, grain boundary misorientation angle, texture and mechanical property are examined respectively. Note that results related to process temperature of 400°C are presented in section 4.2.

4.3.1 Torsion torque

Fig. 4.28 a) and b) demonstrate torsion torque along with equivalent strain (at 3mm from torsion axis) for W and WL10 after different process temperatures. The general trend is that torsion torque is decreasing with temperature increase for both materials. As for pure W, Fig. 4.28 a) shows that the peak value of hardening drops from 223 Nm (300/200°C) to 150 Nm (700°C). However the torsion torque values maintain almost the same level in saturation region. Besides, there is no softening stage when HPT is performed at 700°C for W. Fig. 4.28 b) shows that, as for WL10, torsion torque grows continuously with decreasing process temperature and softening becomes less pronounced at 300/200°C, the torsion torque is around 250Nm after 2 torsion revolutions (strain of 68).

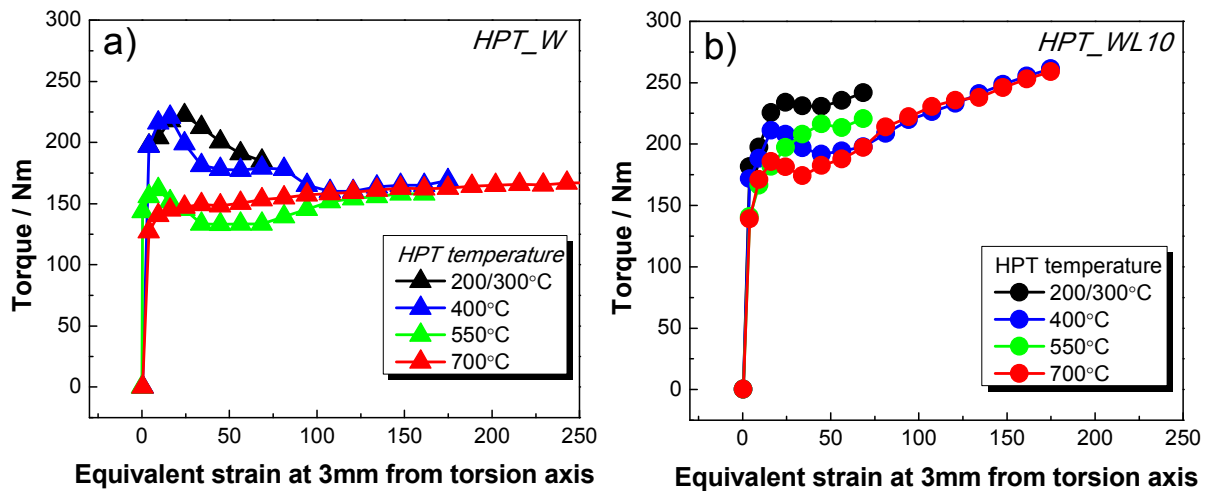


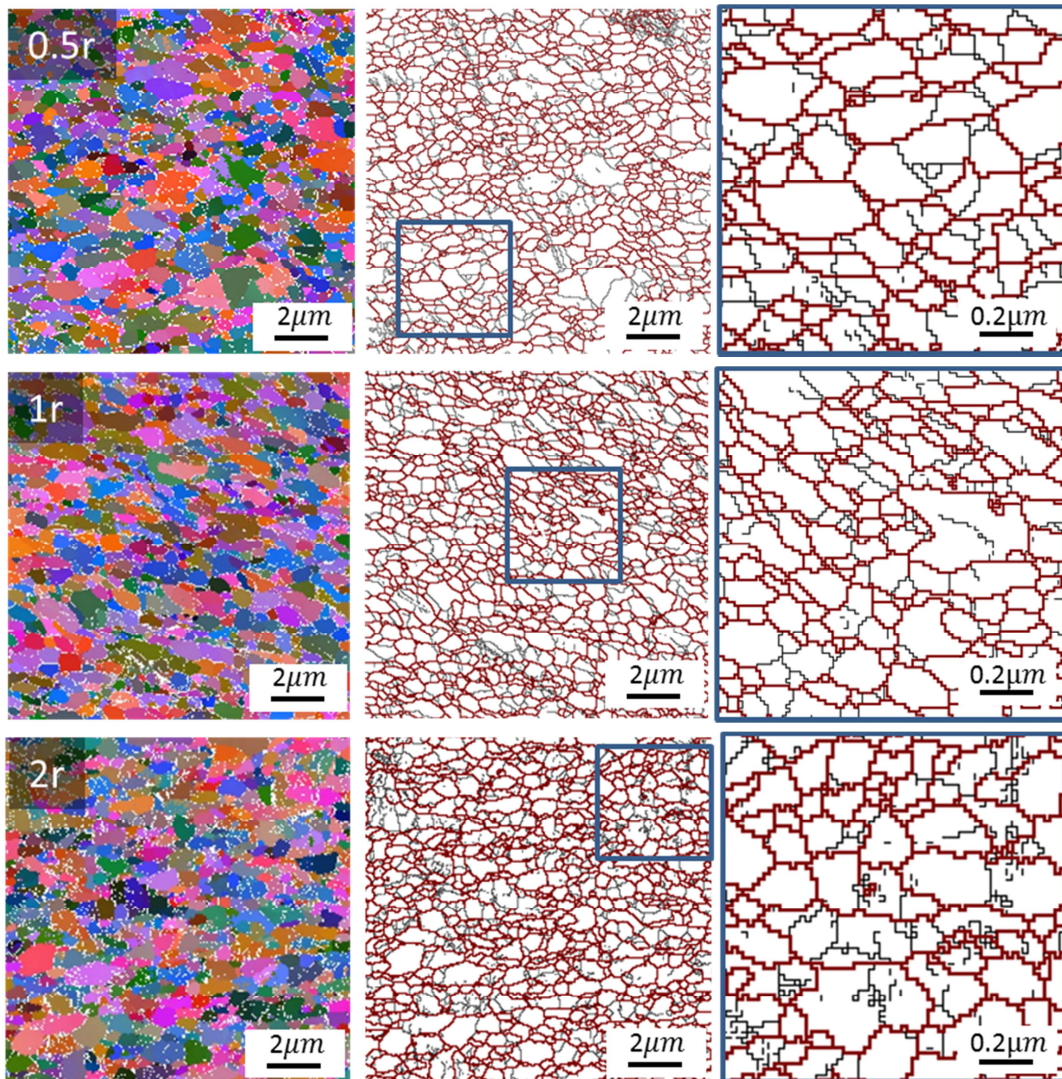
Fig. 4.28: Torsion torque changes along with equivalent strain at 3mm from torsion axis with different high-pressure torsion temperatures. a) W and b) WL10.

4.3.2 Microstructure

In this section, results related to W_rod2 and WL10 deformed by HPT are provided one after the other, and following the order of process temperatures: 700°C, 550°C and 300/200°C. The observation position is 3mm from torsion axis.

Fig. 4.29 and Fig. 4.30 provide the microstructure evolution and the corresponding grain size distribution diagrams for HPT deformed W_rod2 under 700°C. Fig. 4.31 and Fig. 4.32 exhibit

results related to deformed W_rod2 at 550°C. Fig. 4.33 and Fig. 4.34 involve with HPT deformed W_rod2 at 300/200°C. As mentioned in section 4.2.2, the grain size of W_rod2 after HPT at 400°C is reduced from 360nm (0.5 turn) to 170nm (2 turns) (s. Fig. 4.16), while when HPT takes place at 700°C (s. Fig. 4.29 and Fig. 4.30), the grain size does not change much along with equivalent strain after 0.5 torsion revolution, which is stable in between 300nm to 400nm up to 8 revolutions. Besides, elongated grain is barely observed and the grain shape stay equiaxed with sharp grain boundaries. The microstructure after HPT at 550°C is similar to that deformed at 700°C (s. Fig. 4.31 and Fig. 4.32). When HPT process temperature is down to 300/200°C, it is noticed that the grain refinement efficiency is improved by decreasing deformation temperature. As is shown in Fig. 4.34, the grain size of W_rod2 deformed at 300/200°C is refined into nearly 100nm in peak grain size along SD, and the microstructure of which shows large amount of fine grains with occasionally observed large grains (1000nm in length) (s. Fig. 4.33).



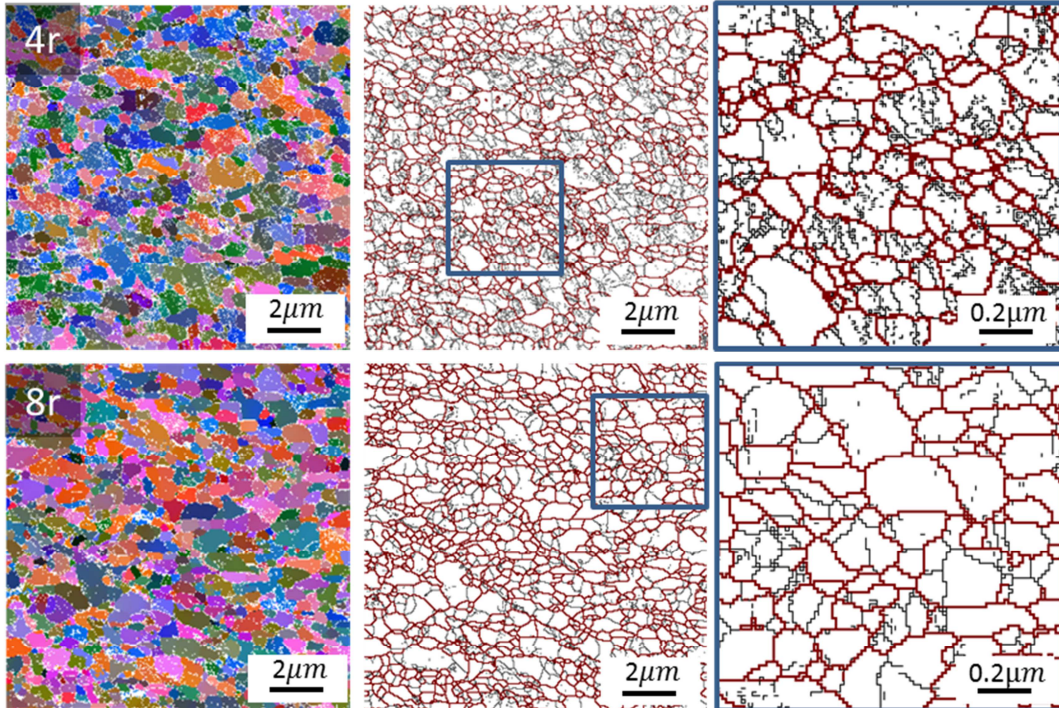
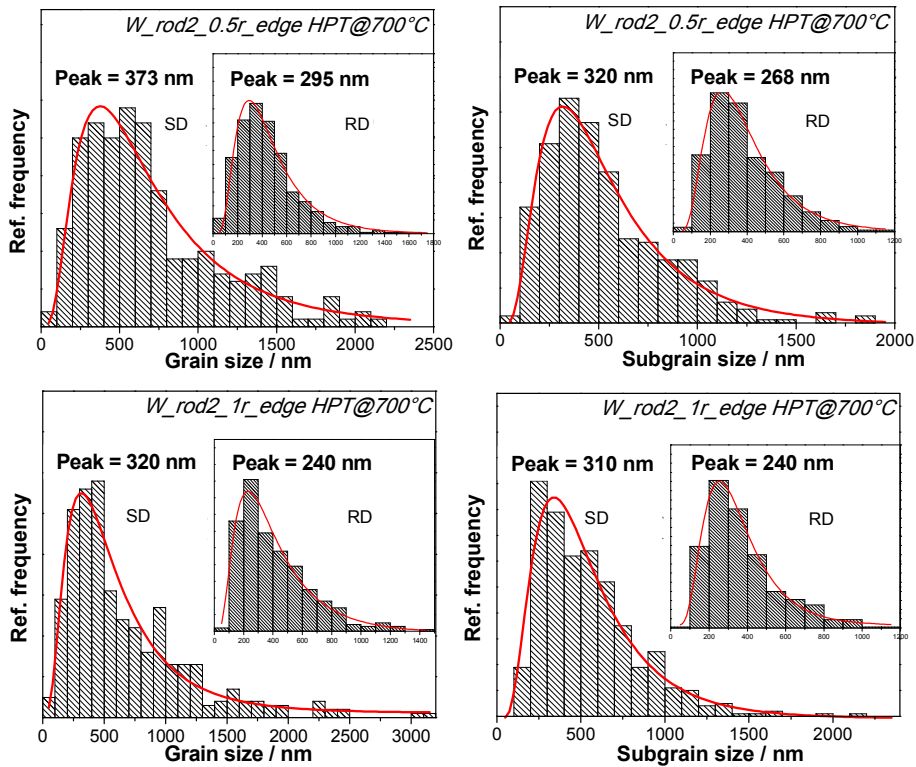


Fig. 4.29: W_rod2 deformed by high-pressure torsion at 700°C after different torsion revolutions.

Left column: Euler contrast maps; Middle column: grain boundary maps;
Right column: larger magnification of blue-frame-covered region in middle column.



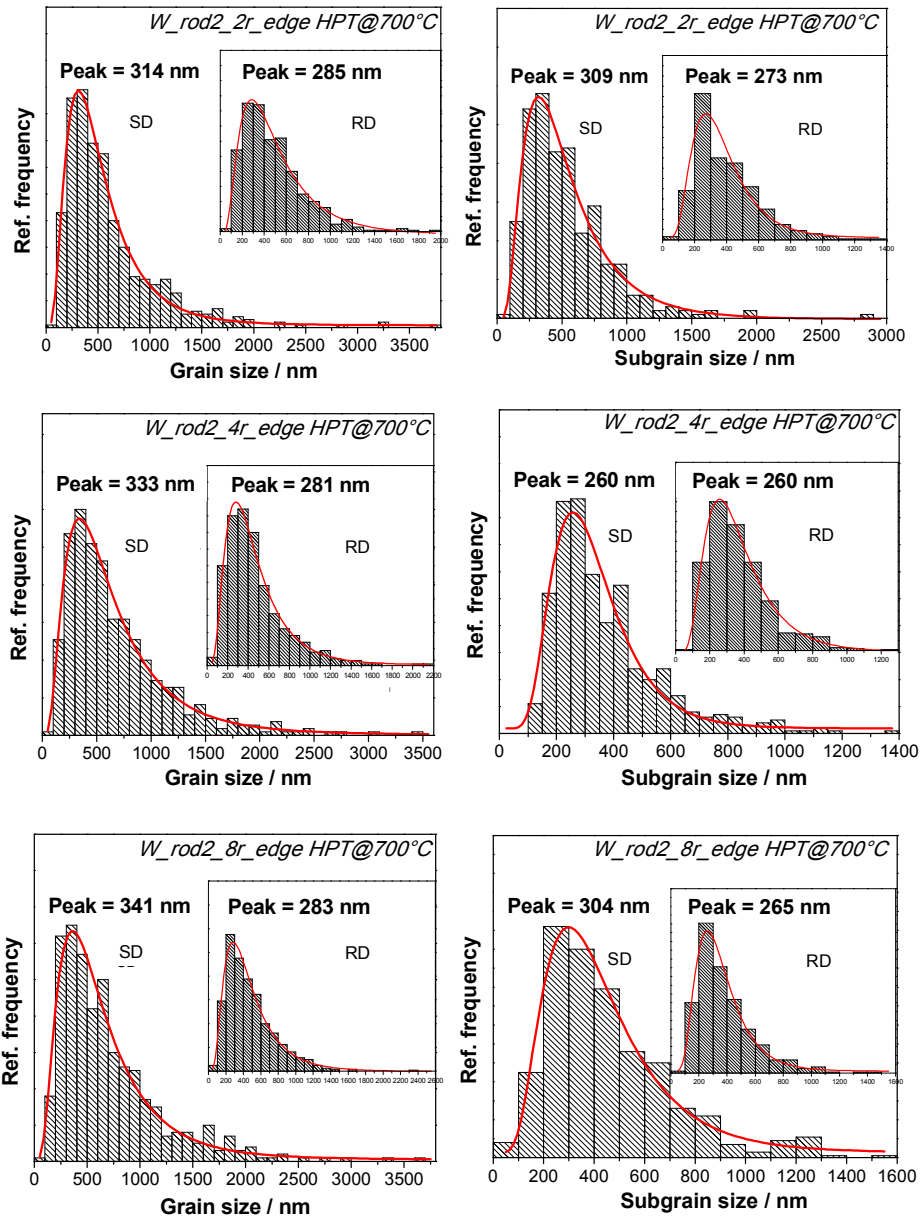


Fig. 4.30: Grain size and subgrain size distribution diagrams of W_{rod2} deformed by high-pressure torsion at 700°C after different torsion revolutions. The position is 3mm from torsion axis.

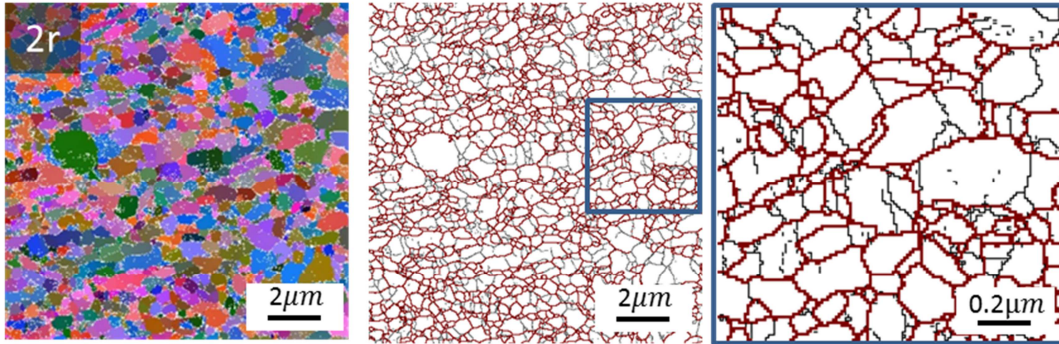


Fig. 4.31: W_rod2 deformed by high-pressure torsion at 550°C after 2 torsion revolutions.
 Left column: Euler contrast map; Middle column: grain boundary map;
 Right column: larger magnification of blue-frame-covered region in middle column.

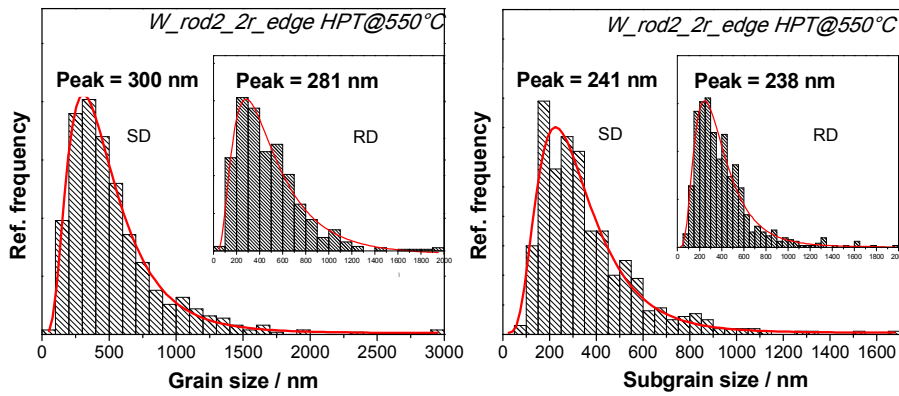


Fig. 4.32: Grain size and subgrain size distribution diagrams of
 W_rod2 deformed by high-pressure torsion at 550°C after 2 torsion revolutions.

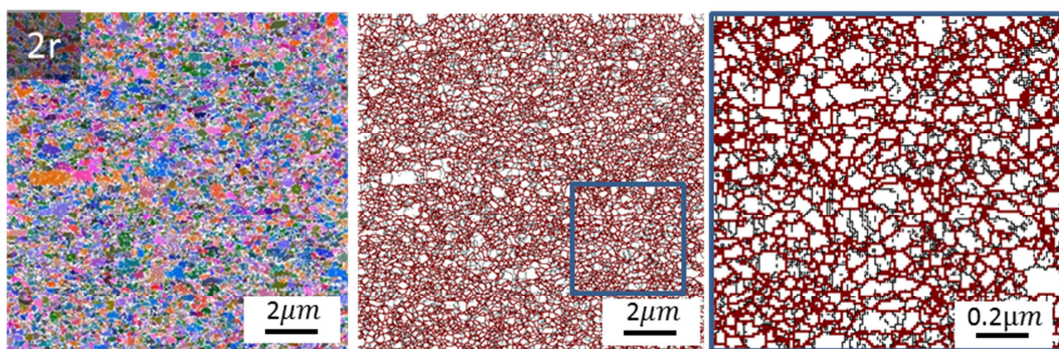


Fig. 4.33: W_rod2 deformed by high-pressure torsion
 at 300/200°C after 2 torsion revolutions.
 Left column: Euler contrast map; Middle column: grain boundary map;
 Right column: larger magnification of blue-frame-covered region in middle column.

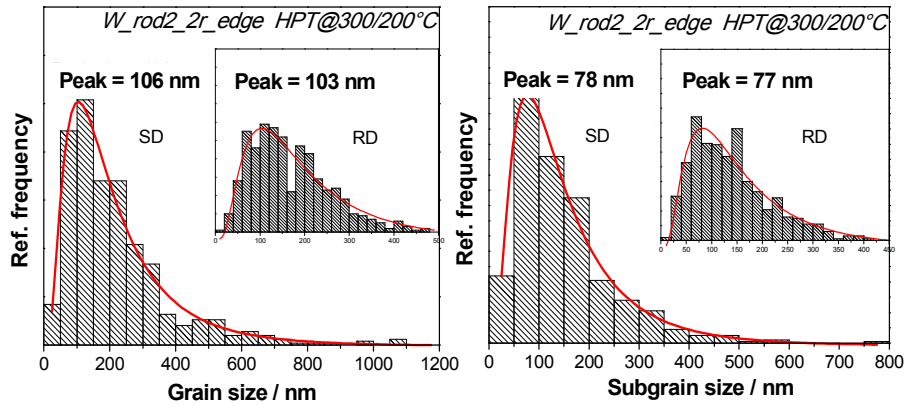
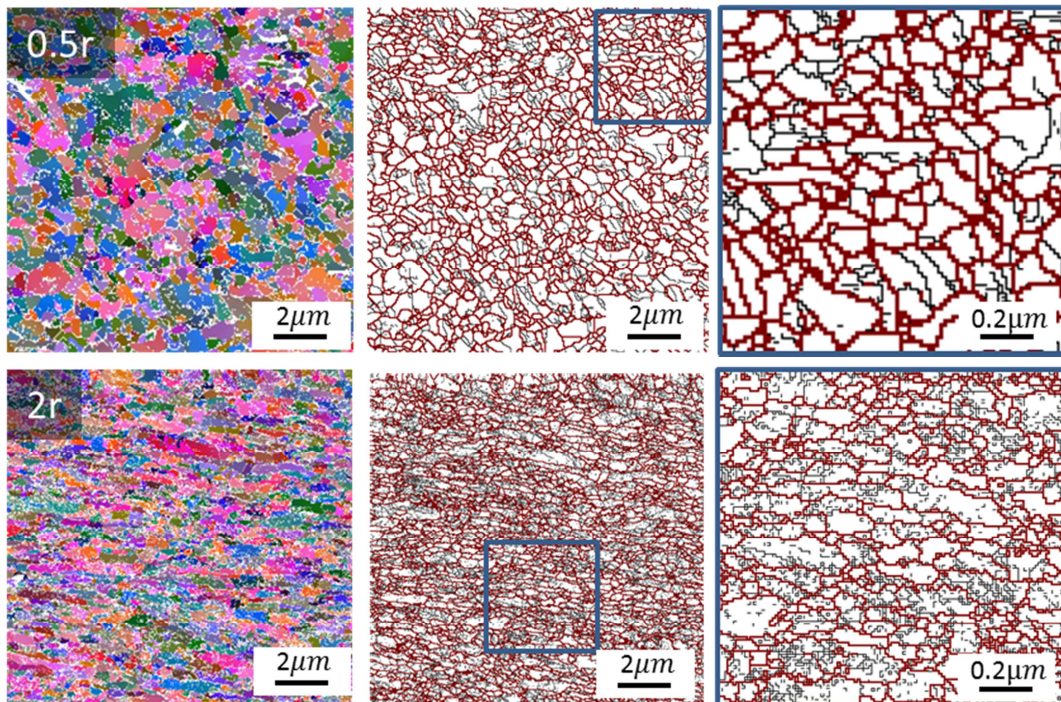


Fig. 4.34: Grain size and subgrain size distribution diagrams of W_{rod2} deformed by high-pressure torsion at 300/200°C after 2 torsion revolutions.

Fig. 4.35 and Fig. 4.36 provide the microstructure evolution and the corresponding grain size distribution diagrams for HPT deformed WL10 under 700°C. It is observed that unlike the equiaxed grain morphology obtained from pure W under the same experimental condition (s. Fig. 4.29), the deformed WL10 displays elongated grains in microstructure after 2 torsion revolutions. While after 4 torsion revolutions at 700°C, the grain boundaries become sharp, however, the microstructure is not uniform any longer and consists of both coarse and fine grains, in which coarse grains are even larger than that obtained from 2 torsion revolutions for WL10.



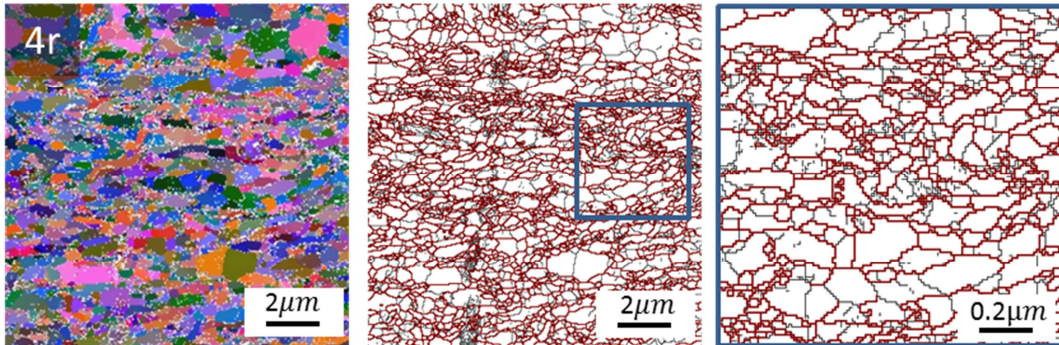
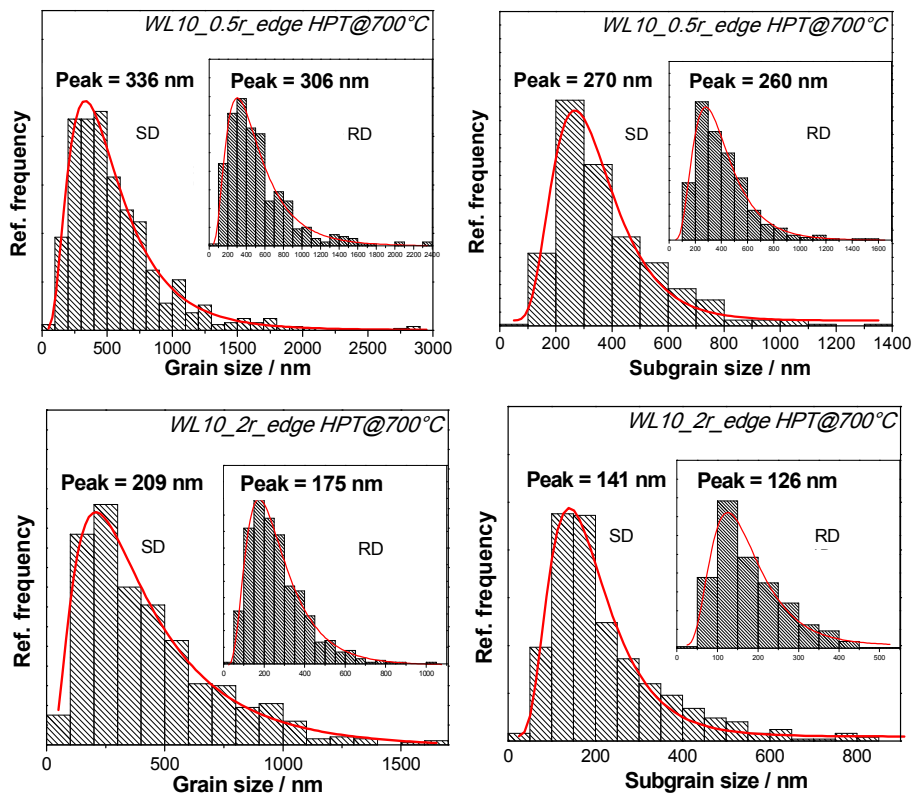


Fig. 4.35: WL10 deformed by high-pressure torsion at 700°C after different torsion revolutions.
 Left column: Euler contrast maps; Middle column: grain boundary maps;
 Right column: larger magnification of blue-frame-covered region in middle column.



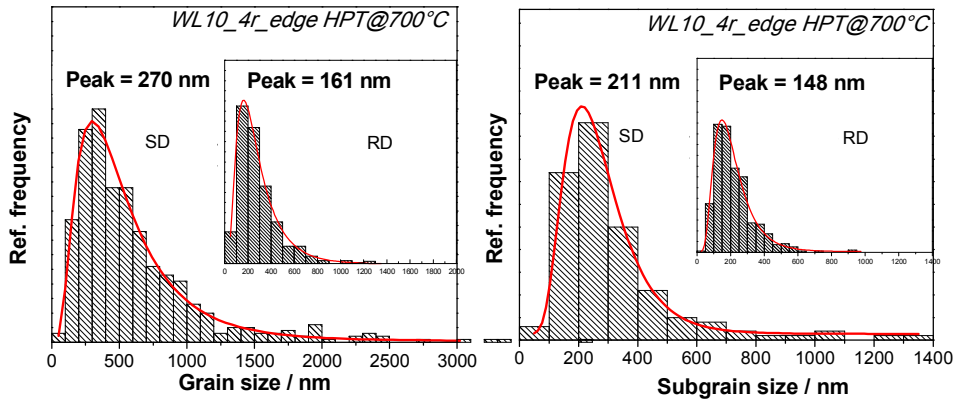


Fig. 4.36: Grain and subgrain size distribution diagrams of WL10 deformed by high-pressure torsion at 700°C after different torsion revolutions.

Fig. 4.37 and Fig. 4.38 demonstrate the microstructure and grain size distribution diagrams from HPT deformed WL10 at 550°C. It exhibits similar grain size as that deformed at 700°C. However, the microstructure morphology shows non-uniform feature with vortexes, which contains also both coarse and small grains within the material.

Fig. 4.39 and Fig. 4.40 provide the microstructure and grain size distribution diagrams involve with HPT deformed WL10 under 300/200°C. It is noticed that similar with deformed W, the lower deformation temperature leads to finer microstructure, the grain size is reduced to 80nm, and the subgrain is even of 50nm, as is displayed in Fig. 4.34. Distinct from pure W deformed under same condition, it shows a fair uniform microstructure with extreme fine grain. Even though the grain size is below 100nm, there are still subgrains within grain. No deformation bands or vortexes can be observed in this material, which may due to the extreme fine grain size.

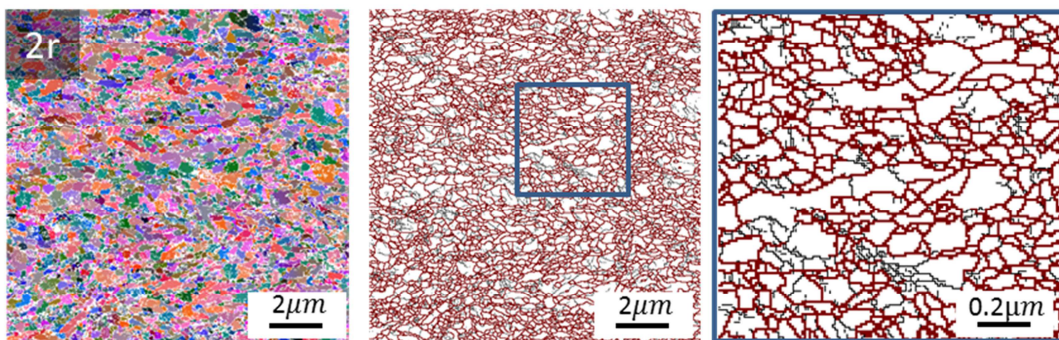


Fig. 4.37: WL10 deformed by high-pressure torsion at 550°C after 2 torsion revolutions.

Left column: Euler contrast map; Middle column: grain boundary map;
Right column: larger magnification of blue-frame-covered region in middle column.

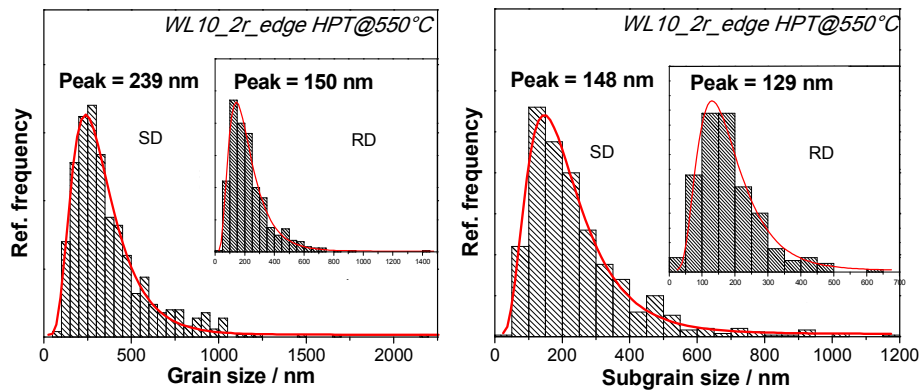


Fig. 4.38: Grain and subgrain size distribution diagrams of WL10 deformed by high-pressure torsion at 550°C after 2 torsion revolutions.

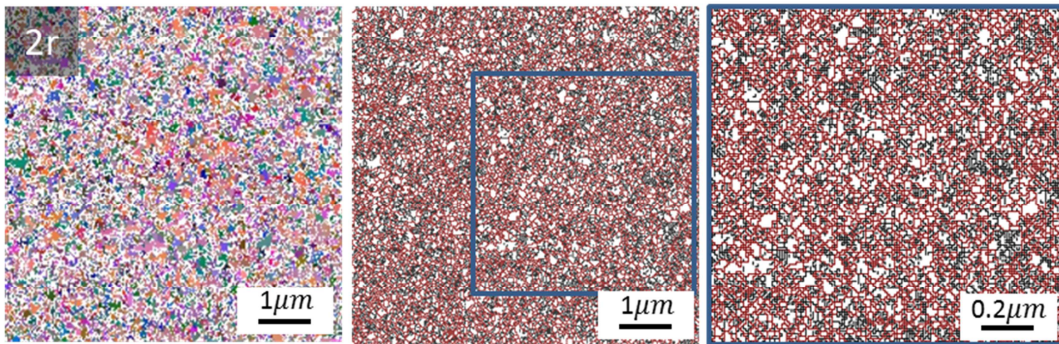


Fig. 4.39: WL10 deformed by high-pressure torsion at 300/200°C after 2 torsion revolutions.

Left column: Euler contrast map; Middle column: grain boundary map; Right column: larger magnification of blue-frame-covered region in middle column.

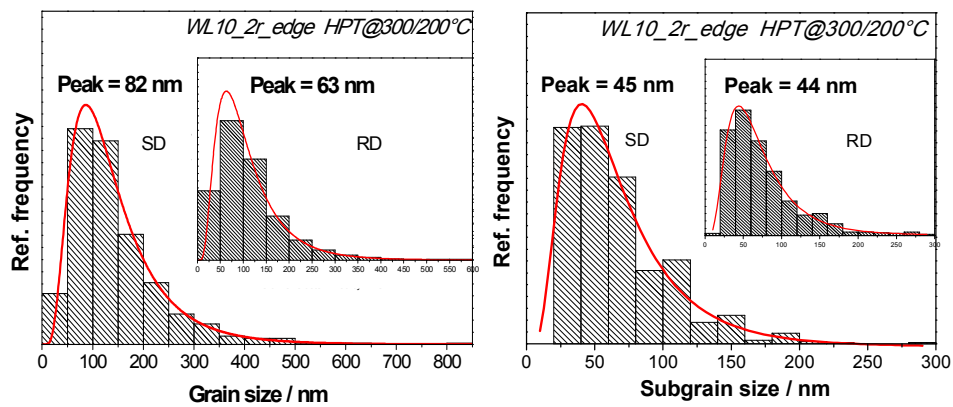


Fig. 4.40: Grain and subgrain size distribution diagrams of WL10 deformed by high-pressure torsion at 300/200°C after 2 torsion revolutions.

The equivalent grain size of HPT deformed W at different process temperatures are plotted in Fig. 4.41 a). It is seen that the grain refinement of HPT is efficient at all process temperatures investigated. The HPT deformed W_rod2 have grain size below 400nm after 0.5 torsion revolution, which is 30 times smaller than that of as-received state. The data in Fig. 4.41 b) excludes that from as-received state and exhibit the enclosed-region in Fig. 4.41 a). It is shown clearly that lower process temperature leads to finer grain size at same equivalent strain amount. The grain size change along with imposed strain is not obvious at 700°C after 0.5 torsion revolution, and the grain size obtained from 550°C is quite near to that deformed at 700°C after 2 torsion revolutions. The finest microstructure obtained for W is related to process temperature of 300/200°C with equivalent grain size of around 120nm.

The grain size of HPT deformed WL10 at different process temperatures are plotted in Fig. 4.42 a). Fig. 4.42 b) is a detail diagram showing grain size evolution after 0.5 torsion revolution. It is found out that the grain size decreases with deformation temperature increase. However the influence of deformation temperature is smaller for WL10 than W_rod2. It is observed that even at process temperature of 700°C, the grain size is still decreasing along with equivalent strain, as is shown in Fig. 4.42 b). The grain size of HPT deformed WL10 at 550°C is comparable with that deformed at 700°C. Moreover, two samples exhibit the finest microstructure in this work, which are WL10 deformed at 300/200°C after 2 torsion revolutions and WL10 deformed at 400°C after 4 torsion revolutions. The equivalent grain sizes in both specimens are below 100nm.

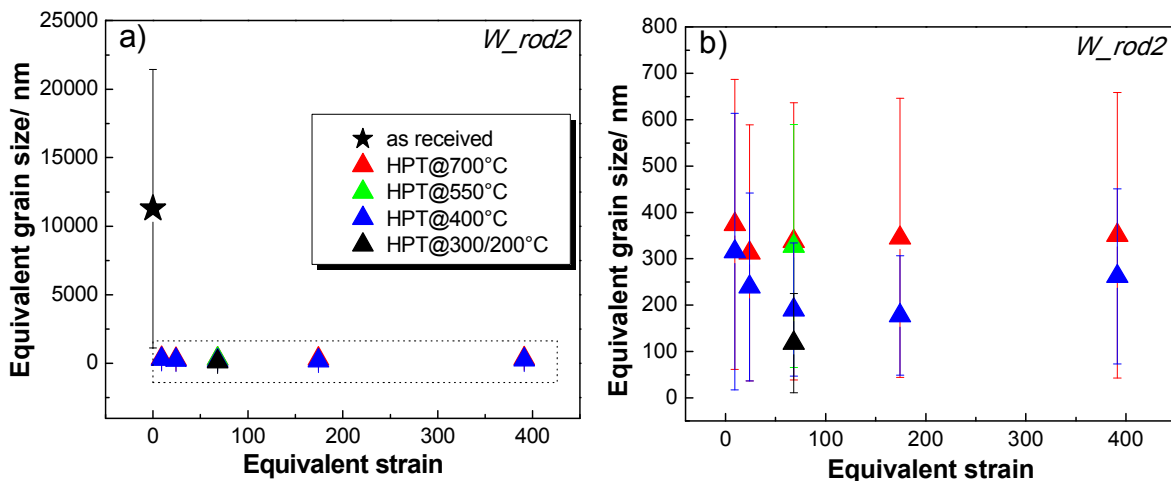


Fig. 4.41: a) Equivalent grain size along with equivalent strain for as-received and high-pressure torsion deformed W_rod2 with different process temperatures; b) Data excludes as-received state.

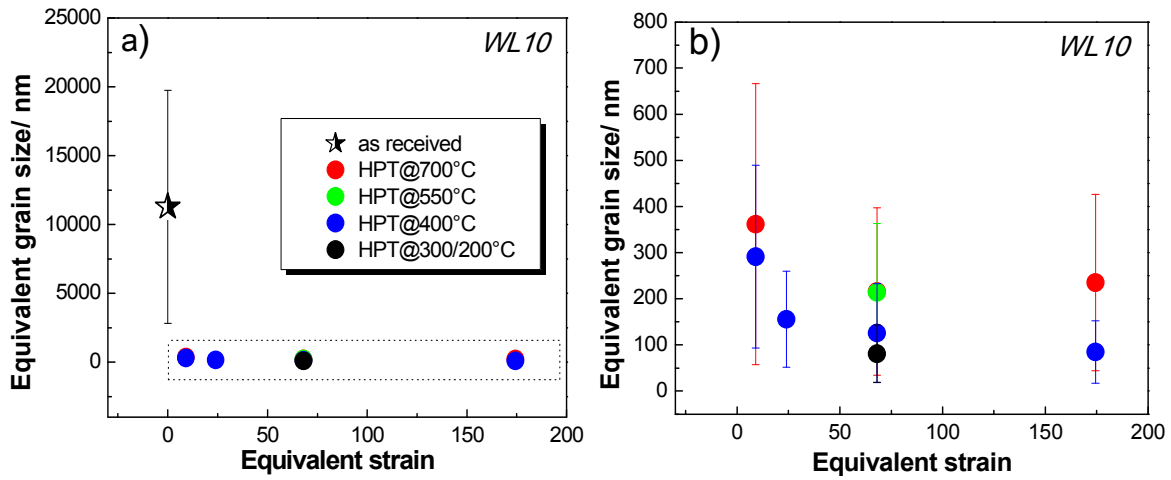


Fig. 4.42: a) Equivalent grain size along with equivalent strain for as-received and high-pressure torsion deformed WL10 with different process temperatures; b) Data excludes as-received state.

Fig. 4.43 is plotted to reveal grain size and subgrain size changes along with deformation temperatures after 2 torsion revolutions. W_rod2 and WL10 are colored in black and red respectively. A mean value of 250°C is used for step deformation of 300/200°C. It is observed from Fig. 4.43 that the grain size increases along with deformation temperatures and shows a flat stage between 550°C to 700°C for both materials. Besides, the grain size and subgrain size for deformed WL10 is smaller than deformed W for all deformation temperatures. In addition, at deformation temperature of 700°C, the subgrain size is comparable to grain size for deformed W, while in contrast to that, the ratio of subgrain size to grain size for WL10 become slight larger along with deformation temperature.

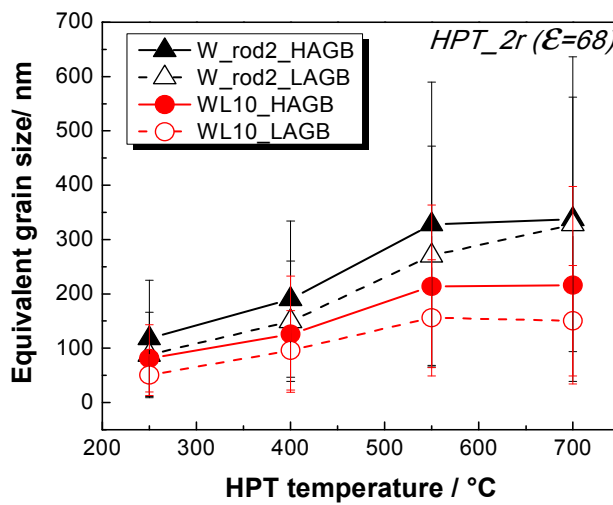


Fig. 4.43: Equivalent grain size changes with high-pressure torsion process temperature for W_rod2 and WL10 at $\epsilon=68$.

4.3.3 Grain boundary misorientation

Fig. 4.44 is plotted to display the average grain boundary misorientation angles of W and WL10 at different deformation temperatures. The same equivalent strain is subjected. It can be seen that the average grain boundary misorientation angle does not change much along with deformation temperatures for both materials. Moreover, the average grain boundary misorientation angle of deformed WL10 is in general $2^\circ \sim 3^\circ$ higher than that of deformed W for all investigated deformation temperatures, which implies the transition from LAGB to HAGB in HPT deformed WL10 seems more complete than in pure W.

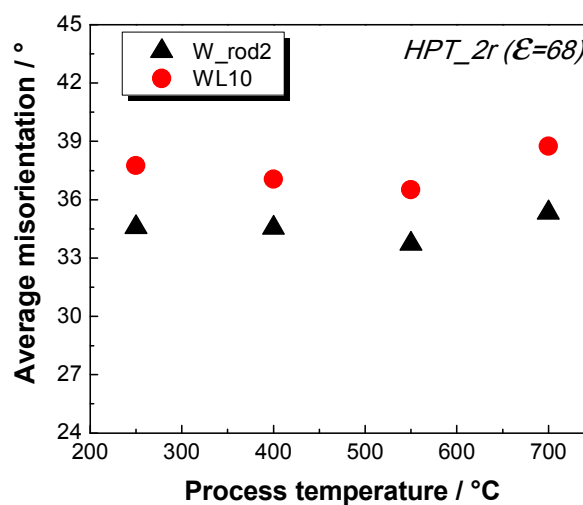


Fig. 4.44: Average grain boundary misorientation angle along with high-pressure torsion process temperatures for W_rod2 and WL10 after at $\epsilon=68$.

So as to evaluate the relationship between equivalent grain size and average grain boundary misorientation angle, Fig. 4.45 is plotted. Different process temperatures are displayed in various colors. Only pure W is chosen to display, including W_rod1, W_rod2 and W_plate.

It is observed from Fig. 4.45 that separate linear lines can be drawn corresponding to different deformation temperatures. Along each linear, the larger the misorientation angle is, the smaller the grain size is. However the average misorientation angle is no more than 36.5° . It is also noticed that original microstructure has seldom influence on relationship between misorientation angles with grain size, as is shown in green triangles in Fig. 4.45. One triangle circled by green doesn't fit the linear, which is HPT deformed W_rod2 at 400°C after 8 torsion revolutions. The grain size displayed here considers only coarse grains. Therefore it is higher than the real

condition. Besides, at a given misorientation angle, the higher the process temperature is, the larger the grain size is.

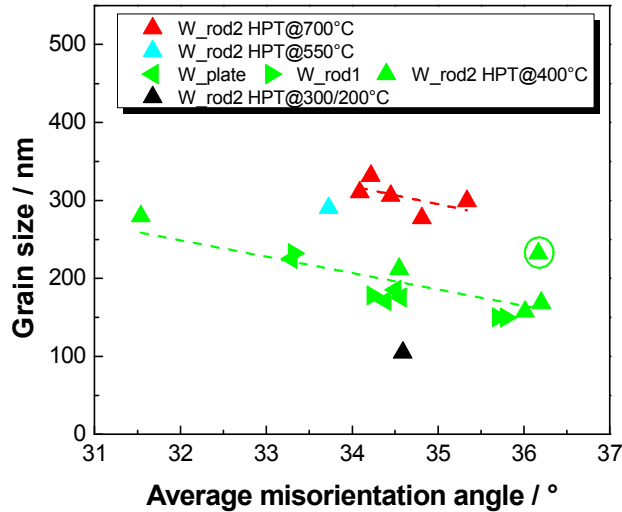


Fig. 4.45: The relationship between equivalent grain size and average misorientation angle for high-pressure torsion deformed W at different process temperatures.

4.3.4 Texture

Fig. 4.46 and Fig. 4.47 provide the pole figure evolutions for W and WL10 after process temperatures of 700°C and 300/200°C respectively. Projection crystal planes of {111}, {110} and {100} are chosen to display the PFs. SD stands for shear direction and RD refers to radial direction. Combining with the PFs from W and WL10 deformed at 400°C (s. Fig. 4.26), it is noticed that:

- i. Different materials have different textures. Specifically, HPT deformed W_rod2 possesses {111} // SD texture component as well as {110} // SPN component, as is shown in Fig. 4.46, which is consistent with HPT deformed W_rod2 at 400°C (s. Fig. 4.26). While HPT deformed WL10 exhibits a relative weak {111} // SPN component, as is shown in Fig. 4.47.
- ii. If one compares the same material under different process temperatures, it is found out that the type of texture components from both W_rod2 and WL10 do not change significantly along with deformation temperatures. As is shown in Fig. 4.46 and Fig. 4.47 separately.
- iii. The texture intensity of HPT deformed WL10 is weaker than W_rod2 for all deformation temperatures range. The former shows a diffused pattern in PF, as is seen in Fig. 4.47.

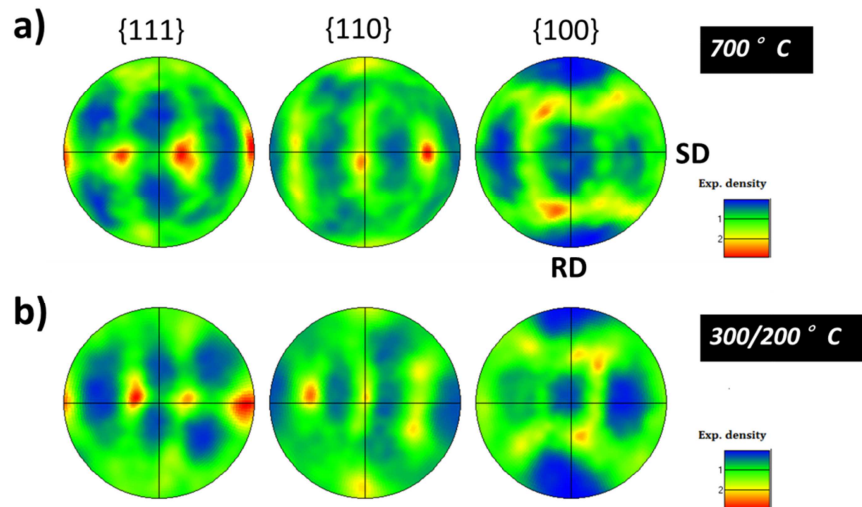


Fig. 4.46: Pole figures of high-pressure torsion deformed W_{rod2} after 2 revolutions at process temperature of a) 700°C and b) 300/200°C.

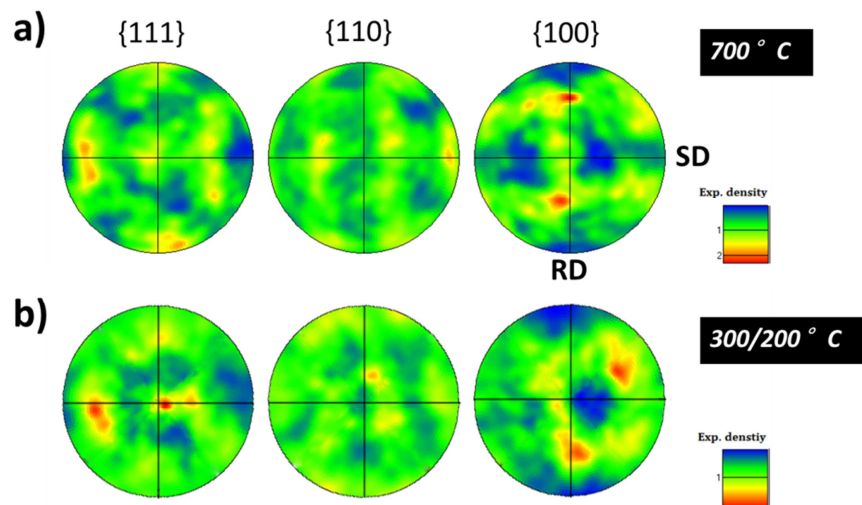


Fig. 4.47: Pole figures of high-pressure torsion deformed WL10 after 2 revolutions at process temperature of a) 700°C and b) 300/200°C.

4.3.5 Hardness

Figure 4.48 provides the relationship between hardness and process temperature for W_{rod2} and WL10 after 2 revolutions. It is observed that with decreasing deformation temperature, hardness increases for both materials. Under the low process temperature of 300/200°C, the hardness

increase for W_rod2 and WL10 are 133% and 210% from as-received state. The highest hardness value obtained in this work is related to WL10 after HPT at 300/200°C, which shows 18.6GPa at 3mm from torsion axis.

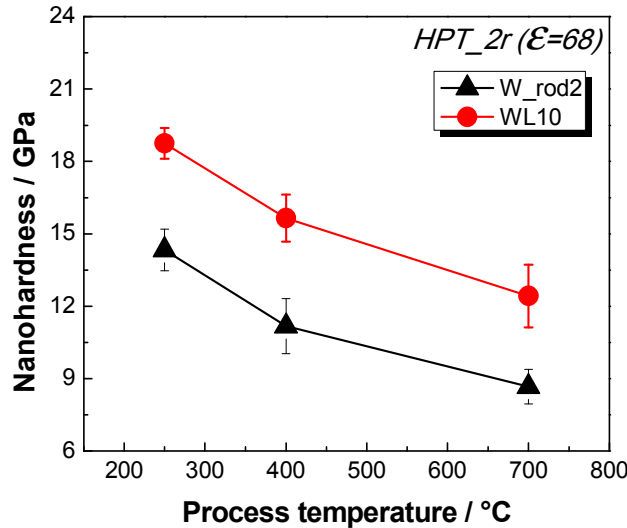


Fig. 4.48: Nanoindentation hardness changes along with high-pressure torsion process temperatures after equivalent true strain of $\epsilon=68$ for W_rod2 and WL10.

4.3.6 Discussion

In this section, the influence of process temperatures on HPT deformed W_rod2 and WL10 are discussed separately.

1) HPT deformed W

As is discussed in section 4.2, the deformation behavior of W during HPT is associated with strain hardening and dynamic recovery (DRV) / dynamic recrystallization (DRX). Strain hardening leads to grain refinement due to imposed strain, while DRV/DRX involve with dislocation annihilation and grain coarsening. The final microstructure is determined by the competition from these two mechanisms. It is known that both mechanisms are thermal activated processes and thus depend highly on process temperature. The torsion torque curves indicate that flow stress within material decreases with temperature increase at stage I and II (s. Fig. 4.28). The peak value of strain hardening is decreasing with process temperature as well. HPT deformed W shows no obvious peak at torsion torque at 700°C. Moreover, process temperature has little influence on flow stress at stage III (ie. saturation stage) for pure W, which implies the dislocation densities are identical for pure W deformed at each process temperature. However, microstructure evolution shows that the grain size in saturation state actually increases with process temperature, as is shown in Fig. 4.41 and Fig. 4.43. For example, the grain size is nearly

2 times larger when comparing W_rod2 deformed at 700°C with that deformed at 300/200°C, The hardness decreases correspondingly (s. Fig. 4.48). This phenomenon is reported for many materials [47, 55-57], and in which, DRV and DRX are main reasons for microstructure coarsening.

Evidences of DRV and DRX are found in HPT deformed W. The first one is related to the morphology of microstructure. After same amount of strain, the grain shape of HPT deformed W turns from elongated structure to equiaxed with the increase of process temperature. Moreover, the grain boundary becomes flatter when raising the process temperature, which is also a common feature for DR and GRX. However, the highest process temperature in this dissertation is 700°C, leading to $T_{\text{HPT}}/T_m=0.2$, which is much lower than that required for traditional hot working ($T/T_m=0.5$). Nevertheless DRX still occurs due to large strains imposed on materials during HPT. According to the theories about DRX [121], for materials with high SFE, under large strain amount, continuous dynamic recrystallization (cDRX) trends to occur even when the process temperature is below hot working condition. During cDRX, subgrain boundaries continuously absorb dislocations and resulting in the transition of LAGB into HAGB (s. Fig. 4.25 and Fig. 4.38). The dislocation density thereby decreases due to coarsening of subgrain, which is consistent with torsion torque curves in Fig. 4.28.

The grain size is proportional to average misorientation angle at each process temperature. Lower the process temperature cannot lead to a larger misorientation angle, which means that the transition from LAGB to HAGB has its limitation, which is around 36.5° under given experimental condition.

2) HPT deformed WL10

HPT deformed WL10 shows increase in grain size with increase in process temperature as well, as shown in Fig. 4.42 and Fig. 4.43. The nanohardness is consequently reduced (s. Fig. 4.48). However in contrast to pure W, the increment of grain size with process temperature is less significant. The elongated microstructure can still be observed after 2 revolutions at 700°C, while the grain shape is equiaxed for pure W at the same condition. It is therefore assumed that the thermal activated dislocation cross-slip and climb are retarded by oxide particles [55], and DRX process is obstructed by the oxide addition in WL10, resulting in slower grain size growth along with increase in process temperature. However, process temperature has seldom influence on grain boundary misorientation angle and texture for HPT deformed WL10, as is displayed in Fig. 4.44 to Fig. 4.47. This implies that the LAGB-HAGB transition is more related to imposed strain rather than process temperature. Besides, the slip system stays the same for deformed WL10 despite the process temperature differences.

4.4 Influence of strain path

In this section, two different strain paths are investigated, including monotonic HPT and high pressure cyclic torsion (HPCT). W_rod2 and WL10 are employed. The process temperatures are 400°C and 300/200°C. Strain rate is 5rpm. The observing position of microstructure is 3mm from torsion axis.

4.4.1 Torsion torque

The typical torsion torque curve during HPCT is given in Fig. 4.49. It is observed that the torsion torque changes its direction in every 90°. The simplified torque curves are obtained by picking peak values and taking the absolute, as is shown in solid and hollow triangles in Fig. 4.49. The torque curves displayed thereafter are all simplified in this way.

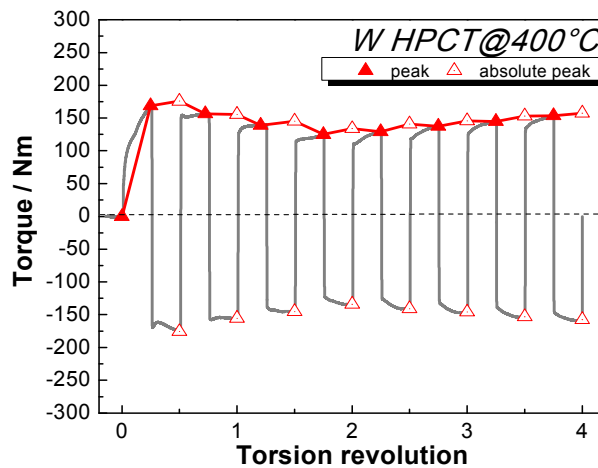


Fig. 4.49: Typical torsion torque from pure W during high-pressure cyclic torsion at 400°C.

Fig. 4.50 displays the torsion torque along with equivalent strain at 3mm from torsion axis by HPT and HPCT respectively. Fig. 4.50 a) and b) are related to W_rod2 and WL10.

It is observed from Fig. 4.50 that the strain path has more significant influence on WL10 than on pure W. As for WL10, the torsion torque value during HPCT is 100 Nm lower than that deformed by HPT, as is shown in Fig. 4.50 b). While the decrease in torsion torque is quite small from HPT to HPCT procedure for pure W, which is around 50Nm at the beginning and the difference becomes too small to be noticed in saturation region. Therefore, the following investigations are concentrated on WL10 and referring to microstructure evolution, grain boundary misorientation and texture changes.

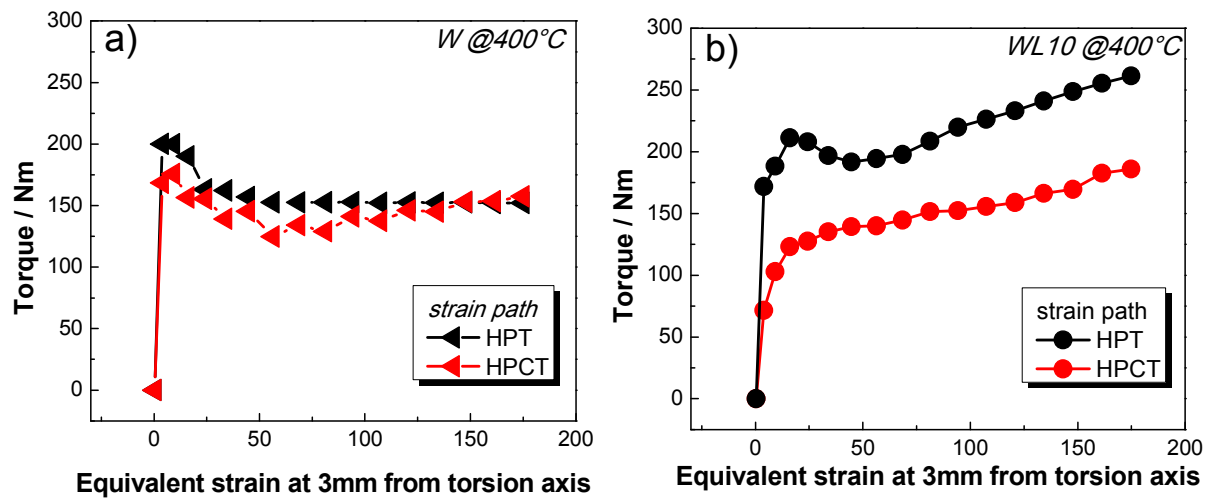


Fig. 4.50: Torsion torque during high-pressure torsion (HPT) and high-pressure cyclic torsion (HPCT) at process temperature of 400°C for a) W_rod2 and b) WL10.

4.4.2 Microstructure

The microstructure images of WL10 deformed by HPT and HPCT after 0.5 revolution are shown in Fig. 4.51. The oxide traces can be seen clearly on both images as dark contrast regions. They are elongated aligning shear direction (SD) for both HPT and HPCT deformed WL10. Compared with monotonic HPT, WL10 deformed by HPCT exhibits more heterogeneous microstructure. For example, oxide traces with relative large scale can be observed on the right image of Fig. 4.51. Besides, shear bands are formed on the HPCT deformed WL10 and perpendicular to the shear direction, as marked in red windows on the right image of Fig. 4.51.

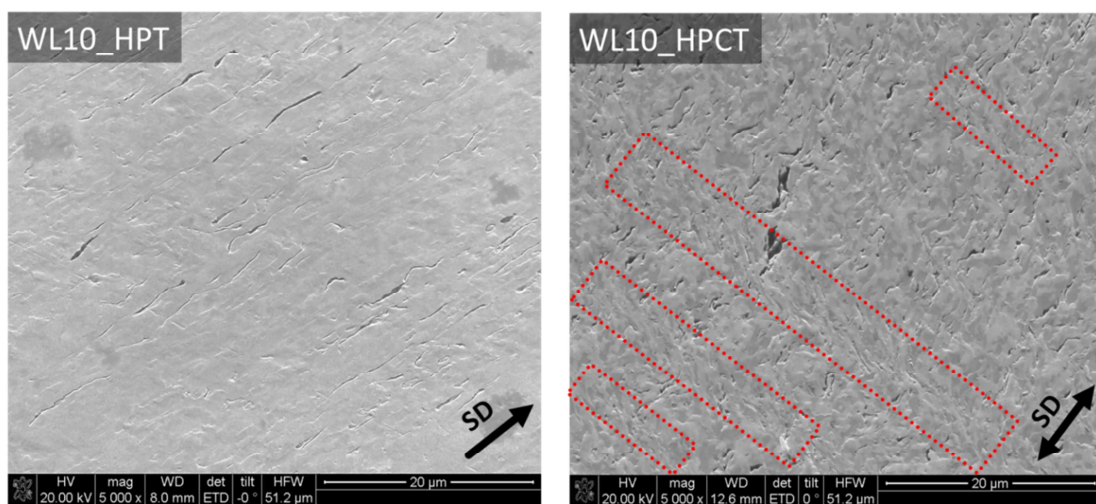
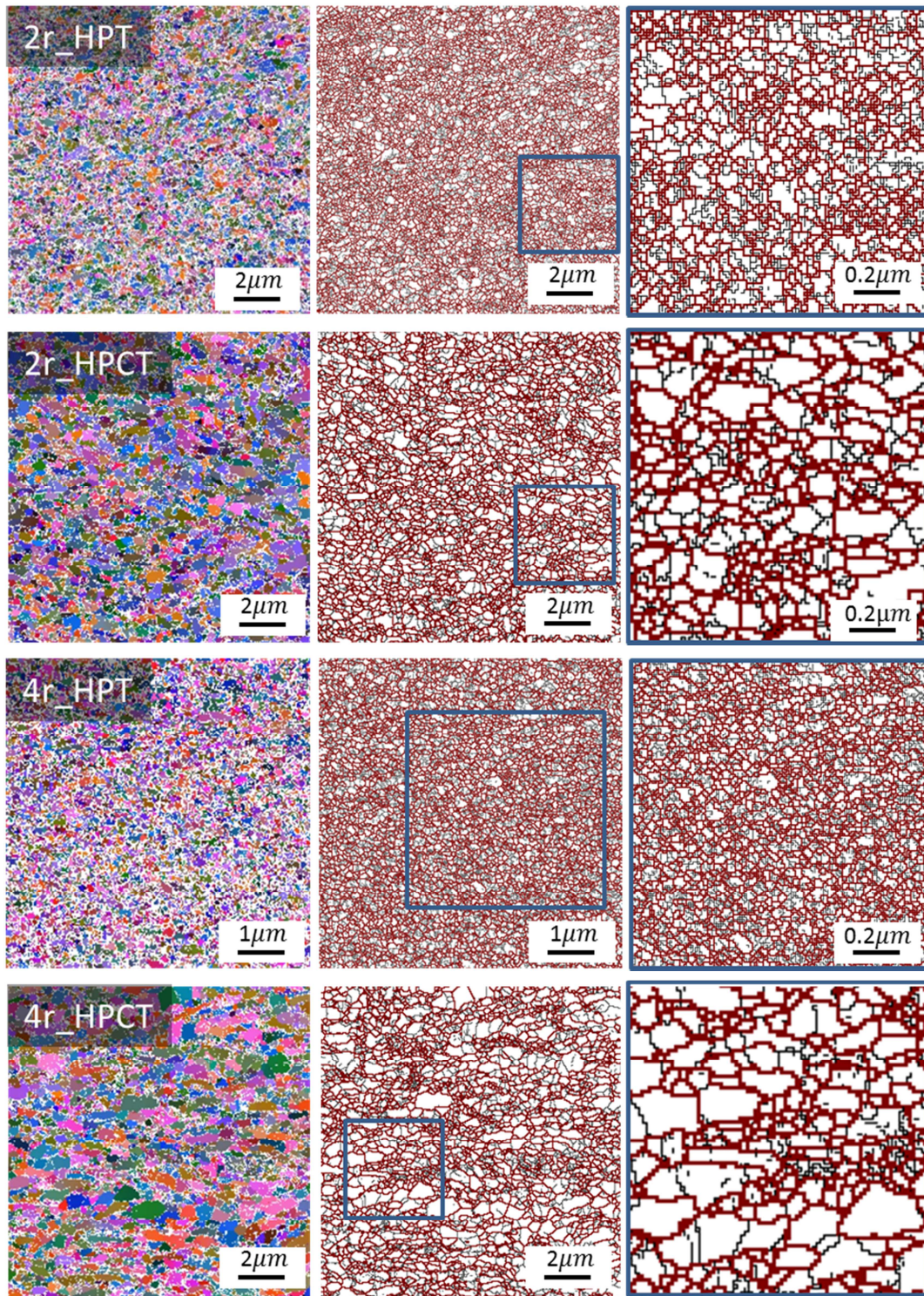


Fig. 4.51: SEM (second electron) images of WL10 after high-pressure torsion (HPT) and high-pressure cyclic torsion (HPCT) at process temperature of 400°C.

Fig. 4.52 demonstrates the Euler contrast maps and grain boundary maps of HPCT deformed WL10, the corresponding grain and subgrain sizes distribution diagrams are exhibited at the end. For better comparison, Euler contrast maps and grain boundary maps from HPT processes are provided aside with their counterparts. The process temperature is 400°C. Torsion revolutions of 2 and 4 are subjected on samples. The equivalent grain sizes are plotted in Fig. 4.53.



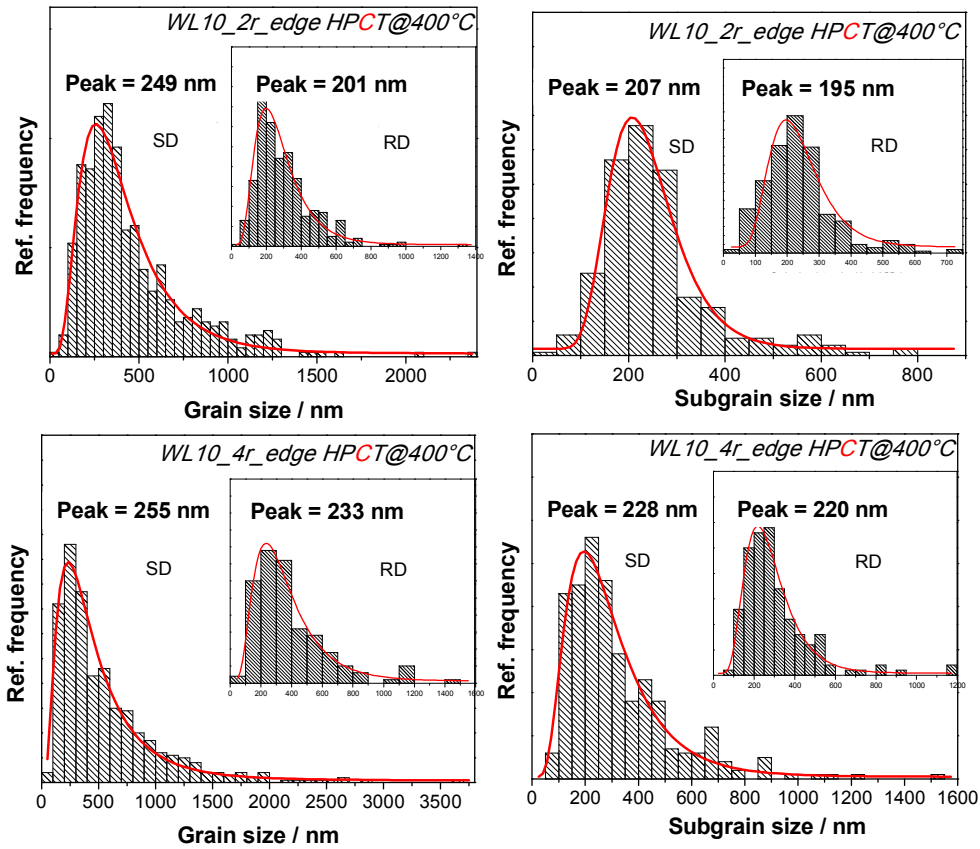


Fig. 4.52: WL10 deformed by high-pressure torsion (HPT) and high-pressure cyclic torsion (HPCT) at 400°C after different torsion revolutions

Left column: Euler contrast maps; Middle column: grain boundary maps;
 Right column: larger magnification of blue-frame-covered region in middle column.
 Grain size distribution diagrams are corresponding to HPCT.

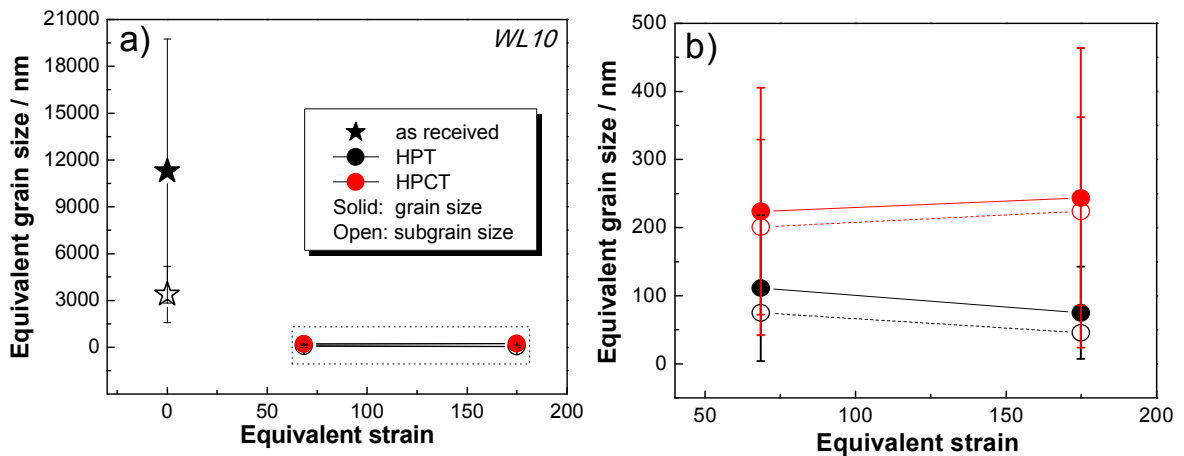
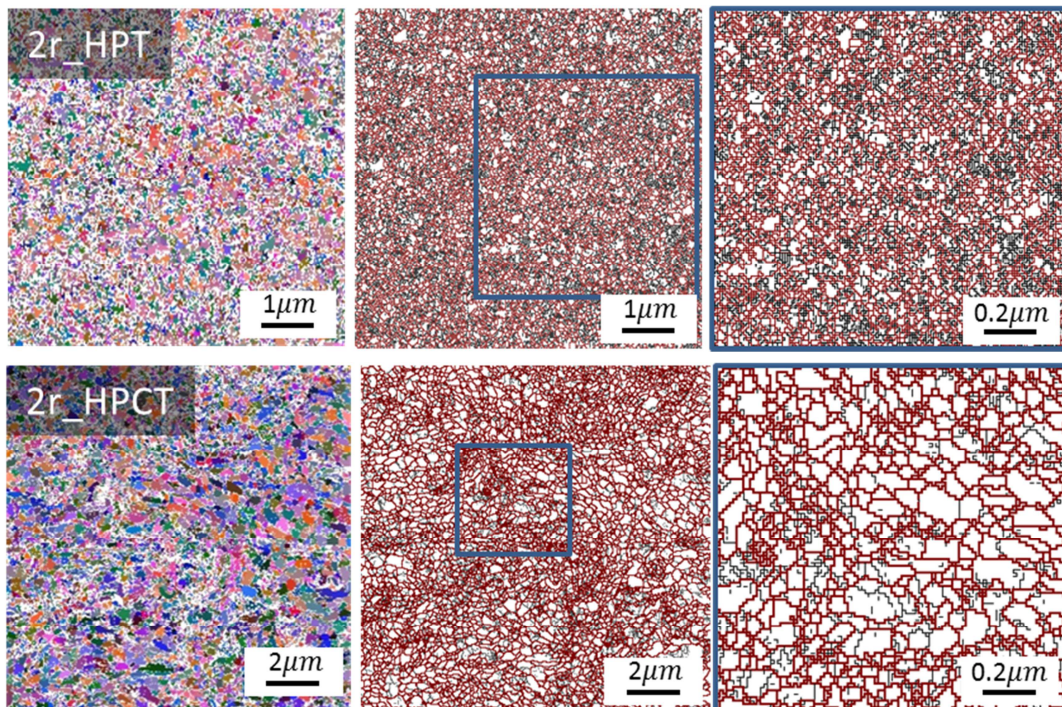


Fig. 4.53: Equivalent grain size along with equivalent strain for high-pressure torsion (HPT) and high-pressure cyclic torsion (HPCT) deformed WL10 at process temperature of 400°C.

It is observed from Fig. 4.52 and Fig. 4.53 that, after 2 torsion revolutions, the grain size of HPCT deformed WL10 is almost doubled that of monotonic HPT deformed WL10. Moreover, as discussed in section 4.2, the grain refinement continues with imposed strain for monotonic HPT. The grain size is reduced from 116nm (2 torsion revolutions) to 76nm (4 torsion revolutions), as is shown in Fig. 4.23. In contrary, as for HPCT process, the grain size increases with imposed strain, which is about twice large over its HPT counterpart after 4 revolutions, as is shown in Fig. 4.53 b). Furthermore, the microstructure from HPT deformed WL10 is relatively homogeneous, while it is noticed that the microstructure obtained from HPCT contains both coarse grains and small grains. The small grains intersperse among large grains like necklace, this distribution may be associated with the shear bands formed in Fig. 4.51.

As is discussed in section 4.3, WL10 deformed by monotonic HPT at 300/200°C after 2 torsion revolutions exhibits the smallest grain size in this work. In this section, HPCT is also conducted at the same condition except strain path. The Euler contrast maps and grain boundary maps are illustrated in Fig. 4.54. Grain/subgrain size distribution diagrams of HPCT deformed WL10 are provided at the end of Fig. 4.54. It is also observed that vortexes are distributed on the microstructure of HPCT deformed WL10, while HPT deformed WL10 exhibits more homogeneous morphology. In addition, the equivalent grain size of HPCT deformed WL10 is 132nm, which is 160% of that from monotonic HPT, as is shown in grain size distribution diagrams in Fig. 4.54.



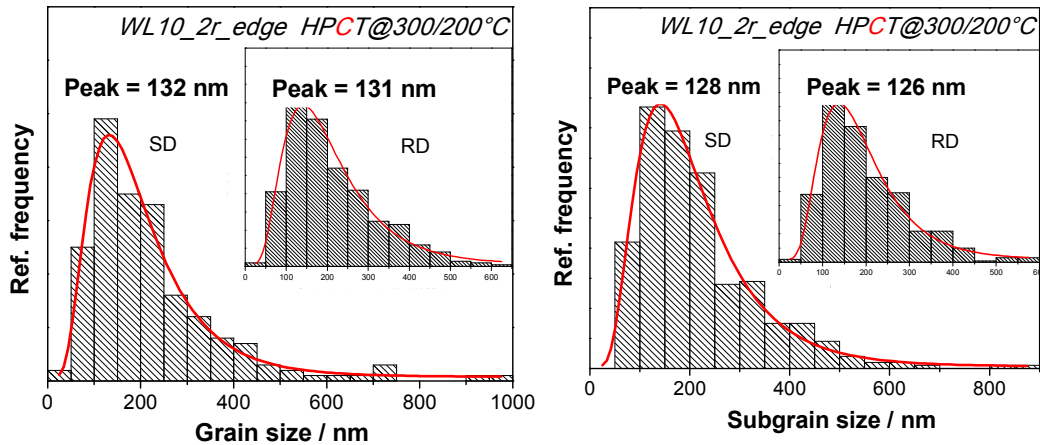


Fig. 4.54: WL10 deformed by high-pressure torsion (HPT) and high-pressure cyclic torsion (HPCT) at 300/200°C after 2 torsion revolutions

Left column: Euler contrast maps; Middle column: grain boundary maps;
 Right column: larger magnification of blue-frame-covered region in middle column.
 Grain size distribution diagrams are corresponding to HPCT.

4.4.3 Grain boundary misorientation

The grain boundary misorientation angles from HPT and HPCT are shown in Fig. 4.55. WL10 samples are deformed at 400°C after 2 torsion revolutions. Both distributions exhibit two peaks, one is at around 7.5° and the other appears at about 47.5°. The LAGB fraction in WL10 after HPCT is slightly higher than that after HPT, such as the misorientation angle of 7.5° occupies 11.8% for HPCT deformed WL10 while the percentage is 7.7% for HPT deformed WL10. This indicates that the transition of LAGB to HAGB during HPCT is not as complete as HPT process for WL10 under experimental condition.

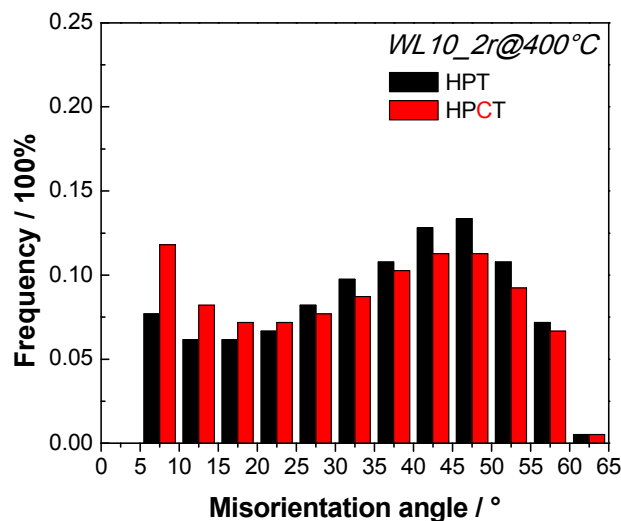


Fig. 4.55: Misorientation angle distributions from high-pressure torsion (HPT) and high-pressure cyclic torsion (HPCT) deformed WL10 at 400°C after 2 torsion revolutions.

4.4.4 Texture

The PFs of HPCT deformed WL10 are provided in Fig. 4.56. Four torsion revolutions are subjected at 400°C. Projection planes $\{111\}$, $\{110\}$ and $\{100\}$ are chosen to display PFs. It is observed that the deformed WL10 consists of strong $[111] // \text{SD}$ texture component and $\{110\} // \text{SPN}$ component. The texture type is nothing like WL10 after monotonic HPT deformation, but is exactly the same as pure W after monotonic HPT, as is shown in Fig. 4.26. Furthermore, the texture intensity in PF in Fig. 4.56 is higher than that from monotonic HPT.

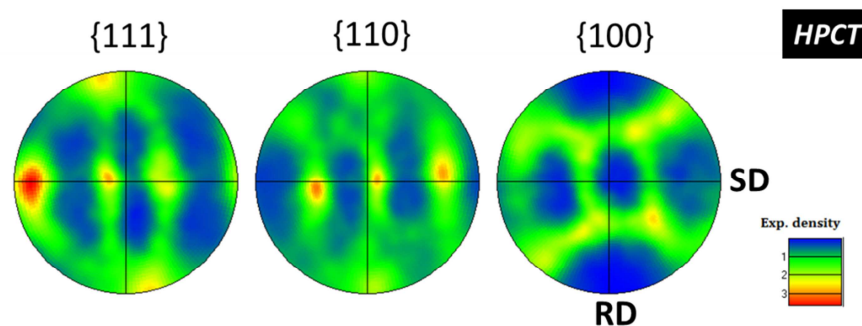


Fig. 4.56: Pole figures from high-pressure cyclic torsion (HPCT) deformed WL10 after 4 torsion revolutions at process temperature of 400°C.

4.4.5 Discussion

The grain refinement efficiency for WL10 is reduced by reversed strain path (HPCT) compared with monotonic one (HPT). This is consistent with the observation stated in section 2.1, in which an efficiency factor η is introduced in equation 2.5. If we assume that the grain refinement efficiency is equal to 1 for monotonic HPT. By comparing the equivalent grain sizes from HPCT and HPT processes, as displayed in Fig. 4.53, it is found out that the efficiency factor η is reduced from 0.5 to 0.3 with increasing strain from 68 to 174 during HPCT at 400°C, corresponding to 2 and 4 revolutions respectively. The coarsening in grain size along with imposed strain during HPCT is probably owing to DRX, which relates to dislocation annihilation closely. Moreover η is equal to 0.55 when WL10 is performed by HPCT at 300/200°C after 2 torsion revolutions, which is higher than 0.5, regarding to 400°C as deformation temperature for WL10 after HPCT. This suggests that the process temperature effect on grain refinement is still not ignorable when subjecting different strain paths. At lower process temperature, the dislocation movement is more restricted during deformation, the dislocation annihilation due to reversed strain path is less active, and therefore grain refinement efficiency factor is increased compared to higher process temperature.

The direct reason for lower grain refinement efficiency through HPCT is incomplete transition from LAGB to HAGB, as is shown in Fig. 4.55. By cyclic torsion, as mentioned in section 2, the geometrically required volume change is limited, thus the dislocation generated through HPCT is not as sufficient as HPT. Furthermore, the newly generated dislocations are more likely to contain similar amount of dislocations with different signs via HPCT. Therefore dislocation annihilation is easier and leading to a lower dislocation density within material, which is confirmed by the lower torsion torque in Fig. 4.50. For the same reason, misorientation gradient is harder to be accumulated within a grain by HPCT than monotonic HPT, and thus the microstructure has smaller fraction of HAGB and larger grain size after HPCT. Besides, the difference between W and WL10 in torsion torque curves in Fig. 4.50 suggests that oxide particles amplify the influence of strain path on grain refinement. This is because that during reversal strain path, the oxide particles cannot be fragmented uniformly, as is indicated in Fig. 4.51 b), the region with finer oxide particles results in smaller grain size, and heterogeneity in HPCT deformed microstructure therefore exists.

As we discussed in section 4.2, during monotonic HPT, oxide particles in WL10 act as obstacles to dislocation movements, and dislocations cannot choose $\{110\}$ $[111]$ to slip freely. However the texture obtained from HPCT deformed WL10 (s. Fig. 4.56) consists of $[111] // SD$ and $\{110\} // SPN$ components, which means that $\{110\}$ $[111]$ slip system is activated during HPCT process even for WL10. It seems that the oxide particles are more or less invalid for prevent dislocations from slipping on the $\{110\}$ $[111]$ system during reversal strain path. Therefore this texture component appears on WL10 and is exactly the same as pure W after HPT.

As can be seen in Fig. 4.52 and Fig. 4.53, the microstructures after HPCT contain both coarse and fine grains. Similar microstructure can be found for low carbon steel by cold rolling [122], and this inhomogeneous distribution of grain sizes are of interest for optimizing strength and ductility.

4.5 Thermal stability

In this section, results from heat treatments performed on HPT deformed W_rod2 and WL10 are presented. The heat treatment temperature is up to 1000°C, with duration is 1 hour, 3 hours, 6 hours and 9 hours respectively. Inverse pole figures (IPF) obtained from shear plane are provided. The observation position is 3mm from torsion axis. Grain boundary misorientation angle changes and texture evolutions are shown as well.

4.5.1 Microstructure

Orientation image maps (OIM) of HPT deformed W_rod2 after heat treatment are displayed first, following with the order of different deformation temperatures, from 700°C to 300/200°C,

referring to Fig. 4.57 to Fig. 4.59 respectively. The color code of all OIMs in this section is exhibited in Fig. 4.57 e). The corresponding grain size distributions of deformed-annealed W_rod2 are provided in Fig. 4.60 to Fig. 4.62.

W_rod2_2r_edge HPT@700°C stands for W_rod2 deformed by HPT at 700°C after 2 revolutions, and edge means 3mm from torsion axis is chosen. Fig. 4.57 exhibits inverse pole figures (IPF) of W_rod2_2r_edge HPT@700°C after heat treatment up to 6 hours. It is observed from Fig. 4.57 that the grain size does not grow much even after 6 hours heat treatment except several slight changes on crystallography aspect. For example, after 1 hour of heat treatment, comparing Fig. 4.57 b) with Fig. 4.57 a), there are more crystals with $\{110\}$ // SPN texture component appears which is colored in green. Please note that images from Fig. 4.56 b) to Fig. 4.57 d) are taken from the same position and position 1 to position 3 is marked to be traced along with duration. The changes observed from position 1, 2 and 3 demonstrate new grains formation, from which it is noticed that if the surrounding areas have the similar crystal orientation, they may expand their territory through heat treatment, a larger grain is thus formed, as shown for position 1, 2 and position 3. The quantitative grain size distribution diagrams are given in Fig. 4.60.

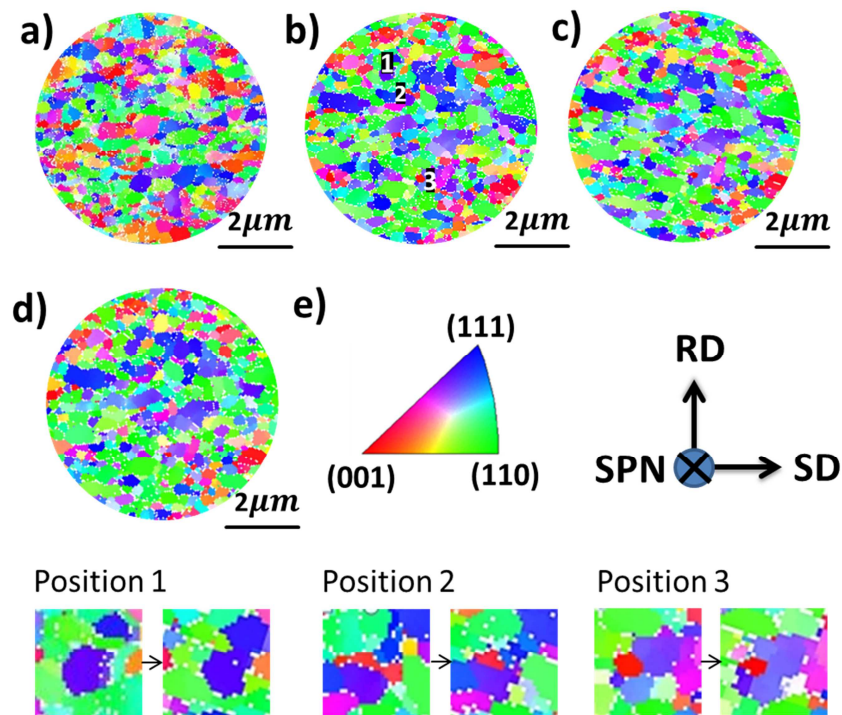


Fig. 4.57: Inverse pole figures of W_rod2 deformed by high-pressure torsion at 700°C after 2 torsion revolutions. a) As-deformed state and after heat treatment at 1000°C with duration of b) 1h, c) 3h and d) 6h. e) Color code map.

Position 1, 2 and 3 exhibit specific orientation changes from b) to c).

Figure 4.58 exhibits inverse pole figures (IPF) of W_rod2_2r_edge HPT@400°C after heat treatment up to 6 hours. Elongated grain microstructure is observed in as-deformed state, while after heat treatment for 1 hour, grain size increases obviously with a faster growth along RD than along SD, which means the aspect ratio of grain is smaller compared to as-received state. However, even so the elongated grain morphology still maintains, as is shown in Fig. 4.58 b). With longer duration, the grain shape turns to almost equiaxed shape after 3 hours and the aspect ratio is near to 1 after 6 hours heat treatment. Larger magnification images from position 1 and 2 are shown at the bottom of Fig. 4.58. It is found out that small crystals rotate their orientations so as to align grains located nearby, indicated by the changes occur at position 1 in Fig. 4.58. Color changes can also be found in position 2 which implies crystal orientation variation during heat treatment. The quantitative grain size distribution diagrams are given in Fig. 4.61.

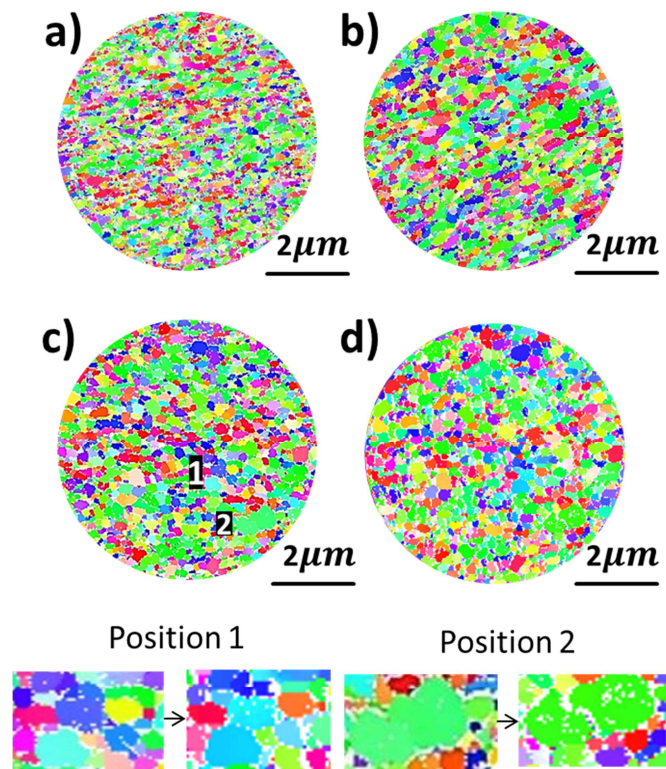


Fig. 4.58: Inverse pole figures of W_rod2 deformed by high-pressure torsion at 400°C after 4 torsion revolutions.

a) As-deformed state and after heat treatment at 1000°C with duration of b) 1h, c) 3h and d) 6h.

Position 1 and 2 exhibit specific orientation changes from c) to d).

Color coding by Fig. 4.57 e).

Figure 4.59 demonstrates the IPFs of W_rod2_2r_edge HPT@300/200°C before and after heat treatment. The duration is up to 6 hours. Please note that the different scale bars are employed in these images because that the microstructure is quite fine in these materials, which are nearly 100nm in diameter. In contrast to as-deformed state, the grain growth induced by heat treatment is obvious after only 1 hour of heat treatment, as is shown in Fig. 4.59 a) and Fig. 4.59 b). However the grain size maintains almost constant afterwards up to 6 hours. Besides, the {110} // SPN texture component starts dominating the microstructure after heat treatment, which is colored in green. The quantitative grain size distribution diagrams are given in Fig. 4.62.

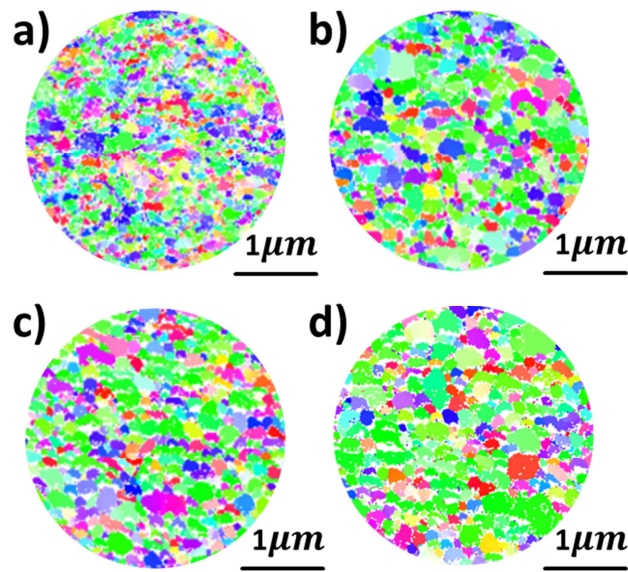
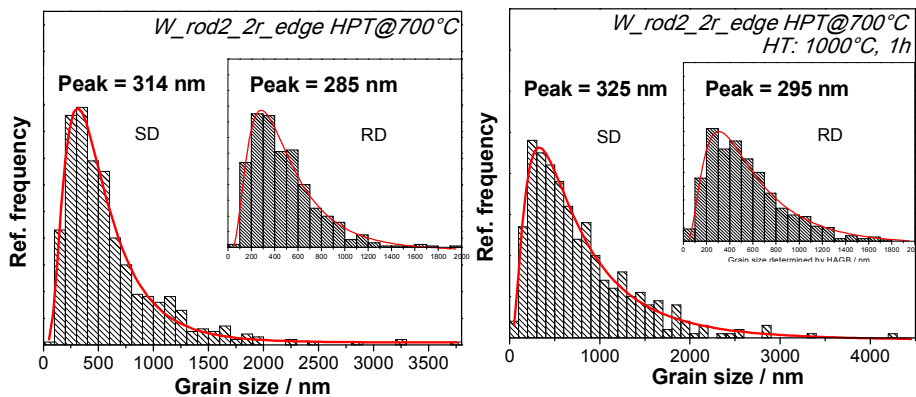


Fig. 4.59: Inverse pole figures of W_rod2 deformed by high-pressure torsion at 300/200°C after 2 torsion revolutions.

a) As-deformed and after heat treatment at 1000°C with duration of b) 1h, c) 3h and d) 6h. Color coding by Fig. 4.57 e).



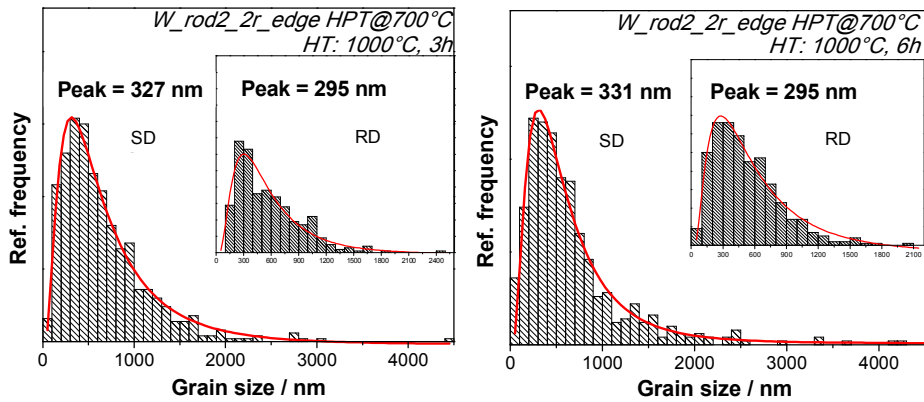


Fig. 4.60: Grain size distributions of W_rod2 deformed by high-pressure torsion at 700°C after 2 torsion revolutions and deformed-annealed at 1000°C with duration of 1h, 3h and 6h.

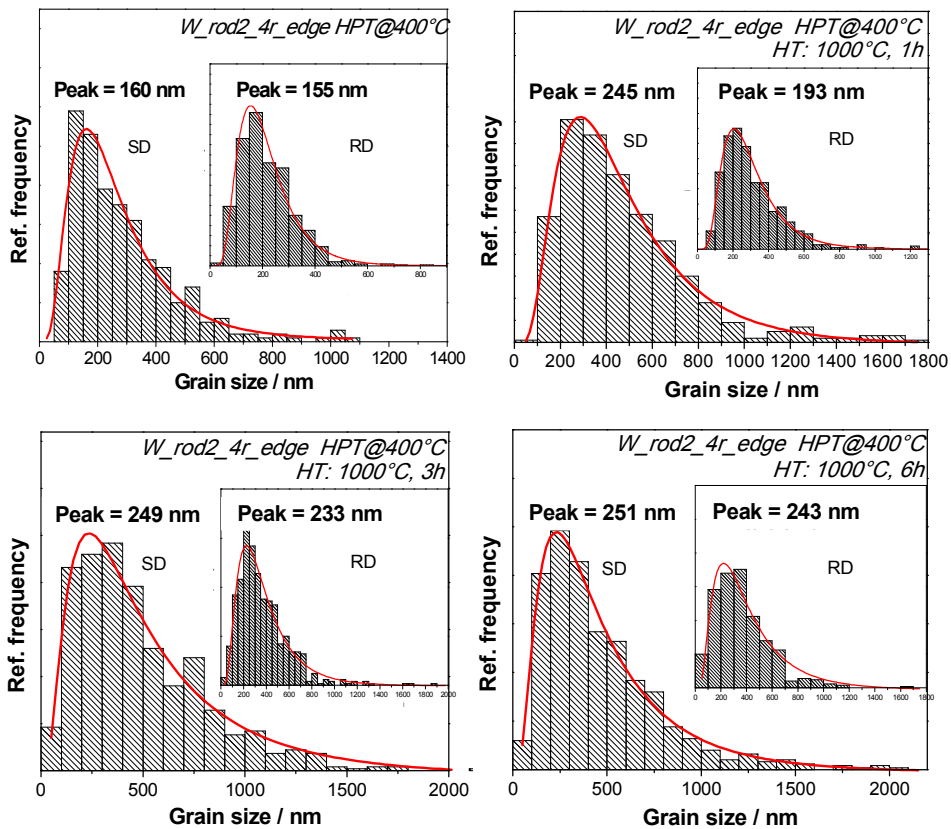


Fig. 4.61: Grain size distributions of W_rod2 deformed by HPT at 400°C after 4 torsion revolutions and deformed-annealed at 1000°C with duration of 1h, 3h and 6h.

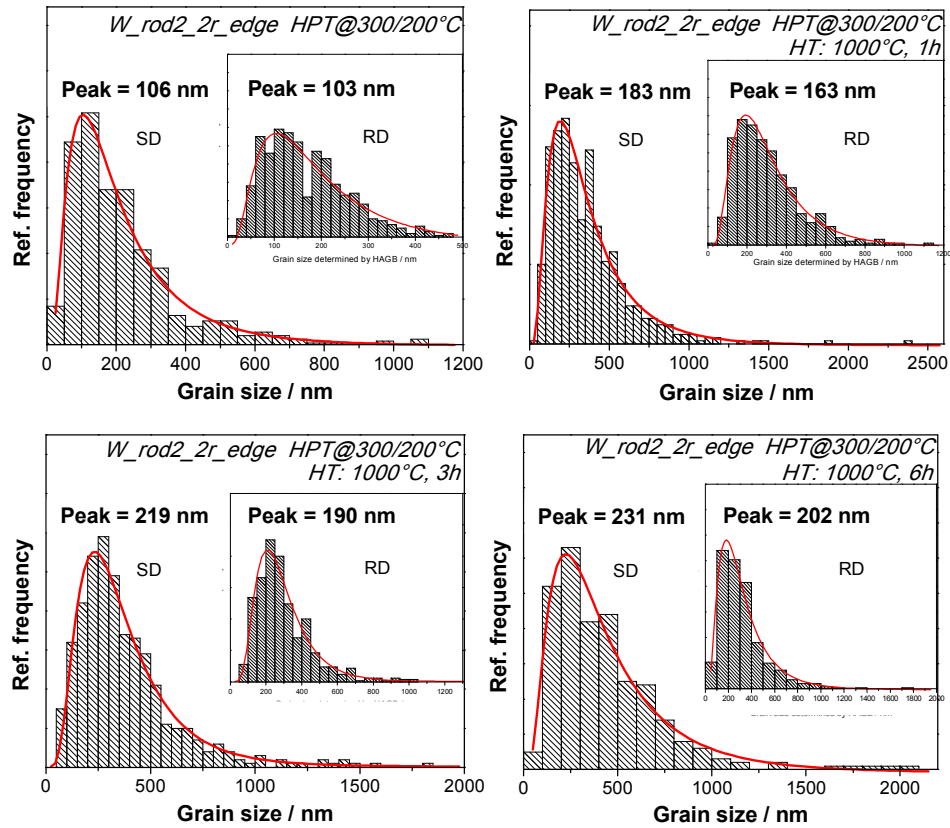


Fig. 4.62: Grain size distributions of W_rod2 deformed by HPT at 300/200°C after 2 torsion revolutions and deformed-annealed at 1000°C with duration of 1h, 3h and 6h.

Orientation image maps (OIM) of HPT deformed WL10 after heat treatment are displayed from Fig. 4.63 to Fig. 4.68, and following the order of deformation temperatures: 700°C, 550°C, 400°C and 300/200°C. The corresponding grain size distributions of deformed-annealed WL10 are provided in the end.

The IPF of as-deformed WL10_2r_edge HPT@700°C is shown in Fig. 4.63 a). After heat treatment of 1 hour, the grain size changes are not remarkable by bare eyes. However the most obvious change relates to texture variation, $\{110\} // \text{SPN}$ component is growing along with heat treatment duration. As is observed in Fig. 4.63 b) to d), the region with green color becomes more and more along with duration. After 6 hours heat treatment, the grains in this material are still elongated. Please note that Fig. 4.56 c) and d) are taken from the same location, and position 1, 2 and 3 are traced. It is observed from the magnified images at the bottom of Fig. 4.56 that $\{110\} // \text{SPN}$ texture spreads its territory by assimilation. The changes in position 1, 2 and 3 show that the crystal with orientation deviating slightly from $\{110\} // \text{SPN}$ rotates to let $\{110\}$ parallel to the shear plane gradually during heat treatment. The corresponding grain size distribution is given in

Fig. 4.66, and from which one could tell that the grain size growth is quite slow at 1000°C even up to 6 hours as well.

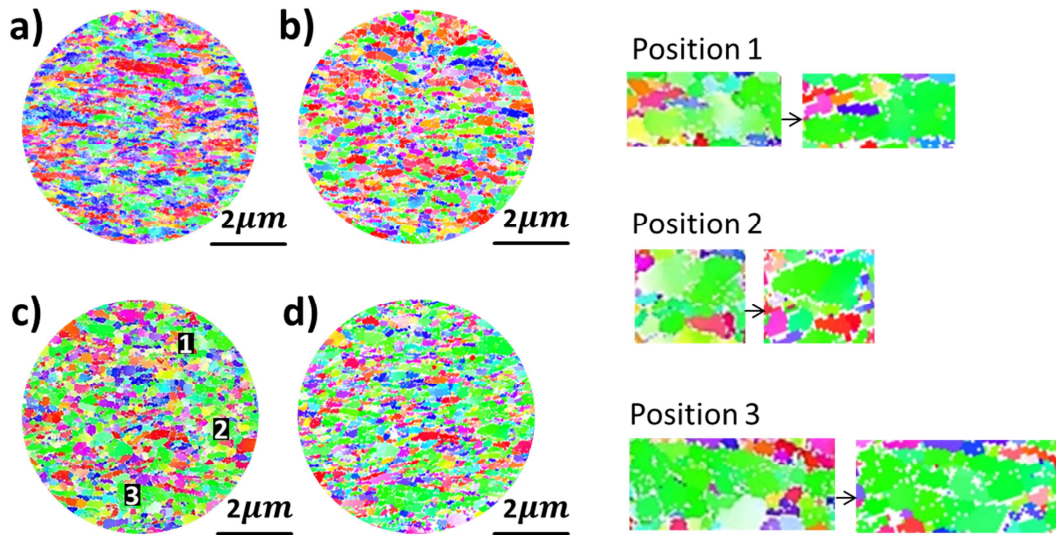


Fig. 4.63: Inverse pole figures of WL10 deformed by high-pressure torsion at 700°C after 2 torsion revolutions.

a) As-deformed state and after heat treatment at 1000°C with duration of b) 1h, c) 3h and d) 6h. Color coding by Fig. 4.57 e).

Position 1, 2 and 3 exhibit specific orientation changes from c) to d).

Fig. 4.64 refers to WL10 deformed at 400°C after 4 torsion revolutions, and the position is 3mm from torsion axis. As mentioned in section 4.2, this material shows quite fine microstructure at as-deformed state with equivalent grain size around 80nm. Therefore we perform the heat treatment longer than other materials to evaluate its thermal stability. The duration is 1, 3, 6 and 9 hours respectively, referring to Fig. 4.64 b) to e). The grain size distribution diagrams before and after heat treatment are provided in Fig. 4.67. It is found out from Fig. 4.64 and Fig. 4.67 that the microstructure thermal stability of this nanostructured WL10 is surprisingly well under 1000°C. The peak grain size is 128nm along SD after 9 hours heat treatment.

Fig. 4.65 relates to WL10 deformed at 300/200°C after 2 torsion revolutions. Both this material and the one shown in Fig. 4.64 have the finest microstructures which are around 80 nm in grain size. Heat treatment is carried out up to 9 hours as well. The grain size distribution diagrams before and after heat treatment are provided in Fig. 4.68. It is observed from Fig. 4.65 that, the grain size evolution is identical to that occurs in WL10 deformed at 400°C for 4 torsion

revolutions. The microstructure coarsening is not dramatic and the peak grain size along SD is 130nm after 9 hours heat treatment. Although the microstructure is too fine to be traced by certain positions, it is observed that the crystal with relative large volume trends to show $\{110\}$ // SPN texture, as is seen in Fig. 4. 65 e).

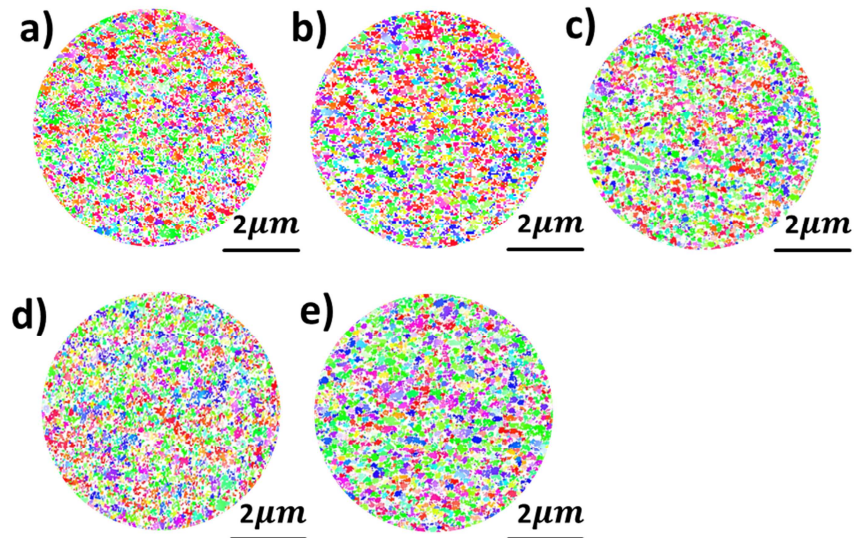


Fig. 4.64: Inverse pole figures of WL10 deformed by high-pressure torsion at 400°C after 4 torsion revolutions. a) As-deformed and after heat treatment at 1000°C with duration of b) 1h, c) 3h, d) 6h and e) 9h. Color coding by Fig. 4.57 e).

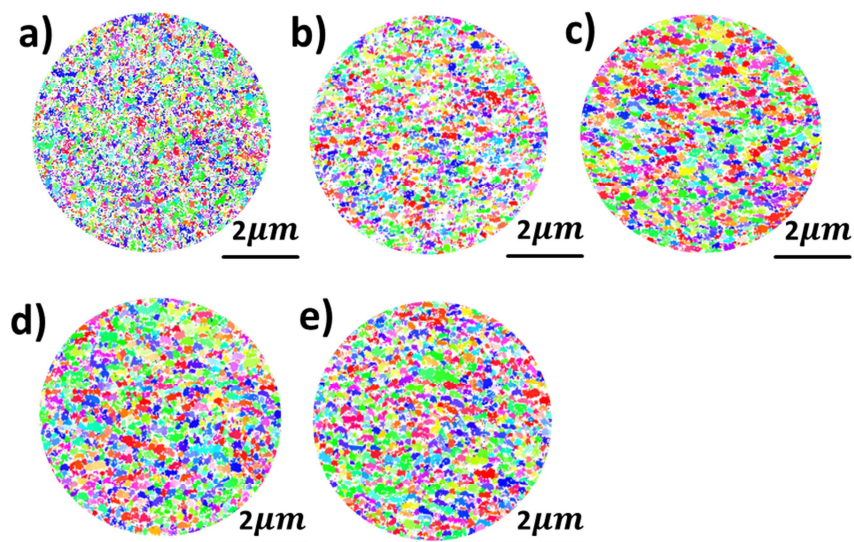


Fig. 4.65: Inverse pole figures of WL10 deformed by high-pressure torsion at 300/200°C after 2 torsion revolutions. a) As-deformed and after heat treatment at 1000°C with duration of b) 1h, c) 3h, d) 6h and e) 9h. Color coding by Fig. 4.57 e).

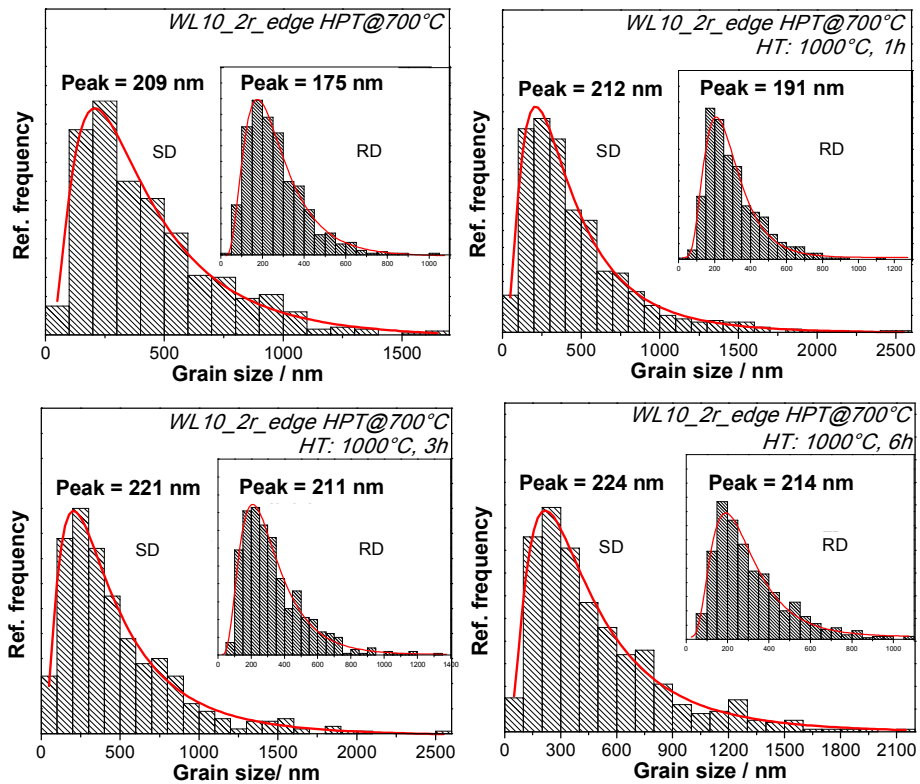
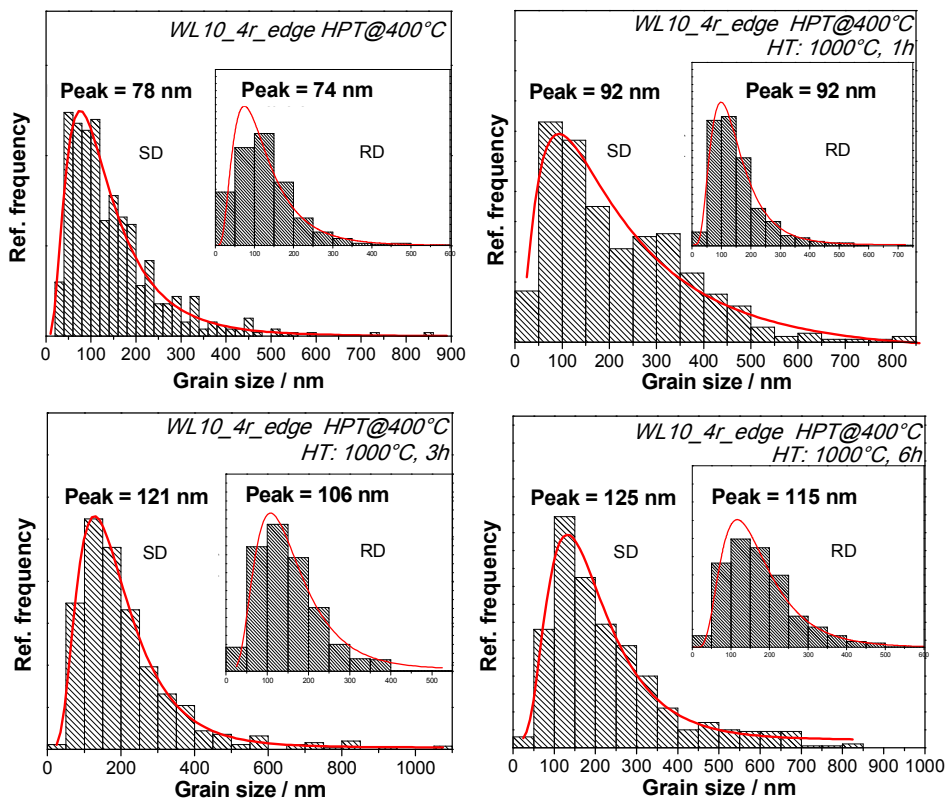


Fig. 4.66: Grain size distributions of WL10 deformed by HPT at 700°C after 2 torsion revolutions and deformed-annealed at 1000°C with duration of 1h, 3h and 6h.



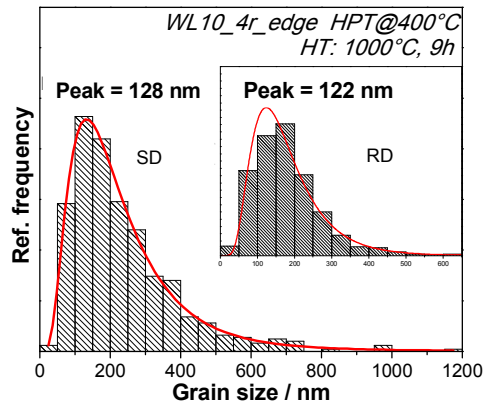
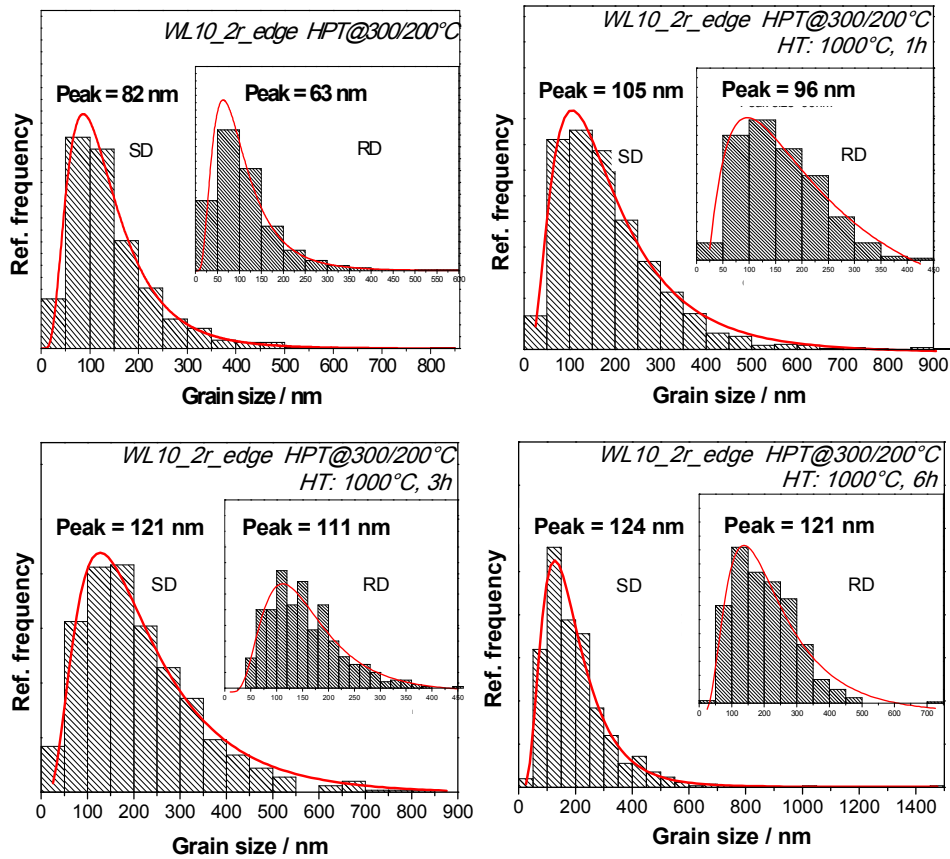


Fig. 4.67: Grain size distributions of WL10 deformed by HPT at 400°C after 4 torsion revolutions and deformed-annealed at 1000°C with duration of 1h, 3h, 6h and 9h.



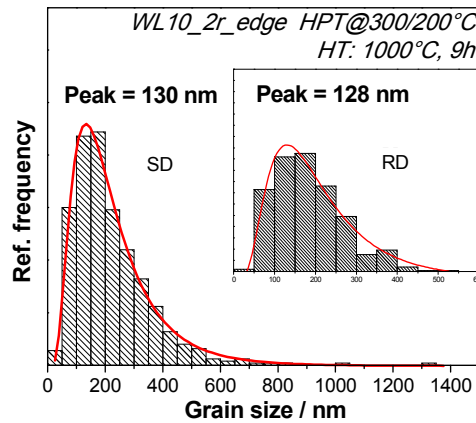


Fig. 4.68: Grain size distributions of WL10 deformed by HPT at 300/200°C after 2 torsion revolutions and deformed-annealed at 1000°C with duration of 1h, 3h, 6h and 9h.

The grain size changes during heat treatment for deformed W and WL10 are plotted in Fig. 4.69. Three groups can be classified according to the grain growth rate:

- A. W_rod2 HPT@700°C, which has the most stable microstructure with a slight increase of 15nm in equivalent grain size after heat treatment of 6 hours, which is only 4% compared to that in as-deformed state.
- B. WL10 HPT@700°C, WL10 HPT@400°C and WL10 HPT@300/200°C. These three deformed WL10 show medium grain size growth rate along with duration. The increase amount of grain size is 31nm, 56nm and 64nm after 6 or 9 hours, corresponding to HPT process temperatures of 700°C, 400°C and 300/200°C, respectively.
- C. W_rod2 HPT@400°C and W_rod2 HPT@300/200°C, which exhibit the fastest increase in grain size of 101nm and 125nm after 6 hours, respectively.

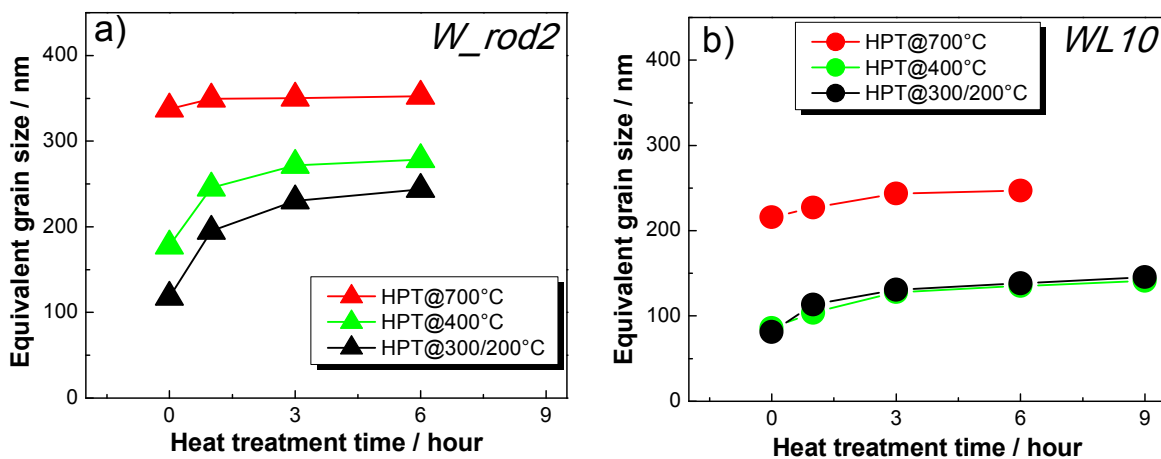


Fig. 4.69: Equivalent grain size growth along with heat treatment duration of high-pressure torsion deformed a) W_rod2 and b) WL10.

4.5.2 Grain boundary misorientation

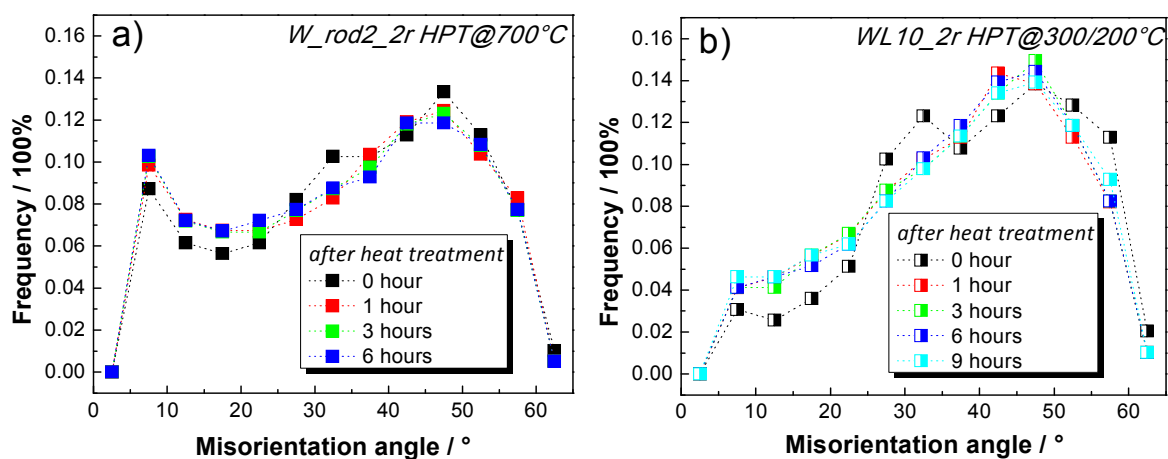
Figure 4.70 illustrates the grain boundary misorientation angle evolutions for HPT deformed W and WL10 along with heat treatment duration. Three typical materials are picked out from each group and refer to Fig. 4.70 a) to c).

Fig. 4.70 a) reveals that basically no change occurs during heat treatment up to 6 hours at 1000°C, except for a slight growth of LAGB. This refers to group A, and contains pure W deformed at 700°C after 2 torsion revolutions, which has the most thermally stable microstructure among all.

Figure 4.64 b) refers to WL10 deformed at 300/200°C, belonging to group B. The as-deformed state has higher fraction of HAGB compared to pure W. While the similar grain boundary misorientation evolution is observed as in Fig. 4.70 a), that is, no obvious change is seen in grain boundary misorientation during heat treatment.

Figure 4.64 c) is about pure W deformed at 300/200°C, which shows the fastest grain growth rate among all, belonging to group C. Distinct from the above two diagrams, there is a slight decrease in grain boundary misorientation angle at LAGB range. However this change is too small to prove anything.

All in all, diagrams in Fig. 4.70 show that the misorientation angle distributions don't change obviously up to 9 hours for materials from each group. This stability of grain boundary misorientation angle distribution is consistent with microstructure analysis.



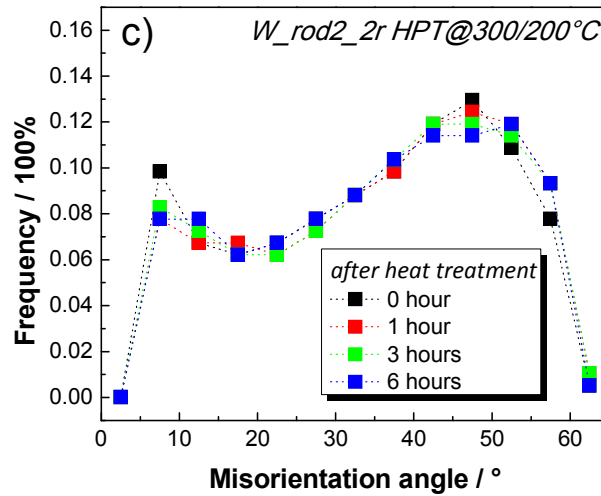


Fig. 4.70: Misorientation angle distribution changes during heat treatment at 1000°C for
a) W_rod2 deformed by high-pressure torsion at 700°C after 2 torsion revolutions (group A);
b) WL10 deformed by high-pressure torsion at 300/200°C after 2 torsion revolutions (group B);
c) W_rod2 deformed by high-pressure torsion at 300/200°C after 2 torsion revolutions (group C).

4.5.3 Texture

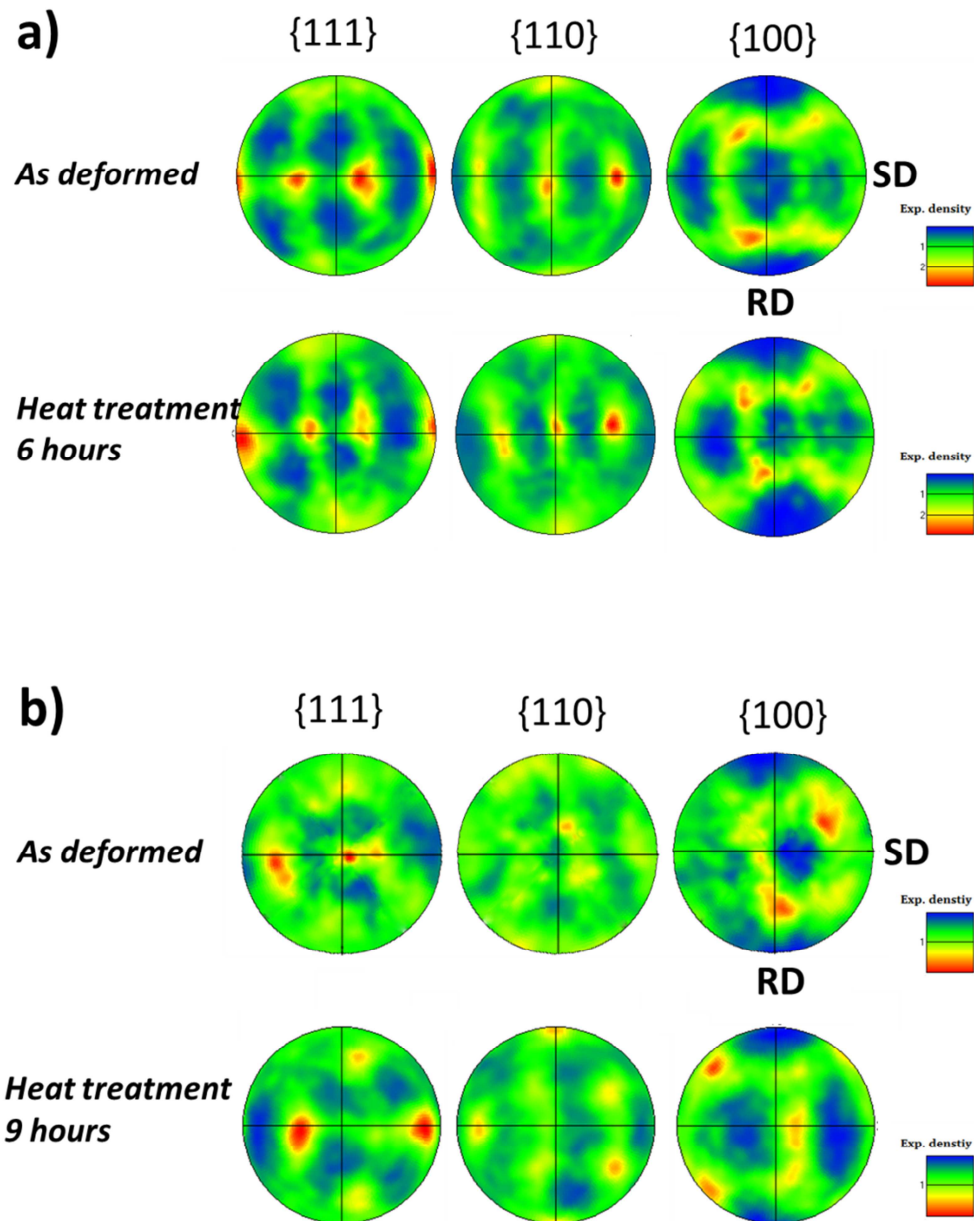
Typical texture evolutions of HPT deformed W and WL10 during heat treatment are displayed in Fig. 4.71. Pole figures at projection crystal planes of {111}, {110} and {100} are provided. Fig. 4.71 a), b) and c) refer to the same materials exhibited in Fig. 4.70, which are corresponding to group A, B and C.

As mentioned before, the microstructure in pure W deformed by HPT at 700°C is most stable during heat treatment. Therefore pole figure of W_rod2_2r HPT@700°C after 6 hours-heat treatment is directly illustrated to compare with as-deformed state, as shown in Fig. 4.71 a). It is noticed that there is seldom changes can be found either on texture component type aspect or texture intensity.

Fig. 4.71 b) refers to WL10_2r HPT@300/200°C, which belongs to group B. In contrast to Fig. 4.71 a), a more complicated texture change is observed in Fig. 4.71 b). The as-deformed state consists of {111} // SPN texture component, while it disappears after 9 hours heat treatment. At the meantime the texture intensity maintains at low level.

Fig. 4.71 c) is related to W_rod2_2r HPT@300/200°C. As mentioned before, the grain growth rate of W_rod2_2r HPT@300/200°C is the highest among all materials investigated. Therefore

the PFs of this material after heat treatment from 1 hour to 6 hours are all presented in Fig. 4.71 c). It is observed that the type of texture components maintain the same after heat treatment up to 6 hours duration. $\{110\}$ // SPN texture remains while $[111]$ // SD texture is fading out. However the texture intensity becomes stronger along with duration, which is indicated by the sharper intensity cluster on the PFs in Fig. 4.71 c).



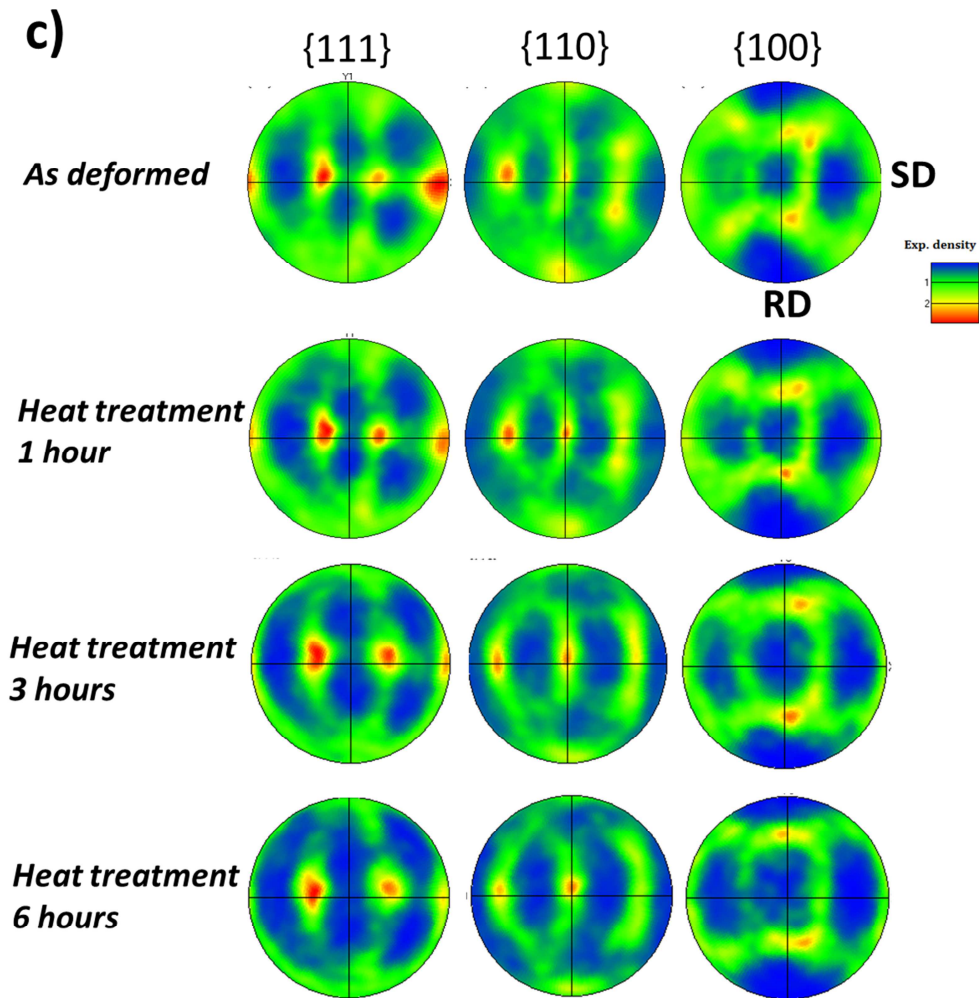


Fig. 4.71: Texture evolution during heat treatment at 1000°C after different duration for
a) W_rod2 deformed by high-pressure torsion at 700°C after 2 torsion revolutions (group A);
b) WL10 deformed by high-pressure torsion at 300/200°C after 2 torsion revolutions (group B);
c) W_rod2 deformed by high-pressure torsion at 300/200°C after 2 torsion revolutions (group C).

4.5.4 Discussion

The operation temperature window for divertor cooling figure is estimated between 800°C to 900°C [4]. Even though the recrystallization temperatures for coarse-grain pure W and WL10 are 1350°C and 1500°C respectively for 100% recrystallization (annealing duration 1 hour), they may decrease to lower temperature region due to severe plastic deformation [123, 124]. Therefore the thermal stability measurements are carried out at 1000°C, and up to 6 or 9 hours duration depending on the material. From the microstructure analysis and grain size distribution statistic results, one could tell that the thermal stabilities of all investigated HPT deformed W and WL10

are quite well, and there is no abrupt growth of grain as far as we observe for all materials. The grain growth is monotonic along with heat treatment duration, as shown in Fig. 4.69, which implies that the continuous static recrystallization mode is followed.

According to grain growth rate during heat treatment, three groups of as-deformed materials can be classified, and in which, the grain growth rate: group A < group B < group C.

Group A: W_rod2_2r HPT@700°C;

Group B: WL10_2r HPT@700°C, WL10_4r HPT@400°C and WL10_2r HPT@300/200°C;

Group C: W_rod2_4r HPT@400°C and W_rod2_2r HPT@300/200°C.

The material in group A refers to pure W obtained from HPT at 700°C, which possesses the largest grain size in as-deformed state among all investigated samples, and the grain morphology is almost equiaxed. As discussed in section 4.3, the higher deformation temperature is, the easier dynamic recovery (DRV) and dynamic recrystallization (DRX) occur. Pure W deformed at 700°C experiences DRV and DRX during the HPT deformation. The driven force for them is stored energy obtained by imposed strain during HPT. Therefore the stored energy in W_rod2 has been consumed already by dynamic DRV and DRX, and there is not so much left during post-annealing for static recrystallization, leading to its highest thermal stability among all.

It is noticed that all materials in group B are related to as-deformed WL10. Two of them have the finest microstructure among all samples in this work, which are WL10_4r HPT@400°C and WL10_2r HPT@300/200°C respectively. As discussed in section 4.3 and section 4.4, HPT deformed WL10 possess large percentage of HAGBs due to their fine grain sizes. Therefore the stored energies within these materials are higher compared to HPT deformed coarser-grain W in group A and C. However, the grain size growth rates are slower for the material in group B than that in group C. The reason for that can be attributed to La₂O₃ particles. Oxide particles play an important role by pinning dislocations during heat treatment, retarding the annihilation of dislocations, thus improve the thermal stability of materials. Another reason may relate also to the high percentage of HAGB in as-deformed WL10, as is shown in Fig. 4.70 b). Even though the HAGB possesses higher stored energy, which may provide the driven force for recrystallization, these HAGB can act as challenge energy barrier for dislocation movement as well. Therefore facilitates the outstanding thermal stability of nanostructured WL10 in group B.

Group C contains two HPT deformed pure W with lower process temperature and smaller grain size compared to that in group A, as stated in section 4.3. The DR and DRX in these two materials are not as complete as at 700°C during HPT. Therefore the stored energies within pure W in group C are relative high, which provide driven force for static recrystallization during post-

annealing. Furthermore, the main reason for its relative poor thermal stability is due to the absent of La_2O_3 particles as well as lower fraction of HAGBs compared to deformed WL10 in group B. Consequently the materials in group C exhibit the fastest grain growth rate among all under given condition.

4.6 Hall-Petch relationship

The relationships between hardness and grain size of W and WL10 are all plotted in Fig. 4.72. The materials shown include HPT deformed as well deformed-annealed W and WL10. Hardness values are all obtained from nanoindentation. The corresponding linear fittings are shown in black and red for W and WL10 respectively. Researchers found out HPT deformed Cu demonstrates abrupt drop in hardness after thermal annealing in fairly short time [65], in which estimation is made that HPT deformed materials are metastable due to large internal stress within materials, and is easily released by heat treatment. However it is observed from Fig. 4.72 that there is seldom deviation from Hall-Petch relationship for both deformed W and WL10 including the deformed-annealed materials, which are shown in hollow. This confirms the thermal stability of HPT deformed W and WL10 in this work.

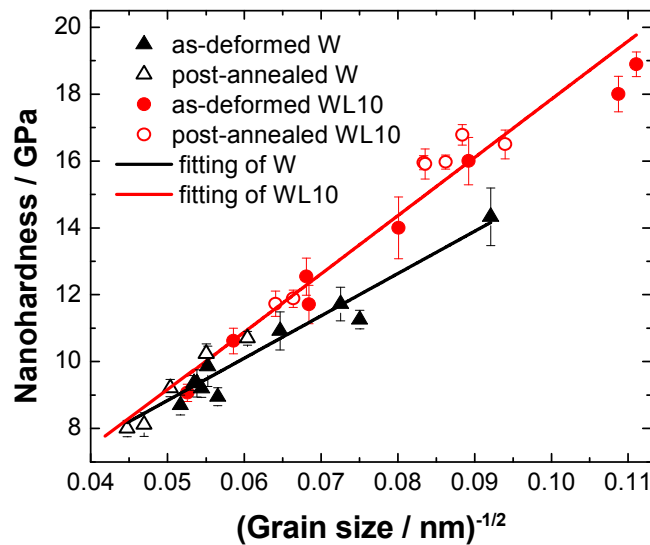


Fig. 4.72: Relationship of nanoindentation hardness and $(\text{grain size})^{-1/2}$ for high-pressure torsion deformed and deformed-annealed W and WL10.

Two data points on the most right exhibit distances from linear fit, which refer to HPT deformed WL10 with around 80nm in grain size and 19GPa in hardness. According to the Hall-Petch linear fit, the hardness of them shall 1GPa higher than they actually are. This may draw a clue for inverse Hall-Petch relationship or just due to measurement error. More data relate to grain size

smaller than 80nm are required if one attempts to obtain the critical grain size for inverse Hall-Petch relationship occurrence.

It is noticed that Hall-Petch slope of WL10 is not parallel to that of pure W. The slope of WL10 becomes larger than that of pure W after the grain size is smaller than 494nm. This is associated to the evolution of La_2O_3 particles in WL10 during deformation. There are several strengthening mechanisms involve in HPT deformed materials. The first one is related to fine grain size, which is Hall-Petch relationship. The second one is concerned to work hardening, by which the dislocation densities are increased by plastic deformation. The third one is about dispersion hardening. Second phase particles can hinder the dislocation movement and strengthen the material. The hardening efficiency is highly dependent on particle size and distance between adjacent particles, as discussed in section 4.2. For pure W and WL10, if the grain size is certain, the contribution from fine grain size for hardness improvement is the same for both materials, and the dislocation densities are also comparable when grain sizes are identical. Therefore the difference is caused by dispersion hardening, which occurs only for WL10. As discussed in section 4.2, the oxide particles are in micrometer scale in as-received state, but they are fragmented with imposed strain. After the equivalent strain of around 20, the oxide particles are assumed to be small enough to facilitate material strengthening (s. Fig. 4.11 b). Therefore the Hall-Petch slope of WL10 is larger than that of pure W after certain amount of imposed strain.

4.7 Fracture toughness

It is reported that the fracture toughness of W and W alloy can be improved by employing SPD [70], in which the evaluation methods include disk-shaped compact tension (DCT) and single-edge notch bending (SENB). Moreover, Vickers indentation can be also employed for fracture toughness measurement [125]. For brittle materials like coarse-grain W and WL10, there will be cracks left on the impression of indentation under certain experimental condition. The fracture toughness is related to the applied load and crack length. The longer the crack is, the lower the fracture toughness is, under the same load condition, as stated in section 3.2.6. In this work, Vickers indentation is performed on as-received and HPT deformed W_rod1 to evaluate the fracture toughness qualitatively.

The as-received W exhibits obvious brittle behavior after indentation, as is shown in Fig. 4.73 a), cracks initialize from corners of the indents and prolong to surrounding area. The length of the crack is about 50 μm . Fig. 4.73 b) exhibits the indentation expression image of as-deformed W_rod1, which undergoes HPT with equivalent true strain of 10 before performing indentation. It is noticed that the diagonals of indent is 30% shorter compared to that in as-received state, which means that the hardness is improved by HPT according to equation (3.4). More importantly, no

cracks are observed on the impression. Therefore it is proved that the fracture toughness of W is improved by HPT even after only equivalent true strain of 10.

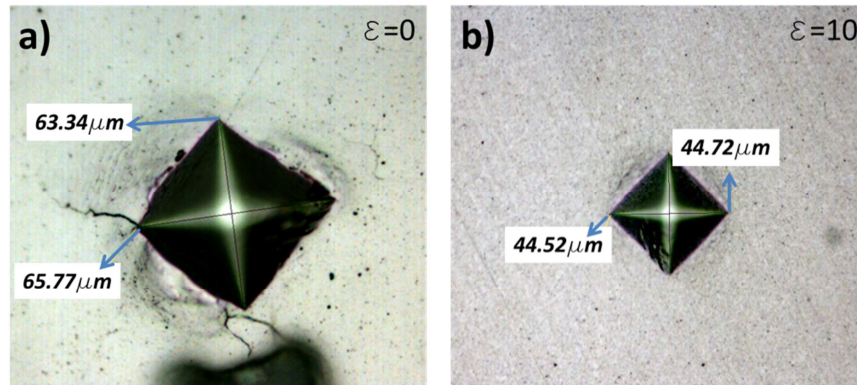


Fig. 4.73: Images of Vickers indents from a) as-received W_rod1 and b) high-pressure torsion deformed W_rod1.

The toughness improvement of W by HPT has many reasons [70, 85]. The most important one is related to microstructure refinement introduced by HPT. It is well known that the impurities, such as O, N, S and P, often segregate to grain boundaries, weaken their strength and thus harm the fracture toughness of materials. However, by subjecting HPT, the grain size in W_rod1 is almost 30 times smaller than that from as-received state. In this case, the refined microstructure contains large fraction of grain boundaries, at which impurities segregate in reduced concentration thus improving the fracture toughness. Furthermore, one of the advantages of HPT is to produce condensed material and lack of micro-crack. Hence fracture toughness can be raised as well. The third reason is related to the high fraction of HAGB in as-deformed W. The complicated structure of grain boundary provides large energy barrier for dislocation movement and enhance the fracture toughness consequently.

4.8 Homogeneity improvement

For conventional application, homogeneous material is always expected. However due to the character of HPT deformation, deformed samples usually show non-uniform properties along radial direction. It is found out increasing torsion revolution can lead to a relative uniform material owing to the existence of microstructure saturation along with imposed strain [126], and it is highly dependent on material properties, such as SFE [6, 7]. However if the HPT setup is in perfect alignment, the un-deformed central region maintains even after many torsion revolutions. For example, un-deformed center region exists for austenitic steel after 16 torsion revolutions [11], and a relative homogenous microstructure is only attained for pure aluminum after 20

torsion revolutions [10]. This is time and energy consuming. In this section, the hardness distribution evolution along with increasing torsion revolution is first addressed. To efficiently improve the homogeneity of HPT deformed W, a multi-center method is introduced afterwards.

4.8.1 Increasing torsion revolution

The hardness distribution of W_rod2 along radial distance from torsion axis is provided in Fig. 4.74 a), in which colors represents different torsion revolutions. All the data are obtained from HPT at 400°C, shear strain rate is 5rpm and pressure is 5GPa. Hardness values are all obtained from nanoindentation. An artificial line of 10.8GPa is drawn to indicate the homogeneity of material, and the corresponding region radiuses with hardness value below 10.8GPa obtained from Fig. 4.74 a) are plotted in Fig. 4.74 b).

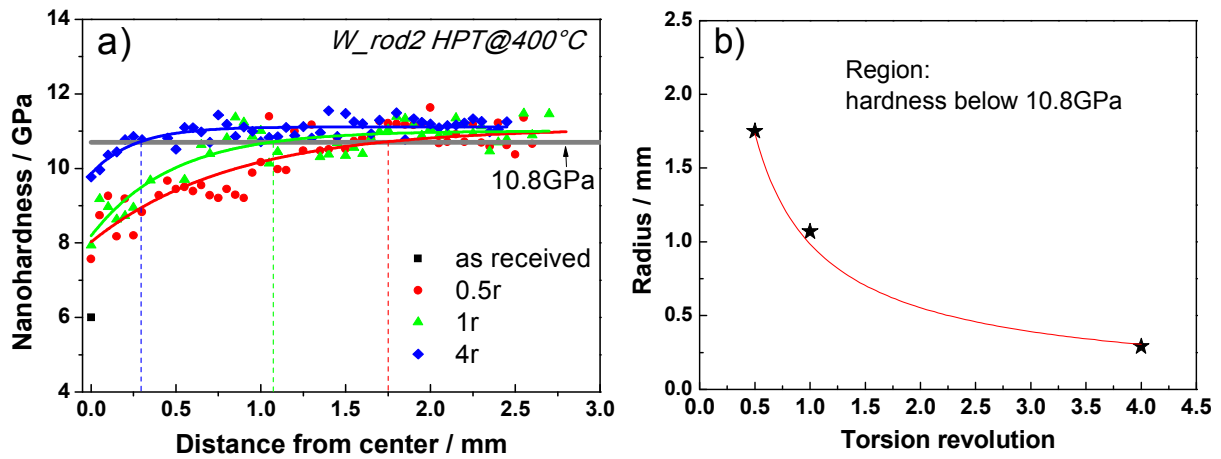


Fig. 4.74: a) Hardness distribution along sample radial direction.

b) Radius (size) changes of region with hardness value below 10.8GPa vs. torsion revolution.

It is observed from Fig. 4.74 that the radius of region with hardness below 10.8GPa is decreasing from 1.75mm to 0.29mm with increasing of torsion revolutions, from 0.5 to 4 torsion revolutions specifically. The slope of fitting curve in Fig. 4.74 b) is decreasing along with torsion revolution, it is therefore suggested that to obtain a total uniform W along radius direction, more torsion revolutions are required to perform, which is time and energy consuming.

4.8.2 Multi-center high-pressure torsion

The principle of multi-center HPT procedure is illustrated in Fig. 3.7, and accomplished by variation of sample position. The idealized equivalent strain distribution for both conventional HPT and multi-center HPT are calculated by Eq. (2.2), and the average height of sample from as compressed state to as-deformed state is used. It should be mentioned that the equivalent strain in

HPT deformed sample consists of not only shear component but also axis component due to the constant compression. However the equivalent strain from axis component is less than 10% of the total equivalent strain value, and thus it is ignored to reduce the complexity in later calculation.

The corresponding calculated strain results are provided in Fig. 4.75, the step order and equivalent torsion revolution are displayed. It is observed that the strain distribution after conventional HPT exhibits concentric circle mapping with an un-deformed center point. This large strain gradient is a typical consequence from HPT. Whereas after multi-center HPT, the strain distribution is more complex and shows an electrical fan shape after 2 revolutions. Even though the overall value of equivalent strain is lower in contrast to conventional HPT, the central region with zero deformation is no longer found.

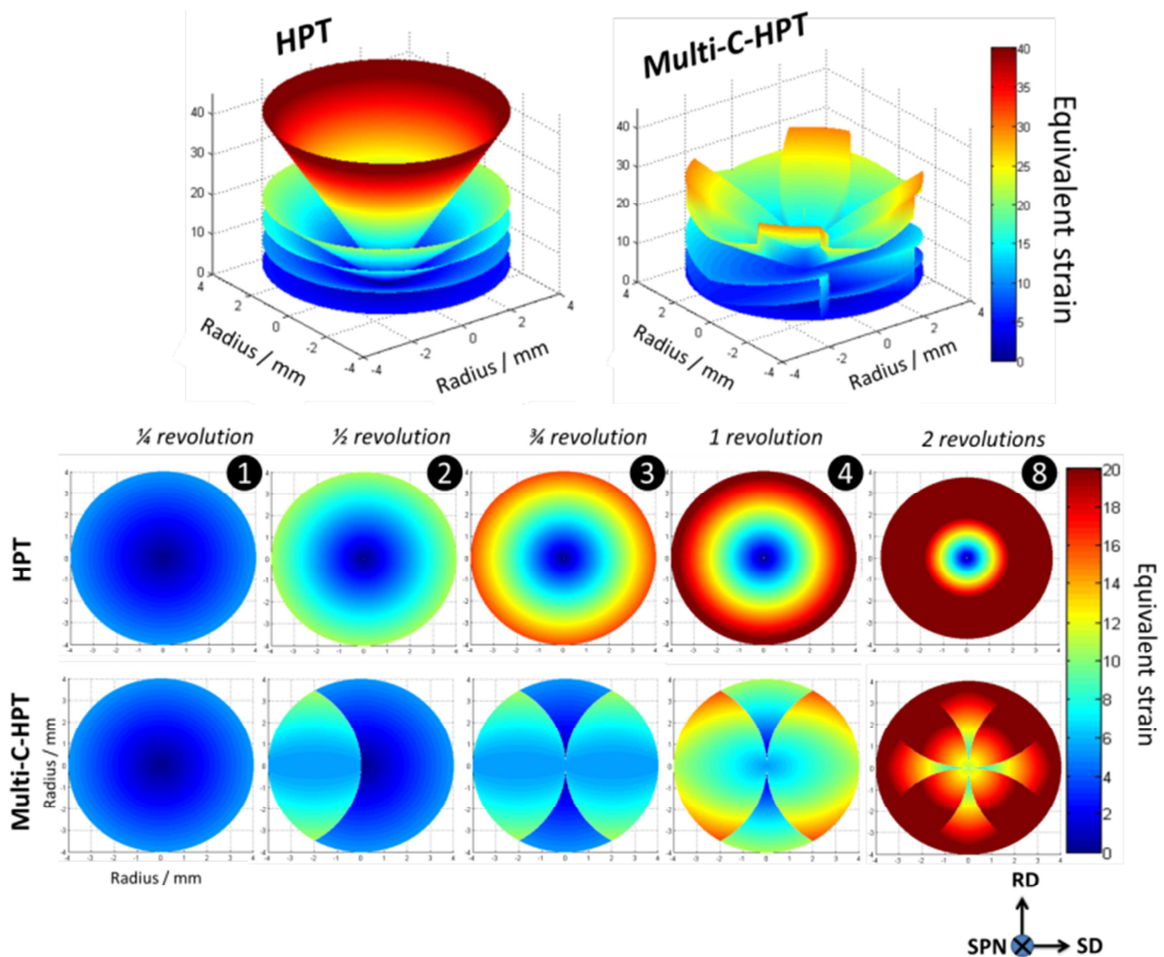


Fig. 4.75: Comparison of idealized equivalent strain from conventional high-pressure torsion and multi-center high-pressure torsion (multi-center HPT) at different torsion revolutions.

(RD: radius direction, SD: shear direction, SPN: shear plane).

Since the eq. (2.2) with average height of sample is employed when evaluating the equivalent strain. Therefore the fitting parameters are different from Table 4.1 which is calculated by equivalent true strain. Fig. 4.76 shows the experimental data of pure W deformed by using conventional HPT at 400 °C, and the results are: $H_0=6$ GPa, $H_s=11.2$ GPa and $c = 0.44$.

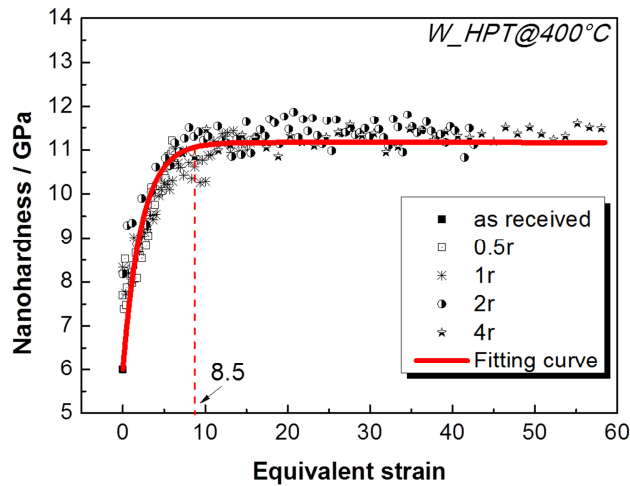


Fig. 4.76: Hardness vs. equivalent strain for high-pressure torsion deformed W at 400°C.

As mentioned before, the nanohardness distribution in the sample shear plane can be described as a function of r , and the color mapping is exhibited in Fig. 4.77. Compared to conventional HPT, the homogeneity improvement of hardness after multi-center HPT method is already apparent after 1 revolution for multi-center HPT. For instance, a quite uniform hardness distribution is expected along Line 1 in Fig. 4.77. However, as depicted in line 2 a small drop of hardness value is still observed in the central region. It is noticeable that the hardness change along RD is depending on the path chosen. Nevertheless, this inhomogeneity in hardness almost diminishes after 2 revolutions. This is due to the existence of saturation in microstructure fragmentation during deformation, therefore induces hardness saturation as consequence. For the investigated pure W, if equivalent strain is larger than saturation onset value (about 8.5), the nanohardness will be constant at 11.22GPa, as shown in Fig. 4.76. Therefore, despite the complex equivalent strain distribution after multi-center HPT, a relative uniform hardness distribution can still be obtained.

Experimental nanohardness data were measured along random chosen radius on the as-received and deformed sample. The data are displayed in Fig. 4.78 a) and b), referring to 1 and 2 revolutions, respectively. The solid and dash lines in each diagram are obtained from Fig. 4.77.

As mentioned before, the hardness variation is path-dependent for multi-center HPT, and the path with lowest hardness value is chosen. Generally speaking, the experimental and calculated data fit well except some scattering data in multi-center HPT after 1 revolution, which suggests that the experiments were close to idealized condition. When comparing conventional and multi-center HPT, the scattering of hardness is reduced from 53% to 15% after 1 revolution, and from 44% to 11% after 2 revolutions, as can be seen in Fig. 4.78 b).

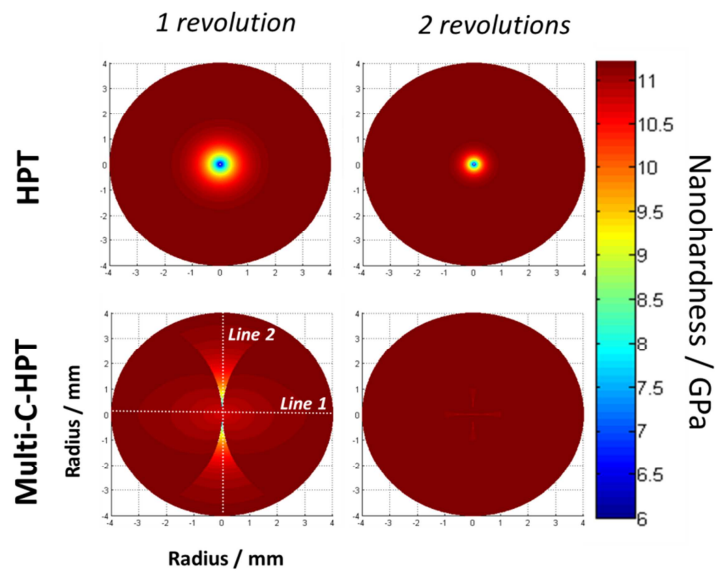


Fig. 4.77: Hardness mapping of high-pressure torsion and multi-center high-pressure torsion (multi-center HPT) after 1 and 2 torsion revolutions.

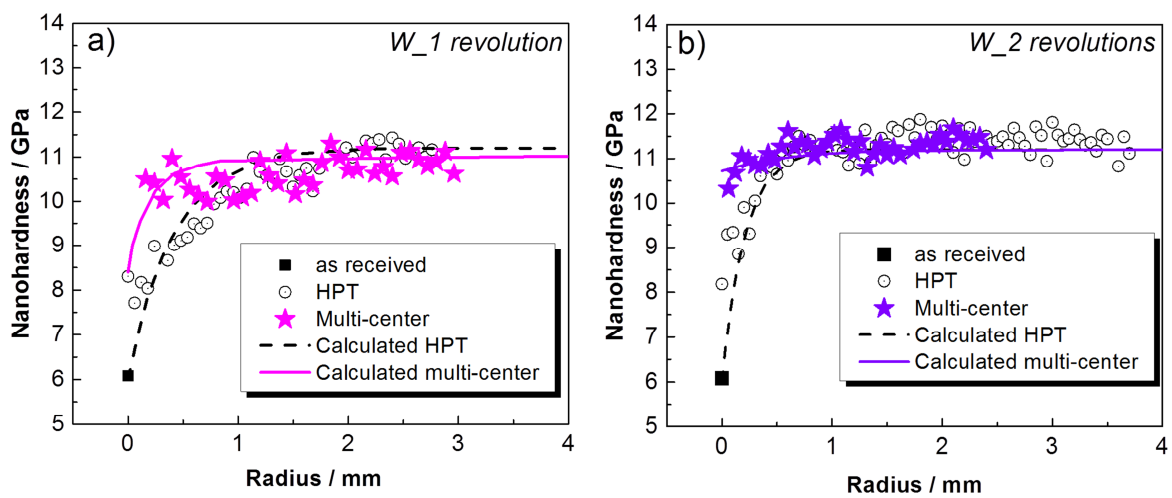


Fig. 4.78: Nanohardness distribution along radius from high-pressure torsion and multi-center high-pressure torsion (multi-center HPT) deformed W after a) 1 and b) 2 revolutions.

4.8.3 Discussion

By increasing strain, the deformation transfers from edge to center gradually. However, according to the character of HPT, the refinement of center region is quite slow (s. Fig. 4.74). Thus this method is inefficient and time/energy consuming. Multi-center HPT generates artificial deviation of sample position. The torsion strain gradient is overlapped by each variation of torsion center, so as to obtain a comparably homogeneous structure all over the sample after limited torsion revolutions. Compared to the first method, multi-center HPT is more effective on fabricating homogeneous material since after only 1 torsion revolution, the hardness shows almost linear distribution along the center line (s. Fig. 4.74 b). Besides, the strain or hardness distribution can be well predicted by calculation. Therefore possibilities are provided that through manipulating strain distribution during HPT to meet specific requirements.

5 Conclusions and outlook

5.1 Conclusions

Nanostructured W and WL10 are successfully fabricated by HPT. The equivalent grain sizes for as-deformed W and WL10 range from 80nm to 400nm under given experimental condition. The grain refinement occurs aside with LAGB-HAGB transition. HAGB subdivide microstructure as well as interaction between “strong” and “weak” textures are two mechanisms involved in grain fragmentation during HPT. By “strong” texture, it means $\{110\}$ $[111]$, which is related to the dominating dislocation slip system in HPT deformed W.

Pure W exhibits saturation in grain refinement (170nm~178nm) and hardness improvement (11GPa~11.2GPa) during HPT at 400°C, and the onset equivalent true strain values are 24~68 and 12~33 respectively. Original microstructure and initial product form have little effect on saturation for pure W. Lower process temperature can lead to finer microstructure. However, the torsion torque required during deformation is correspondingly higher in this case. Moreover, the fracture toughness of W at room temperature is improved by HPT.

The La_2O_3 particles in WL10 have original large scale (several micrometers in diameter), and it can still stabilize the original “weak” texture and thus benefit HAGB formation regardless of misorientation gradient. After equivalent true strain of ~20, the La_2O_3 particles are fragmented small enough to exhibit their effect on grain refinement with superiority over pure W. No saturation in grain size/hardness is observed in WL10 up to equivalent true strain of 174 at process temperature of 400°C. Besides, La_2O_3 particles maintain the duty of grain refinement when the HPT is conducted at 700°C. However, during reversal strain path, La_2O_3 particles are more or less invalid for prevent dislocations from slipping on the $\{110\}$ $[111]$ system. Therefore resulting in microstructure consists of coarse and fine grains in WL10 with texture of $\{110\}$ $[111]$.

The finest grain size obtained in this work is around 80nm in equivalent grain size. Two HPT deformed WL10 are concerned, including WL10 deformed after 2 torsion revolutions at 300/200°C (first revolution at 300°C, the second revolution at 200°C) and WL10 deformed after 4 torsion revolutions at 400°C. Both of them exhibit the highest hardness of nearly 19GPa from nanoindentation, and perform outstanding thermal stability under 1000°C up to duration of 9 hours.

The improvement of homogeneity along radial direction of HPT deformed W by increasing torsion revolution is time/energy consuming. Multi-center HPT is introduced and it is more effective on fabricating uniform W sample.

5.2 Outlook

Even though this work represents systematic investigation on HPT deformed W and WL10, there are still more aspects that one can pursue. Nanostructured material below 100nm in diameter is fabricated from W-1wt%La₂O₃ by HPT, and exhibits outstanding thermal stability. The contents and types of oxide can be varied to discover the optimal composition for achieving the minimum grain size for W alloy system. Besides, the La₂O₃ particles are initially in micrometer scale, but they can be fragmented during deformation and facilitate the microstructure refinement with remarkable local uniformity, which suggests that the initial geometry of second phase could be in large scale theoretically. Therefore the critical size of second phase is of interest for commercial reason as well as for deep understanding of alloy fabrication.

From the technical point of view, the solution to heterogeneous along radial direction of HPT deformed sample is essential, besides the multi-center HPT, a unique cone-shaped sample can be employed instead of traditional disk-shaped sample. The experiment and result are provided in Appendix-B. Inspired by cone-shaped sample method, a double-cone-shaped sample is also introduced (s. Appendix-B).

Bibliography

- [1] E. Lassner and W.-D. Schubert, "Tungsten: Properties, Chemistry, Technology of the Element, Alloys, and Chemical Compounds," 1999.
- [2] H. Bolt, *et al.*, "Plasma facing and high heat flux materials - needs for ITER and beyond," *Journal of Nuclear Materials*, vol. 307–311, pp. 43-52, 2002.
- [3] K. Cui, *et al.*, "Microstructural characteristics of commercial purity W and W–1% La₂O₃ alloy," *International Journal of Refractory Metals and Hard Materials*, 2013.
- [4] M. Rieth and B. Dafferner, "Limitations of W and W–1%La₂O₃ for use as structural materials," *Journal of Nuclear Materials*, vol. 342, pp. 20-25, 2005.
- [5] P. Norajitra, *et al.*, "Development of a helium-cooled divertor concept: design-related requirements on materials and fabrication technology," *Journal of Nuclear Materials*, vol. 329-333, pp. 1594-1598, 2004.
- [6] X. H. An, *et al.*, "Evolution of microstructural homogeneity in copper processed by high-pressure torsion," *Scripta Materialia*, vol. 63, pp. 560-563, 2010.
- [7] M. Kawasaki, *et al.*, "The development of hardness homogeneity in pure aluminum and aluminum alloy disks processed by high-pressure torsion," *Materials Science and Engineering: A*, vol. 529, pp. 345-351, 2011.
- [8] G. Sakai, *et al.*, "Grain refinement and superplasticity in an aluminum alloy processed by high-pressure torsion," *Materials Science and Engineering: A*, vol. 393, pp. 344-351, 2005.
- [9] M. Kawasaki and T. G. Langdon, "The significance of strain reversals during processing by high-pressure torsion," *Materials Science and Engineering: A*, vol. 498, pp. 341-348, 2008.
- [10] M. Kawasaki, *et al.*, "An investigation of hardness homogeneity throughout disks processed by high-pressure torsion," *Acta Materialia*, vol. 59, pp. 308-316, 2011.
- [11] A. Vorhauer and R. Pippan, "On the homogeneity of deformation by high pressure torsion," *Scripta Materialia*, vol. 51, pp. 921-925, 2004.
- [12] P. Gumbsch, "Controlling Factors for the Brittle-to-Ductile Transition in Tungsten Single Crystals," *Science*, vol. 282, pp. 1293-1295, 1998.
- [13] A. Einstein, "Does the inertia of an object depend upon its energy content?," 1905.

-
- [14] M. Faleschini, "Severe Plastic Deformation of Tungsten Alloys and its Influence on the Fracture Behaviour," Doktor der montanistischen Wissenschaften, Department Materialphysik der Montanuniversität, Erich Schmid Institut für Materialwissenschaft der Österreichischen Akademie der Wissenschaften, Leoben, 2006.
- [15] "<http://www.iter.org/>."
- [16] L. V. Boccaccini, "FZK-Nachrichten," 2004.
- [17] A. Kohyama, *et al.*, "Low-activation ferritic and martensitic steels for fusion application," *Journal of Nuclear Materials* vol. 233-237, pp. 138-147, 1996.
- [18] J. Reiser, *et al.*, "Tungsten foil laminate for structural divertor applications – Analyses and characterisation of tungsten foil," *Journal of Nuclear Materials*, vol. 424, pp. 197-203, 2012.
- [19] J. P. Morniroli, "Low Temperature Embrittlement of Undoped and Doped Tungsten," *The Metallurgy of Doped/Non-sag Tungsten*, 1989.
- [20] P. L. Raffo, "Yielding and fracture in tungsten and tungsten-rhenium alloys," National aeronautics and space administration, Washington, D. C. 1968.
- [21] C. T. Liu and H. Inouye, "Study of iridium and iridium-tungsten alloys for space radioisotopic heat sources," Oak bidge national laboratory, Tennessee 1976.
- [22] M. A. Yar, *et al.*, "Chemically produced nanostructured ODS–lanthanum oxide–tungsten composites sintered by spark plasma," *Journal of Nuclear Materials*, vol. 408, pp. 129-135, 2011.
- [23] T. G. Langdon, "Twenty-five years of ultrafine-grained materials: Achieving exceptional properties through grain refinement," *Acta Materialia*, vol. 61, pp. 7035-7059, 2013.
- [24] J. Du, *et al.*, "Feasibility study of a tungsten wire-reinforced tungsten matrix composite with ZrO_x interfacial coatings," *Composites Science and Technology*, vol. 70, pp. 1482-1489, 2010.
- [25] J. Du, *et al.*, "Interfacial fracture behavior of tungsten wire/tungsten matrix composites with copper-coated interfaces," *Materials Science and Engineering: A*, vol. 527, pp. 1623-1629, 2010.
- [26] M. Battabyal, *et al.*, "Microstructure and mechanical properties of a W–2wt.%Y₂O₃ composite produced by sintering and hot forging," *Journal of Nuclear Materials*, vol. 442, pp. S225-S228, 2013.

-
- [27] H. Gleiter, "Nanostructured materials: basic concepts and microstructure," *Acta materialia*, vol. 48, pp. 1-29, 2000.
- [28] K. S. Kumar, *et al.*, "Mechanical behavior of nanocrystalline metals and alloys11The Golden Jubilee Issue—Selected topics in Materials Science and Engineering: Past, Present and Future, edited by S. Suresh," *Acta Materialia*, vol. 51, pp. 5743-5774, 2003.
- [29] R. Z. Valiev, *et al.*, "Bulk nanostructured materials from severe plastic deformation," *Progress in Materials Science*, vol. 45, pp. 103-189, 2000.
- [30] A. Shanaghi, *et al.*, "Effect of plasma CVD operating temperature on nanomechanical properties of TiC nanostructured coating investigated by atomic force microscopy," *Materials Research Bulletin*, vol. 47, pp. 2200-2205, 2012.
- [31] Y. C. Lee, *et al.*, "Deposition of nanostructured thin films using an inductively coupled plasma chemical vapor deposition technique," *Ceramics International*, vol. 30, pp. 1869-1872, 2004.
- [32] P. Panjan, *et al.*, "Growth defect density in PVD hard coatings prepared by different deposition techniques," *Surface and Coatings Technology*, vol. 237, pp. 349-356, 2013.
- [33] L. Ding, *et al.*, "Effects of sintering temperature on fine-grained tungsten heavy alloy produced by high-energy ball milling assisted spark plasma sintering," *International Journal of Refractory Metals and Hard Materials*, vol. 33, pp. 65-69, 2012.
- [34] J. Saida, *et al.*, "Nanostructure controlling in Zr-based metallic glasses using icosahedral local structure," *Journal of Alloys and Compounds*, vol. 483, pp. 231-234, 2009.
- [35] A. Inoue and A. Takeuchi, "Recent progress in bulk glassy, nanoquasicrystalline and nanocrystalline alloys," *Materials Science and Engineering: A*, vol. 375-377, pp. 16-30, 2004.
- [36] V. M. Segal, "Equal channel angular extrusion: from macromechanics to structure formation," *Materials Science and Engineering: A*, vol. 271, pp. 322-333, 1999.
- [37] Y. Saito, *et al.*, "Novel ultra-high straining process for bulk materials—development of the accumulative roll-bonding (ARB) process," *Acta Materialia*, vol. 47, pp. 579-583, 1999.
- [38] P. Bridgman, "Effects of High Shearing Stress Combined with High Hydrostatic Pressure," *Physical Review*, vol. 48, pp. 825-847, 1935.
- [39] R. Z. Valiev, *et al.*, "Plastic deformation of alloys with submicron-grained structure," *Materials Science and Engineering: A*, vol. 137, pp. 35-40, 1991.

-
- [40] L. J. Kecskes, *et al.*, "Grain size engineering of bcc refractory metals: Top-down and bottom-up—Application to tungsten," *Materials Science and Engineering: A*, vol. 467, pp. 33-43, 2007.
- [41] A. Zhilyaev and T. G. Langdon, "Using high-pressure torsion for metal processing: Fundamentals and applications," *Progress in Materials Science*, vol. 53, pp. 893-979, 2008.
- [42] P. Bridgman, "Studies in large plastic flow and fracture," 1952.
- [43] Y. Ito and Z. Horita, "Microstructural evolution in pure aluminum processed by high-pressure torsion," *Materials Science and Engineering: A*, vol. 503, pp. 32-36, 2009.
- [44] Y. Z. Tian, *et al.*, "Microstructural evolution and mechanical properties of a two-phase Cu–Ag alloy processed by high-pressure torsion to ultrahigh strains," *Acta Materialia*, vol. 59, pp. 2783-2796, 2011.
- [45] B. Srinivasarao, *et al.*, "On the relation between the microstructure and the mechanical behavior of pure Zn processed by high pressure torsion," *Materials Science and Engineering: A*, vol. 562, pp. 196-202, 2013.
- [46] H. P. Stüwe, "Equivalent Strains in Severe Plastic Deformation," *Advanced Engineering Materials*, vol. 5, pp. 291-95, 2003.
- [47] R. Pippan, *et al.*, "Saturation of Fragmentation During Severe Plastic Deformation," *Annual Review of Materials Research*, vol. 40, pp. 319-343, 2010.
- [48] Z. Horita and T. G. Langdon, "Microstructures and microhardness of an aluminum alloy and pure copper after processing by high-pressure torsion," *Materials Science and Engineering: A*, vol. 410-411, pp. 422-425, 2005.
- [49] F. Wetscher and R. Pippan, "Cyclic high-pressure torsion of nickel and Armco iron," *Philosophical Magazine*, vol. 86, pp. 5867-5883, 2006.
- [50] S. Scheriau, *et al.*, "Deformation mechanisms of a modified 316L austenitic steel subjected to high pressure torsion," *Materials Science and Engineering: A*, vol. 528, pp. 2776-2786, 2010.
- [51] D. A. Hughes and N. Hansen, "High angle boundaries formed by grain subdivision mechanisms," *Acta Materialia*, vol. 45, pp. 3871-3886, 1997.
- [52] F. A. Mohamed and S. S. Dheda, "On the minimum grain size obtainable by high-pressure torsion," *Materials Science and Engineering: A*, vol. 558, pp. 59-63, 2012.

-
- [53] Y. B. Wang, *et al.*, "The role of stacking faults and twin boundaries in grain refinement of a Cu–Zn alloy processed by high-pressure torsion," *Materials Science and Engineering: A*, vol. 527, pp. 4959-4966, 2010.
- [54] Y. H. Zhao, *et al.*, "Evolution of defect structures during cold rolling of ultrafine-grained Cu and Cu–Zn alloys: Influence of stacking fault energy," *Materials Science and Engineering: A*, vol. 474, pp. 342-347, 2008.
- [55] A. Vorhauer, *et al.*, "Influence of processing temperature on microstructural and mechanical properties of high-alloyed single-phase steels subjected to severe plastic deformation," *Materials Science and Engineering: A*, vol. 410-411, pp. 281-284, 2005.
- [56] F. Wetscher, *et al.*, "Structural refinement of low alloyed steels during severe plastic deformation," *Materials Science and Engineering: A*, vol. 387-389, pp. 809-816, 2004.
- [57] G. B. Rathmayr and R. Pippan, "Influence of impurities and deformation temperature on the saturation microstructure and ductility of HPT-deformed nickel," *Acta Materialia*, vol. 59, pp. 7228-7240, 2011.
- [58] I. Sabirov and R. Pippan, "Characterization of tungsten fragmentation in a W–25%Cu composite after high-pressure torsion," *Materials Characterization*, vol. 58, pp. 848-853, 2007.
- [59] F. A. Mohamed, "A dislocation model for the minimum grain size obtainable by milling," *Acta Materialia*, vol. 51, pp. 4107-4119, 2003.
- [60] Y. H. Zhao, *et al.*, "Influence of stacking fault energy on the minimum grain size achieved in severe plastic deformation," *Materials Science and Engineering: A*, vol. 463, pp. 22-26, 2007.
- [61] E. O. Hall, "Variation of Hardness of Metals with Grain Size," *Nature*, vol. 173, pp. 948-949, 1954.
- [62] M. A. Meyers and K. K. Chawla, *mechanical behavior of materials*, second ed. New York: Cambridge University Press, 2009.
- [63] A. P. Zhilyaev, *et al.*, "The microstructural characteristics of ultrafine-grained nickel," *Materials Science and Engineering: A*, vol. 391, pp. 377-389, 2005.
- [64] A. P. Zhilyaev, *et al.*, "Microstructural characteristics of nickel processed to ultrahigh strains by high-pressure torsion," *Materials Science and Engineering: A*, vol. 489, pp. 207-212, 2008.

-
- [65] Honggang Jiang, *et al.*, "Microstructural evolution, microhardness and thermal stability of HPT-processed Cu," *Materials Science and Engineering A*, vol. 290, pp. 128-138, 2000.
- [66] Y. T. Zhu and T. G. Langdon, "Influence of grain size on deformation mechanisms: An extension to nanocrystalline materials," *Materials Science and Engineering: A*, vol. 409, pp. 234-242, 2005.
- [67] G. J. Fan, *et al.*, "A model for the inverse Hall–Petch relation of nanocrystalline materials," *Materials Science and Engineering: A*, vol. 409, pp. 243-248, 2005.
- [68] T. G. Nieh and J. Wadsworth, "Hall-petch relation in nanocrystalline solids," *Scripta Metallurgica et Materialia*, vol. 25, pp. 955-958, 1991.
- [69] C. S. Pande and K. P. Cooper, "Nanomechanics of Hall–Petch relationship in nanocrystalline materials," *Progress in Materials Science*, vol. 54, pp. 689-706, 2009.
- [70] M. Faleschini, *et al.*, "Fracture toughness investigations of tungsten alloys and SPD tungsten alloys," *Journal of Nuclear Materials*, vol. 367-370, pp. 800-805, 2007.
- [71] Y. H. Zhao, *et al.*, "Determining the optimal stacking fault energy for achieving high ductility in ultrafine-grained Cu–Zn alloys," *Materials Science and Engineering: A*, vol. 493, pp. 123-129, 2008.
- [72] Y. B. Wang, *et al.*, "Introducing a strain-hardening capability to improve the ductility of bulk metallic glasses via severe plastic deformation," *Acta Materialia*, vol. 60, pp. 253-260, 2012.
- [73] S. V. Dobatkin, *et al.*, "Grain refinement and superplastic flow in an aluminum alloy processed by high-pressure torsion," *Materials Science and Engineering: A*, vol. 408, pp. 141-146, 2005.
- [74] M. Kai, *et al.*, "Developing grain refinement and superplasticity in a magnesium alloy processed by high-pressure torsion," *Materials Science and Engineering: A*, vol. 488, pp. 117-124, 2008.
- [75] A. V. Sergueeva, *et al.*, "Superplastic behaviour of ultrafine-grained Ti–6Al–4V alloys," *Materials Science and Engineering: A*, vol. 323, pp. 318-325, 2002.
- [76] X. H. An, *et al.*, "Enhanced strength–ductility synergy in nanostructured Cu and Cu–Al alloys processed by high-pressure torsion and subsequent annealing," *Scripta Materialia*, vol. 66, pp. 227-230, 2012.
- [77] X. H. An, *et al.*, "High strength and utilizable ductility of bulk ultrafine-grained Cu–Al alloys," *Applied Physics Letters*, vol. 92, p. 201915, 2008.

-
- [78] P. Zhang, *et al.*, "Optimizing strength and ductility of Cu–Zn alloys through severe plastic deformation," *Scripta Materialia*, vol. 67, pp. 871-874, 2012.
- [79] G. Langdon, "The use of severe plastic deformation for microstructural control," 2002.
- [80] H. Yilmazer, *et al.*, "Heterogeneous structure and mechanical hardness of biomedical - type Ti–29Nb–13Ta–4.6Zr subjected to high-pressure torsion," *Journal of the Mechanical Behavior of Biomedical Materials*, vol. 10, pp. 235-245, 2012.
- [81] R. Pippan, "Influence of impurities and deformation temperature on the saturation microstructure and ductility of HPT-deformed nickel," *Acta Materialia*, vol. 59, pp. 7228-7240, 2011.
- [82] S. Qu, *et al.*, "Microstructural evolution and mechanical properties of Cu–Al alloys subjected to equal channel angular pressing," *Acta Materialia*, vol. 57, pp. 1586-1601, 2009.
- [83] A. Hohenwarter and R. Pippan, "A comprehensive study on the damage tolerance of ultrafine-grained copper," *Materials Science and Engineering: A*, vol. 540, pp. 89-96, 2012.
- [84] X. Sauvage, *et al.*, "Nanostructure and properties of a Cu–Cr composite processed by severe plastic deformation," *Scripta Materialia*, vol. 58, pp. 1125-1128, 2008.
- [85] R. Wadsack, *et al.*, "The effect of pre-deformation on the ductility of chromium," *Journal of Nuclear Materials*, vol. 307–311, pp. 701–704, 2002.
- [86] A. Hohenwarter and R. Pippan, "Fracture of ECAP-deformed iron and the role of extrinsic toughening mechanisms," *Acta Materialia*, vol. 61, pp. 2973-2983, 2013.
- [87] A. Bachmaier, *et al.*, "The formation of supersaturated solid solutions in Fe–Cu alloys deformed by high-pressure torsion," *Acta Materialia*, vol. 60, pp. 860-871, 2012.
- [88] R. Vafaei, *et al.*, "Evaluation of mechanical behavior of nano-grained 2024 Al alloy during high pressure torsion (HPT) process at various temperatures," *Materials Science and Engineering: A*, vol. 536, pp. 73-81, 2012.
- [89] Q. Wei, *et al.*, "Microstructure and mechanical properties of super-strong nanocrystalline tungsten processed by high-pressure torsion," *Acta Materialia*, vol. 54, pp. 4079-4089, 2006.
- [90] Q. Wei, *et al.*, "Microstructure and mechanical properties at different length scales and strain rates of nanocrystalline tantalum produced by high-pressure torsion," *Acta Materialia*, vol. 59, pp. 2423-2436, 2011.

-
- [91] R. Valiev, *et al.*, "The effect of annealing on tensile deformation behavior of nanostructured SPD titanium," *Scripta Materialia*, vol. 49, pp. 669-674, 2003.
- [92] N. Krasilnikov, *et al.*, "Tensile strength and ductility of ultra-fine-grained nickel processed by severe plastic deformation," *Materials Science and Engineering: A*, vol. 397, pp. 330-337, 2005.
- [93] V. R. Olaf Engler, "Introduction to Texture Analysis Macrotexture, Microtexture, and Orientation Mapping, Second Edition," 2009.
- [94] N. S and K. S, "The diffraction of cathode rays by calcite," *Proc Imperial Acad (Japan)*, vol. 4, pp. 475-477, 1928.
- [95] A. J. Schwartz, *et al.*, *Electron Backscatter Diffraction in Materials Science*: Springer Science+Business Media, LLC 2009, 2009.
- [96] H. J. Bunge, "Texture Analysis in Materials Science: Mathematical Methods," *Butterworths, London*, 1982.
- [97] H. J. Bunge, "Texture analysis in materials science: mathematical methods.," *Cuvillier Verlag, Gottingen*, 1993.
- [98] H. J. Bunge, "Partial Texture Analysis," *Textures and Microstructures*, vol. 12, pp. 47-63, 1990.
- [99] F. J. Humphreys, "Review: Grain and subgrain characterisation by electron backscatter diffraction," *Journal of Materials Science*, vol. 36, pp. 3833-3854, 2001.
- [100] P. T. Austin Day, "HKL Technology CHANNEL 5 Handbook," 2004.
- [101] S. Meister, "grain and particle analysis with line intersection method," 2012.
- [102] J. K. Mackenzie, "second paper on statistics associated with the random disorientation of cubes," *Biometrika*, vol. 45, pp. 229-240, 1958.
- [103] A. Meneses-Amador, *et al.*, "An expression to determine the Vickers indentation fracture toughness obtained by the finite element method on Fe2B layers," *Surface and Coatings Technology*, 2012.
- [104] W. G. Mao, *et al.*, "Evaluation of microhardness, fracture toughness and residual stress in a thermal barrier coating system: A modified Vickers indentation technique," *Surface and Coatings Technology*, vol. 206, pp. 4455-4461, 2012.
- [105] A. Leonardi, *et al.*, "Numerical analysis of brittle materials fractured by sharp indenters," *Engineering Fracture Mechanics*, vol. 77, pp. 264-276, 2010.

-
- [106] J. H. Lee, *et al.*, "Cohesive interface simulations of indentation cracking as a fracture toughness measurement method for brittle materials," *Acta Materialia*, vol. 60, pp. 5448-5467, 2012.
- [107] J. J. Kruzic, *et al.*, "Indentation techniques for evaluating the fracture toughness of biomaterials and hard tissues," *Journal of the Mechanical Behavior of Biomedical Materials*, vol. 2, pp. 384-395, 2009.
- [108] W. C. Oliver and G. M. Pharr, "An improved technique for determining hardness and elastic modulus using load and displacement sensing indentation experiments," *Journal of Materials Research*, vol. 7, pp. 1564-1583, 1992.
- [109] W. C. Oliver and G. M. Pharr, "Measurement of hardness and elastic modulus by instrumented indentation Advances in understanding and refinements to methodology," *Materials Research Society*, vol. 19, pp. 3-20, 2003.
- [110] G. M. Pharr and A. Bolshakov, "understanding nanoindentation unloading curves," *Journal of Materials Research*, vol. 17, pp. 2660-2671, 2002.
- [111] D. Kuhlmann-wilsdorf, "Theory of Workhardening 1934-1984," *Metallurgical Transactions*, vol. 16A, pp. 2091-2108, 1985.
- [112] B. Yang, *et al.*, "Strain effects on the coarsening and softening of electrodeposited nanocrystalline Ni subjected to high pressure torsion," *Scripta Materialia*, vol. 58, pp. 790-793, 2008.
- [113] A. P. Zhilyaev, *et al.*, "Particle and grain growth in an Al-Si alloy during high-pressure torsion," *Scripta Materialia*, vol. 57, pp. 763-765, 2007.
- [114] S. Ni, *et al.*, "Grain growth and dislocation density evolution in a nanocrystalline Ni - Fe alloy induced by high-pressure torsion," *Scripta Materialia*, vol. 64, pp. 327-330, 2011.
- [115] S. Ni, *et al.*, "Strain softening in nanocrystalline Ni-Fe alloy induced by large HPT revolutions," *Materials Science and Engineering: A*, vol. 528, pp. 4807-4811, 2011.
- [116] S. Ni, *et al.*, "Elemental redistribution in a nanocrystalline Ni-Fe alloy induced by high-pressure torsion," *Materials Science and Engineering: A*, vol. 528, pp. 7500-7505, 2011.
- [117] I. V. Alexandrov, *et al.*, "Analysis of the deformation mechanisms in bulk ultrafine grained metallic materials," *Materials Science and Engineering: A*, vol. 463, pp. 27-35, 2007.

-
- [118] K. Edalati, *et al.*, "Dynamic recrystallization and recovery during high-pressure torsion: Experimental evidence by torque measurement using ring specimens," *Materials Science and Engineering: A*, vol. 559, pp. 506-509, 2013.
- [119] Y. Cao, *et al.*, "A visualization of shear strain in processing by high-pressure torsion," *Journal of Materials Science*, vol. 45, pp. 765-770, 2009.
- [120] Y. Cao, *et al.*, "Three-dimensional shear-strain patterns induced by high-pressure torsion and their impact on hardness evolution," *Acta Materialia*, vol. 59, pp. 3903-3914, 2011.
- [121] F. J. Humphreys, *Recrystallization and Related Annealing Phenomena*. Oxford: Elsevier Ltd, 2004.
- [122] H. Azizi-Alizamini, *et al.*, "A novel technique for developing bimodal grain size distributions in low carbon steels," *Scripta Materialia*, vol. 57, pp. 1065-1068, 2007.
- [123] E. Schafler and R. Pippan, "Effect of thermal treatment on microstructure in high pressure torsion (HPT) deformed nickel," *Materials Science and Engineering: A*, vol. 387-389, pp. 799-804, 2004.
- [124] H. W. Zhang, *et al.*, "Thermal behavior of Ni (99.967% and 99.5% purity) deformed to an ultra-high strain by high pressure torsion," *Acta Materialia*, vol. 58, pp. 1698-1707, 2010.
- [125] G. R. Anstis, *et al.*, "A Critical Evaluation of Indentation Techniques for Measuring Fracture Toughness: I, Direct Crack Measurements," *Journal of the American Ceramic Society*, vol. 64, pp. 533-538, 1980.
- [126] Y. Estrin, *et al.*, "Strain gradient plasticity modelling of high-pressure torsion," *Journal of the Mechanics and Physics of Solids*, vol. 56, pp. 1186-1202, 2008.

Appendix

A. Equivalent strain calculation

The strain status of HPT deformed material can be described as:

$$\varepsilon = \begin{pmatrix} \varepsilon_{rr} & 0 & 0 \\ 0 & \varepsilon_{\varphi\varphi} & \varepsilon_{\varphi z} \\ 0 & \varepsilon_{z\varphi} & \varepsilon_{zz} \end{pmatrix} \quad (1)$$

$$\varepsilon_{rr} = \varepsilon_{\varphi\varphi} = -\frac{1}{2}\varepsilon_{zz} \quad (2)$$

the von Mises strain can be expressed as following combining eq. (1) and eq. (2):

$$\varepsilon_v = \sqrt{\frac{2}{3} \cdot \varepsilon : \varepsilon} = \sqrt{\frac{2}{3} \cdot \sqrt{\varepsilon_{rr} \cdot \varepsilon_{rr} + \varepsilon_{\varphi\varphi}^2 + \varepsilon_{zz}^2 + \varepsilon_{\varphi z}^2 + \varepsilon_{z\varphi}^2}} = \sqrt{\varepsilon_{zz}^2 + \frac{4}{3} \cdot \varepsilon_{\varphi z}^2} \quad (3)$$

if h is constant,

$$\varepsilon_{zz} = 0 \quad (4)$$

besides,

$$\varepsilon_{\varphi z} = \frac{\gamma}{2} \quad (5)$$

where γ is shear strain. Shear strain incremental is given by:

$$d\gamma = \frac{dl}{h} = \frac{rd\theta}{h} \quad (6)$$

in which h is the height of specimen, other parameters are displayed in Fig. 2.1. Besides, $\theta = 2\pi N$, where N is the torsion revolution, shear strain can be written as:

$$\gamma = \frac{2\pi N \cdot r}{h} \quad (7)$$

Therefore, combining eq. (3), eq. (4), eq. (5) and eq. (7), von Mises strain with constant height can be expressed as:

$$\varepsilon_E = \frac{\gamma}{\sqrt{3}} = \frac{2 \cdot \pi \cdot N \cdot r}{\sqrt{3} \cdot h} \quad (8)$$

by this equation, equivalent engineering strain in Fig. 2.4 is plotted by using initial height $h=1\text{mm}$; Reference strain is calculated for comparison by using finite height $h=0.2\text{mm}$. This equation is marked eq. (2.2) in chapter 2.

However, actually h is not constant during HPT. For calculating equivalent true strain during HPT, fitting function of sample height is given in equation (2.3), with $h_\infty = 0.2\text{mm}$; $h_0 = 0.8\text{mm}$; $b = 0.28$. The axial strain component in eq. (3) can be written as:

$$\varepsilon_{zz} = \int_{h_0}^h \frac{1}{h} dh = \ln\left(\frac{h(\theta)}{h_0}\right) = \ln\left(\frac{h_\infty - (h_\infty - h_0) \cdot e^{-b \cdot 2\pi N}}{h_0}\right) \quad (9)$$

increment of shear strain is different compared to eq. (6), and is as:

$$d\gamma = \frac{dl}{h} = \frac{r d\theta}{h(\theta)} \quad (10)$$

thus the shear strain component is expressed as:

$$\varepsilon_{\phi z} = \int_{\theta_0}^{\theta} \frac{r}{2h(\theta)} d\theta = \frac{r}{2bh_\infty} \left(\ln(e^{b\theta} - \left(1 - \frac{h_0}{h_\infty}\right)) - \ln(e^{b\theta_0} - \left(1 - \frac{h_0}{h_\infty}\right)) \right) \quad (11)$$

Besides, $\theta = 2\pi N$,

$$\varepsilon_{\phi z} = \frac{r}{2bh_\infty} \left(\ln(e^{b \cdot 2\pi N} - \left(1 - \frac{h_0}{h_\infty}\right)) - \ln(e^{b \cdot 2\pi N_0} - \left(1 - \frac{h_0}{h_\infty}\right)) \right) \quad (12)$$

substituting eq. (9) and eq. (12) to eq. (3), the true von Mises strain is given by:

$$\varepsilon_T = \sqrt{\left(\ln\left(\frac{h_\infty - (h_\infty - h_0)e^{-b \cdot 2\pi N}}{h_0}\right) \right)^2 + \frac{4}{3} \left[\frac{r}{2bh_\infty} \left(\ln(e^{b \cdot 2\pi N} - \left(1 - \frac{h_0}{h_\infty}\right)) - \ln\left(\frac{h_0}{h_\infty}\right) \right) \right]^2} \quad (13)$$

the calculated equivalent true strain plotted in Fig. 2.4 is using eq. (13), which is marked as eq.(2.4) in chapter 2.

When Finite element simulation conducted in ABAQUS, the axisymmetric model is employed, the geometry and the mesh are displayed as following:

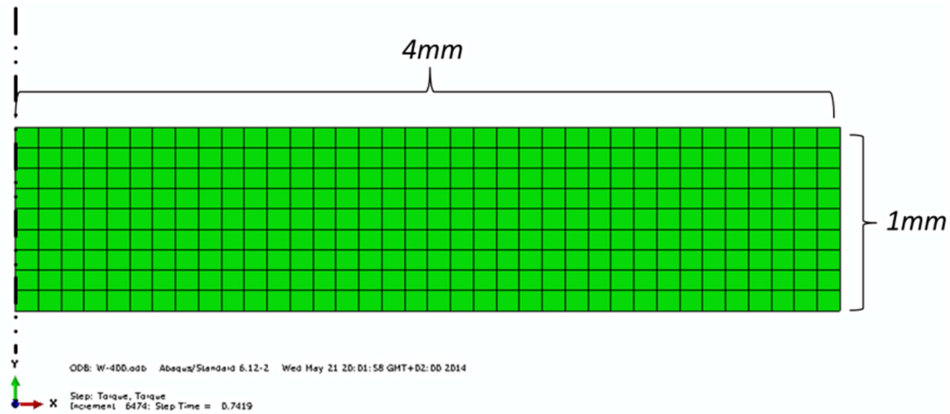


Fig. 1: Geometry and mesh of axisymmetric model used in ABAQUS.

The material properties of W are listed:

Table 1: Material properties of W employed in ABAQUS.

Temperature	Young's modulus	Poisson's ratio	Yield stress
/°C	/MPa		/MPa
400	394480	0.3	947.86

The displacement along axis direction is set stepwise, from I to III in the sample height reduction figure, as is shown in Fig. 2.

The displacement along shear direction is static from 0 to 2π . During the simulation, none linear button is on. The algorithm is quasi newton method. After each $\pi/8$ torsion angle, the equivalent strain from the position, which is 3mm from torsion axis is recorded, the data is plotted as simulated equivalent true strain in Fig. 2.4.

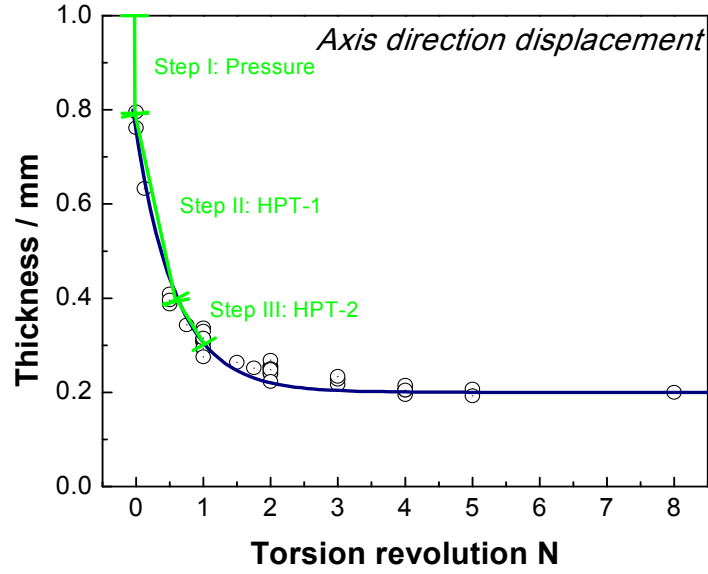


Fig. 2: Sample height reduction and the stepwise of axial displacement of sample in ABAQUS.

While by Finite element simulation in ABAQUS, one considers the von Mises strain in the integral of strain rate, and it can be written as:

$$\delta = \int_0^t \frac{\partial \delta}{\partial t} dt = \int_0^\theta \frac{\partial \delta}{\partial \theta} d\theta = \int_0^\theta \sqrt{\left(\frac{\partial \delta_{zz}}{\partial \theta}\right)^2 + \frac{4}{3} \left(\frac{\partial \delta_{\varphi z}}{\partial \theta}\right)^2} d\theta \quad (14)$$

the integral of both components are:

$$\frac{\partial \delta_{zz}}{\partial \theta} = \frac{b(h_\infty - h_0)e^{-b\theta}}{h_\infty - (h_\infty - h_0)e^{-b\theta}} \quad (15)$$

$$\frac{\partial \delta_{\varphi z}}{\partial \theta} = \frac{r}{2h(\theta)} = \frac{r/2}{h_\infty - (h_\infty - h_0)e^{-b\theta}} \quad (16)$$

combining eq. (14), eq. (15) and eq. (16), the expression of von Mises in the integral of strain rate can be obtained. However, there is no analytical solution but numerical solution, which is acquired by Matlab Quad function, as listed as following table:

Table 2: Numerical solution of eq. (14) combining eq. (15) and eq. (16).

Torsion revolution	strain	Torsion revolution	strain
0.1	1.3957	1.2	31.6972
0.2	2.9955	1.3	35.7727
0.3	4.8119	1.4	40.0207
0.4	6.8553	1.5	44.4248
0.5	9.1342	2	68.2464
0.6	11.6538	3	120.4869
0.7	14.416	4	174.5109
0.8	17.4194	5	228.8573
0.9	20.6589	6	283.2595
1	24.1261	7	337.6715
1.1	27.81	8	392.0851

B. Cone-shaped sample method

This method refers to employing cone-shaped sample instead of traditional disk-shaped sample during HPT, aiming to obtain a homogenous sample within limited torsion revolution. The sketches for cone-shaped and traditional disk-shaped samples are illustrated in Fig. 3 a). Considering the sharp tip may act as an indenter during HPT, Nicrofer is chosen to fabricate the sample because its ductility. HPT are conducted at room temperature with pressure of 2GPa. Strain rate is 5rpm.

At the beginning of HPT, when the compressive load is subjected to cone-shaped sample, a strain accumulation gradient is generated on sample, which has the maximum value at the center of sample. The sample height is reduced from 5mm to ~2mm due to compression. Therefore, the geometry of reference disk-shaped sample is designed to achieve similar height after compression for better comparison. HPT experiments are conducted under the same condition for both samples. After one torsion revolutions, the Vickers indentation is performed on the sample surface, and the results are shown in Fig. 3 b). It is observed that the disk-shaped sample exhibits basin curve which is typical after conventional HPT. While the cone-shaped sample demonstrates less difference between sample center and edge. This is suggesting that by employing cone-shaped sample, the material obtained from HPT is more homogeneous than traditional disk-shaped sample after only one torsion revolution.

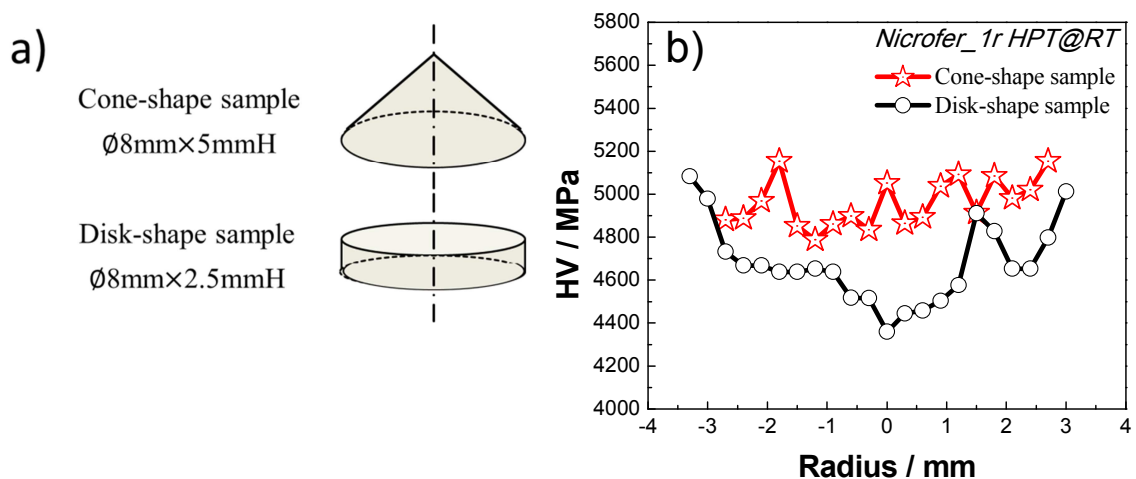


Fig. 3: a) Sketches of cone-shaped sample and traditional disk-shaped sample;
b) Hardness distribution along sample radius after high-pressure torsion at room temperature with 1 torsion revolution.

Inspired by the results from cone-shaped Nicrofer, a surface treatment method is introduced. As is illustrated in Fig. 4, the sample geometry consists of double-cone and a cylinder main body. By subjecting to HPT, the both sides of the sample could obtain a uniform nanoscale microstructure concurrently. While by assistance of ring part positioned surrounding the sample, as well as by carefully controlled compression process during HPT, the main body might maintain its geometry. This combination of coarse-grain body and nanostructured surfaces could be of interest for specific requirements.

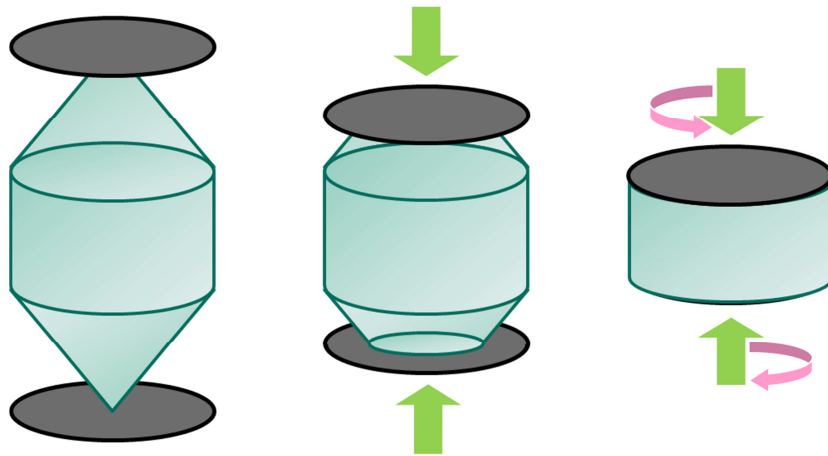


Fig. 4: Illustration of double-cone-shaped sample subjected to high-pressure torsion.

List of publications

Yiming Wang*, Jarir Aktaa, “Development of nanostructured WL10 with outstanding thermal stability by High-Pressure Torsion”, in preparation.

Yiming Wang*, Widodo Basuki, Jarir Aktaa, “Development of homogeneous materials processed by High-Pressure Torsion”, in preparation.

Yiming Wang*, Widodo Basuki, Stefan Knaak, Jarir Aktaa, “Investigation of nanostructured W and WL10 by high pressure torsion” Poster, 16th International Conference On Fusion Reactor Materials (2013) Beijing, China.

Yiming Wang, Lijing Zheng*, Shujie Pang, “Formation and mechanical properties of MgCuAlGd Bulk metallic glass composites” Materials Science Forum, Vol. 650 (2010) pp.290-294.

Zhe Lv, Yiming Wang, Lijing Zheng,* Wenli Gao, “Finite element analysis of effect of route on strain uniformity of 7050 aluminum alloys during ECAE” Poster, “International Conference on Advanced Materials, Development and Performance” (2008) Beijing, China.

Zheng Zhou, Lu Wang, Fuchi Wang, Huanwu Cheng, Haifeng Zhang, Saihua Xu, Yiming Wang, “Microstructure and Properties of Fe-Based Amorphous Alloy Coatings”, Transactions of Beijing institute of technology (2008).

Curriculum Vitae

Personal information:

Name: Yiming Wang
Email: claire_wangym@163.com
Nationality: Chinese

Education background:

09.2007 – 03.2010 M. Sc. in material science and engineering, Beijing University of Aeronautics and Astronautics (BUAA), Beijing, China
09.2010 – 06.2014 Ph.D. student in Karlsruhe Institute of Technology (KIT), Karlsruhe, Germany